Growth from melt by micro-pulling down (μ-PD) and Czochralski (Cz) techniques and characterization of LGSO and garnet scintillator crystals

Valerii Kononets

N° d'ordre Année 2014

THESE DE L'UNIVERSITE DE LYON

Délivrée par
L'UNIVERSITE CLAUDE BERNARD LYON 1

ECOLE DOCTORALE
Chimie

DIPLOME DE DOCTORAT
(Arrêté du 7 août 2006)
Soutenue publiquement le 15 décembre 2014

par

VALERII KONONETS

Titre

Croissance cristalline de cristaux scintillateurs de LGSO et de grenats à partir de l'état liquide par les techniques Czochralski (Cz) et micro-pulling down (µ-PD) et leurs caractérisations

Directeur de thèse :
M. Kheirreddine Lebbou
Co-directeur de thèse :
M. Oleg Sidletskiy

JURY

Mme Etiennette Auffray Hillemans	Rapporteur
M. Alain Braud	Rapporteur
M. Alexander Gektin	Examinateur
M. Christophe Dujardin	Examinateur
M. Julien Houel	Examinateur
M. Kheirreddine Lebbou	Directeur de thèse
M. Oleg Sidletskiy	Co-directeur de thèse

UNIVERSITE CLAUDE BERNARD - LYON 1

Président de l'Université	**M. François-Noël GILLY**
Vice-président du Conseil d'Administration	M. le Professeur Hamda BEN HADID
Vice-président du Conseil des Etudes et de la Vie Universitaire	M. le Professeur Philippe LALLE
Vice-président du Conseil Scientifique	M. le Professeur Germain GILLET
Directeur Général des Services	M. Alain HELLEU

COMPOSANTES SANTE

Faculté de Médecine Lyon Est – Claude Bernard	Directeur : M. le Professeur J. ETIENNE
Faculté de Médecine et de Maïeutique Lyon Sud – Charles Mérieux	Directeur : Mme la Professeure C. BURILLON
Faculté d'Odontologie	Directeur : M. le Professeur D. BOURGEOIS
Institut des Sciences Pharmaceutiques et Biologiques	Directeur : Mme la Professeure C. VINCIGUERRA
Institut des Sciences et Techniques de la Réadaptation	Directeur : M. le Professeur Y. MATILLON
Département de formation et Centre de Recherche en Biologie Humaine	Directeur : Mme. la Professeure A-M. SCHOTT

COMPOSANTES ET DEPARTEMENTS DE SCIENCES ET TECHNOLOGIE

Faculté des Sciences et Technologies	Directeur : M. F. DE MARCHI
Département Biologie	Directeur : M. le Professeur F. FLEURY
Département Chimie Biochimie	Directeur : Mme Caroline FELIX
Département GEP	Directeur : M. Hassan HAMMOURI
Département Informatique	Directeur : M. le Professeur S. AKKOUCHE
Département Mathématiques	Directeur : M. le Professeur Georges TOMANOV
Département Mécanique	Directeur : M. le Professeur H. BEN HADID
Département Physique	Directeur : M. Jean-Claude PLENET
UFR Sciences et Techniques des Activités Physiques et Sportives	Directeur : M. Y.VANPOULLE
Observatoire des Sciences de l'Univers de Lyon	Directeur : M. B. GUIDERDONI
Polytech Lyon	Directeur : M. P. FOURNIER
Ecole Supérieure de Chimie Physique Electronique	Directeur : M. G. PIGNAULT
Institut Universitaire de Technologie de Lyon 1	Directeur : M. le Professeur C. VITON
Ecole Supérieure du Professorat et de l'Education	Directeur : M. le Professeur A. MOUGNIOTTE
Institut de Science Financière et d'Assurances	Directeur : M. N. LEBOISNE

Acknowledgement

In connection with versatility of this work a lot of scientists from different institutions and countries were involved. Originally the work was done in the frame of collaboration between the Institute for Scintillation Material (ISMA) (Ukraine) and Institut Lumière Matière (ILM), UMR5306 CNRS, Universite de Lyon 1, France.

In the first instance I can never thank enough my supervisors. Dr. Kheirreddine Lebbou taught me how to grow crystals by micro-pulling down method which I have never done before. It is an honor for me to be a PhD student of Dr. Oleg Sidletskiy who is a chief of the Single Crystal Growth Technology Department of ISMA. With their help my work was originally destined for success.

Doctor Etiennette Auffray Hillemans (CERN) and Dr Alain Braud from (CIMAP, Caen University) accepted to review this work as referee and members of the jury. I thank them strongly for their time, and their helpful advices and remarks.

I am eager to express my gratitude to members of the jury that accepted to judge this work: Professor Alexander Gektin (ISMA, Kharkov), Professor Christophe Dujardin (ILM, UCB Lyon 1) and Doctor Julien Houel (ILM, UCB Lyon 1)

This work was realized in the frame of joint cotutelle PHD thesis between UCB Lyon 1 and ISMA, Kharkov. I am deeply indebted to the members of ISMA. I would like to thank for helping me scientists from my home institution. V. Bondar, S. Tkachenko, O. Voloshina, D. Kurtsev, P. Arhipov, S. Vasyukov, E. Galenin and I. Gerasymov from ISMA helped me a lot in the understanding of Czochralski growth process. I am thankful to S. Gridin, S. Neicheva, N. Starzhinsky, I. Zenya (ISMA), V. Baumer and K. Belikov (SSI “Institute for Single Crystals” NAS of Ukraine) for characterization of the grown crystals.

In the course of the work a part of microscopy measurements was made in Semiconductor Physics Department and Institute of Applied Research, Vilnius

University, Lithuania. Thank so much to D. Dobrovolskas, G. Tamulaitis and A. Vaitkevičius.

I am very grateful to O. Benamara (ILM) and X. Xu (Shanghai Institute of Optics and Fine Mechanics) for their great assistance during my work in France. I thank very much indeed to G. Patton, F. Moretti for help in the fibers characterization in ILM laboratory provided. Special thanks to A. Belsky and C. Dujardin for their professional advises.

Many thanks to W. Su (Jiangsu University, China) and T. Duffar (SIMAP-EPM, France) whom I am obliged for a modeling of the growth process. Their advices and recommendation were very important to take benefit from the simulation and modeling results.

I am deeply indebted to K. Pauwels, M. Lucchini, A. Benaglia and E. Auffray (CERN, PH-CMX, laboratory 27), who also made testing of grown fibers in Fermi National Laboratory, USA.

This work was supported by the Project FP7-INCO-2011-6 ("SUCCESS"), Eiffel grant, and Project No. 28317ZC in the framework of French-Ukrainian Science and Technical Collaboratrion "DNIPRO". The study at Vilnius University was funded from the European Community's Social Foundation under Grant Agreementn. VP1-3.1-ŠMM-08-K-01–004/KS-120000-1756. The works provided in CERN were in the frame of Crystal Clear Collaboration. Part of results were obtained in the frame of INFINHI ANR project, we thank ANR for their financial support.

Contents

Abstract

A set of rare earth orthosilicate and garnet scintillators were grown by the micro-pulling down (μ-PD) and Czochralski methods. Ce-doped $Lu_{2x}Gd_{2-2x}SiO_5$ (LGSO:Ce) fibers were grown by the micro-pulling down (μ-PD) method for the first time. In order to determine the optimal activator concentration with regard to the best scintillating parameters, cerium concentration in the melt was varied within 0.01-1.5 at.%. A set of results on optical and scintillation characteristics of the grown fibers with the different activator content was determined and discussed. Distribution of Gd^{3+} and Ce^{3+} in LGSO:Ce structure was compared to the Czochralski grown crystals. Spatial distribution of cations across LGSO:Ce scintillation shaped crystals grown by the micro-pulling-down method is studied using wide-field microscopy under simultaneous excitation of both cerium-related centers and confocal microscopy under selective excitation of Ce^{3+} in CeO6 crystallographic sites.

Undoped fibers of $Lu_3Al_5O_{12}$ (LuAG) and doped by Ce^{3+}, Pr^{3+}, mixed $(Lu,Y)_3Al_5O_{12}$ (LuYAG) and $Y_3Al_5O_{12}$ (YAG) both doped by Ce^{3+} were produced to evaluate a possibility of their potential use in the new dual-calorimeter planned to operate in the upgraded Large Hadron Collider in CERN. The choice of grown crystals was made to detect scintillation (activated materials) and Cherenkov radiation (LuAG). Growth conditions for the improvement of fibers quality were selected basing on measurements of attenuation length of the fibers. The activator segregation coefficient in LuAG:Ce and LuYAG:Ce fibers was evaluated by the cathodoluminescence measurements. The effect of annealing and radiation damage was studied. The good productivity of the grown fibers was verified on the test beam calorimeter.

Structure and scintillation yield of $Y_3(Al_{1-x}Ga_x)_5O_{12}$:Ce solid solution crystals are studied. Crystals are grown from melt by the Czochralski method. Distribution of host cations in crystal lattice is determined. The trend of light output at Al/Ga substitution in $Y_3(Al_{1-x}Ga_x)_5O_{12}$:Ce is determined. Light output in mixed crystals reaches 130%

comparative to Ce-doped yttrium–aluminum garnet. The evolution of luminescence properties at Al/Ga substitution is studied.

Keywords: μ-PD method, high energy physics, oxides, silicates, garnets, scintillation crystals, fibers, light yield, attenuation length.

Résumé

Des lots de terres rares d'orthosilicates et de grenats scintillateurs ont été cristallisés par les méthodes micro-pulling down (μ-PD) et Czochralski. Pour la première fois des fibres $Lu_{2x}Gd_{2-2x}SiO_5$ dopées Ce (LGSO:Ce) (x = 0.5) ont été tirées par la méthode micro-pulling down (μ-PD). Dans le but de déterminer la concentration optimale de l'ion activateur avec les meilleurs paramètres de scintillation, la concentration du cérium dans le liquide a été variée dans l'intervalle 0.01-1.5at%. En fonction de la concentration de l'ion activateur nous avons discuté les caractéristiques optiques et scintillatrices dans les fibres cristallisées. La distribution du Gd^{3+} et du Ce^{3+} dans la structure LGSO :Ce a été comparée à celle des cristaux tirés par la méthode Czochralski. La distribution spatiale des cations le long des cristaux LGSO :Ce tirés par la méthode de la micro-pulling down a été étudiée par microscopie à champ proche et microscopie Confocale à travers l'excitation du Ce^{3+} sur les sites cristallographiques du CeO_6. Des fibres de composition $Lu_3Al_5O_{12}$ (LuAG) non dopées et dopées Ce^{3+} et Pr^{3+}, des matrices mixtes $(Lu,Y)_3Al_5O_{12}$ (LuYAG) et $Y_3Al_5O_{12}$ (YAG) dopés Ce^{3+} ont été fabriqués pour evaluer les possibilités de développer un calorimètre dual-readout pour fonctionner dans le Grand collisionneur de hadrons du CERN. Les cristaux LuAG ont été choisis dans le but de détecter la scintillation (ion activateur) et les radiations Chernkov. Pour confirmer l'amélioration de la qualité des fibres cristallines à travers les conditions de croissance cristalline, nous avons réalisé des mesures d'atténuation le long des fibres. Le coefficient de ségrégation de l'ion activateur dans le LuAG :Ce et LuYAG:Ce a été évalué par des mesures de cathodoluminescence. L'effet du recuit et la résistance aux radiations ont été étudiés. La bonne reproductivité des fibres a été vérifiée par des tests faisceau en conditions de calorimètre. Nous avons étudié la

structure et la scintillations dans les cristaux appartenant à la solution solide $Y_3(Al_{1-x}Ga_x)_5O_{12}$:Ce. Les cristaux ont été tirés à partir de l'état liquide par la méthode Czochralski. La distribution des cations de la matrice a été étudiée. L'effet de la substitution du Al/Ga dans $Y_3(Al_{1-x}Ga_x)_5O_{12}$:Ce sur le rendement de scintillation a été déterminé. Le rendement de scintillation a atteint 130% par rapport au grenat aluminium-yttrium dopé Ce. L'évolution des propriétés de luminescence en fonction de la substitution Al/Ga a été étudiée.

Mots clés : méthode μ-PD, Physique des hautes énergie, oxydes, silicates, grenats, cristaux scintillateurs, rendement de scintillation, longueur d'atténuation.

Introduction

Single crystal materials are widely used as detectors of ionizing radiations. Scintillation materials emit light when undergo ionizing radiation. Improvement of trustworthy and acquisition speed of medical diagnostics devices, border control and security systems is a driving force of search for new scintillators with improved properties. In the last decades, application of crystalline materials in ionizing radiation detectors has played a crucial role in fundamental research and promoted continuous progress in the detecting technique leading to huge electromagnetic calorimeters such as the CMS-ECAL at LHC [1] or future projects such the PANDA-EMC at FAIR [2]. The high quality of the CMS electromagnetic calorimeter based on $PbWO_4$ (PWO) and its good performance has allowed the discovery of the Higgs boson [3]. New concepts for next generation experiments include combined electromagnetic (EM) and hadron calorimeter based on dual readout by detecting the Cherenkov and scintillation light in different fiber materials [4]. The construction at FAIR, the announcement of the LHC upgrade (HL-LHC) and intensive developments of the ILC Program [5] will require cheap and radiation hard materials, capable for mass production.

For the decades scientists try to improve the scintillation efficiency of materials and to find new practical applications for them. Taking in account the difference in requirements to scintillators for the range of applications, there is no ideal scintillator. High scintillation yield and density, low cost are the basic criteria of material choice for most of applications. Nowadays the design of scanning devices in high energy physics, medicine and introscopy is based on different single crystal materials. Inorganic single crystals are the most appropriate due to the high density and stopping power, and the high light yield. Aluminates and silicates which are studied in this work rank among the most popular compounds used in these applications. For instance, the improvement of energy resolution of hadrons and jets measurements in high energy physics could be achieved in $Lu_3Al_5O_{12}$ (LuAG) fibers doped with Ce^{3+} [4, 6, 7]. Different inorganic scintillators are used in the positron emission tomography (PET) to identify

abnormalities in human and animal bodies [8, 9, 10]. High afterglow level in many oxide scintillators interferes their application in ranges where operation speed (computer tomography) or large signal-to-noise ratio (introscopy) are needed [11]. In this connection, $Lu_{2x}Gd_{2-2x}SiO_5$:Ce (LGSO:Ce) crystal can be considered as a promising scintillation material [11, 12, 13, 14].

LGSO is the one from the series of new efficient scintillators developed recently on the base of mixed crystals. Among the examples one can note solid solutions of oxide scintillators, such as $Lu_{2x}Y_{2-2x}SiO_5$:Ce (LYSO) [15], $Lu_xY_{1-x}AlO_3$:Ce (LuYAP) [16], $Lu_xGd_yY_{1-x-y}AlO_3$:Tm [17] $(Lu_xGd_{1-x})_3(Al_yGa_{1-y})_5O_{12}$:Ce (LuGAGG) [18], based on isovalent substitution of host cations. In LYSO:Ce and LGSO:Ce crystals the Lu^{3+} substitution by Y^{3+}, or Gd^{3+} improves energy resolution and suppresses afterglow [15, 19]. Light yield in LuYAP at optimal Lu/Y ratio is by twice higher than that in YAP and 4 times higher than that in LuAP [16]. The reported light yield in LuGAGG is more than 40,000 phot/MeV, that is, by several times higher than in its constituents – LuAG or YAG [18]. These examples demonstrate a clear tendency to improvement of scintillation characteristics in $(Lu_{1-x}Y_x)_3Al_5O_{12}$:Ce (LuYAG) and $Y_3(Al_{1-x}Ga_x)_5O_{12}$:Ce (YAGG) solid solutions.

Difficulties in crystal growth of some compounds prevent the obtaining good quality boules. Besides the need for efficient scintillators some raw materials for their production are too expensive. Crystal growth methods are also should be verified regarding their economic efficiency. Search for new compounds with the reduced cost is always a “hot” topic. Considering the above factors production of crystals requires the use of different growth methods.

There is an increasing demand for fiber-shaped scintillators used in detectors for high-energy physics and medicine. Micro pulling down (μ-PD) method is well known as a progressive and cheap crystal growth method. This growth approach is widely used for production of different shaped crystals. The inorganic scintillating fibers utilization arises with high detection granularity needs [20]. High stopping power can be obtained only with dense crystals (the density of organic fibers is too small). In addition, the scintillating fibers with the similar shape are convenient for application in medical

imaging (positron emission tomography) in a transverse configuration, which requires small pixels combined with depth of interaction as well as good stopping power [21]. This area of interest is a spin-off activity from high-energy detection research. From the beginning of the century a significant progress has been made to control the technology and to improve fiber quality and reproducibility in terms of optical performance.

Future calorimeters require improvement of their performance while operating in intensive conditions. The recent progress in micro-pulling down method allows growing heavy scintillating crystals, like LuAG, directly into fiber geometry of variable lengths and diameters [6, 7]. Exploiting the granularity of the detector is a possible solution which would allow improving the overtaxing and tracking capabilities as well as the description of the shower development. Because of the flexibility of this geometry, combined with the high density and good radiation hardness of the material, such a technology represents a powerful potential for the development of future calorimeters [4, 22, 23].

μ-PD method also attracts interest from the scientific point of view. Besides possibility to grow long and thin fibers it is a fast way to make a single crystal of enough size for examination of new compounds. It is a practicing method to obtain different shaped materials as well. On the other hand it differs a lot from the growing of bulk crystals. Therefore, it is reasonable to compare the outcome of different methods. Nevertheless, the growth of crystals which can be shaped specially for the application with minimal subsequent treatment is one more additional advantage of μ-PD. In this work the feasibility to grow shaped fibers for the use in high energy physics application is demonstrated.

LGSO:Ce shaped crystals represent the example of complications which may arise during the micro-PD growth, in particular, in uniform distribution of the components across the crystal and cracking . These crystals were grown with the main purpose to find out the maximally beneficial activator concentration. In the case of garnet fibers growth the main target was to produce single crystal fibers with the required length for the new dual-readout calorimeter. Aluminates with the garnet structure – undoped LuAG and doped by Ce^{3+}, Pr^{3+}, $Y_3Al_5O_{12}$:Ce (YAG:Ce) Ce^{3+} are

relatively easy-to-grow crystals compared to silicates. However, to achieve the required fiber shape and properties the growth technology has to be modified. Drawbacks of the μ-PD grown garnets include inuniformity of activator concentration both in axial and radial directions. This can be overcome by the transfer to mixed $Lu_{3-x}Y_xAl_5O_{12}$:Ce (LuYAG) crystals with higher segregation coefficient of Ce^{3+}. Besides this, the moderate light yield and density of garnets can be significantly improved by the Al^{3+}/Ga^{3+} substitution in the host. Both these approaches are successfully implemented in the present work. Also, this work represents a status of the optical quality on recently obtained LuAG fibers and the test beam results obtained with a sampling calorimeter module constructed from 64 LuAG fibers embedded into a brass absorber.

The manuscript thesis is presented as the follows:

Chapter I introduces a literature review and monography about scintillator oxides crystal growth technology and the problem encountered during the growth process. The content also present a large information about GSO, LGSO, YAG, LuAG and rare earth activator dopants such Ce^{3+} and Pr^{3+}.

Chapter II is focused on the experimental part related to the growth and the characterization of the pulled crystals.

Chapter III presents the results part related to the growth and the characterization of LGSO:Ce fibers.

Chapter IV presents the results part related to the growth and the characterization of Ce-doped garnet fibers.

Chapter V describes the results on bulk $Y_3Al_{5-x}Ga_xO_{12}$:Ce mixed scintillation crystals as the promising garnet material with the improved light yield and increased density.

The last part summarizes the main conclusions and the outlook for the future research work.

Chapter I: Literature review

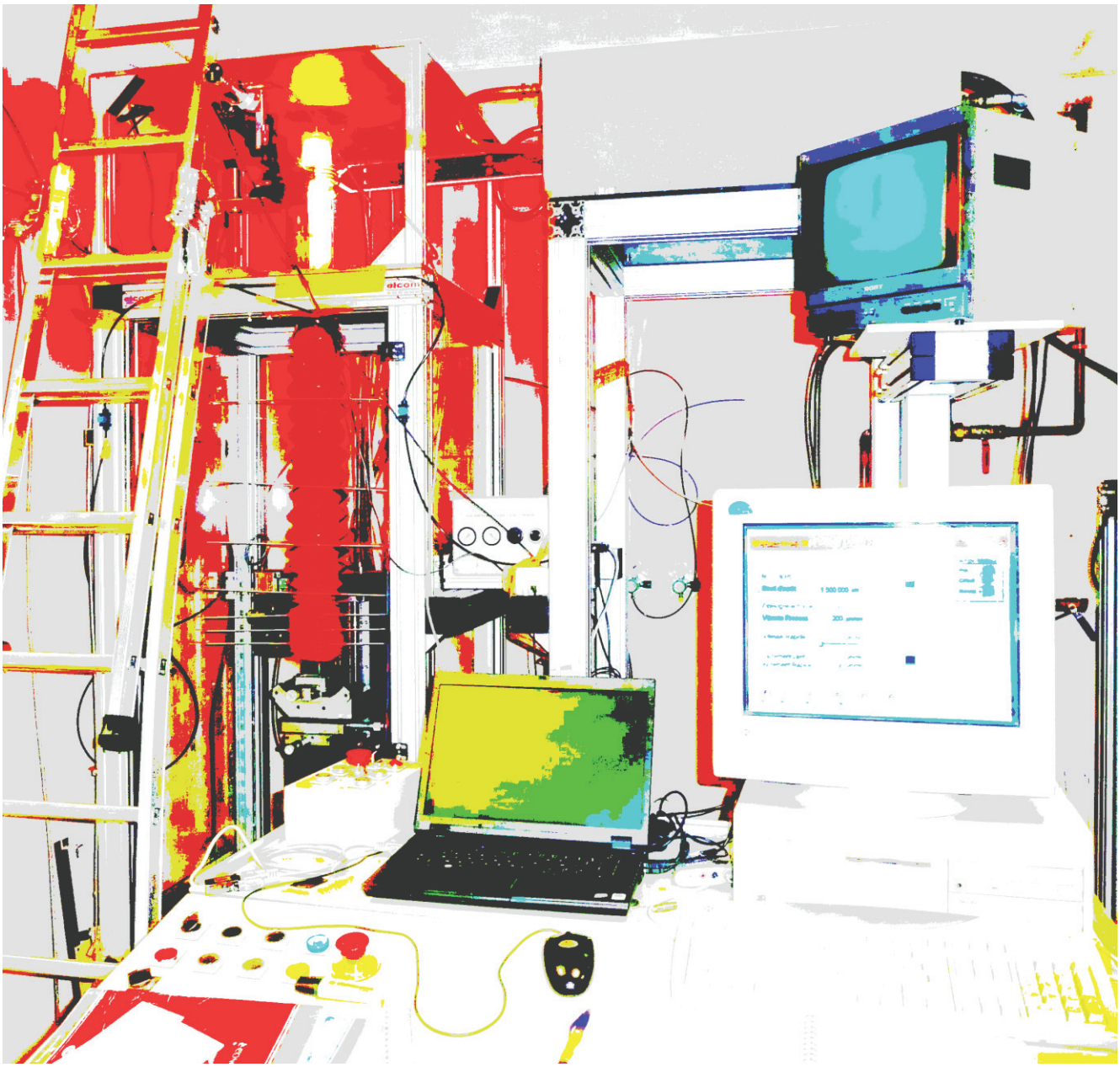

At present the crystal growers widely produce about two dozen types of inorganic crystalline scintillators. Many other inorganic compounds are considered as good scintillation candidates for scintillation application. In this chapter, we present an overview on silicate (GSO, LGSO) and garnet (YAG, LuAG) scintillating crystals. We have also discussed the achievements in growth of fiber-shaped crystals by micro-pulling down (μ-PD) method.

1.1. Choice of the growth method

The most commonly used single crystal production approach is growth from the melt. Nowadays, depending on the crystal mechanical properties and sizes of the crystals, different methods of growth from the melt are used. In general, growth methods can be divided into two groups. The first group belongs to the growth without a crucible owing to the ability of the melt react with the crucible material, or higher melting temperature of the raw material compared to the crucible melting point. These methods are represented by the Verneuil method [24], Skull method [25], and the Floating Zone method [26].

Crucible-free methods of growing single crystals are used for the industrial production of the crystals. For example, sapphire is grown by the Verneuil method for the jeweler industry and the growth of pure silicon for the electronics by the Floating Zone with high-frequency heating. In most cases, these methods are used for the rapid preparation of crystalline samples or seeds. The main disadvantages of the these methods are the limit of the grown crystal, as well as the relatively high stress in the crystals, resulting from the growth process, and often lead to the destruction of the crystal.

Another group of methods correspond to the growth of crystals from crucible filled with the melt. The most popular growth methods from the melt are Czochralski [27], Kyropoulos [28], Bridgeman [29 - 31] and the variety of the floating zone methods [32]. These methods are commonly used for experimental and industrial growth of large bulk crystals. The comparative features of these methods are discussed in [32 - 39].

Since LGSO and LuAG were reported as congruent melting materials (solid and liquid have the same composition), it is reasonable to grow them from the melt using Czochralski (Cz) method [40, 41]. LGSO:Ce crystals were grown in all the Lu/Gd substitution range (Figure I.1).

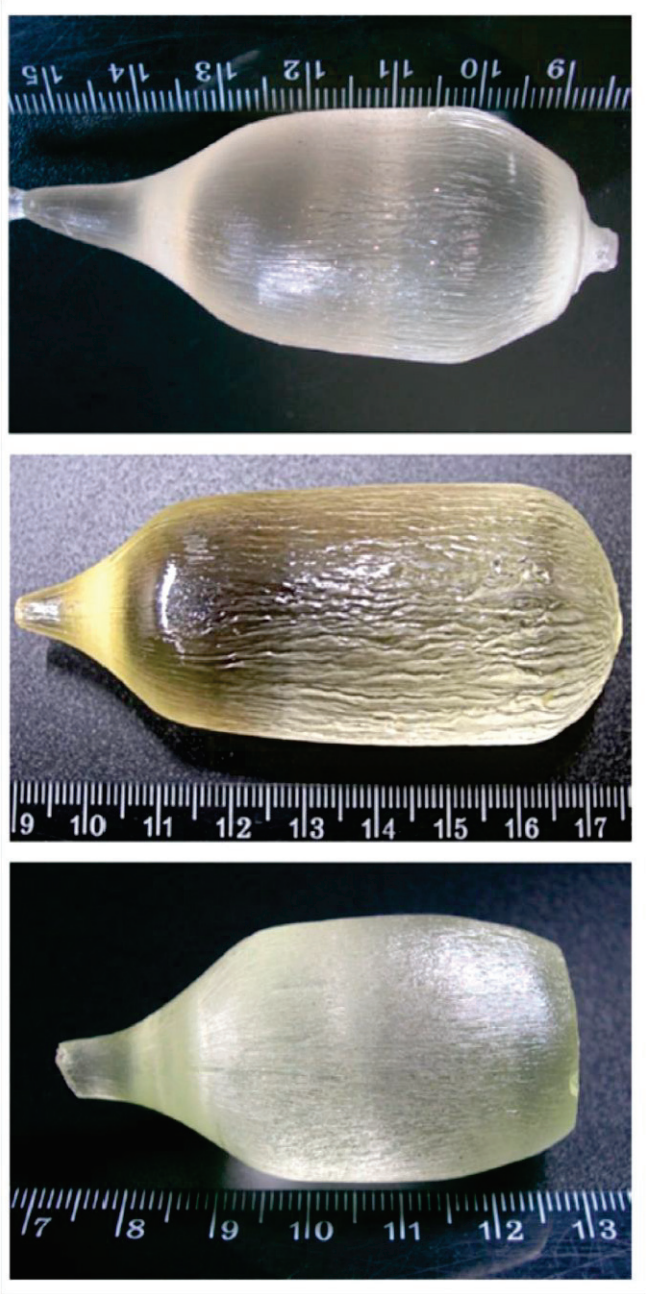

Figure I.1. As-grown $Lu_xGd_{1-x}SiO_5$:Ce crystals with x = 0.2 (left), x = 0.6 (middle), and x = 0.75 (right) [43].

The example of LuYAG crystals grown by the Czochralski method was presented in [42] (Figure I.2).

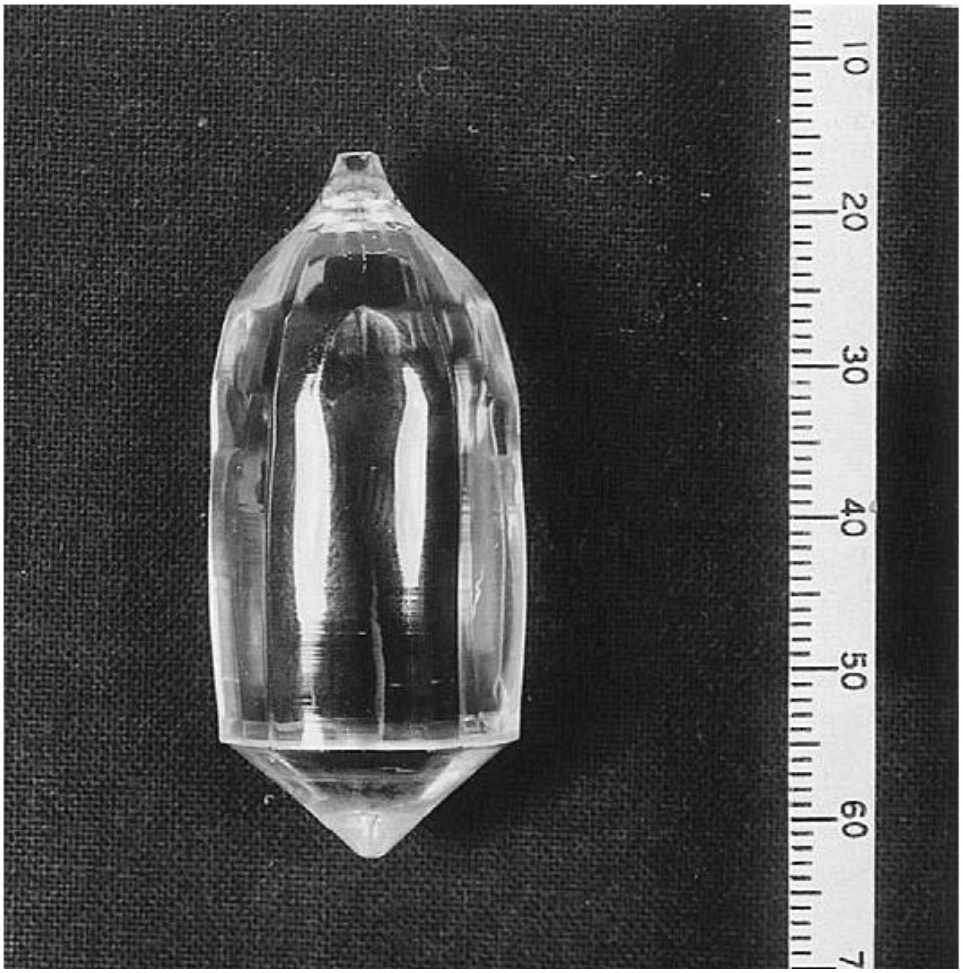

Figure I.2. Photograph of the as-grown $Lu_{1.5}Y_{1.5}Al_5O_{12}$ single crystal [42]

Need for developing of the technology for large-size crystal production and material losses at cutting of crystals into piece makes Czochralski method relatively more expensive. Crystal growth by the μ-PD method posess a feasibility to obtain single crystals fibers, rods, plates directly after the growth process. Capability of the fast growth and the crystalyzation of 100 % of melt is additional advantage of the μ-PD method [44]. The samples can also be directly produced in a shape suitable for

construction of detectors consisting of arrays of different crystals providing high detection granularity [45]. Fibers grown by μ-PD can be used in the development of a new generation of detectors for high-energy physics based on single-crystal fiber design [46].

There is a fertile history of the shaped crystal growth illustrated by numerous publications related to the different applications of plastic/organic scintillators. However, the low effective Z of the atomic components restricts their sensitivity to ionizing radiations. Due to the recent development of the micro pulling down method, fibers based on inorganic crystalline scintillator can be grown with statically improving quality. Relatively novel micro-pulling-down crystal growth method (μ-PD) is well recommended and promissing in production of crystal materials [47, 48]. The μ-PD growth method [49] substantially differs from the Cz method.The molten zone is situated at the bottom of the crucible on its capillary die surface. During the growth, melt flows down through capillary and there is no diffusion of impurities from crystallization interface back to the crucible basic, in contrast Czochralski growth procedure. Therefore, Dopants and, impurities are concnetrated in the molten zone. They are pushed by melt flow to the periphery of the meniscus and, then, are captured by the growing crystal. As the result, the distribution of the components along the fiber remains almost constant. Meanwhile, a substantial gradient of the Ce concentration might appear in the radial direction and have a negative impact on the fiber scintillation characteristics.

Previously fiber-shaped materials with garnet structure were grown by the μ-PD [50, 51] method. The next step at the growth of garnets is enhancement of their growth procedure to minimize the distribution of activator across the fiber. In particular, the production of LuAG:Ce and LYSO:Ce, which are bright scintillators and possess high radiation hardness, and short radiation length, imposes additional complications due to their high melting point and the large difference in geometrical dimensions of the host and activator ions. For both materials, which are considered for a new generation of sampling calorimeters with dual read-out for hadron detection or pure electromagnetic calorimetry and additional applicability in PET-tomography, significant progress has

been achieved [6, 7, 52]. The improvement of growth conditions of LuAG and LuAG:Ce fibers was reported in [7]. Such important parameters like wetting of the melt (Figure I.3 a, I.3b), diameter control (Figure I.3c, I.3d) and pulling rate influence were discussed.

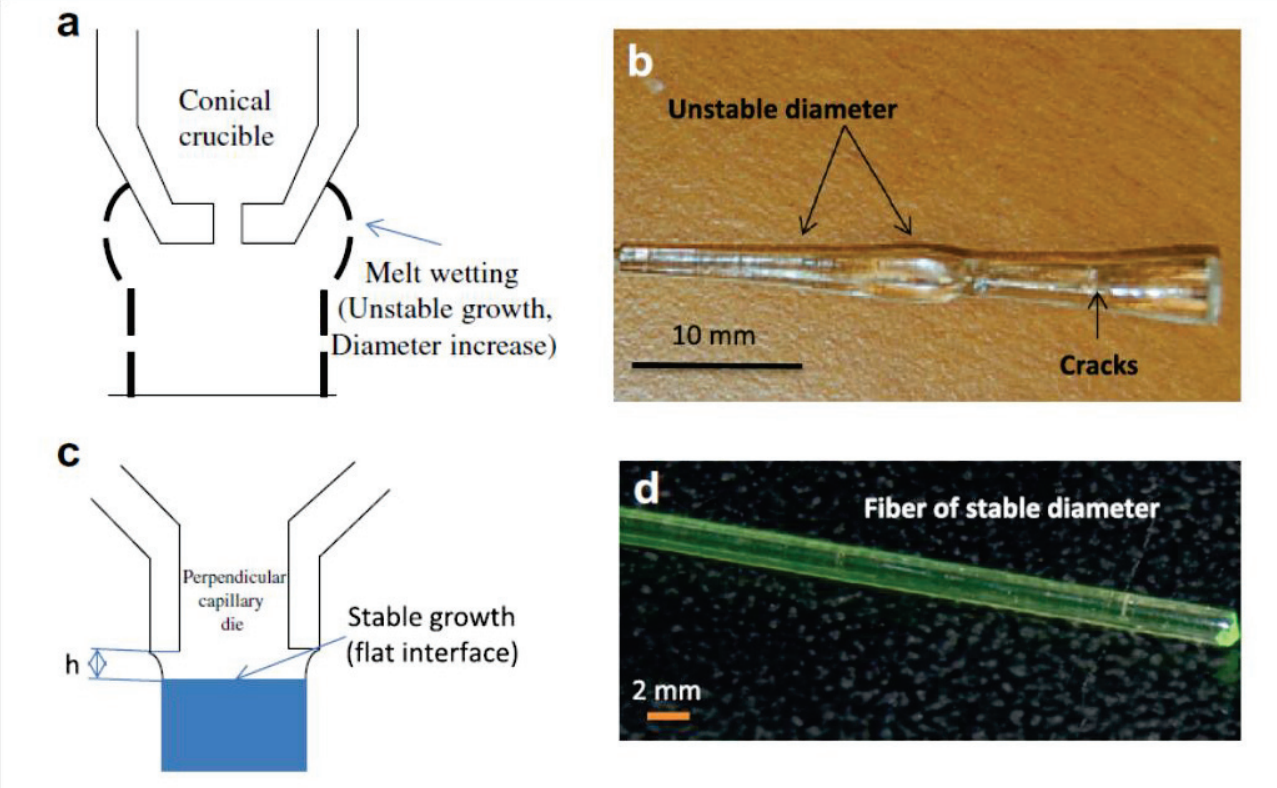

Figure I.3. Undoped LuAG (b) grown with conical crucible (a) and LuAG:Ce fibers (d) obtained with crucible with modified cappillary die (c) [7].

In contrast to the Cz grown crystals, there is a radial gradient in activator concentration in fibers grown by μ-PD grown method (Figure I.4) [7]

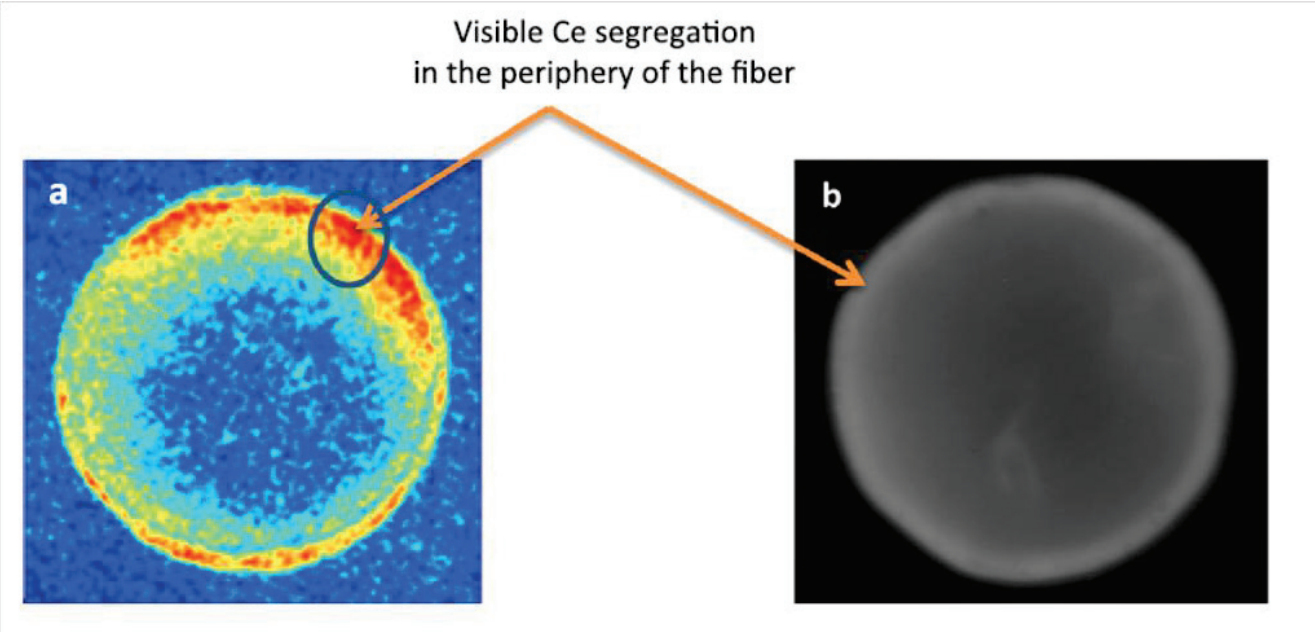

Figure I.4. Transversal cut view of the 0.12 at.% LuAG:Ce fibers excited under X-rays (a) and electrons (b), presenting a distribution of Ce activator to the periphery of the fiber samples [7].

In comparison to fabrication of the pixelated detectors by cutting bulk crystals, micro-pulling down [53] is an efficient method for production of long single crystal fibers of variable cross-section. This method enables reaching the growth rate up to 5 mm/min, which is beyond the limits of the majority of other melt crystal growth methods [54]. The μ-PD method has already been successfully applied for growing complex high-melting-point oxide scintillators: $Lu_{2x}Y_{2-2x}SiO_5$:Ce (LYSO:Ce) [52] rare earth garnets [6, 7], $Bi_4Ge_3O_{12}$ [55], complex borates [56], etc. Moreover, the μ-PD growth process for mixed crystals is complicated, because the different ionic radii of both the activator Ce^{3+} and one of the host cations (Gd^{3+} or Y^{3+}) are significantly larger than that of the Lu^{3+} host cation [57]. This discrepancy results in cracking of bulk LGSO:Ce crystals. Therefore, the axial and radial distributions of Ce^{3+} and Gd^{3+} in the LGSO:Ce fibers were in the focus of the present study.

1.2. General information about rare-earth silicates

Oxyorthosilicate phase exists in the system RE_2O_3-SiO_2 (RE – rare-earth element). The oxyorthosilicate inorganic scintillating crystals comprise lutetium oxyorthosilicate (LSO) [58, 59], gadolinium oxyorthosilicate (GSO) [60], yttrium oxyorthosilicate (YSO) [61, 62], which correspond to the RE_2SiO_5 composition. With the increase of SiO_2 percentage the structure changes to the oxyapatite with a general formulae $RE_{9.33}Si_6O_{26}$ [63], pyrosilicates or diorthosilicates with the $RE_2Si_2O_7$ formula [64, 65]. It is shown for the LSO case in Figure. I.5, that oxyorthosilicate phase exists in the composition range between the lines marked by the arrows 1, 2, 3. With a substitution of one RE1 by another RE2, it is possible to grow mixed crystals.

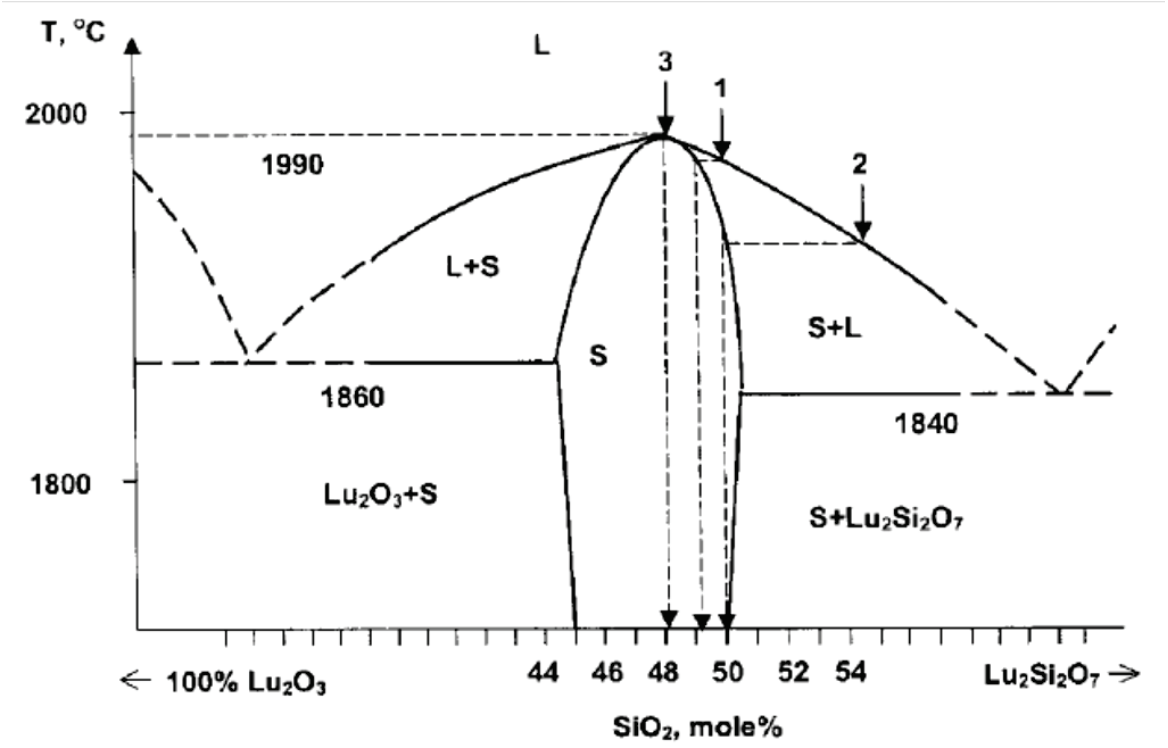

Figure I.5. Lu_2O_3 – SiO_2 phase diagram [73].

Such examples are represented by lutetium-yttrium oxyorthosilicate $Lu_{2x}Y_{2-2x}SiO_5$ (LYSO) [66, 67], gadolinium-yttrium oxyorthosilicate $Gd_{2x}Y_{-2x}SiO_5$ (GYSO) [68, 69], and, finally, lutetium-gadolinium oxyorthosilicate $Lu_{2x}Gd_{2-2x}SiO_5$ (LGSO) [70,

71]. As a consequence, the nomenclature of crystals became wider [72, 73]. From the variety of scintillating crystals we choose the LGSO:Ce compound for the fiber technology development.

Since LGSO is the mixture of GSO and LSO components, in the following subsections, the properties of these components are reviewed.

1.2.1. General information on GSO

The Gd_2SiO_5 (GSO) was discovered in 1983 [60]. Ce-doped GSO (GSO:Ce) properties exceed BGO single crystals by light yield and 5 times lower decay time. However, GSO:Ce light yield is by 3 times lower compared to LSO:Ce or YSO:Ce. Nevertheless it is applied in the high energy physics, and nuclear physics. GSO:Ce demonstrate good radiation hardness [74] and has relatively lower production cost due to cheaper raw material components and lower melting temperature. However, the monoclinic $P2_1/c$ structure of GSO:Ce light yield is insufficient for use in modern PET scanners, and large GSO crystals are difficult to produce because of easy cleavage [75].

The typical excitation and emission spectra of GSO:Ce are shown in Figure. I.6. The maximum wavelength of the scintillator emission spectrum is at 430 nm. The excitation spectrum for the emission at 430 nm has the three peaks at 250 nm, 284 nm, and 340 nm. The excitation peaks at 340, 284, and 250 nm are attributed to the direct excitation of the 4f–5d transitions of Ce^{3+}. The emission spectrum is assigned to 5d-4f transitions of Ce^{3+}.

The another advantage of GSO:Ce crystals is the low afterglow level. On the Figure I.7 one may compare the Ce-doped GSO, LSO, and $Gd_2Si_2O_7$ (GPS) afterglow curves. Afterglow level for GSO:Ce is by several times lower comparing to LSO:Ce and GPS:Ce (Figure I.7). Phenomenon of afterglow in orthosilicates is usually attributed to the presence of deep oxygen vacancies on non-silicon bound oxygen atoms [77].

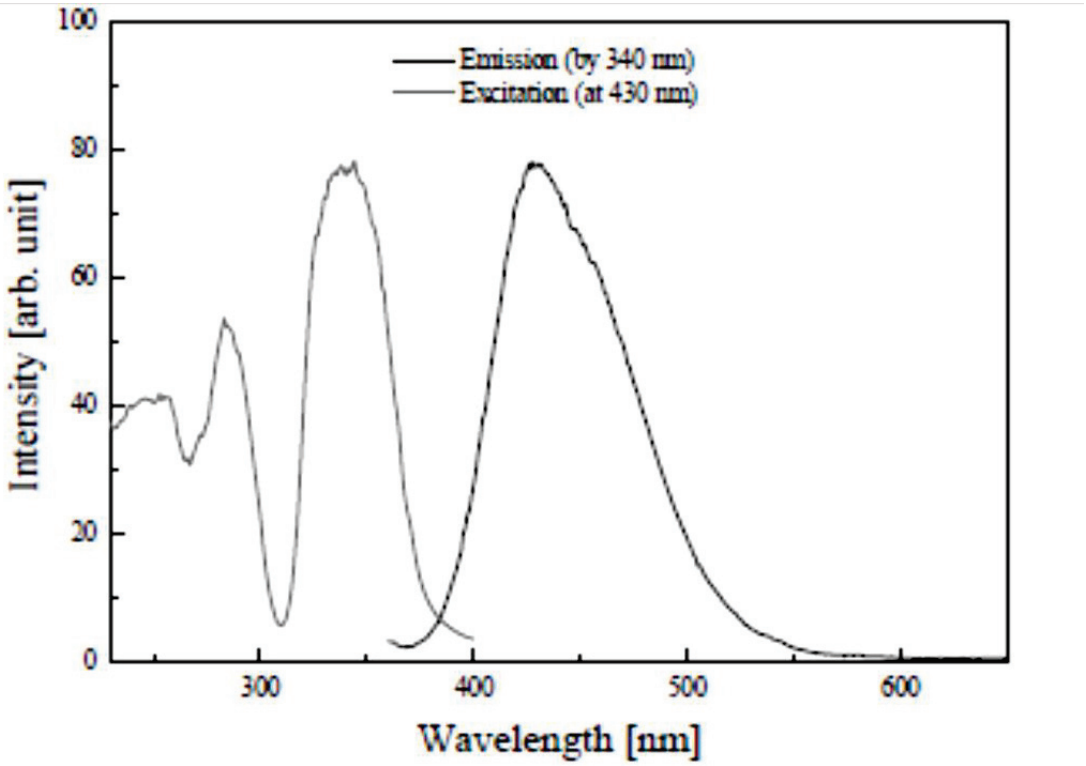

Figure I.6. Excitation and emission spectra of GSO:Ce crystal at the room temperature [76].

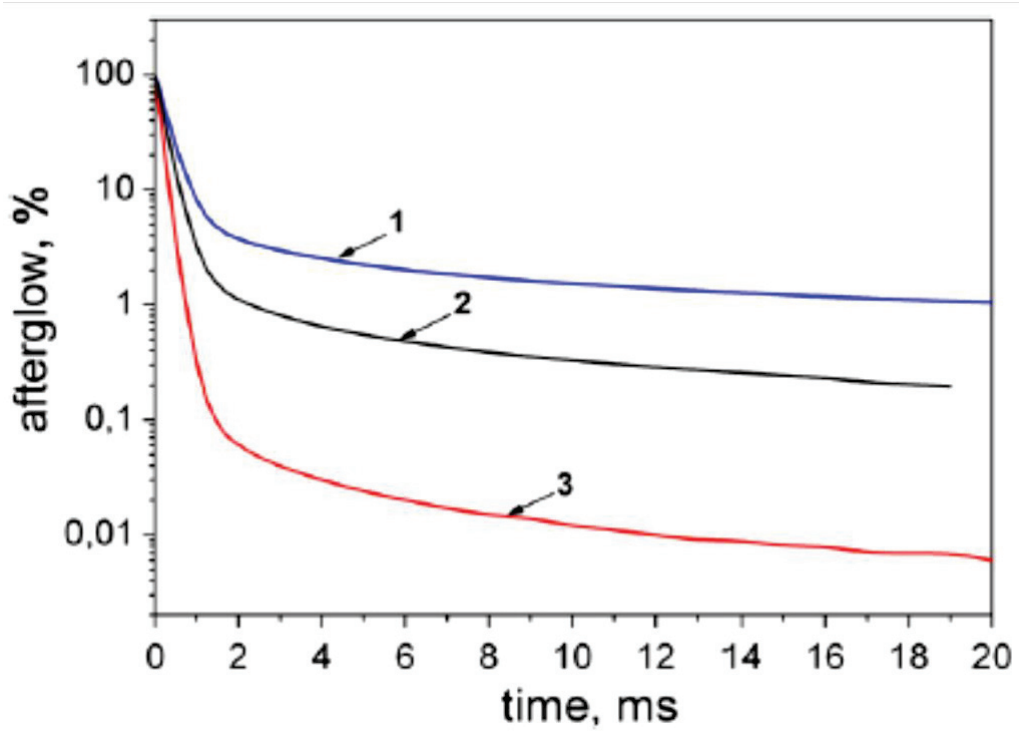

Figure I.7. Afterglow kinetics for LSO:Ce (1), GPS:Ce (2), and GSO:Ce (3) [78].

1.2.2. General information about LSO

Since 1990s, Lu_2SiO_5:Ce (LSO:Ce) is produced as one of the best scintillation detector material for PET [79, 80]. LSO with the monoclinic C2/c crystal structure, as a dense, bright and fast scintillation crystals doped by Ce was extensively studied during the recent two decades. The main disadvantage of this chemically stable and non-hygroscopic material is the high afterglow level, which limits the application range of LSO:Ce. In addition, this material melts at 2150°C which is so high for the crucible container such as Iridium material. The LSO scintillation parameters can be optimized by the proper choice of activator content and host composition. The first way is comprised by the codoping with the divalent cations [81], for example, Ca^{2+}. With Ca^{2+} codoping the higher light yield, lower afterglow, and faster scintillation decay in LSO:Ce crystals were achieved. Meanwhile, the Ca^{2+} co-doping brings some instability to the crystal growth process [82].

Another way is to modify the properties of LSO:Ce with the incorporation of another host cation. Following this possibility the new $Lu_{2x}Gd_{2-2x}SiO_5$:Ce (LGSO:Ce) [11-14] and $Lu_{2x}Y_{2-2x}SiO_5$:Ce (LYSO:Ce) [15] mixed crystals were introduced.

The positions of the peaks on LSO:Ce excitation and emission spectra are similar to LYSO:Ce crystals (Figure I.8). The emission maximum at UV-excitation is peaked at 402 nm, and 5 peaks corresponding to the 4f-5d transition in Ce^{3+} (only 3 peaks are shown in Figure I.8 in the selected wavelength range) with the main peak at 358 nm are observed on excitation spectrum.

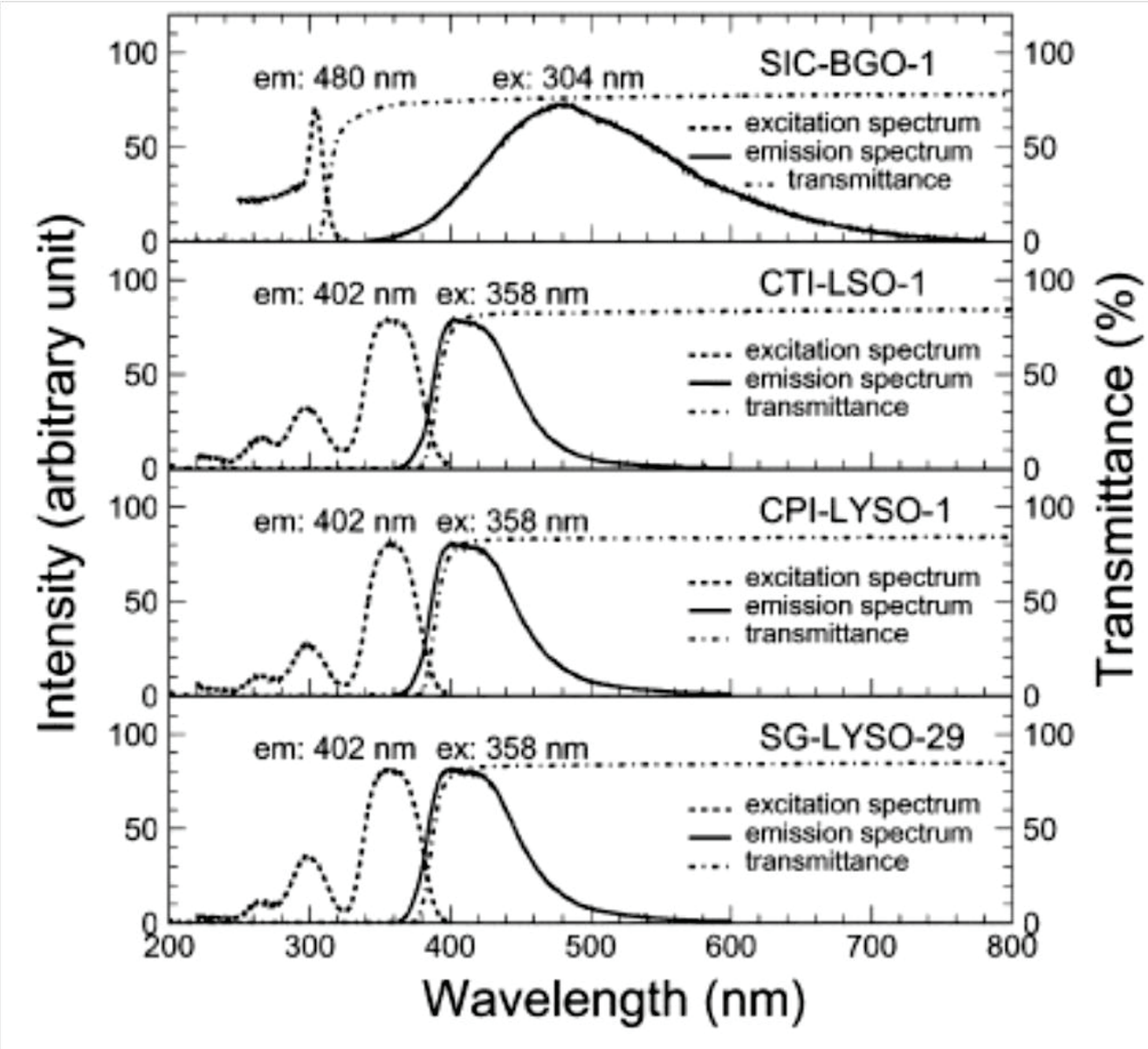

Figure I.8. Optical properties are shown as a function of wavelength. The excitation and emission spectra correspond to the left vertical scale, and the transmittance spectra correspond to the right one [15].

LSO:Ce in contrast to GSO:Ce has the high light yield around 25000-30000 phot/MeV [83, 84]. The highest light yield is observed with the 0.25 at. % activator content (Figure I.9) [15].

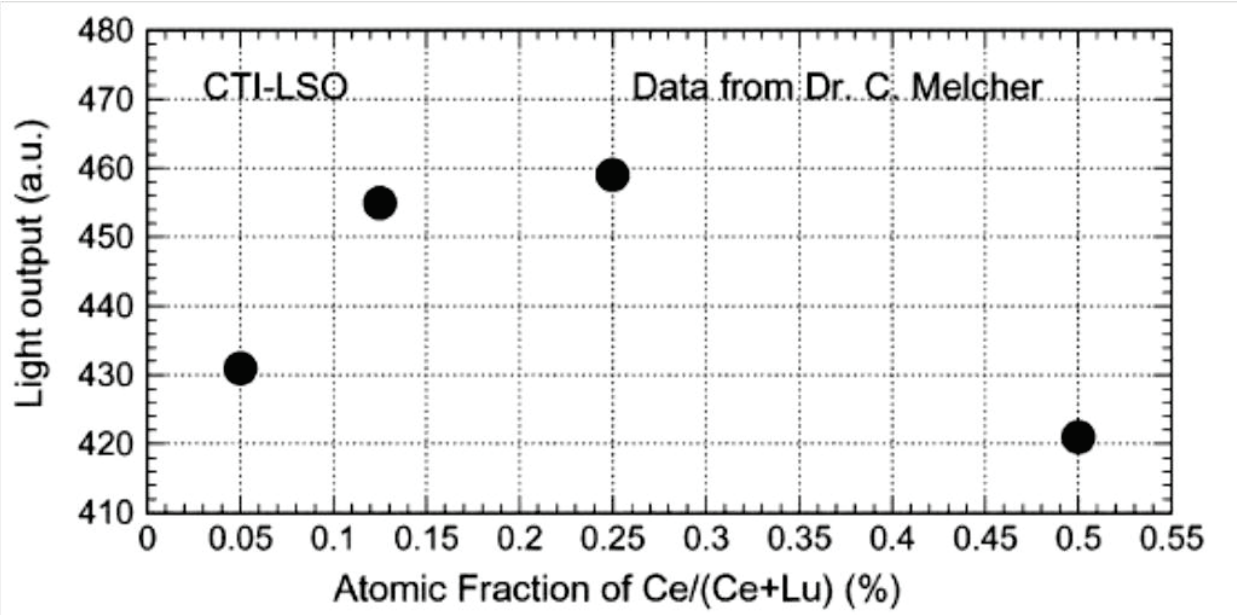

Figure I.9. The light output is shown as a function of the cerium concentration in LSO [15].

1.2.3. Structure of mixed LGSO:Ce crystals

The main idea of LGSO:Ce synthesis is a combination of superior properties of GSO:Ce with low afterglow and LSO:Ce with high light yield. Accounting for the lower cost of Gd_2O_3 in comparison with Lu_2O_3 and lowering of crystallization temperature with Gd addition into the host, these crystals are good candidates for substitution of LSO/LYSO in PET or CT [85, 86, 87]. Since the first patent concerning LGSO:Ce growth is dated by 1993 [88] this material has been grown by different groups. According to the phase diagrams on the Figure I.5 and the Figure I.10, the oxyorthosilicate phase is formed at the 1:1 ratio in the RE_2O_3 – SiO_2 system. The moderate atomic radii values difference makes it possible to substitute Lu by Gd. As Lu and Gd cations sizes differ, a lot of efforts were done for the investigation of this compound.

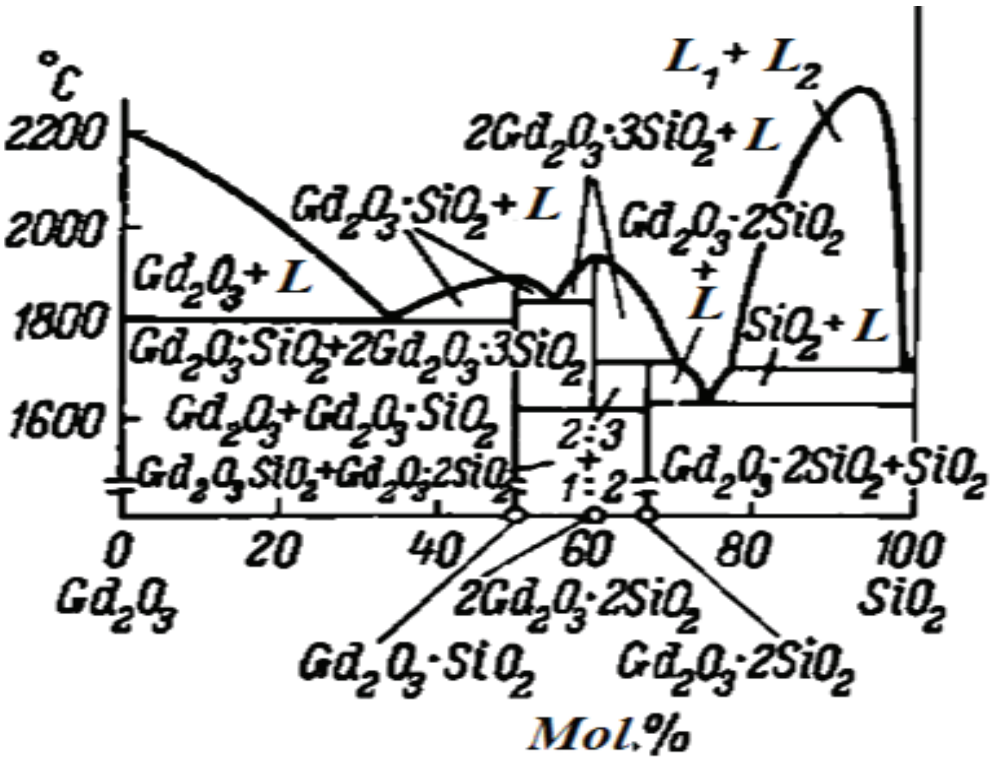

Figure I.10. Phase diagram for Gd_2O_3 – SiO_2 system [89]

The Gd ionic radius is 0,94 Å and the Lu one is 0,86 Å [68, 90]. This calls the lattice structure switch from the $P2_1/c$ space group of GSO to the C2/c space group of LSO with the increase of Lu content [43, 91]. The lattice $P2_1/c$ symmetry occurs until the x = 0.1 in $Lu_{2x}Gd_{2-2x}SiO_5$:Ce, and the C2/c symmetry forms starting from x = 0.2. For the growth of crystals with the GSO-type lattice the [010] oriented seeds were used, and the [210] seeds are used for the LSO-type lattice. In the x range from 0.1 to 0.2 the structure type of growing crystal depends on the seed orientation (Figure I.11). The crystals with such 'intermediate' compositions often contain cracks and inclusions. Note that LSO structure retains at up to 90% substitution of Lu by Gd.

The change of the space group of symmetry has the impact on the unit cell volume (Figure I.12). In the GSO structure with the addition of up to 20% of Lu the decrease of unit cell volume is observed. The same is observed at $0.2<x< 1$ where the unit cell volume decreases down to the parameters of LSO C2/c-type unit cell [91]. The jump of the unit cell volume at x=0.2 is called by the different quantity of atoms in the GSO [88] and LSO [92] elementary cells.

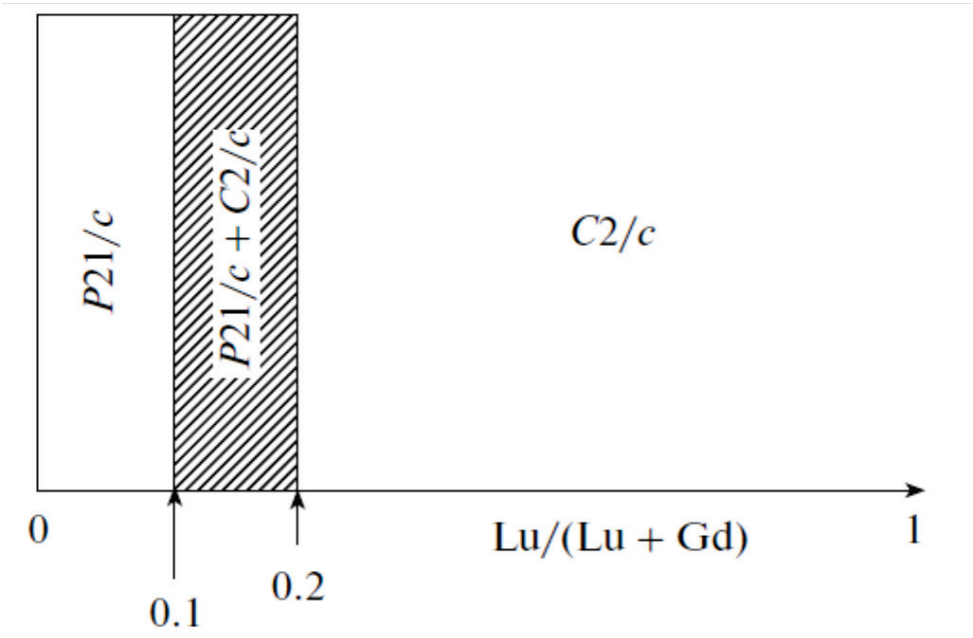

Figure I.11. Polymorphism in LGSO crystals [91].

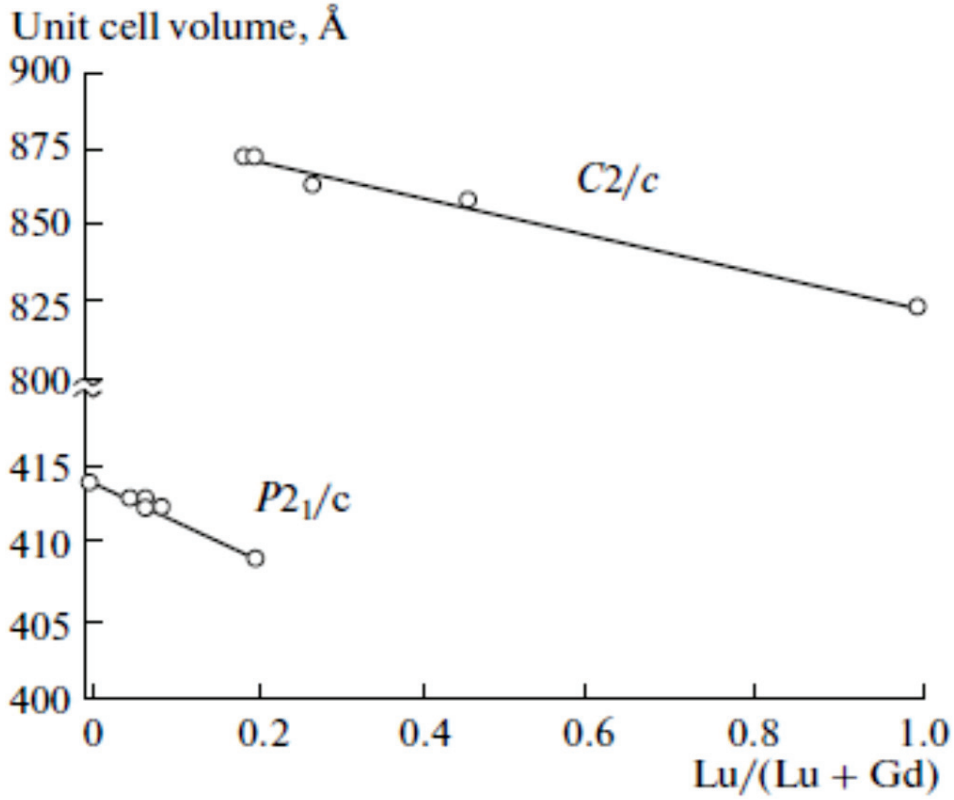

Figure I.12. Unit cell volume for the LGSO crystals with different lattice types [91].

In spite of the difference in the ionic radii of the substituted host components, their overall content in crystal is about the same as in melt (Figure I.13). The unit cell with the space group $C_{2/c}$ contains 64 ions. It contains eight lutetium polyhedra LuO7 and eight lutetium polyhedra LuO6. The energy of the substitution of Lu in LuO7 for Ce^{3+} is equal to +6.90 eV, and the energy of the substitution Ce^{3+} Lu in LuO6 is +7.25 eV [91]. In both cases, the substitution energy is positive because of the larger ionic radius of Ce^{3+} (1.01 Å). The different displacements of oxygen ions after the substitutions by Ce^{3+} in the LuO7 and LuO6 coordination polyhedra are responsible for different rate of Ce^{3+} incorporation into these sites. The number of Ce^{3+} ions replacing Lu ions in the different sites affects the light yield, the position of the luminescence maximum, and the scintillation decay time. The same relates to the distribution of Lu^{3+} and Gd^{3+} in the six- (LnO6) and sevenfold (LnO7) sites. It is illustrated by Figure I.14.

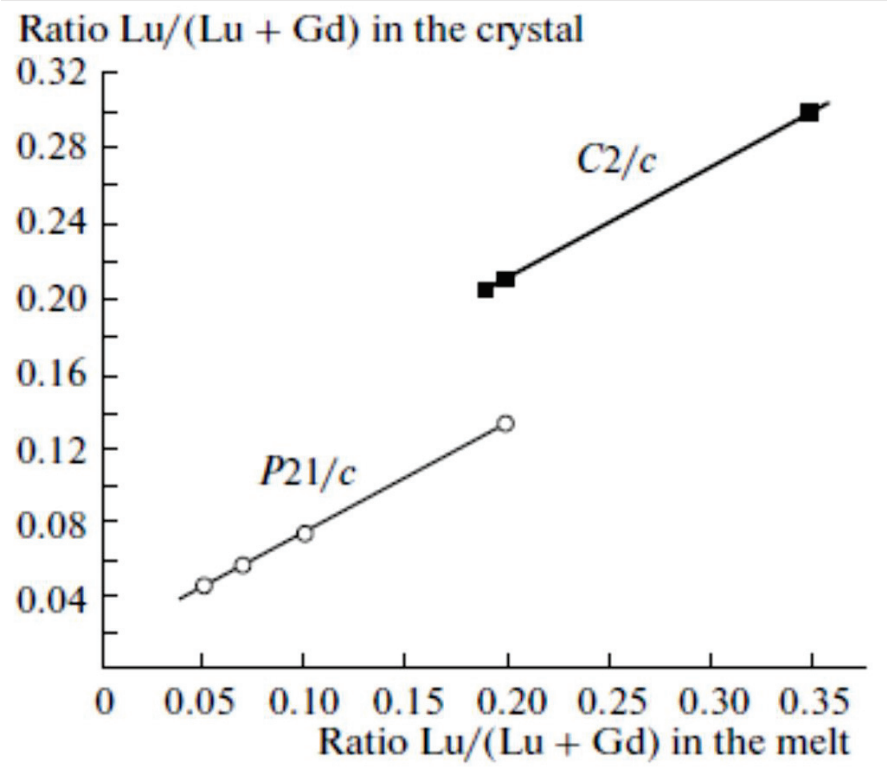

Figure I.13. Lutetium concentration in the crystal as a function of the melt composition.

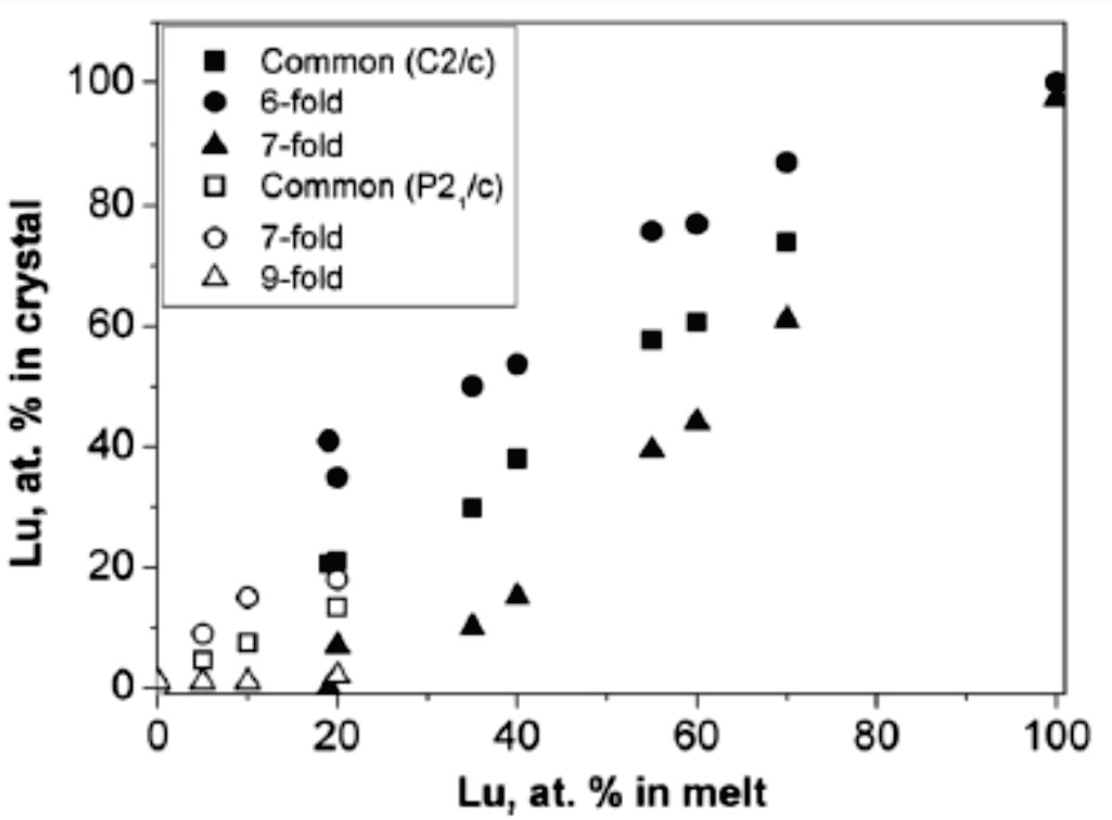

Figure I.14. Concentration of Lu^{3+} in crystals with the different space symmetries vs. Lu content in melt. Data on Lu^{3+} distribution between polyhedra are obtained by X-ray analysis. These results are in good agreement with the values for common Lu content in these crystals determined by the ICP-AES method.

The LGSO phase diagram was studied in [93]. It shows (Figure I.15) the melting temperature for LGSO compositions in the whole range of Lu/Gd substitution. The steep melting temperature fall with the Gd addition is observed within the Gd content 0-84 at. %. This diagram helped to choose the optimal compositions at the fiber growth by micro-pulling down method in this work regarding the scintillation parameters and melting temperature.

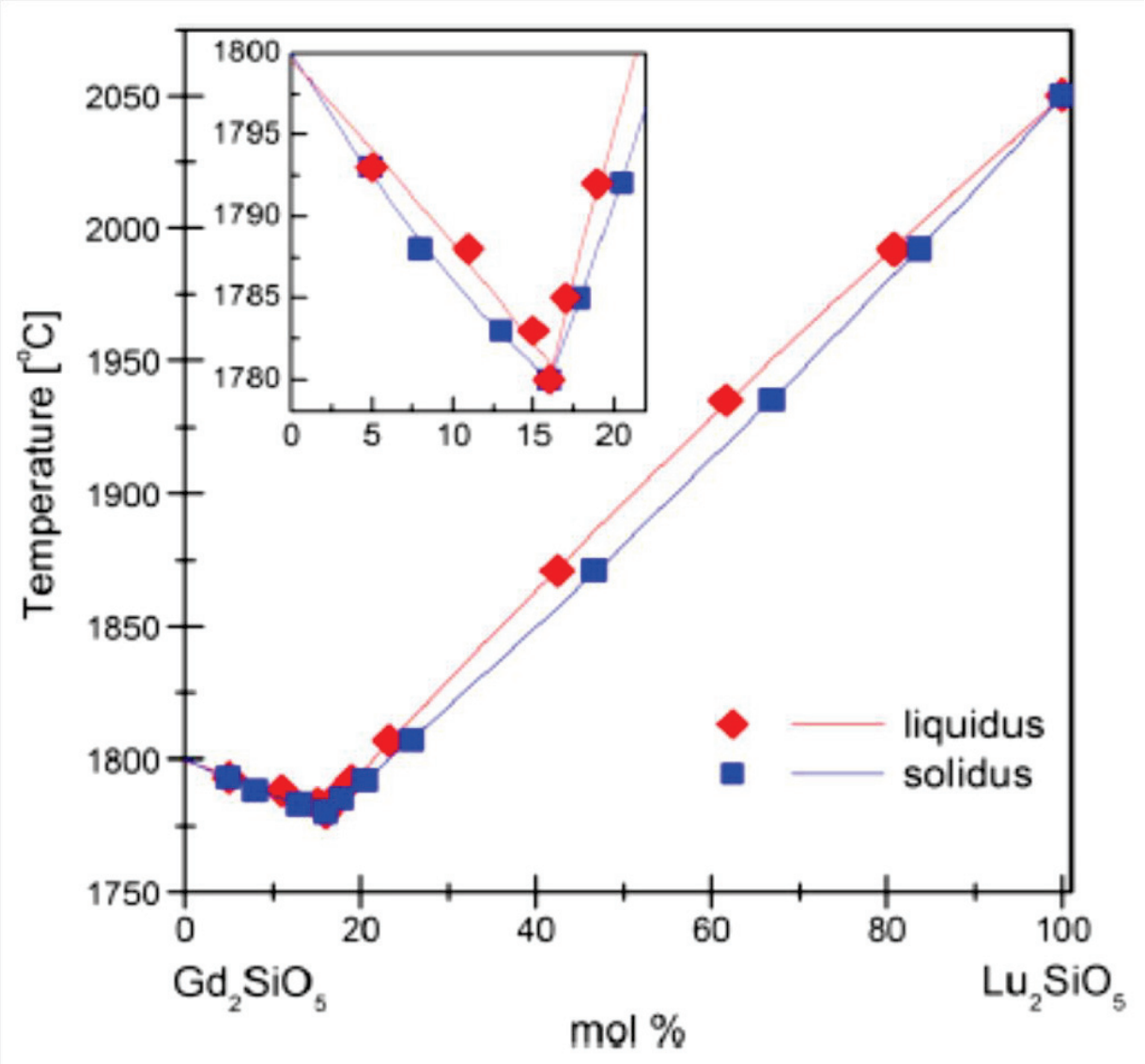

Figure I.15. Schematic phase diagram for Gd_2SiO_5- Lu_2SiO_5 solid-solutions [93].

The LGSO x-ray diffraction patterns difference for the LGSO with the 15% and 17% content of Lu [93] confirms the structure transition between the C2/c and $P2_1/c$ structures around 16 at.% of Lu (Figure I.16).

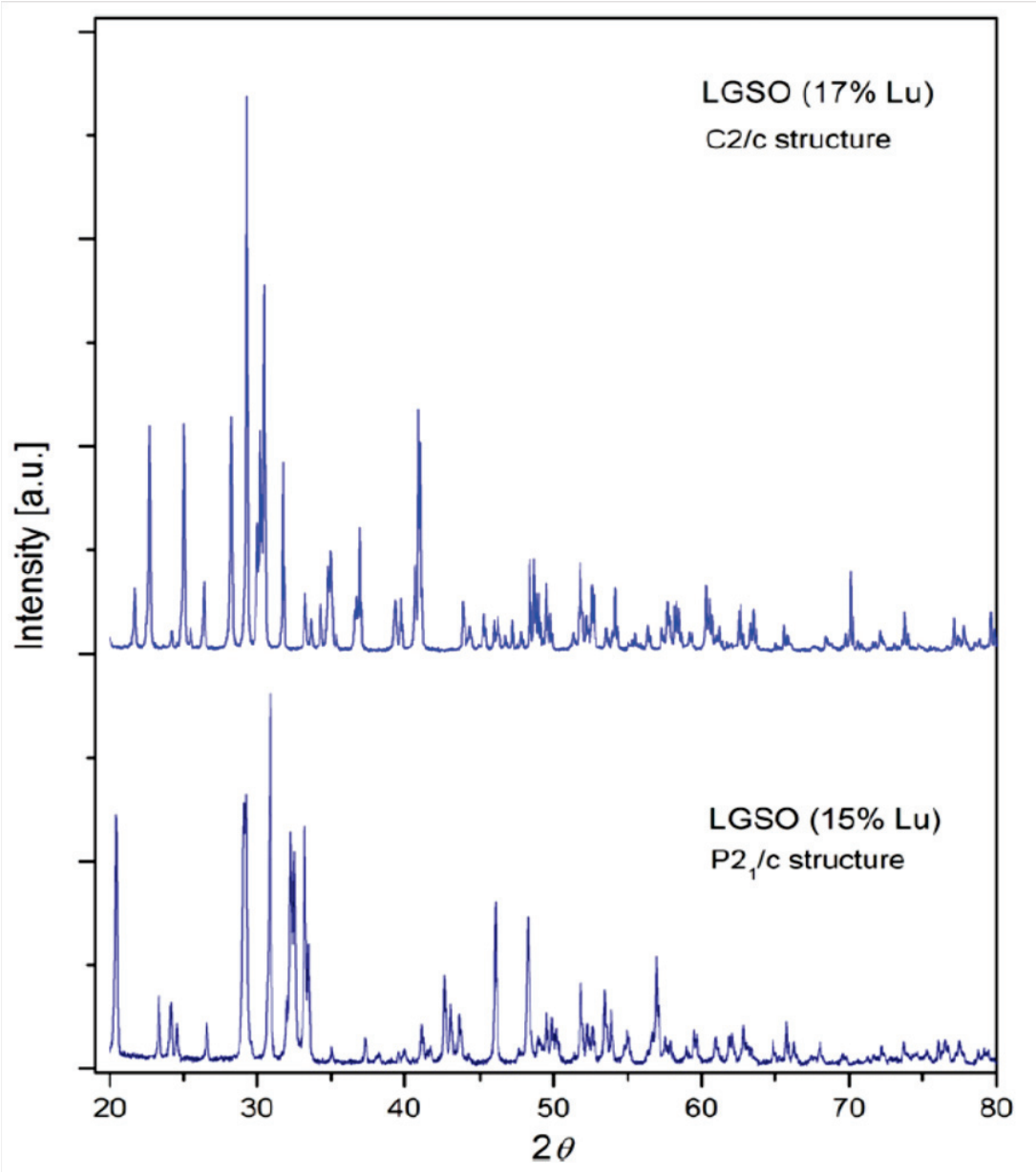

Figure I.16. X-ray diffraction patterns of the $(Lu_xGd_{1-x}Sm_{0.005})_2SiO_5$ solid solution crystals with x = 0.15 and 0.17 in the melt [93].

1.2.4. The improvement of scintillation properties in mixed LGSO:Ce crystals

Three approaches were used to improve the light yield in LGSO-based crystals. The two of them are identical with the case of LSO - the optimization of Ce concentration, which generally should not exceed 0.5 at % [94], and codoping with the divalent ions [95]. In mixed crystal, such as LGSO, we also may optimize the host composition by isovalent substitution of the host cations [19, 96].

The entire range of LGSO mixed crystals with different relation of lanthanides in the host was investigated first in 1997 [90]. No relationship between scintillation characteristics and crystal structure type was observed. The best scintillation characteristics were found in the C2/c structure range. Meanwhile, it was shown that basic scintillation parameters of LGSO:Ce are not deteriorated with the substitution of up to 80 % of Lu^{3+} in the host [19]. Substitution of Gd^{3+} and Lu^{3+} host cations in LGSO, as well as in LYSO:Ce crystals improves energy resolution and suppresses afterglow [19]. The substitution of cations in LGSO:Ce leads to the improvement of scintillation properties. Mixed crystals LGSO:Ce demonstrate the light yield of up to 29000 phot/MeV (33700 Photons/MeV with Ca^{2+} codoping) and the 6,7 % (662 KeV, ^{137}Cs) energy resolution [43]. The scintillation decay time decreases down to 30 ns. With the increase of Gd concentration in crystals the afterglow level decreases by 1-3 orders of magnitude in comparison to LSO:Ce [43]. The Ce segregation coefficient reaches 0.8 certifying nearly homogeneous chemical composition and a good uniformity of scintillation parameters across the crystal.

Ce concentration in LGSO also affects both the luminescence peak position, and scintillation parameters. It was shown that with the increase of the Ce content in the LGSO (60 % Lu) the luminescence peak shifts towards longer wavelengths and the intensity of luminescence in the 450–500 nm range rises (Figure I.17) [19]. It is caused by a redistribution of Ce into the LuO6 coordination polyhedra. The noticed [97] increase of long-wavelength luminescence intensity in LGSO was accompanied by the improvement of light yield and other scintillation parameters. On the contrary, the light

output decrease, increase in the slow decay component contribution, and worsening of the energy resolution was observed in [19] as CeO6 luminescence rises [19].

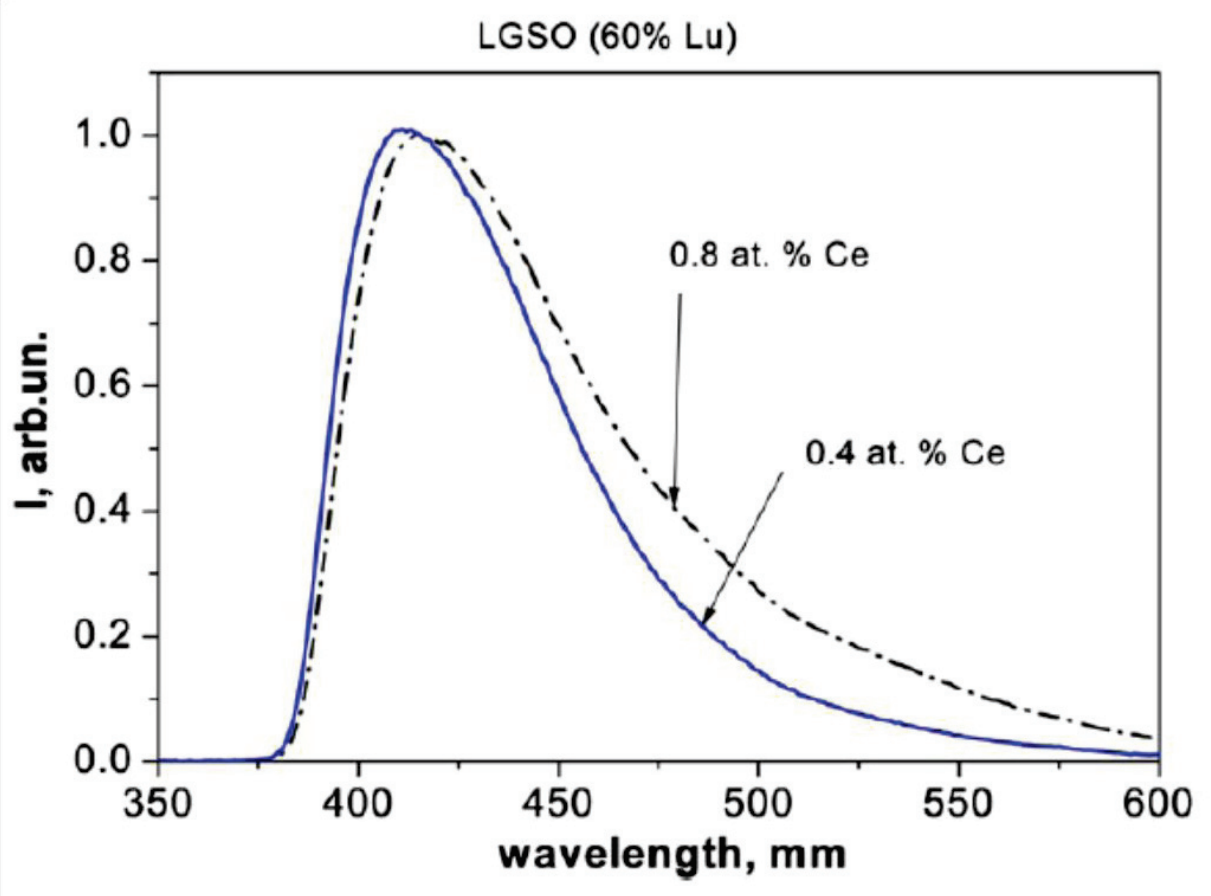

Figure I.17. Red shift of Ce^{3+} emission on X-ray luminescence spectra for $Lu_{1.2}Gd_{0.8}SiO_5$:Ce crystals illustrates the rise of impact from CeO6 centers as common Ce^{3+} concentration increases [19].

X-ray luminescence spectra in dependence on Lu/Gd ratio in the host demonstrate broadening of Ce^{3+} luminescence band toward longer wavelengths as Gd concentration increases (Figure .I.18). The difference spectra on the inset clearly demonstrate that this effect is called by the rise of 450–500 nm luminescence contribution linked to Ce in six-

fold polyhedra. The cerium concentration in all the samples is kept in the range 0.2–0.6 at.% [19].

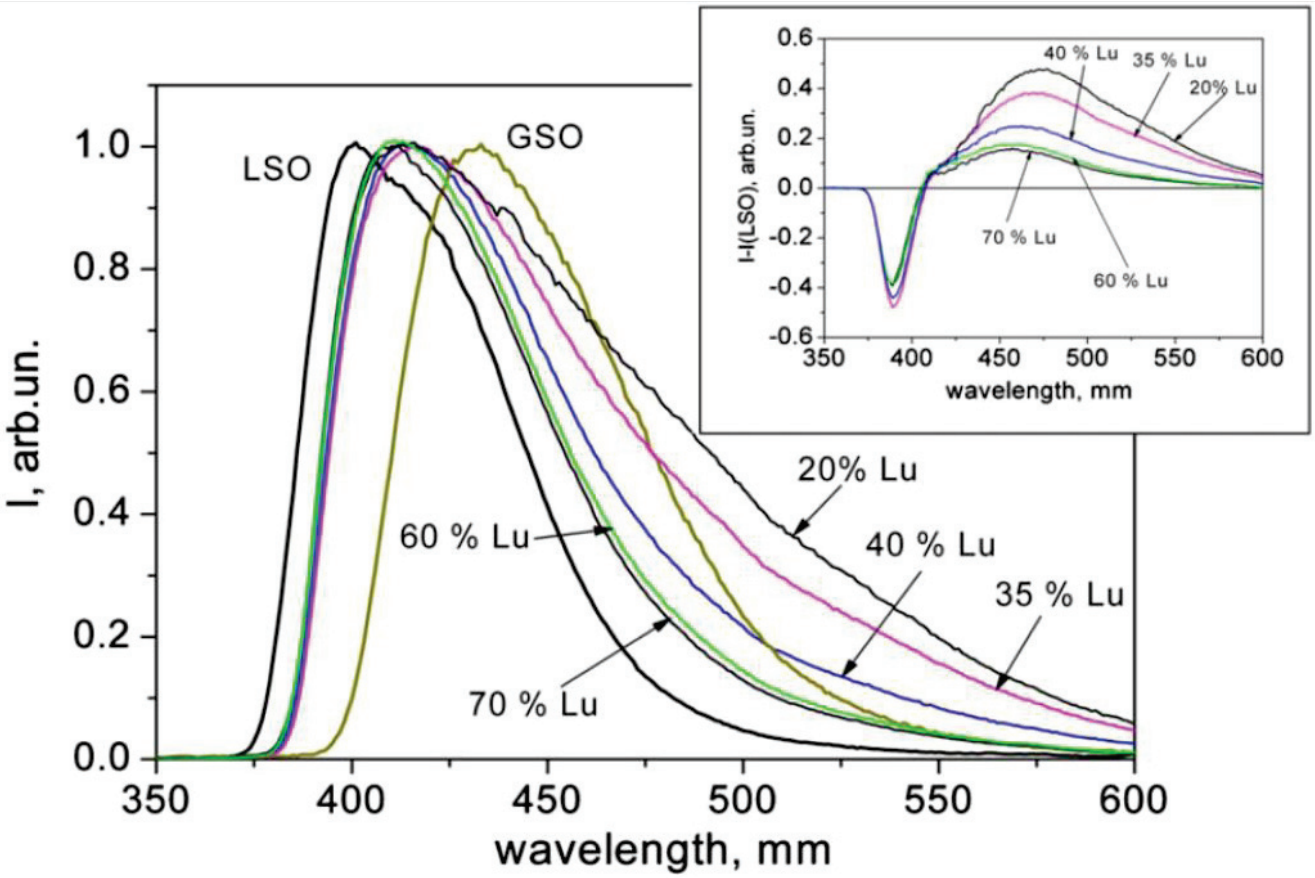

Figure I.18. X-ray luminescence spectra for all solid-solution range of Lu/Gd substitution and their difference spectra on the inset [19].

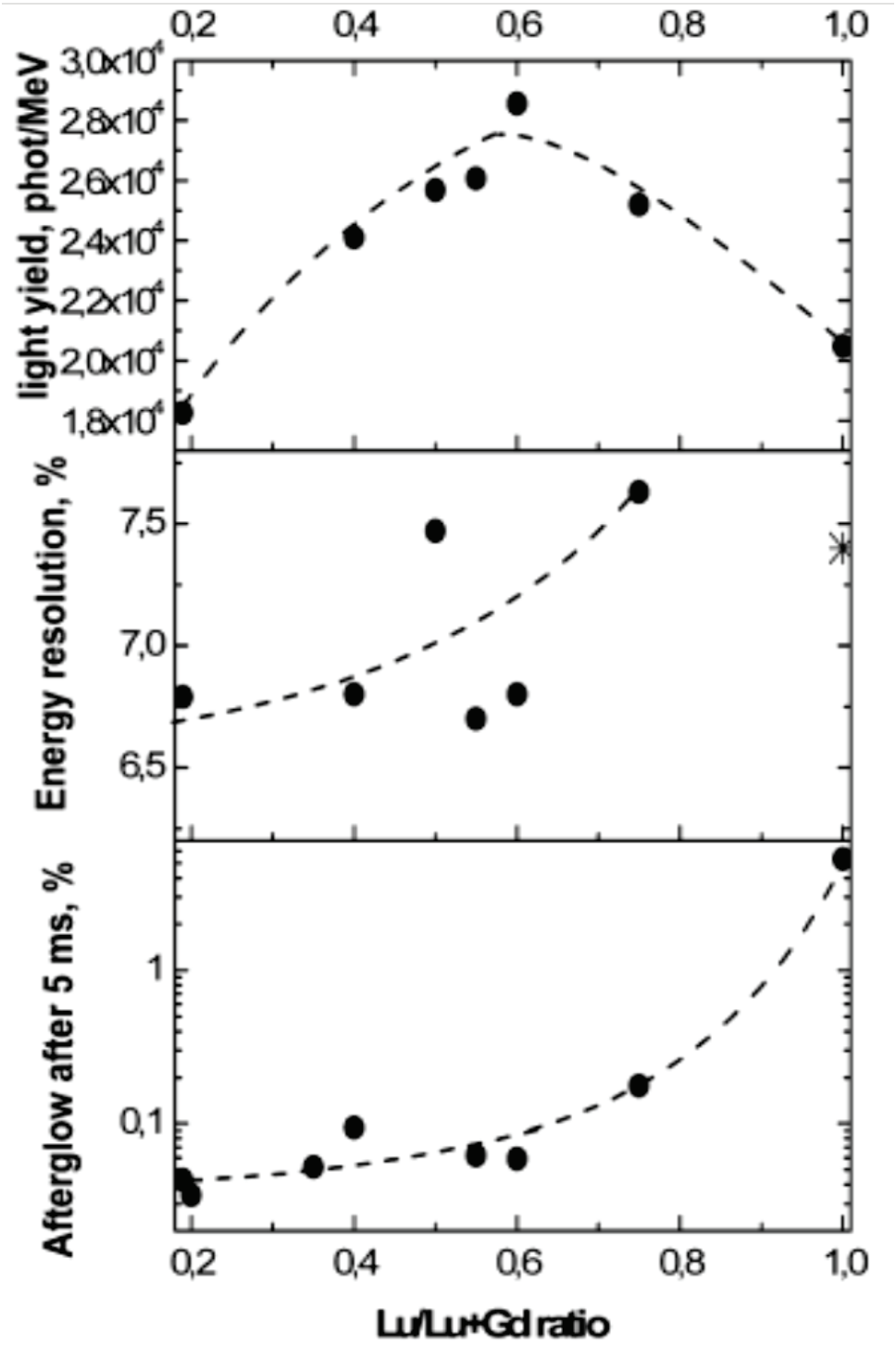

Figure I.19. Light yield (a), energy resolution (b) at 662 KeV, and afterglow (c) after 5 ms in LGSO:Ce crystals with the C2/c structure vs. Lu concentration in host. The asterisk in the middle section corresponds to the best value of LSO:Ce energy resolution found in the literature. [43]

The maximal light yield was observed at around 60 % of Lu concentration in the crystals and at the same time comprised 130% of the LSO:Ce yield (Figures I.19, I.20) [43]. In the case of codoping by Ca^{2+} the highest light yield was 33700 phot/MeV in crystals with 83% Lu. However, Ca^{2+} does not influence the energy resolution (8.1% at 662 KeV) and afterglow (0.46% after 5 ms) [43]. As the influence of Ca^{2+} incorporation was not verified for the compositions with the same Ce content, there is a room for further improvement of scintillation parameters in LGSO:Ce crystals. Comparative parameters of LGSO:Ce and its constituents are presented in the Table 1.

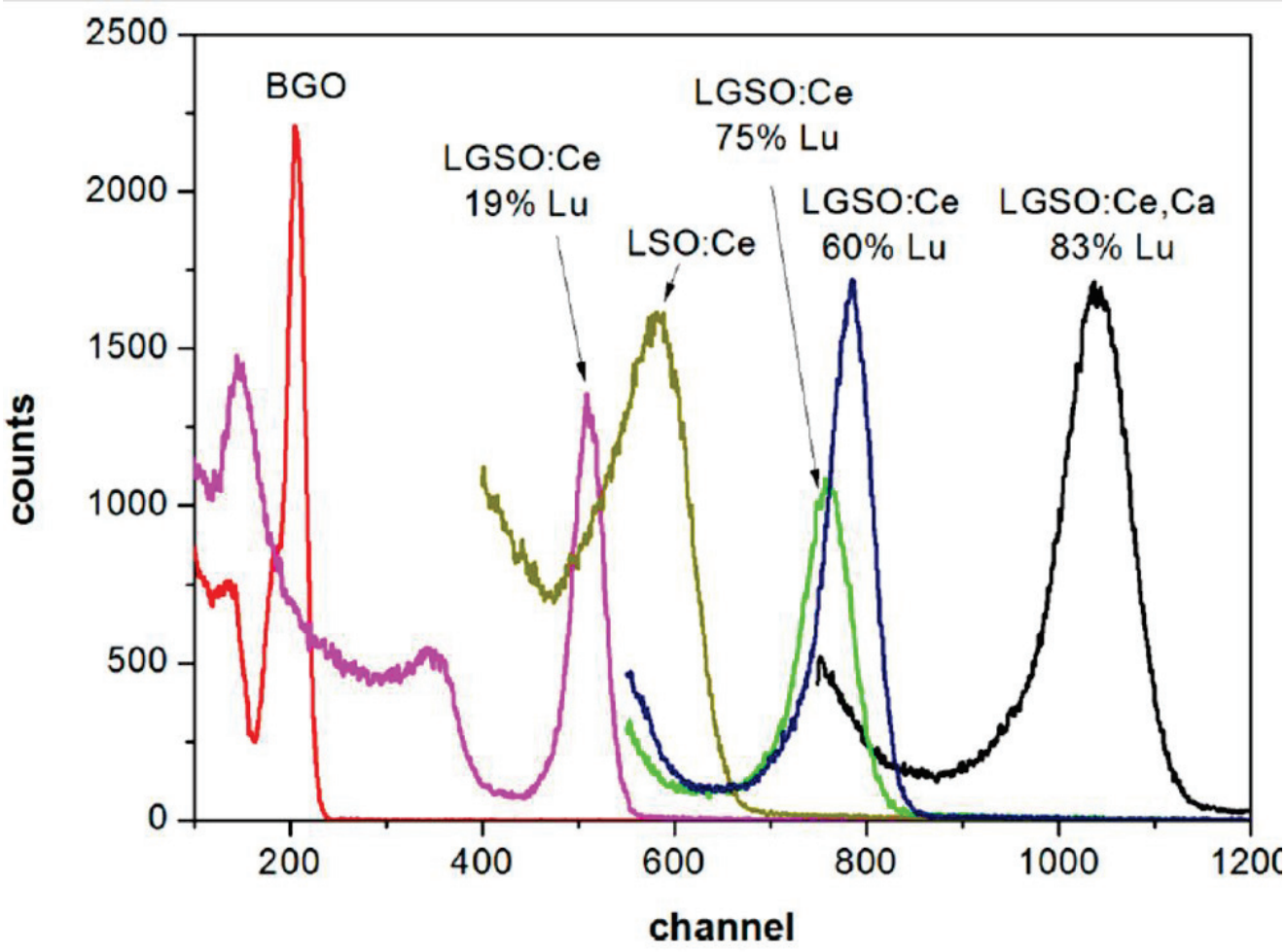

Figure I.20. Pulse height spectra of some LGSO:Ce and LGSO:Ce,Ca crystals in comparison with BGO and LSO:Ce [43].

Table 1.Scintillation parameters of GSO:Ce, LSO:Ce, and LGSO:Ce [43, 96]

Crystal		GSO:Ce	LSO:Ce	LGSO:Ce
γ – radiation ^{137}Cs, 662 KeV	Light yield, Phot/MeV	8000	25000-30000	up to 29000
	Energy resolution, %	9-11	7.3-9.7	6.9-7.3
Decay time, ns		56, slow	40	31
Afterglow level, after 3 ms, %		0.02	5	0.02-0.1

1.3. General information on garnets scintillators. LuAG, LuAG:Ce, YAG:Ce and LuAG :Pr crystals

The $A_3B_5O_{12}$ compounds (where A are rare-earth elements and B are Al^{3+}, Cr^{3+}, Fe^{3+}, Ga^{3+}, In^{3+}, Sc^{3+}) complement the diversity of oxide crystals. The most popular scintillation materials in this category are $Lu_3Al_5O_{12}$ (LuAG) and lighter $Y_3Al_5O_{12}$ (YAG) cubic garnets with the first references since 1928 [98, 99]. The isostructural LuAG- and YAG-based crystals are used for laser and scintillator applications and has a large knowledge base associated with their growth conditions, crystal structure characterization, optical and scintillation properties. Cubic LuAG and other rare earth aluminum garnets were shown to crystallize with the space group symmetry Ia3d. The phase diagram of mixing the Lu_2O_3 and Al_2O_3 is shown in Figure I.21 [100]. YAG crystals are formed from Y_2O_3 and Al_2O_3 oxides and their phase diagram is also well known (Figure I.22) [101]. The garnet phase is the most stable phase in these binary systems. It can be easily obtained as a single phase via solid-state reaction. Its cubic eight-coordination is favorable for obtaining of transparent ceramics [102].

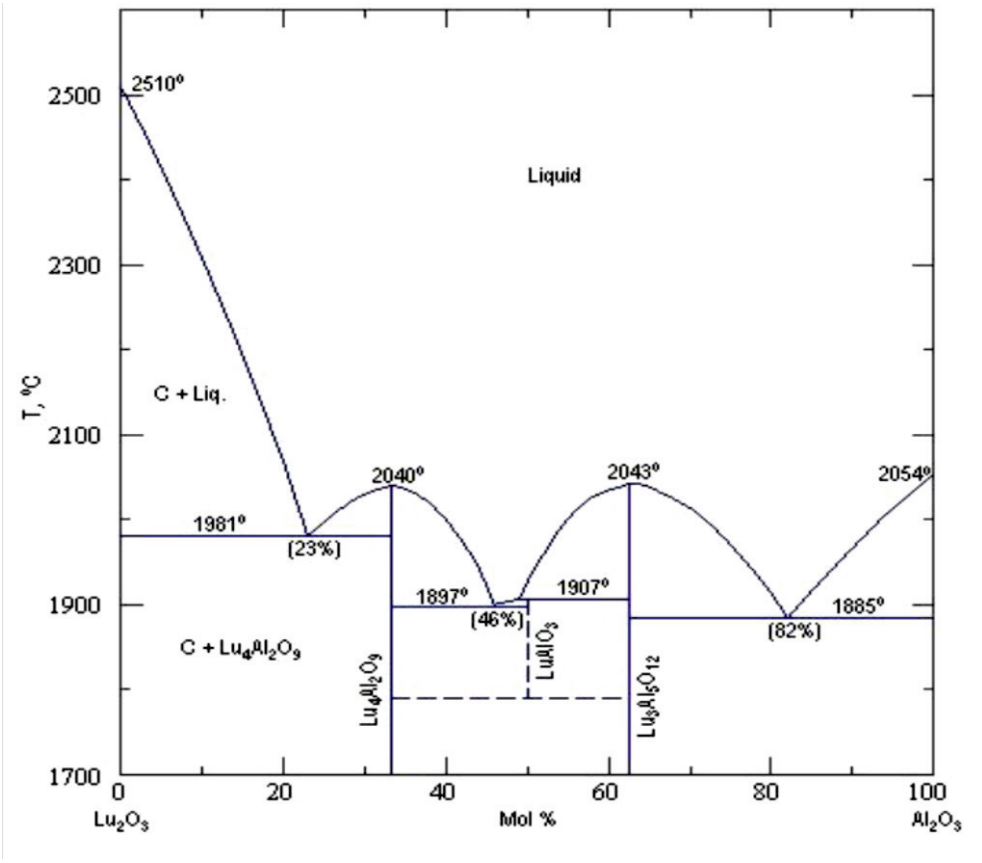

Figure I.21. Phase diagram of the Lu_2O_3-Al_2O_3 system. [100]

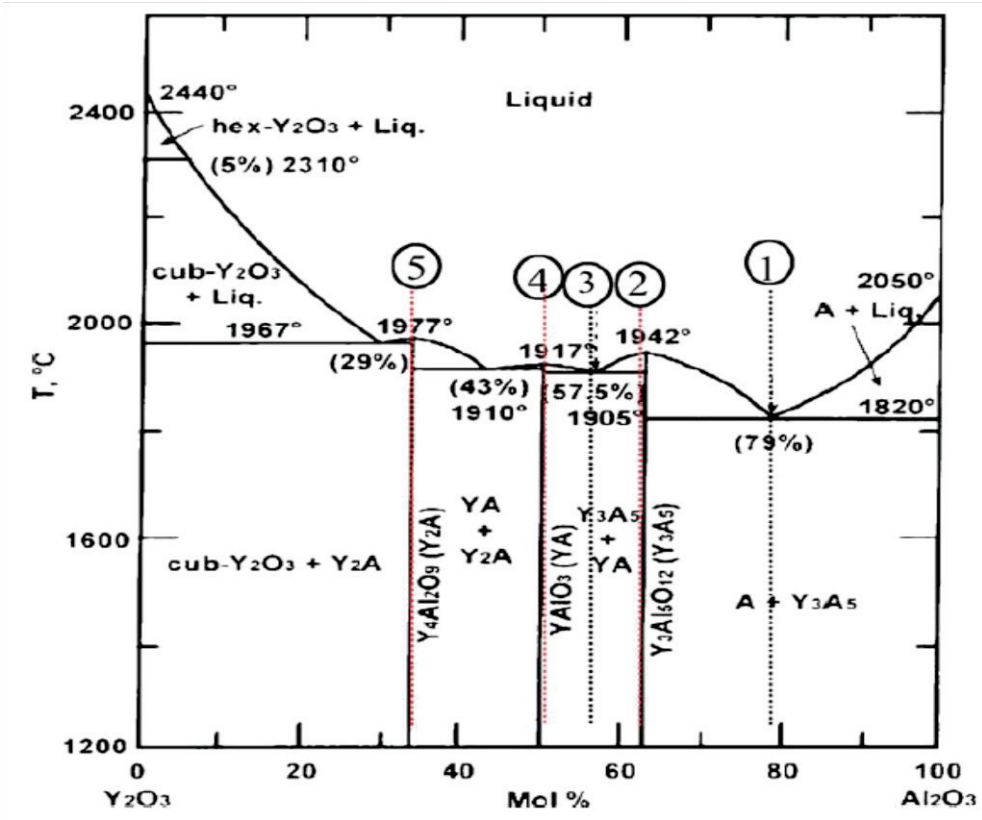

Figure I.22. Y_2O_3-Al_2O_3 phase diagram [101]

Over the past decade, Ce^{3+}-doped rare earth aluminate crystals, such as $Lu_3Al_5O_{12}$:Ce [103, 104, 105], attracted much interest in radiation detection. Ce-doped LuAG and YAG crystals are highly demanded scintillators due to their high hardness, good mechanical and chemical stability, high light yield, variable density from 6.7 g cm^{-3} in lutetium garnet down to 4.56 cm^{-3} in yttrium garnet, and relatively short decay time of 60 ns and 90 ns, respectively [103-106].

The luminescence band corresponding to $5d^1$–4f radiative transitions in Ce^{3+} garnets is peaked at 500-550 nm, which is in a good match with Si photodiodes spectral sensitivity [107]. The luminescence decay time in the case of Pr-doping is reduced by twice [106], but the luminescence band is located in the deep UV band.

LuAG and LuAG:Ce crystals were previously grown by the different methods, and their properties were presented in connection with the different applications [108, 109, 110]. $Y_3Al_5O_{12}$:Ce crystals were thoroughly studied side by side to lutetium garnets [111, 112, 113]. Ce-doped YAG scintillator possesses moderate density (4.55 g/cm^3) and light yield (16,000 phot/MeV) [114].

A detailed study of the LuAG and LuAG:Ce fibers growth process was made with a purpose of further usage in high energy physics. The special attention was paid to the improvement of propagation of the scintillating signal along the fibers [7]. The criterion to characterize the transparency of fibers was their attenuation length, that is, the distance where the emission signal weakens by *e* times [104]. Following the Figure I.23, the authors noticed [7] that with the increase of distance between the falling beam place and the photodetector on the end of the fiber the self-absorption in crystal and reflection losses reduced the propagation of the signal. As the issue, the intensity of luminescence decreased and the emission bands shifted to the longer wavelengths.

With optimization of growth conditions the investigated crystals had shown the promising results on optical attenuation of scintillation light within the fibers (Figure I.24).

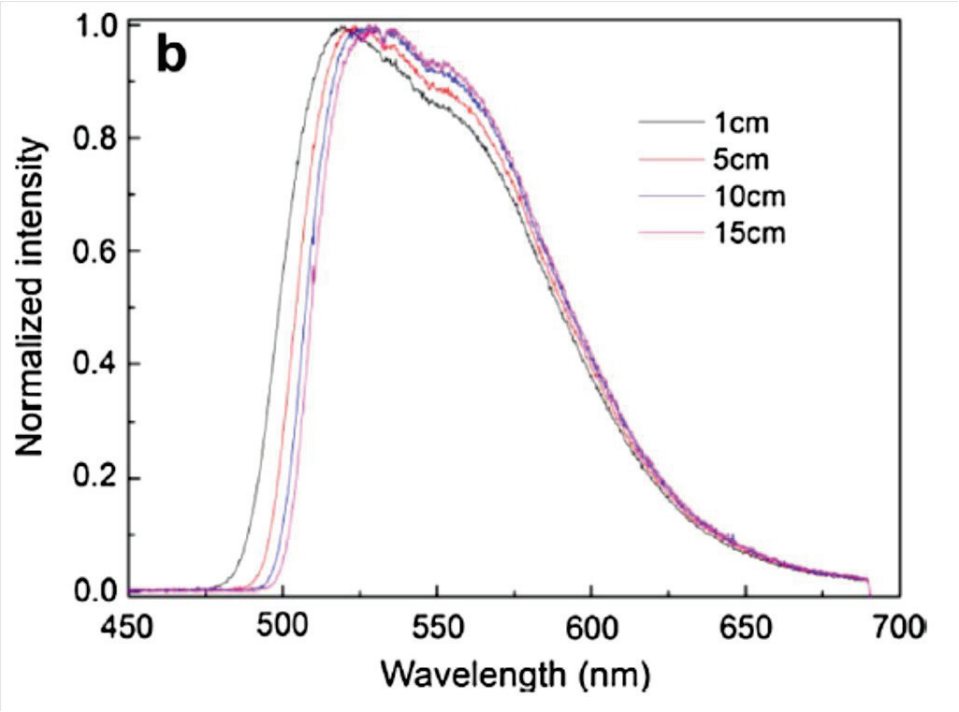

Figure I.23. Comparison of the normalized emission spectra for 1, 5, 15 and 20 cm distance between the falling beam and the end of the fiber [7].

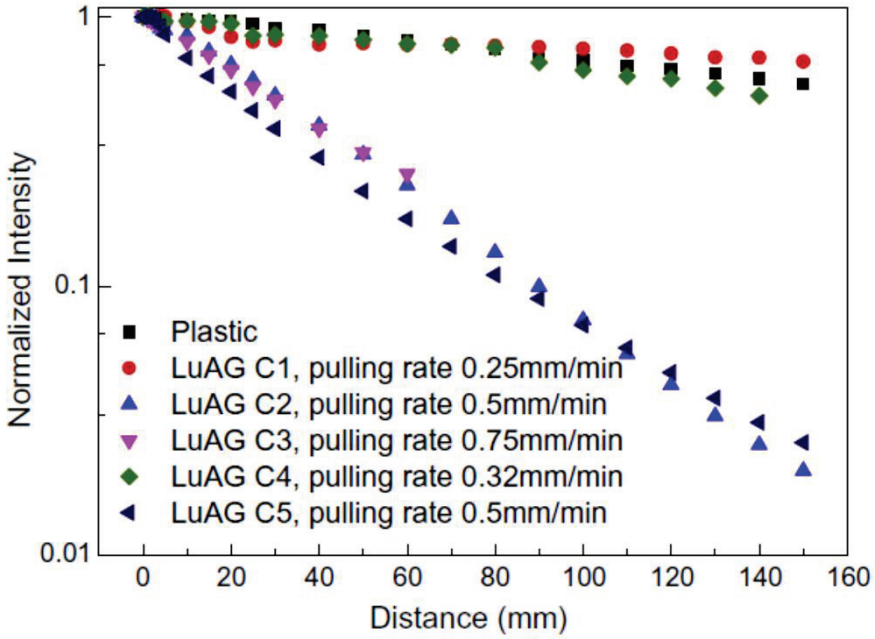

Figure I.24. Attenuation curves for plastic fiber and Ce (<1 at.%)-doped LuAG fibers as a function of pulling rate [7].

The LuAG:Pr crystals possess a good scintillation properties with the light yield of 17000 phot/MeV, and the 20 ns decay time [106].

The antisite defects (Y or Lu ions substituting Al at the octahedral site) are the basic type of intrinsic defects in aluminum garnets [115]. Similarity of thermoluminescence glow curves in the case of Ce-doped and Pr-doped LuAG host, Figure I.25, supports their relation to shallow electron traps, which give rise to thermoluminescence glow peaks within 120–200 K [116]. Both the Ce^{3+} and Pr^{3+} ions play the role of recombination centers, which was proved by the characteristic TSL emission spectra (inset of Figure I.25), while TSL glow curves are determined by the similar electron traps in both systems. Light yield of Czochralski-grown Pr-doped LuAG approaches 200% of BGO at the optimized Pr concentration of about 0.2–0.3 mol% [117]. Pr-doped aluminum garnets scintillation characteristics are closely similar for both the μ-PD and Cz methods. Therefore, LuAG:Pr is a very promising fast and efficient scintillator.

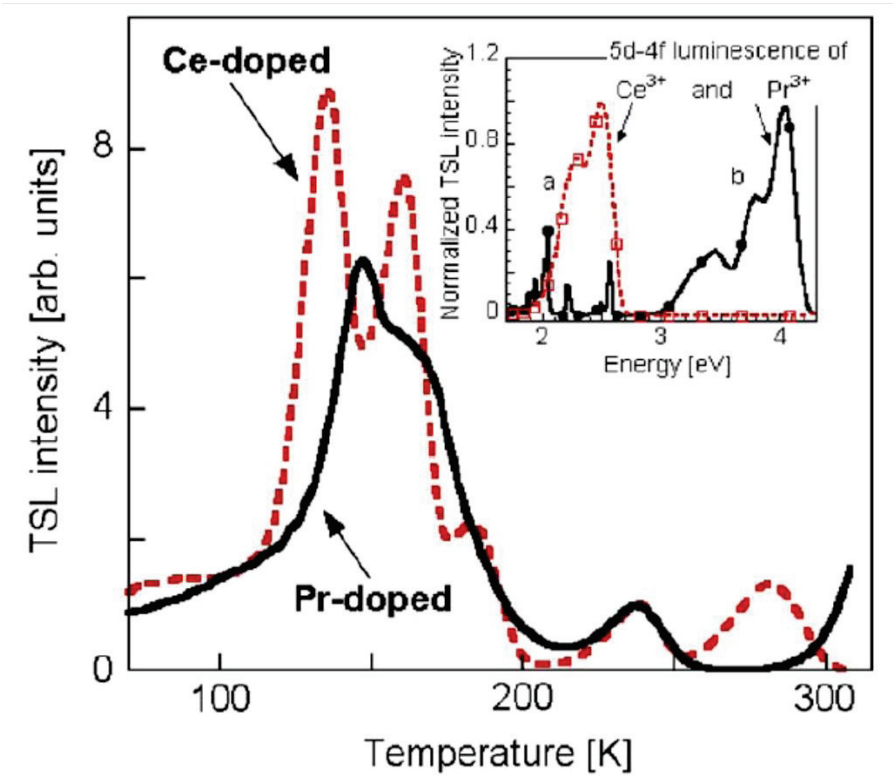

Figure I.25. Thermoluminescence glow curves of Pr- and Ce-doped LuAG single crystal after X-ray irradiation at 10 K. In the inset, the TSL spectra taken within 120–160 K are displayed featuring characteristic Pr^{3+} and Ce^{3+} emission, respectively [117].

1.3.1. LuYAG:Ce mixed crystal

There is few information on the $Lu_3(Al_{1-x}Ga_x)_5O_{12}$:Ce properties in the literature. It is known that undoped bulk crystals were grown by Czochralski method, and their structure was determined and discussed versus LuAG and YAG crystals [92]. The LuYAG:Ce density varies within 4.5 – 6.7 g/cm^3 depending on Lu/Y ratio. Variation of the lattice parameters of LuYAG solid solution as a function of x was presented (Figure I.26). The decrease of effective segregation coefficient was observed with increasing of Lu content in the crystals (Figure I.27). The solidification temperature of LuYAG crystals changed almost linearly from 1930°C (YAG) to 2010°C (LuAG) in the solid solution range.

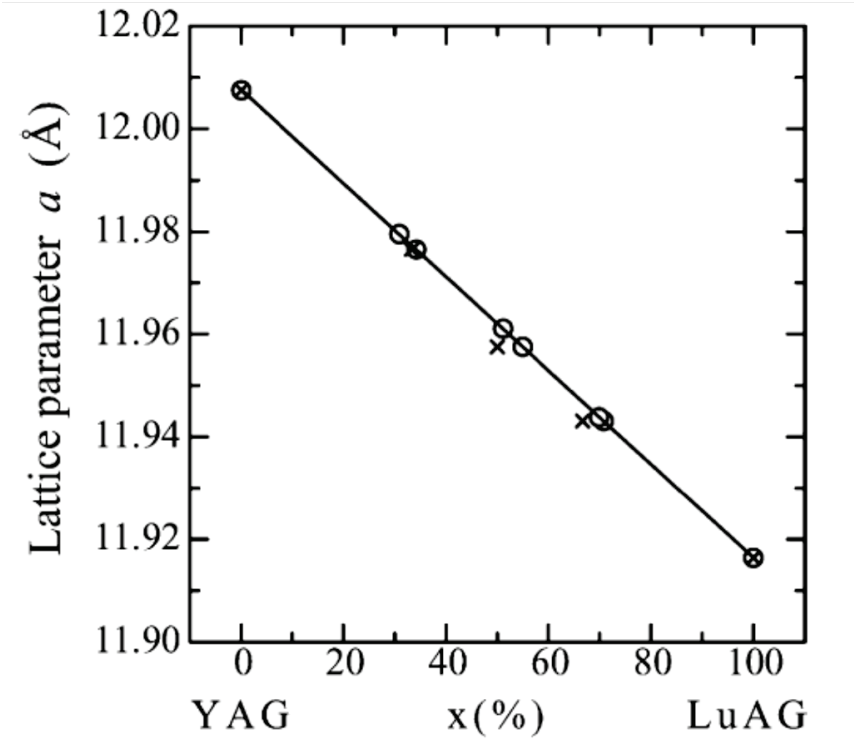

Figure I.26. Lattice parameter of $(Lu_xY_{1-x})_3Al_5O_{12}$ solid solution. The open circles are those with calibrated compositions based on the Vegard's law, and the crosses are those without corrections [92].

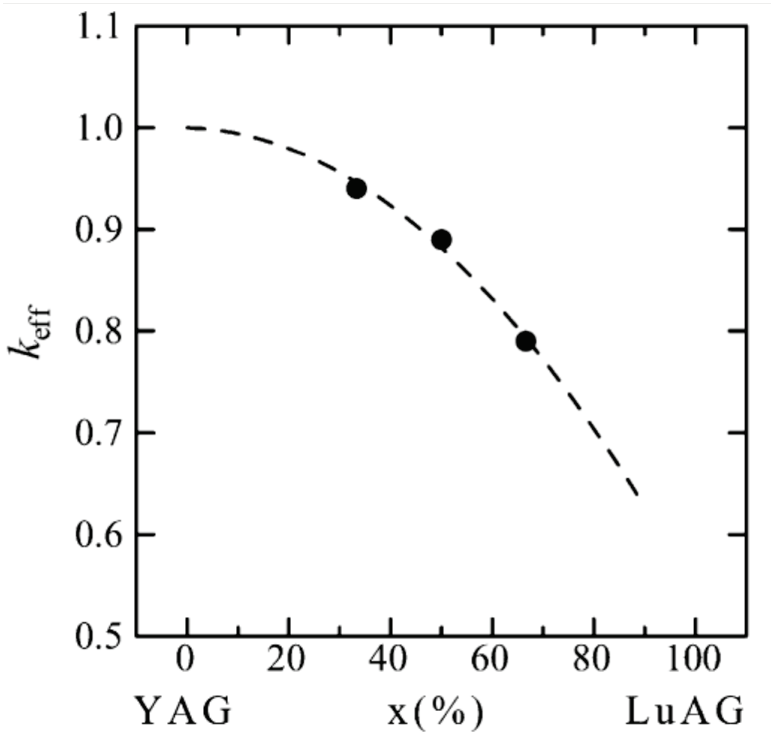

Figure I.27. Effective segregation coefficients k_{eff} for Y atoms of $(Lu_xY_{1-x})_3Al_5O_{12}$ crystals, with a dashed curve fitted by a quadric function passing through the point k_{eff} = 1 at YAG composition for viewing convenience [92].

Mixed Ce^{3+}- or Pr^{3+}-doped $Lu_xY_{1-x}AG$ (x=0.9-1) crystals show the light yield and energy resolution similar to those in doped LuAG, but the contribution of the slow components into scintillation yield was reduced [118] .

In [107] it was shown that two bands (339 nm and 454 nm) on the LuYAG absorption spectra corresponding to 4f-5d transitions are blue-shifted (Figure I.28) relatively to the annealing atmosphere. The emission band appears at 524 nm at the 468 nm excitation. On the X-ray excited fluorescence spectra the peaks related both to host (302 and 360 nm) and Ce^{3+} emission at 524 nm were observed (Figure I.29). Authors noticed that Lu ions incorporation into YAG can reduce the population of antisite defects.

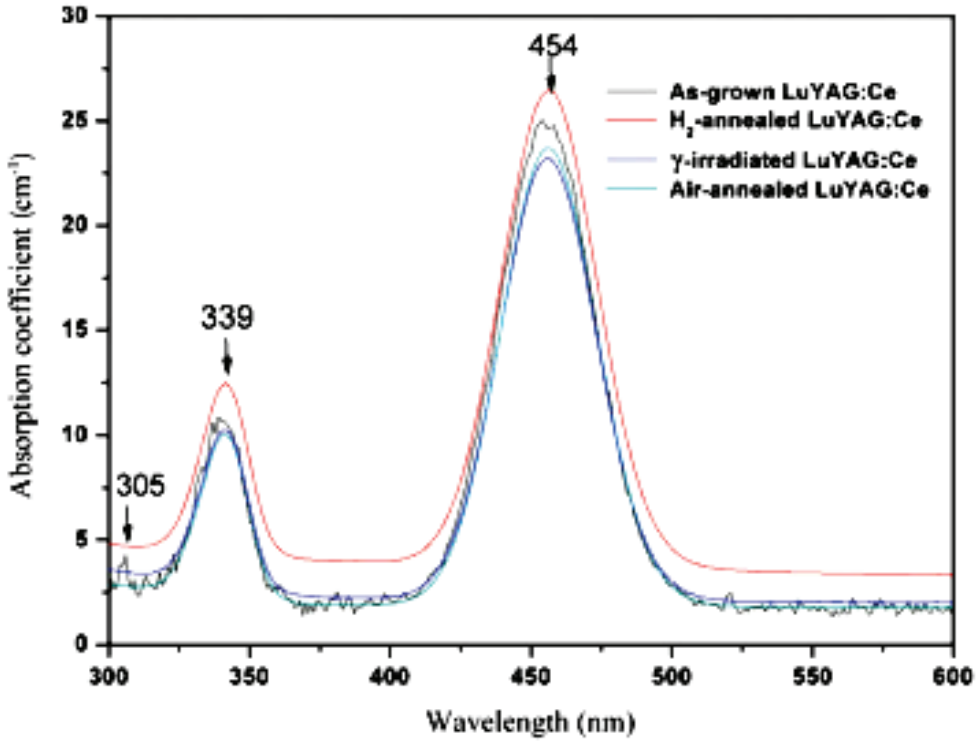

Figure I.28. Absorption spectra of the LuYAG:Ce crystals [107].

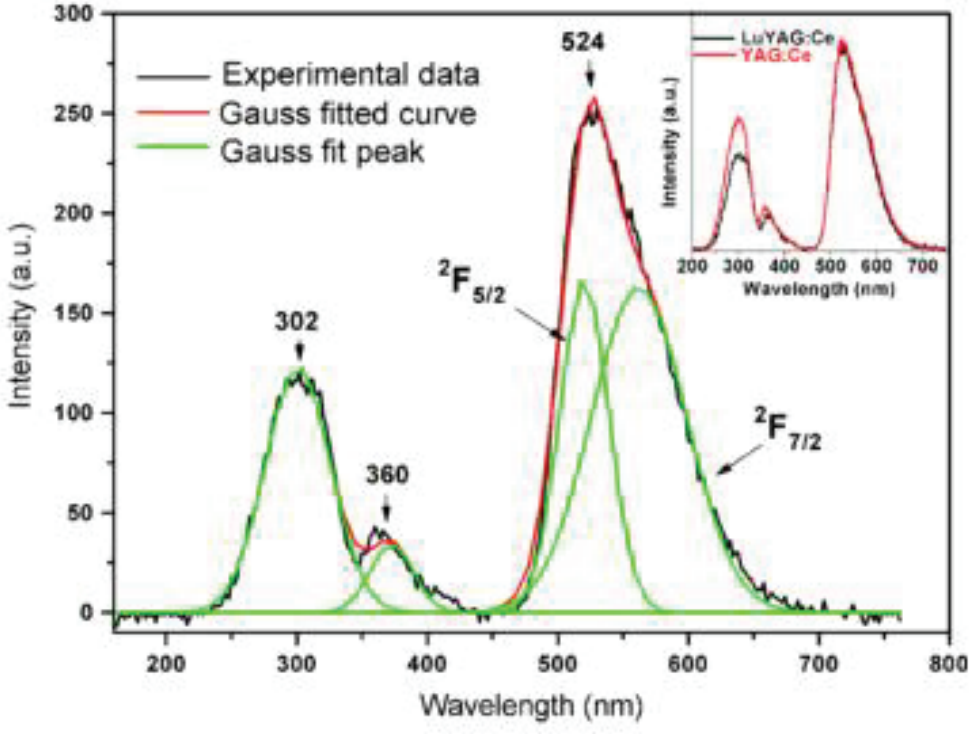

Figure I.29. X-ray excited fluorescence spectra of the as-grown LuYAG:Ce crystal. The figure on the inset is the comparison of X-ray excited fluorescence spectra of the LuYAG:Ce and YAG:Ce crystals [107].

Basically, the reported light yield in LuAG:Pr does not exceed 17000 phot/MeV [106]. However, surprisingly high light yield of 33000 phot/MeV for LuYAG doped with Pr^{3+} was reported recently [119]. Taking into account the energy resolution of 4.4% (at 662 keV) [119], and the density of 6.2 g/cm^3, LuYAG:Pr is a good example of improvement of scintillation parameters in mixed crystals.

1.3.2. YAGG:Ce mixed crystals

Growth of mixed crystals is justified also from the economical point. Substitution of Lu^{3+} by Y^{3+} or Gd^{3+} lowers the production cost due to decrease of raw material cost and decreases the crystallization temperature. Consequently, YAG:Ce or mixed crystals are good alternatives to LuAG and LuAGG-based scintillators.

$Y_3(Al_{1-x}Ga_x)_5O_{12}$:Ce (YAGG:Ce) scintillator was studied in the present work. Some structure and luminescence properties of YAGG based materials were reported previously in [120]. Solid solution crystals with garnet structure became popular hosts for laser and optical applications, see for example [121]. However, their application as scintillation host was limited due to low-to-moderate light yield and low density and effective atomic number compared to perovskite- or orthosilicate-based scintillators. For example, Ce-doped YAG scintillator possesses moderate density (4.55 g/cm^3) and light yield (16,000 phot/MeV) [114]. Full substitution of Al^{3+} with Ga^{3+} leads to the increase the scintillator density up to 5.80 g/cm^3 [122]. It was reported [120] that light output efficiency decreases at Al/Ga substitution, however recent results on $Lu_3(Al_{1-x}Ga_x)_5O_{12}$:Ce LuAGG [18] pushed us to more detailed study of yttrium mixed garnets.

Summary

In this chapter, we review the development of inorganic scintillating oxides crystals and the growth technology to get scintillating crystals with the improved performance. Single crystals such Ce doped GSO, LGSO, LSO, LuAG and YAG remain a strategic materials for scintillation and detection applications. The scintillation performances are strongly connected to the crystal composition and the growth technology.

Chapter II: Growth and characterization methods

In this chapter the various experimental methods to grow fiber-shapes and bulk single crystals, and the methods of their optical and scintillation parameters determination are reported in this section.

2.1. Raw materials preparation

At growth of LGSO:Ce fibers the initial growth runs by μ-PD method were accomplished using the broken crystal chunks of LGSO:Ce with x= 0.2 and 0.5 and 0.01 at.% Ce grown by the Czochralski method. At the next research stage, powders of Lu_2O_3, Gd_2O_3, CeO_2, and SiO_2 with purity not worse than 99.99% mixed at stoichiometric ratios were utilized as raw materials for the rest of fibers. SiO_2 powder was preliminary calcined at 300 ºC to remove moisture. The synthesis of undoped LGSO by solid state reaction was carried out according to the following chemical reaction:

$$x\cdot Lu_2O_3 + (1-x)\cdot Gd_2O_3 + SiO_2 \rightarrow Lu_{2x}Gd_{2-2x}SiO_5. \quad (2.1)$$

As CeO_2 is added to the melt, the reaction transforms to:

$$x\cdot Lu_2O_3 + (1-x-y)\cdot Gd_2O_3 + y\cdot Ce_2O_3 + SiO_2 \rightarrow Lu_{2x}Gd_{2-2x-2y}Ce_{2y}SiO_5 \quad (2.2)$$

The Ce^{+3} activator concentration in the raw material was in the range 0.01 - 1.5 at.%. After the mixing, the second annealing was accomplished at 1200ºC.

At growth of LuAG-based and YAG fibers the chunks of LuAG and YAG crystals previously grown by the Czochralski and micro-PD methods were used as starting raw material, correspondingly. Preliminary calcined powders of yttrium, cerium and praseodymium oxides with the purity not worse than 99.99 % were added to raw materials in the cases of crystal doping. The concentrations of Ce and Pr in melt did not exceed 0.15 at.% in fibers.

2.2. Growth of LGSO crystal by the μ-PD method

$Lu_{2x}Gd_{2-2x}SiO_5$:Ce fibers with $x = 0.2$, and $x = 0.5$ were chosen for fiber growth in view of the optimal combination of scintillation properties [19] and relatively low melting temperatures [93]. The raw materials were loaded into the iridium crucible of 16 mm in diameter with the square capillary die of 2x2 mm^2 in cross-section with the hole of 1 mm in diameter (Figure II.1). The crucible was mounted on the cylindrical iridium afterheater of 16 mm in diameter.

Figure II.1. Ir crucible and afterheater

The crucible and the afterheater were surrounded by the thermal insulation made of alumina ceramics (Figure II.2). The raw materials were heated and melted inside the crucible by RF heating. To protect the iridium crucible and the afterheater from oxidation, the growth was performed under argon gas flow. The melted raw material flowed out from the capillary die through the opening hole at the bottom of the crucible and crystallized on the seed touching the melt meniscus (Figure II.2, II.3b, II.3c).

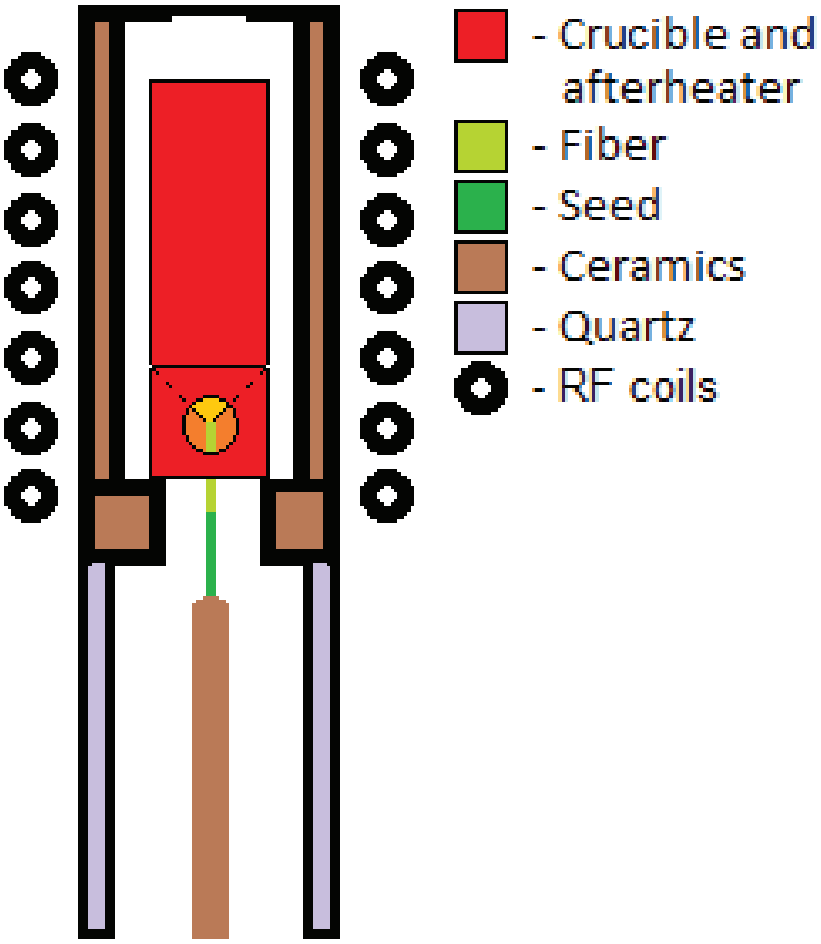

Figure II.2. Schematical view of the growth chamber equipment in μ-PD growth method

This growth chamber was placed inside a quartz tube (Figure II.3a). The afterheater has the hole on the side surface for monitoring the crystallization zone with a CCD camera. During the growth process the seed was pulled down at the rates from 200 to 1000 μm/min. The visual control of the meniscus and the crystal was provided by a CCD camera coupled to a personal computer (PC). LGSO:Ce and LYSO:Ce rods with the 2x2 mm^2 cross section and oriented along the [210] direction were used as seeds. After the growth, the temperature of the fibers was ramped down to room temperature during 3 - 26 hours.

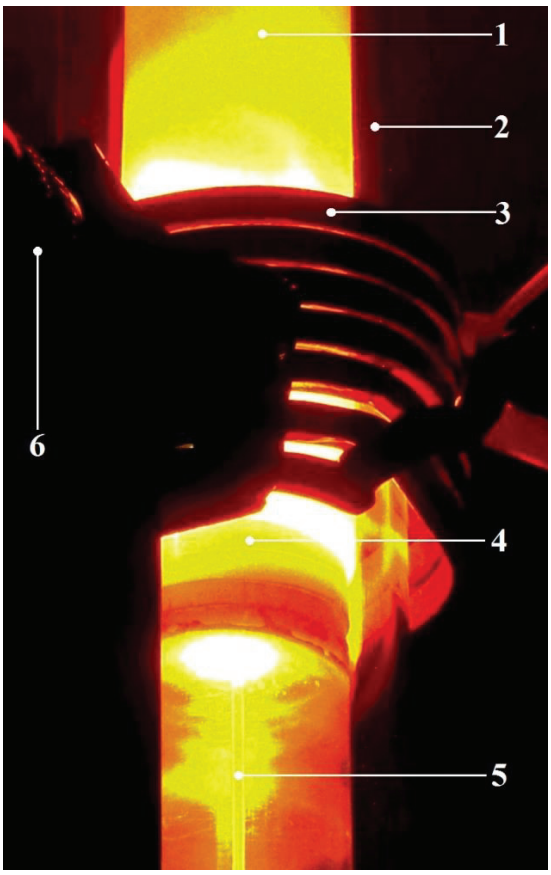

a

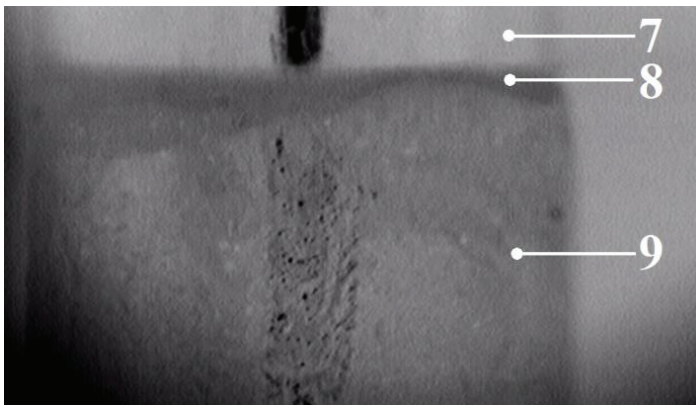

b

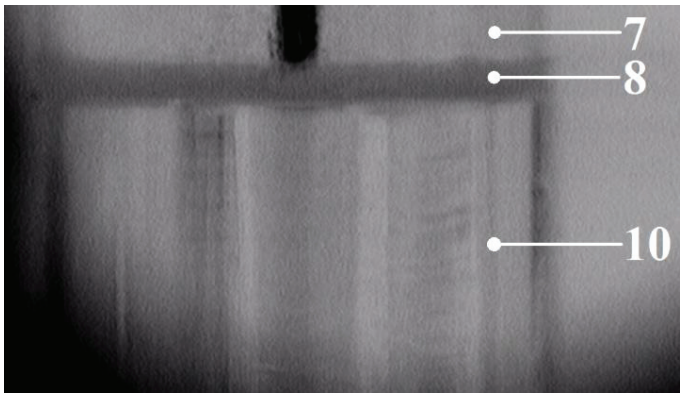

c

Figure II.3. The view of the LGSO:Ce fiber-shaped crystal growth facility (1 – thermal insulating ceramics, 2 – quartz tube, 3 – RF heating coils, 4 – hot zone, 5 – seed mounted on the motorized shaft, 6 – CCD camera) (a); CCD camera view of the crystallization zone in the moment of seeding (7 – capillary at the Ir crucible bottom, 8 – molten zone, 9 – seed) (b); CCD camera view of crystallization zone during the fiber growth (10 – growing crystal).

2.3. LGSO:Ce characterization methods

2.3.1. Determination of crystal structure and composition

The X-ray study of LGSO samples was carried out using a single crystal diffractometer "*Xcalibur*-3" by *Oxford Diffraction* (MoK α-radiation, $\lambda = 0.71073$ A°, graphite monochromator, a *Sapphire*-3 CCD-detector, ω/θ scanning in the range of $2\theta \leq 901$, corrections due to absorption by equivalent reflections were taken into account). The structure calculations were carried out using a SHELX-97 and WinGX software. The elementary cell parameters were refined by the Rietveld method using the diffractogram obtained by studying the powders of the same crystalline samples using a *Siemens* D500 powder diffractometer. The results obtained by applying the single crystalline method were taken as the initial data for refinement. The XRD-spectra were obtained by another *Siemens* D500 setup. The elementary cell parameters were calculated according to the 2-theta peak positions. Elemental concentrations were evaluated using an iCAP 6300 (*Thermo Scientific*) inductively-coupled plasma (ICP) atomic emission spectrometer, using the following wavelengths: 404.076 nm and 456.236 nm for determination of the Ce content, and 335.047 nm and 336.223 nm for determination of Gd content. Two different calibration methods were used: i) the external aqueous calibration for the determination of the Gd content, and ii) the standard addition calibration for the determination of Ce. The reference solutions for the determination of the gadolinium content were prepared on the basis of the stock solution of Gd. The final acidity of the reference solutions was maintained constant for the samples to be analyzed.

All the used reagents were of analytical grade. The single element stock solutions of Gd(III) and Ce(IV) at a concentration of 1 g/L were prepared by dissolving the appropriate amount of Gd_2O_3 or CeO_2 in nitric acid and diluting the solution to the desired volume with ultrapure water. The samples taken from the top of the fiber (2-3 mm beyond the place of seeding) were crushed in pieces and finely ground in an agate

mortar. The amount of 20 mg of the crystal material was transferred into a 50-ml beaker, where 5 ml of orthophosphoric acid were added. The beaker was heated on a hot plate until the sample dissolution. After cooling, the resulting solution was transferred to a 50 ml graduated flask and was brought up to the necessary volume with ultrapure water.

2.3.2. Optical and scintillation measurements

The distribution of Ce dopant across the crystals can be evaluated using the spatial distribution of luminescence under different types of excitations. The luminescence spectrum of Ce^{3+} in orthosilicates with monoclinic C2/c structure consists of two bands [30]. The first band peaks at ~420 nm and is caused by emission of Ce^{3+} in CeO_7 polyhedra. The second one is peaked at ~510 nm and occurs as a result of the emission of Ce^{3+} in CeO_6 polyhedra. Both centers have specific excitation and luminescence spectra [123]. It is reported that the luminescence intensity due to emission of Ce^{3+} in CeO_6 sites correlates well with the gadolinium content in LGSO:Ce crystal [19]. Therefore, the intensity of luminescence related to Ce^{3+} at CeO_6 sites can serve as an indication of Gd content. We showed that the microscale uniformity of Lu/Gd ratio in bulk LGSO:Ce scintillation crystals can be revealed by the spatial distribution of photoluminescence parameters.

The samples for photoluminescence study were cut from the crack-free parts of the crystal and polished for the measurements of their optical and scintillation properties.

The light yield of the samples was evaluated at under 661.7 keV γ-ray-irradiation. The full absorption peak position was evaluated at the excitation by a ^{137}Cs radioactive source. The pulse height spectra were measured with a XP2020Q photomultiplier connected to a *Lecroy* LT 372 oscilloscope. The emission decay was measured by the oscilloscope and the signal was time-integrated.

The X-ray-excited luminescence spectra were studied using a *LOMO* KSVU-23 spectrometer and an X-ray emitter (U = 40 kV, I_a = 25 mA, Cu anode) as an excitation source. The afterglow after the X-ray irradiation with the dose of 5 R was measured using the special measurement setup consisting of a RAPAN-200 pulsed X-ray emitter (E_x = 100–160 keV), a S8594 photodiode, a current–to–voltage converter, a multiplexer, a controller, an A/D converter, a PC, oscilloscope, and a control unit for the X-ray emitter.

2.3.3. Microscopy measurements

The cathodoluminescence (CL) was excited with an electron gun EMG4212 from *Kimbal Physics*. The samples were attached to a metal sample holder and placed into a vacuum chamber with the electron gun. The cathode-to-anode voltage of 10 kV was used, while the electron current was varied between 5 and 20 μA. The emission spectra under the cathode beam excitation were measured at 300 K using an *ANDOR Shamrock* 163 CCD spectrometer. The sample surface was monitored by a CCD digital camera with and without electron beam irradiation.

The spatial distribution of the PL parameters under the selective excitation of the Ce^{3+} at CeO_6 centers was investigated using confocal microscopy. The PL was measured by employing the *WITec* microscopy system *Alpha 300* coupled with the spectrometer *UHTS 300* equipped with a thermoelectrically cooled CCD camera. A CW laser diode emitting at 405 nm was used for excitation. Both samples were measured at the same excitation power density. The objective with NA = 0.55 ensured the spatial resolution of 400 nm in the X-Y plane and 1600 nm in the Z direction perpendicular to the crystal surface.

PL intensity of both CeO_7 and CeO_6 centers was investigated using a wide-field fluorescence microscope *Olympus BX51*. The spectral range between 320 nm and 400 nm of a halogen lamp emission was used for excitation. A long-pass filter with cut-

off wavelength of 420 nm was used to pass the spectrally-integrated PL to a CCD camera. All the PL measurements were performed at room temperature.

For detection of inhomogeneous distribution of Gd across the grown LGSO:Ce we applied the method of Gd sensitization in LGSO:Ce developed on the base of Cz grown crystals developed by us. The two sub-bands observed in the LGSO:Ce luminescence spectra at ~ 420 and ~ 520 nm (Figure II.4) can be attributed to 5d-4f transitions of Ce^{3+} at Ce1 (CeO_7) and Ce2 (CeO_6) polyhedra. In LSO:Ce, approximately 90-95% of Ce^{3+} is situated at Ce1 sites, since a bigger cation (1.03 Å vs. 0.86 Å in Lu^{3+}) tends to occupy a bigger site [124, 125]. The averaged distances between the lanthanide and the surrounding oxygen atoms here are in Ce1 and in Ce2 site [19]. The addition of gadolinium leads to loosening of the crystal lattice, and the cerium distribution between the sites becomes more homogeneous. This can be evaluated from the relative intensity of the Ce1 and Ce2 bands in the luminescence spectrum as it is shown in Figure II.4. Accordingly, there is a direct correlation between the Gd content and the ratio of the Ce1/Ce2 band intensity (Figure II.4). This plot also shows that the relative intensities of Ce1 and Ce2 bands linearly change with Lu content despite the possible fluctuations in Ce concentration within 0.2 to 0.9 at.% in different samples under study. Therefore, the local Lu/Gd ratio can be evaluated using the features of luminescence spectra.

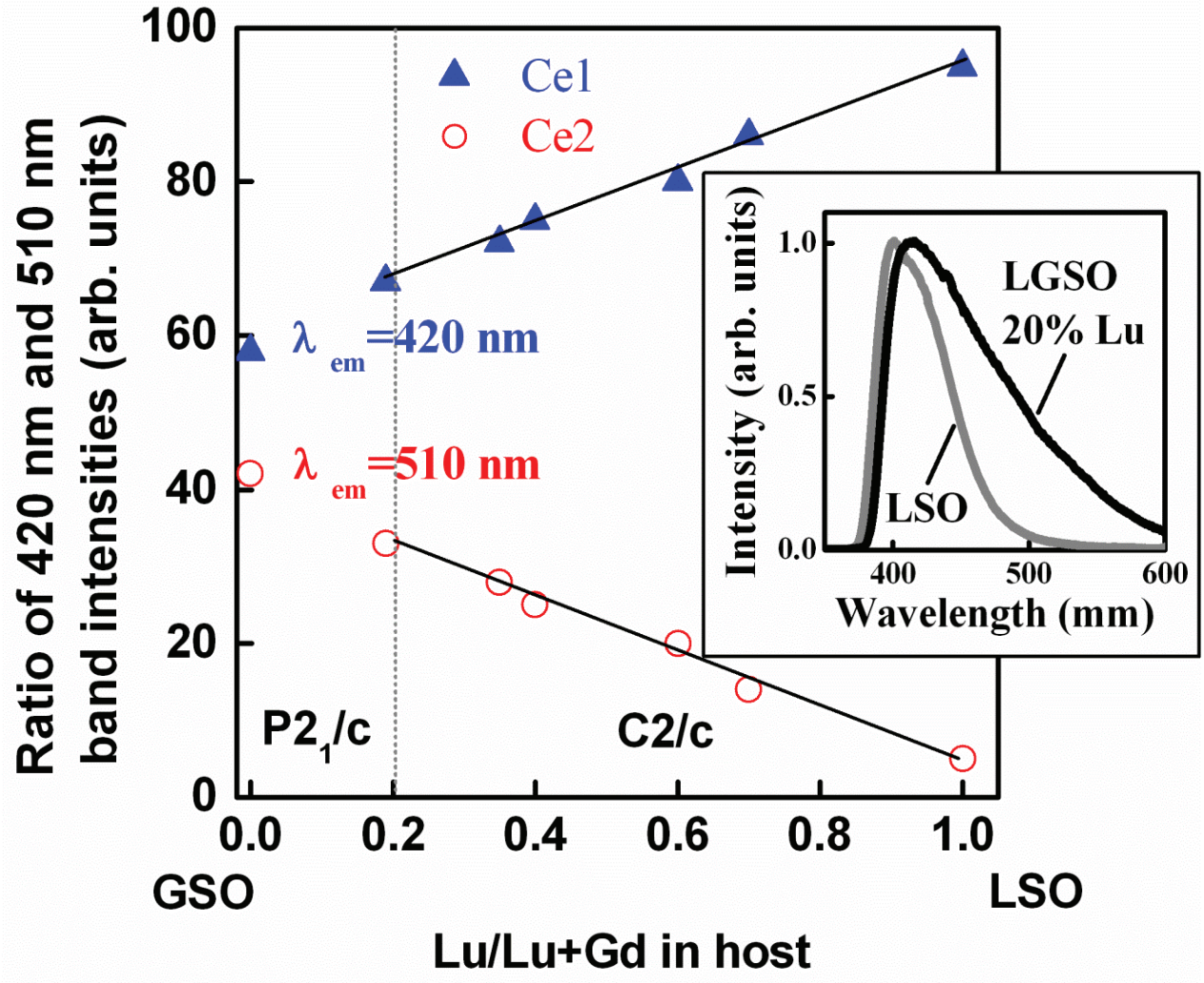

Figure II.4. Contributions of Ce1 (CeO7) and Ce2 (CeO6) luminescence bands into the overall luminescence as a function of LGSO:Ce composition. Inset: typical spectra of LSO:Ce and LGSO:Ce X-ray luminescence. Ce concentration is maintained within the range of 0.2–0.85 at. %.

The excitation and emission spectra of Ce1 and Ce2 luminescence in LSO and LGSO presented in Figure II.5 show that the excitation bands of Ce1 and Ce2 strongly overlap, and contributions of both components in the luminescence spectrum are difficult to distinguish. Meanwhile, excitation at 405 nm (marked by arrows in Figure. II.5) used in confocal microscopy experiments should provide selective excitation of Ce2 centers.

Using the confocal microscopy, the spatial distributions of spectrally-integrated photoluminescence (PL) intensity, full width at half maximum (FWHM), and PL

spectral center-of-mass were determined in LSO:Ce and LGSO:Ce samples. The X-Y scan along the sample surface was not informative, because the surface scratches left by polishing impose substantial distortions of photoluminescence spectra shape.

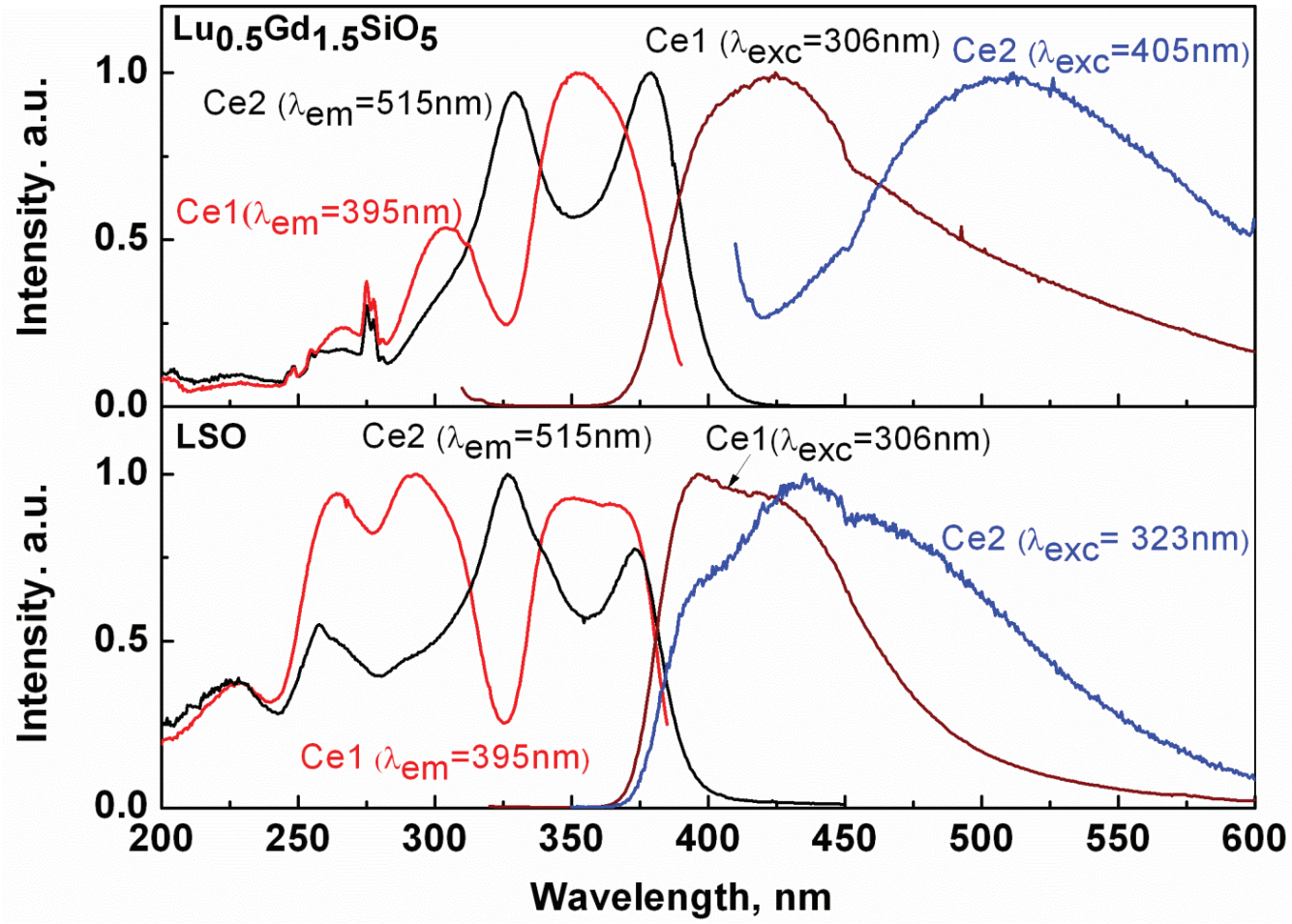

Figure II.5. Excitation and emission spectra of LSO:Ce and $Lu_{0.5}Gd_{1.5}SiO_5$:Ce

To separate the contribution of the surface phenomena, the spatial distribution of the photoluminescence parameters were also measured in the direction perpendicular to the sample surface.

The spatial distributions of all the parameters were nearly homogeneous, except the center-of-mass distribution (Figure II.6). The spatial distributions in LSO:Ce and LGSO:Ce crystals are qualitatively different. In LSO:Ce the PL band gradually shifts to longer wavelength with increasing distance from the surface. This behavior can be explained by reabsorption due to fluctuations in Ce overall concentration in the regions

under study. Meanwhile, this feature is less pronounced in LGSO:Ce, probably, due to better homogeneity in overall Ce distribution. This assumption is supported by higher segregation coefficient (up to 0.8) in $Lu_{0.5}Gd_{1.5}SiO_5$:Ce [43] compared to LSO:Ce (0.22) [83].

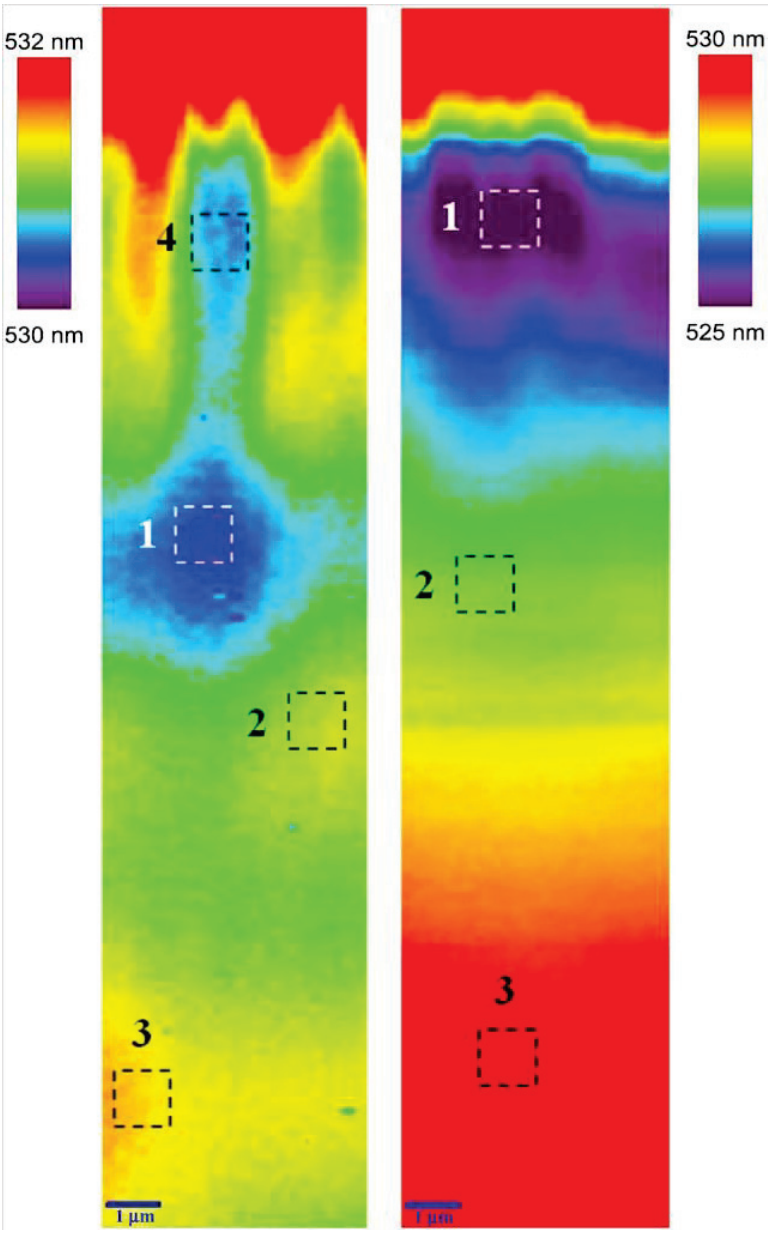

Figure II.6. Spatial distribution of PL band center-of-mass position in LGSO:Ce (left), LSO:Ce (right).

Basically, inhomogeneity in Ce distribution in LSO:Ce is a well-known phenomenon [126]. Meanwhile, in LGSO:Ce was observed spatial inhomogeneities of the order of 1 –3 μm in diameter chaotically distributed in the crystal volume. To reveal the nature of these inhomogeneities the spectra taken from them were compared. The luminescence spectra of both LSO:Ce and LGSO:Ce under 405 nm excitation are peaked near 500 nm with no remarkable short-wavelength component. The differential spectra for LSO:Ce measured at different distances from the surface exhibit a "zigzag" at 400-600 nm, which is obviously linked to the redshift of the PL spectrum due to reabsorption phenomena.

Meanwhile, the shapes of the differential spectra in LGSO:Ce are more complex. Besides the "zigzag", a spectral component peaked in the vicinity of 500-700 nm is observed only in LGSO:Ce (Figure II.7).

Three possible interpretations of the origin of the observed long-wavelength component can be considered: 1) impurity luminescence, 2) increase in the intensity of Ce2 luminescence in the long wavelength part of the emission band, and 3) existence of structural defect areas (domains) in crystal. Significant impurity-related luminescence seems to be not feasible, since to the best of knowledge, only Dy^{3+} among the trivalent ions has luminescence bands in similar host (Gd_2SiO_5) at 450-500 nm and 550-700 nm [127]. However, the shape of these bands is different, and, in contrast to the GSO:Ce,Dy, the luminescence bands in LGSO:Ce (Figure II.6) do not contain any fine structure. Moreover, the band position varies in different subtracted spectra. This is an indication that optical transitions at Dy^{3+} can be excluded as the origin of this spectral component.

The second and third interpretations, in fact, do not contradict to each other, because defects are more probable to occur on the boundaries between domains with different composition and lattice parameters. Herein, the band position evidences in favor of defect related luminescence. Anyway, the content of both Ce2 and defects is determined by introduction of Gd, since the corresponding spectral features are not observed in LSO:Ce. Consequently, the intensity of the 500-700 nm band clearly corresponds to Gd concentration. Thus, our results evidence the inhomogeneity in Gd

distribution in the crystal (see Figure II.4). Qualitatively the same difference spectrum, just with absolute intensities several times larger, see Figure II.6, are obtained when comparing the areas in LGSO:Ce and LSO:Ce situated at approximately the same distance from the surface. This is additional evidence that the intensity of 550-600 nm band depends on Gd concentration.

Therefore, according to the data presented in Figure II.6, we evaluate that, a part of the region 4 located near the surface, the Gd concentration in the studied areas decreases in the sequence from area 2 to area 3 to area 1.

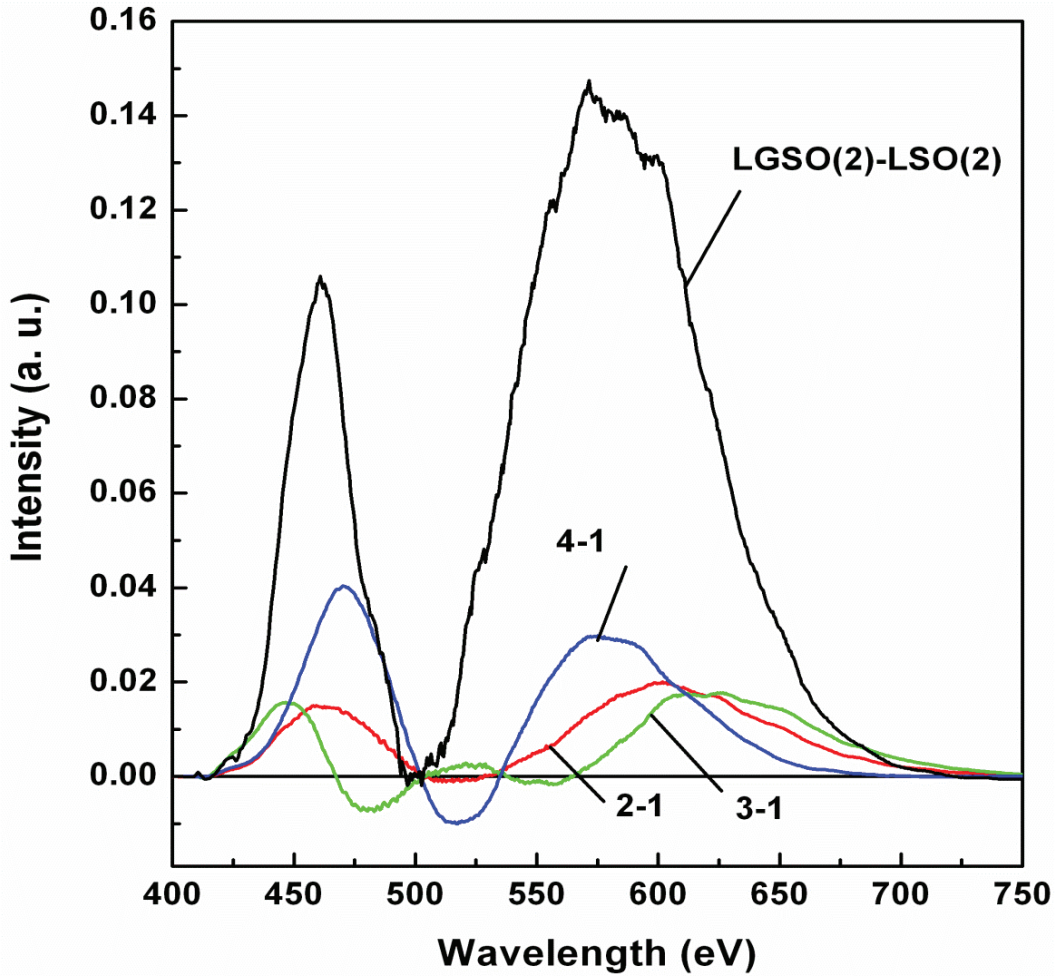

Figure II.7. Differential PL spectra in LGSO:Ce samples at different locations. The PL spectra were normalized before subtraction. Difference spectrum between area in LGSO:Ce and area in LSO:Ce is added for comparison.

To directly confirm the existence of the domains enriched with one of the cations and to reveal the origin of these domains, a detailed structural analysis (e.g., using EXAFS method) is necessary.

The comparison of the spatial distributions of PL parameters in LSO:Ce and LGSO:Ce crystals reveals the presence of spectral component in LGSO:Ce at > 500 nm. Though the origin of this component is not completely clear, its intensity obviously reflects fluctuations in Gd concentration across the crystal, i.e., reveals the existence of areas enriched with Gd or Lu atoms.

2.4. Growth of LuAG, LuAG:Ce, LuAG:Pr, YAG:Ce and LuYAG:Ce by the μ-PD method

The LuAG fibers were grown from the melt by the micro-pulling down method. All the experiments were done in inert Ar atmosphere. All LuAG-based and LuYAG:Ce fibers were grown using the Ir crucible with a round 2 mm diameter shaper (die) and afterheater, YAG:Ce fibers using the conical crucible (Figure II.8). A conical crucible die formed 1 mm round shaped fibers of YAG:Ce.

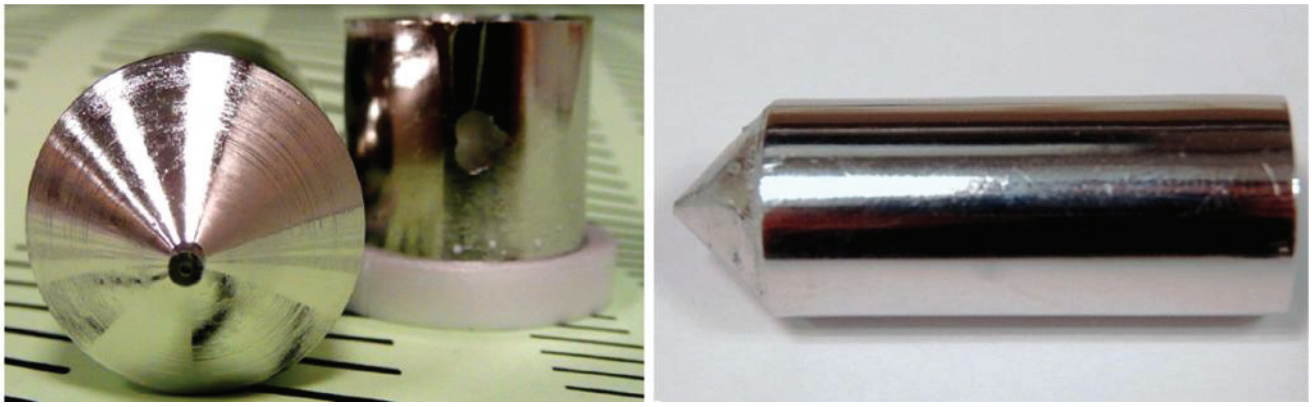

Figure II.8. Ir crucible and afterheater used for LuAG-based fibers (left) and a crucible used for YAG:Ce growth.

The details of the method were described in [7]. To find the optimum balance between pulling rate and crystal quality, the fibers were grown with the rates 300, 350,

and 500 μm/min. In order to estimate the seed orientation effect the fibers were obtained with the seed orientations [111] and [100]. LuAG:Pr fibers were grown with the pulling rate 300 μm/min, with [111] and [100] seed, YAG:Ce fibers were grown only with the [111] orientation and 300 μm/min pulling rate. The seeds used (Figure II.9) were doped and undoped fibers previously grown by the μ-PD, or fibers cut from bulk crystals.

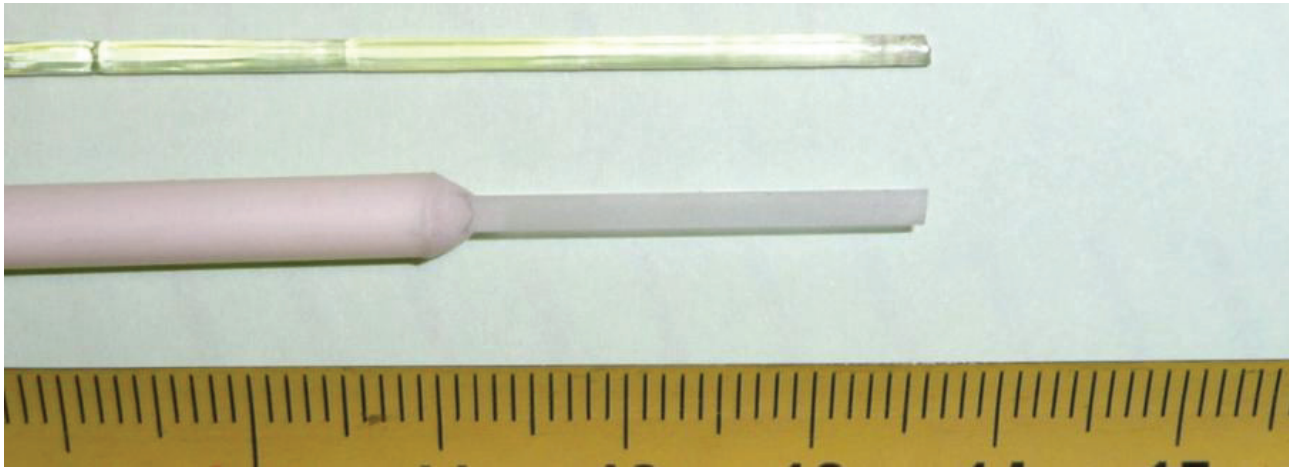

Figure II.9. LuAG:Ce seed [111] made of previously grown fiber (upper) and the seed of undoped LuAG [100] cut from the bulk crystal (lower).

2.5. Garnet crystals characterization methods

2.5.1. Attenuation length measurements

Attenuation length (i.e., the fiber length where which the intensity of LED-excited light falls by *e* times) was taken as the indicator of fiber optical quality. This parameter was measured by the three methods described below:

LED bench

The most of attenuation length measurements were carried out using the custom made setup in CERN PH-CMX under excitation with blue light (475 nm) for undoped

and Ce-doped fibers (Figure II.10). A fast LED driver (SP5601 from CAEN) was used; the light was transported with a clear fiber to the sample. For LuAG:Pr, 250 nm excitation was used ultrafast pulsed UV-LED driver from CAEN. Both extremities of the LuAG and YAG fibers were coupled to MPPCs, also called SiPMs, (Model S10931-050P from Hamamatsu). The output of these MPPCs were amplified with a dedicated instrumental amplifier (gain of 180) operated in a differential mode. Signals (of both left and right photodetectors) were then acquired with a digitizer (Model DT5720 from CAEN). The fibers were moved with a translating stage (Model M-413.32S from PI).

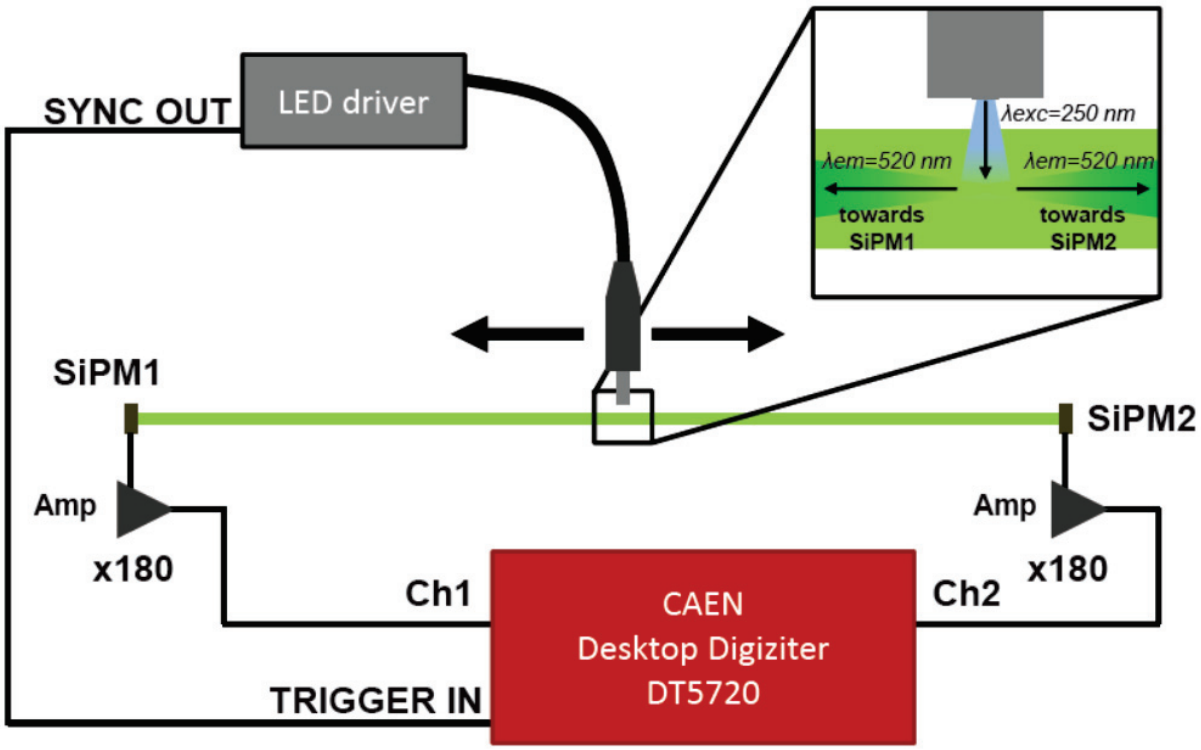

Figure II.9. Setup for the measurement of light attenuation of the fibers.

Xe lamp bench

Preliminary results on attenuation length of some LuAG:Ce fibers were obtained using the custom made setup in ILM with Xe lamp excitation at 350 nm. The beam from the source was focused on the side of the fiber. Scintillation light propagated through the fiber was registered on its end face. The signal was transferred by the

optical fiber to the monochromator (Triax series 320) and a CCD camera. In comparison to the LED experiment the bench with the fiber was moved manually with 1 cm increment perpendicularly to excitation beam carrying out the attenuation mapping measurements.

2.5.2. Cathodoluminescence

The distribution of CL intensity across the fibers was measured by the AVT Pike F-100B CCD camera, with a magnification 3.95X. LuAG:Ce and LuYAG:Ce samples were cut perpendicularly to the growth axis. Before the installation on the holder the side not exposed to the electron beam was covered in black paint in order to avoid presence of reflected light (Figure II.11). The beam from the electron gun EMG-4212 Kimball Physics was left unfocussed in order to have a uniform electron flux on the entire sample surface.

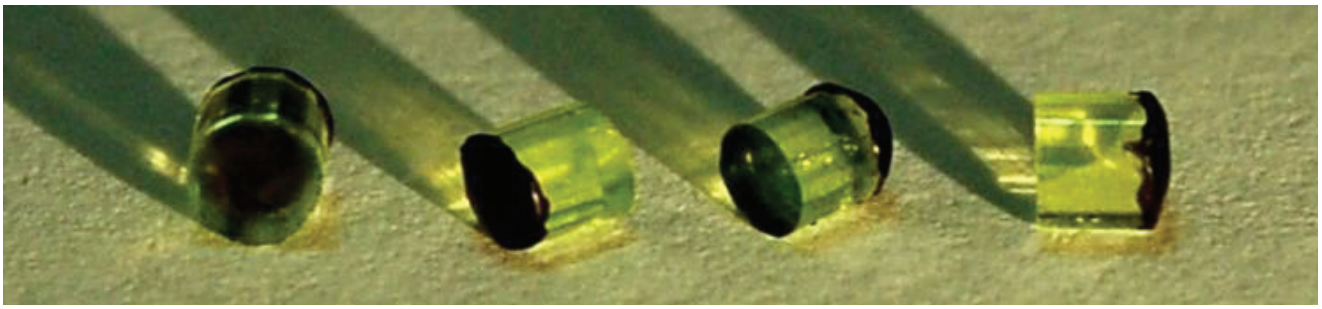

Figure II.11. Samples of LuAG:Ce prepared for cathodoluminescence measurements.

2.6. YAGG:Ce growth by the Czochralski method

$Y_3(Al_{1-x}Ga_x)5O_{12}$:Ce (YAGG) crystals with the 30–35 mm diameter and 100 mm length were grown along [111] direction by the Czochralski method using Ir crucibles with the 60 mm diameter and 60 mm height. The raw material was loaded into the

crucible and was inductively heated (Figure II.12). The seed situated at the seed support was moved towards the melted compound surface. Since the connection was made the seed was pulled upwards with rotation and, the melt was crystallized on it. Additional heater was used for the thermal gradient stabilization along the as-grown crystal. Heat insulation of the growth chamber was provided with ZrO2 and Al2O3 hear insulating theramics.Corresponding mixture of Y_2O_3, Al_2O_3, Ga_2O_3, and CeO_2 powders with 99.99% purity were used as starting raw materials. YAG:Ce crystals were obtained from stoichiometric melt, and in case of Ga-containing crystals, the 1% Ga_2O_3 excess was introduced into the melt to compensate ignition loss. Growth atmosphere was Ar + 1% O_2. Oxygen was added to atmosphere to inhibit melt evaporation. CeO_2 concentration in melt was maintained at 1 mol.% level.

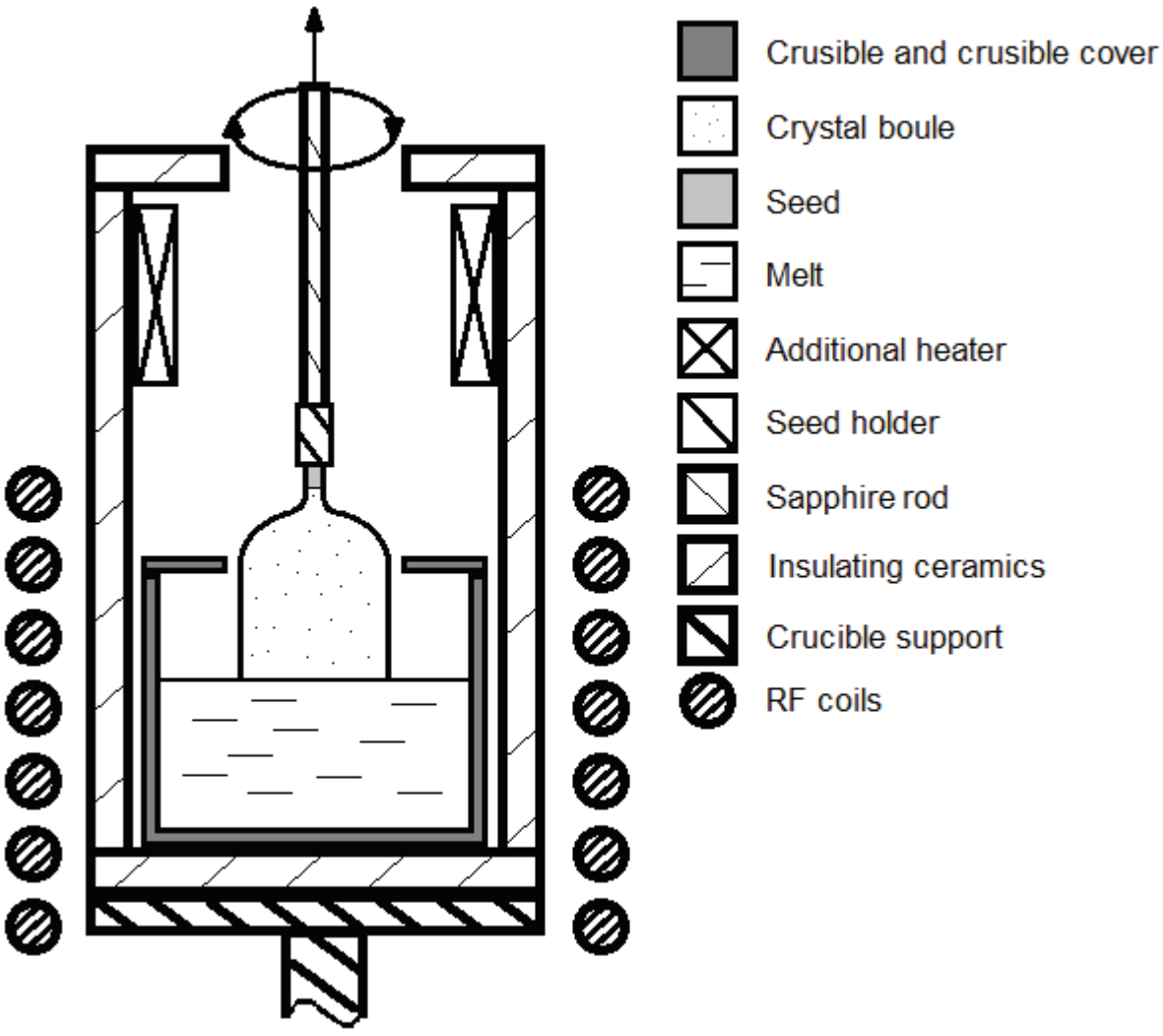

Figure II.12.Schematical view of the Czochralski bulk crystal growth process.

2.7. YAGG:Ce characterization methods

Lattice parameters and host cation composition were detected by X-ray studies of the crystalline samples were carried out using a single crystal diffractometer ‘‘Xcalibur-3’’ by Oxford Diffraction (Mo Kα-radiation, l = 0.71073 A˚, graphite monochromator, a Sapphire-3 CCD-detector, v/θ scanning in the range $2\theta \leq 90°$, accounting for absorption by equivalent reflections). Structure calculations were carried out using a SHELX-97 and WinGX software. Elementary cell parameters were refined by the Rietveld method, from diffractogram obtained on powders of the same crystalline samples using a Siemens D500 powder diffractometer. Results obtained by the single crystalline method were taken as initial data for refinement.

The Ce concentration and Al/Ga content in samples were determined by the ICP-AES method by the analogy to LGSO:Ce crystals.

Samples with the dimensions 10 mm x 10 mm x 2 mm with polished 10 x 10 faces were fabricated from crack-free parts of crystals for study of scintillation and luminescence properties.

Measurements of light output in the ‘‘current mode’’ were carried out using an IRI X-ray source (U = 100 kV, I_a = 1 mA, W anode). Block of registration consists on platform for mounting of studied scintillator and FD-288 PMT connected to V7-35 voltmeter. Setup for light output determination was described in detail in [128].

Excitation and emission spectra in the 230–800 nm range, as well as decay curves at photo excitation were determined using combined fluorescent lifetime and steady-state spectrometer FLS 920 (Edinburgh Instruments) equipped with Xe lamp.

Summary

In this chapter we have presented the raw materials preparation procedure and the crystal growth technology used in the frame of this PhD thesis to grow undoped and Ce -doped LGSO shaped crystals and Ce and Pr-doped garnet fibers. The grown crystals were microscopically and macroscopically characterized. In addition, we have described the methods we have used to determine the scintillation and optical properties of the crystals.

Chapter III: Results & Discussion: Growth and characterization of LGSO:Ce fibers

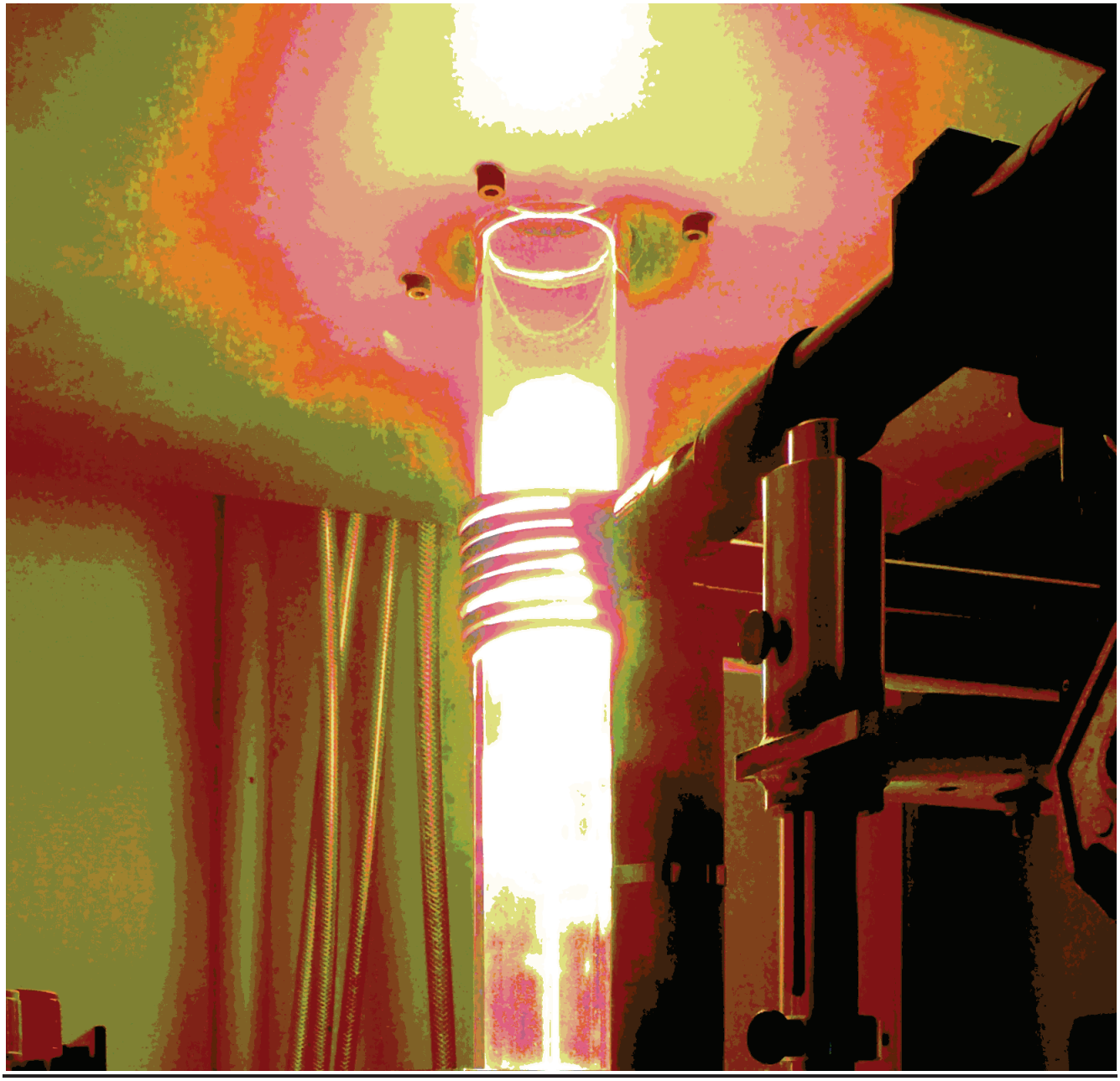

A set of LGSO:Ce fibers with the different Ce concentrations have been grown by the micro-PD method with aim to determine the optimal composition regarding the growth conditions and scintillation parameters. The causes of fibers cracking are discussed using the analysis of cation distribution in crystals.

3.1. LGSO:Ce fiber growth by the micro-PD method

As the first step, a series of $Lu_{2x}Gd_{2-2x}SiO_5$:Ce fibers were grown with x= 0.2 and 0.5 in the melt. Due to proximity to the polymorph phase transition at x = 0.17, the grown crystals with x = 0.2 contained more cracks than those grown with x = 0.5. Several approaches were used to avoid cracks. Decreasing the pulling rate to 200 μm/min and the optimization of the heating regime provided significant improvement. The fiber with 0.01 at.% Ce was completely transparent. Meanwhile, for the fibers with the Ce concentrations of 0.3, 0.5, and 1 at.%, only the parts with the 1 – 3 cm length were without cracks (Figure III.1). Based on the input power to the heater, the LGSO:Ce melting point was evaluated as being in the range from 1900 to 1950°C. This is in a good agreement with the reported phase diagram at the Lu/Gd ratio of 1/1 [93]. Meanwhile, the growth of LGSO:Ce with 1.5 at.% Ce was successful only at the melt overheating by ~ 5 – 10°C.

However, such overheating leads to the increase of the melt meniscus thickness. We had to increase the pulling rate up to 1000 μm/min to maintain the constant volume and shape of the molten zone. Without the pulling rate increase the melt drop was formed at the capillary die and diameter control became difficult to control.

Evidently, the increase of meniscus thickness with overheating ensures better melt mixing in the molten zone and suppresses the dopant segregation to the periphery. We suppose that the melt convective flow in this zone is reinforced due to higher thermal gradients calling an enhancement of Marangoni flow. Smaller admixture gradient might result in reduction of cracks in the fiber. The distribution of cations across the fibers is discussed in detail in Section 3.4.

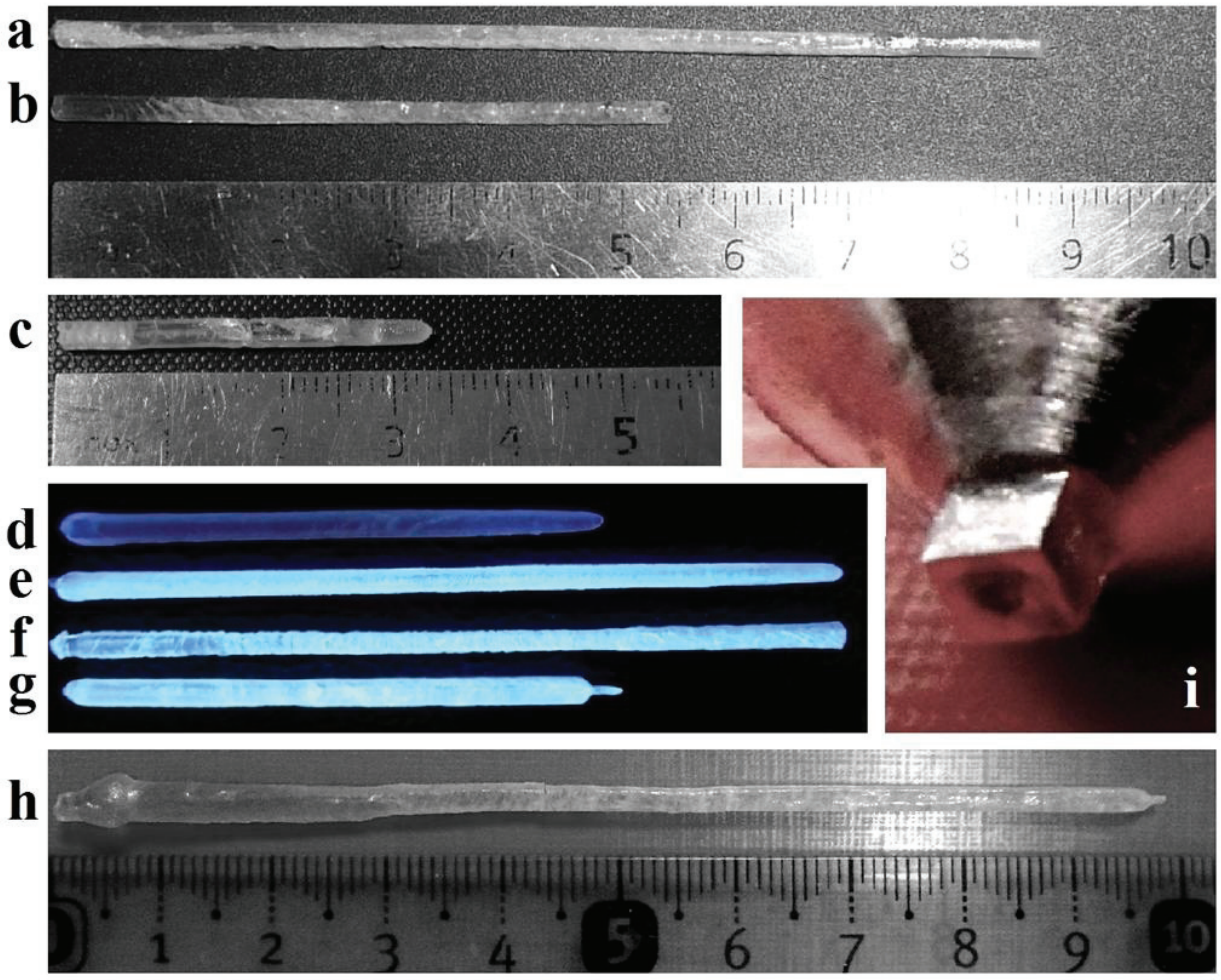

Figure III.1. As-grown $Lu_{2x}Gd_{2-2x}SiO_5$ fibers with x = 0.2 (a), x = 0.5 made of Cz-grown crystals fragments 0.01 at.% of Ce^{3+} (b - d); made of powder: 0.3 (e), 0.5 (f), 1at.% of activator (g); 1,5 at.% of activator (h); i) – capillary die of the Ir crucible.

3.2. Structure and cation distribution coefficients in LGSO:Ce

According to room temperature XRD data, the LGSO crystals with the Lu/Gd ratio around 1:1 had monoclinic C2/c structure (Figure III.2). No foreign phases were observed for any Ce concentration in the initial melt. The elementary cell volumes for the crystals with 1 and 1.5 at.% of Ce were measured to be 857.20(5) $Å^3$ and 852.90(4) $Å^3$, respectively. The substantial difference is evidently caused by fluctuations of Ce

and Gd content in the μ-PD-grown crystals. According to the data of Cz-grown LGSO:Ce crystals [19], these cell volumes corresponds to the Gd content of 51 and 44 at.%, respectively.

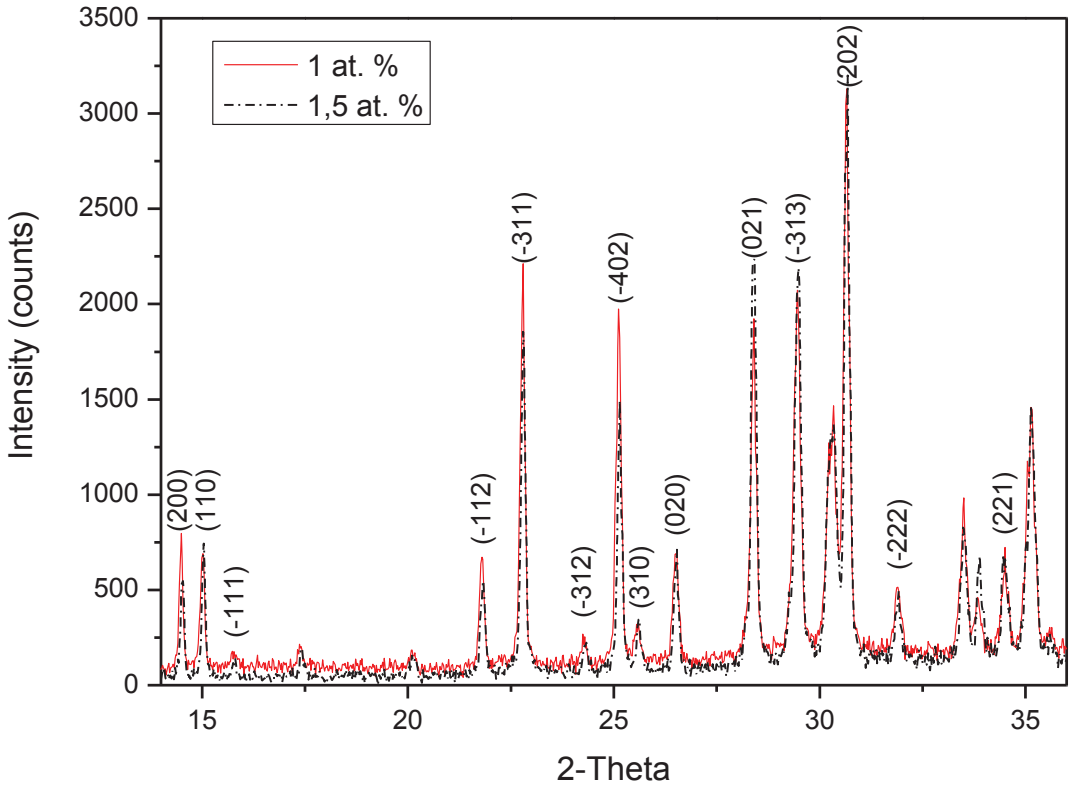

Figure III.2. XRD peaks of LGSO:Ce. The curves represent the fibers with the concentrations 1 and 1.5 at. %.

The distribution coefficients for Gd and Ce dopants determined by ICP are presented in Table 2. The corresponding data calculated using the phenomenological formula suggested by Brandle et al [129] are also presented for comparison there. Since the samples used for measurements were taken from the beginning of the crystal, the effective distribution coefficient can be evaluated as C_S/C_1, where C_S is the concentration measured in the crystal and C_1 is the element concentration in the raw material. The data on k_0(Ce) are basically consistent with the values of 0.4 and 0.6 obtained in Cz–grown $(Lu,Gd)_2SiO_5$:Ce [43] with the similar Lu/Gd ratio. The

significant difference between the experimental values and the phenomenological prediction based on Cz–grown crystals [129] is, evidently, caused by different crystallization conditions in Cz and μ-PD methods.

Table 2. Concentrations and distribution coefficients of Gd and Ce dopants in LGSO:Ce fibers

Initial raw material composition	Concentration in samples, at. %		k_0		Theoretical k_0 in accordance with [129]	
	Gd	Ce	Gd	Ce	Gd	Ce
$LuGd_{0.99}Ce_{0.01}SiO_5$	32	0.19	0.65	0.38	0.77	0.11
$LuGd_{0.98}Ce_{0.02}SiO_5$	30	0.35	0.61	0.35		
$LuGd_{0.97}Ce_{0.03}SiO_5$	33	0.62	0.68	0.41		

It was shown that Gd^{3+} and Ce^{3+} with the bigger ionic radii in Cz-grown LGSO:Ce crystals tend to occupy sevenfold coordination polyhedra with larger distances from the ligand to oxygen environment [19]. It was demonstrated that increasing concentration of Ce^{3+} in CeO_6 polyhedron sites basically causes light yield decrease, enhancement of slow decay components, and a red shift of the luminescence band [19]. Despite the different crystallization conditions in Cz and μ-PD, XRD analysis made in the present work shows no substantial difference in Lu^{3+} distribution between the polyhedral of different type. In LGSO:Ce with 51 at.% of Lu, lutetium occupies 70% of CeO_6 sites and 32 % of CeO_7 sites.

3.3. Optical and scintillation properties

Distribution of Ce^{3+} between the crystallographic sites can be evaluated by studying X-ray luminescence spectra (Figure III.3). In addition to the basic

luminescence band, which is caused by CeO_7 centers and is peaked at 420 nm, long-wavelength shoulder rises with increasing Ce^{3+} concentration. This emission is associated with CeO_6 polyhedra and evidences the partial redistribution of Ce^{3+} from CeO_7 to CeO_6 polyhedra in Ce^{3+}-rich samples.

The optimal concentration of Ce^{3+} in the melt for growing orthosilicates by Czochralski method was reported to be 0.25 at.% in LSO:Ce [15] and 1 at.% in $Lu_{0.4}Gd_{1.5}SiO_5$:Ce [130].

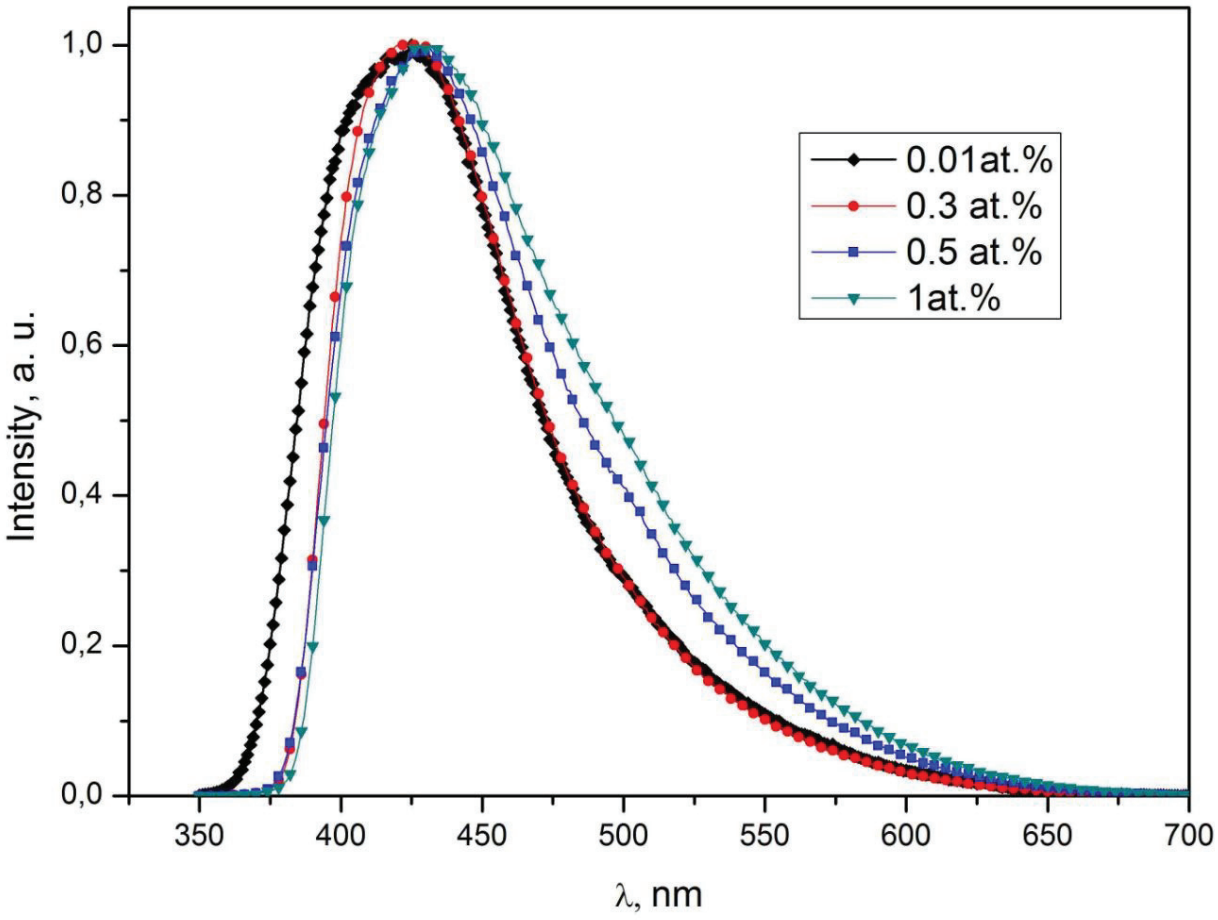

Figure III.3. Normalized X-ray luminescence spectra of LGSO:Ce at different Ce concentrations (indicated).

The light yield of LGSO:Ce crystals increases with Ce concentration in the range from 0.01 to 1 at.% (Figure III.4). The light yield decreases at 1.5 % Ce, possibly, because we have not found the right conditions for stable growth at this Ce^{3+}

concentration. The 1.5 at.% Ce crystal has too many cracks to make a valid light output measurements and compare it with other samples. Therefore, we assume that 1 at. % in melt is the optimal Ce concentration among the successfully grown fibers.

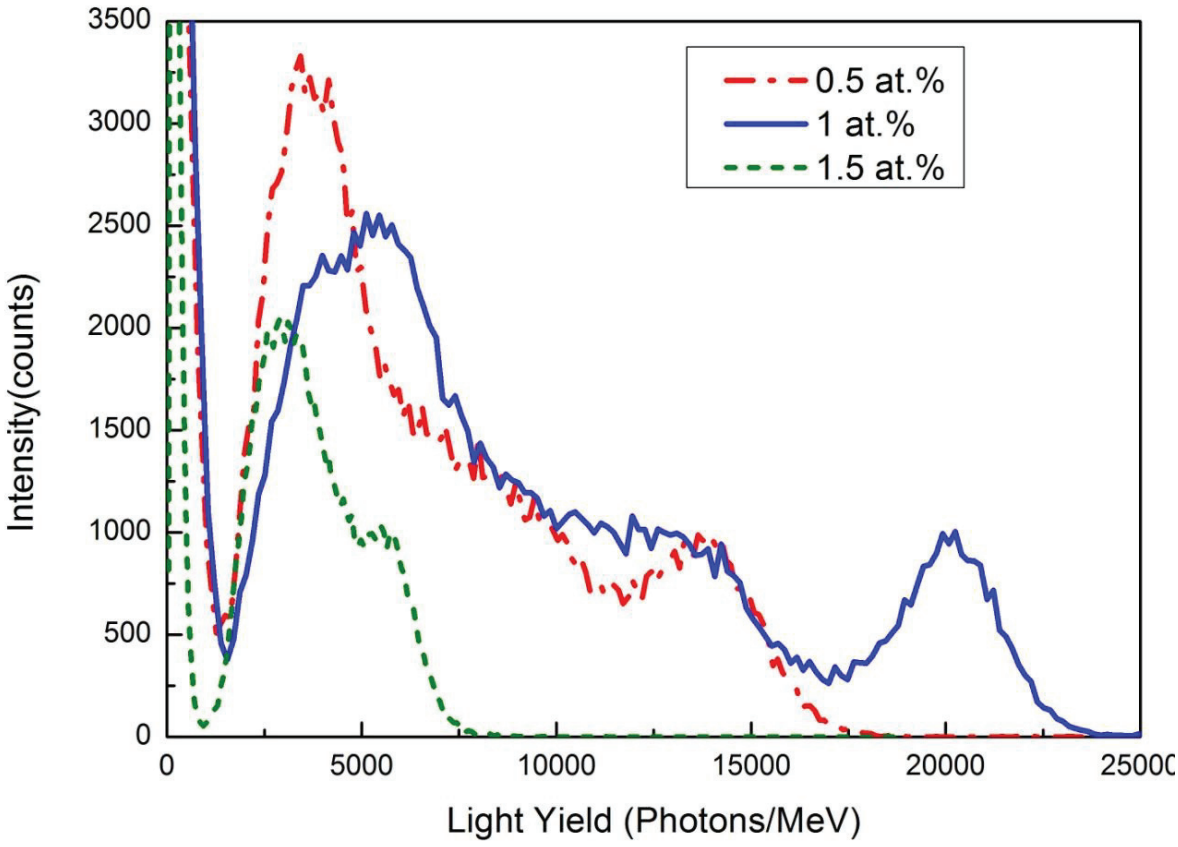

Figure III.4. Pulse height spectra of LGSO:Ce crystals grown by μ-PD with different Ce concentrations (indicated).

The afterglow in Cz–grown $Lu_{2-2x}Gd_{2x}SiO_5$:Ce at $x = 0.5$ is 0.07 - 0.10 % after 5 ms [19]. In μ-PD–grown fibers the afterglow decreases with the increase of Ce^{3+} concentration (Figure III.5). As the result, the crystals grown by μ-PD demonstrate even lower afterglow down to 0.02 % at 0.5 at.% Ce. This can be attributed by a larger concentration of activator compared to Cz–samples, thus, increasing the probability for direct capture of electrons by Ce^{4+} without intermediate capture on deep traps related to oxygen vacancies.

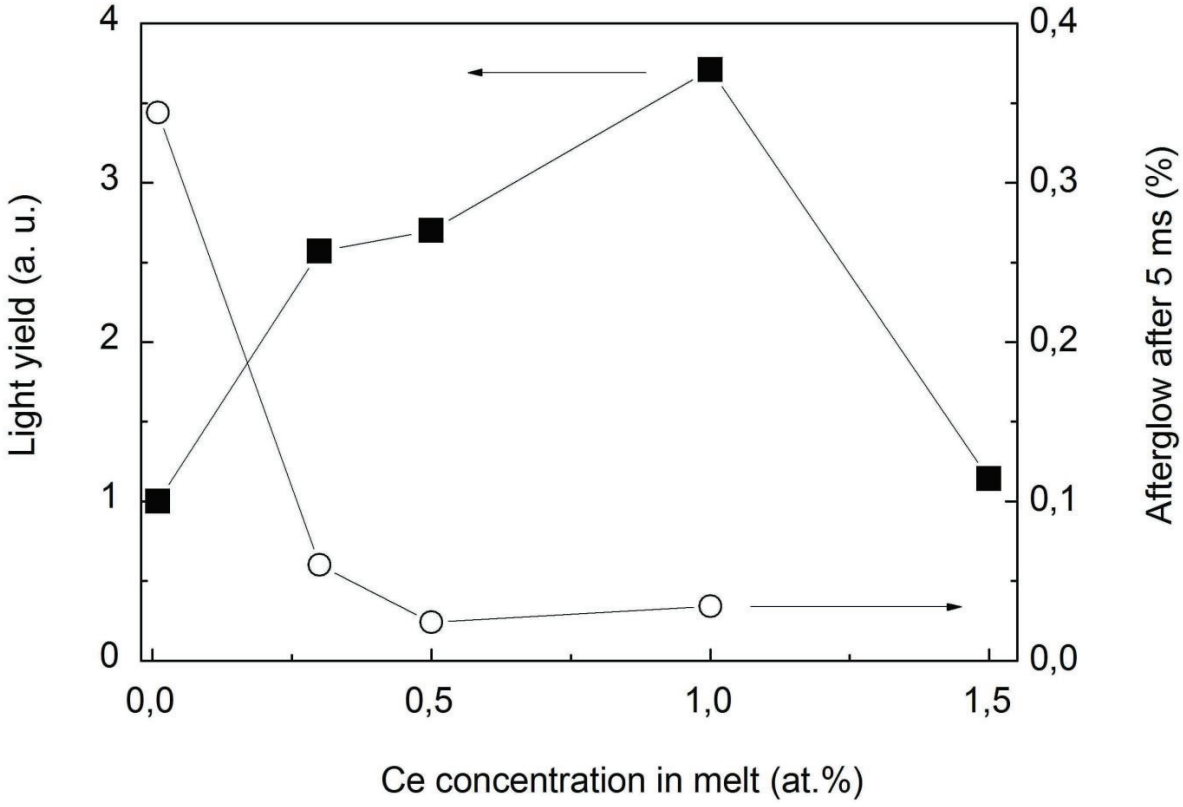

Figure III.5. Relative light output (squares) and afterglow level (circles) after 5 ms in LGSO:Ce fibers as a function of Ce concentration in the host.

3.4. Confocal and wide-field microscopy measurements

3.4.1. Selection of samples

The LGSO crystalline fiber with 1.5 at.% of Ce selected for microscopy measurements contained a visually transparent single crystalline section of 40 mm in length (Figure III.6a). The rest of the crystal contained inclusions and cracks. Transverse and longitudinal samples were cut from the transparent part of the crystal (Figure III.6b and III.6c, respectively) with an inner blade saw. The samples were polished. The diameter of the transversely cut sample (sample TC) was 4 mm and the

thickness was 2 mm. The dimensions of the longitudinally cut sample (sample LC) were 2×2×5 mm^3. The large faces of the samples were studied by confocal and wide-field microscopy.

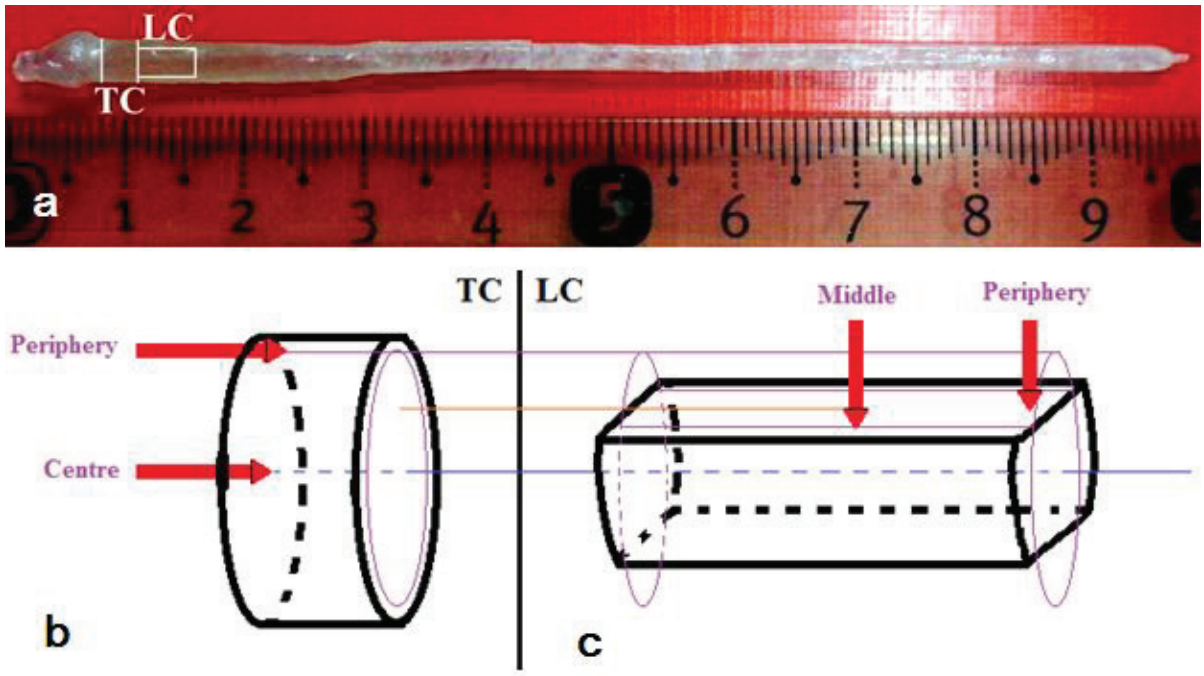

Figure III.6. $Lu_{2x}Gd_{2-2x}SiO_5$:Ce crystal grown by μ-PD method. The TC (transversely cut) and LC (longitudinally cut) samples were cut as indicated in (a) and are schematically depicted in (b) and (c), respectively.

3.4.2. Electron beam excitation

Typical photos of both samples under electron beam excitation are presented in Figures III.5a and III.5c. The cathodoluminescence (CL) image of TC sample (Figure III.7) shows inhomogeneous emission intensity on the sample surface. These features are more pronounced in the periphery of sample TC. The bright lines in the periphery of sample LC probably correspond to cracks reflecting the emitted light. They are predominantly accumulated in the periphery. Nevertheless, there is no observable gradient in the CL brightness from the center to the periphery, in contrast to that previously observed, e.g., in LuAG:Ce [6] studied under similar conditions. This is an

indication that Ce^{3+} distribution in LGSO is more uniform than in scintillation crystals of the garnet group. On the other hand, many small bright spots can be observed in Figures III.7b and III.7c. These spots might be caused by gas bubbles or inclusions of dopant forming scattering centers in the crystal. However, it is feasible that a part of these spots are just glares from the sample holder surface, because many of them are also seen in Figure III.7c under illumination with external light source without electron beam excitation.

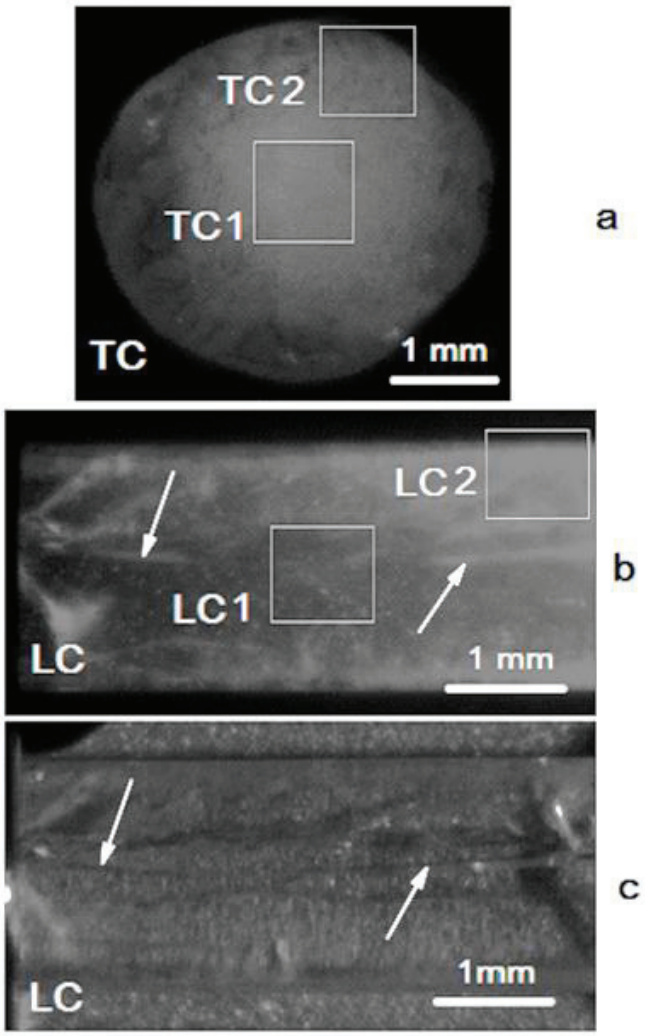

Figure III.7. Cathodoluminescence image of sample TC (a) and sample LC (b) and a photo in reflected light of sample LC (c). The areas selected for microscopic study are indicated and labeled.

3.4.3. Photoexcitation

A significant radial gradient of dopant concentration is inherent in the μ-PD method [44]. To elucidate the cation distribution in crystals grown by μ-PD in more detail, we utilized the confocal microscopy with a high spatial resolution under selective laser excitation of CeO_6 centers and wide-field microscopy under excitation of the both Ce centers (using a halogen lamp).

The wide-field microscopy images of the samples under halogen lamp excitation are shown in Figure III.8. The areas TC1, TC2, LC1, and LC2 are selected, as indicated in Figure III.7, at the center and periphery of the corresponding samples, respectively. The wide-field microscopy measurements do not show any significant change of PL intensity from the center to the periphery in sample TC or along the crystal in sample LC. The bright lines marked by the arrows in Figure III.7b are cracks. They are also seen on the image in reflected light (Figure III.7c). In addition, there are many stripes of inclusions oriented along the rod axis. As we can see from the image of TC1 in Figure III.8, the crystal contains a core of about 1 mm in diameter with the low density of cracks, and periphery with a considerably higher density of bright inclusions and cracks. This might be caused by faceted growth at constitutional supercooling in conditions of low thermal gradient and high content of Gd, Ce, and admixtures in the melt meniscus periphery. The images of the areas TC2, LC1, and LC2 show that the inclusions have the shape of distorted lines or plates oriented along the rod axis. The thickness of these lines or planes is 1-3 μm, and the length is up to several millimeters. Higher PL intensity in the vicinity of the inclusions might be caused by both an increase of local Ce concentration and light scattering.

To get a better insight into the spatial distribution of the cations, smaller (60×60 μm^2) areas of the samples were selected and studied using confocal microscopy under selective excitation of the CeO6 center. Spatially integrated PL spectra from the center and periphery areas of the TC sample are shown in Figure III.9. It was found that the PL peak intensity was by a factor of 5.4 larger in the peripheral areas (TC2) of the sample than in the central area (TC1). This is an indication of higher Ce concentration

in the areas closer to the sample edge. Moreover, the PL spectrum of TC2 is red-shifted by 14 nm relatively to that of TC1, and its long wavelength shoulder is more pronounced. This might be an indication of an increase in Gd concentration in the direction from the center to the periphery of the fiber [19].

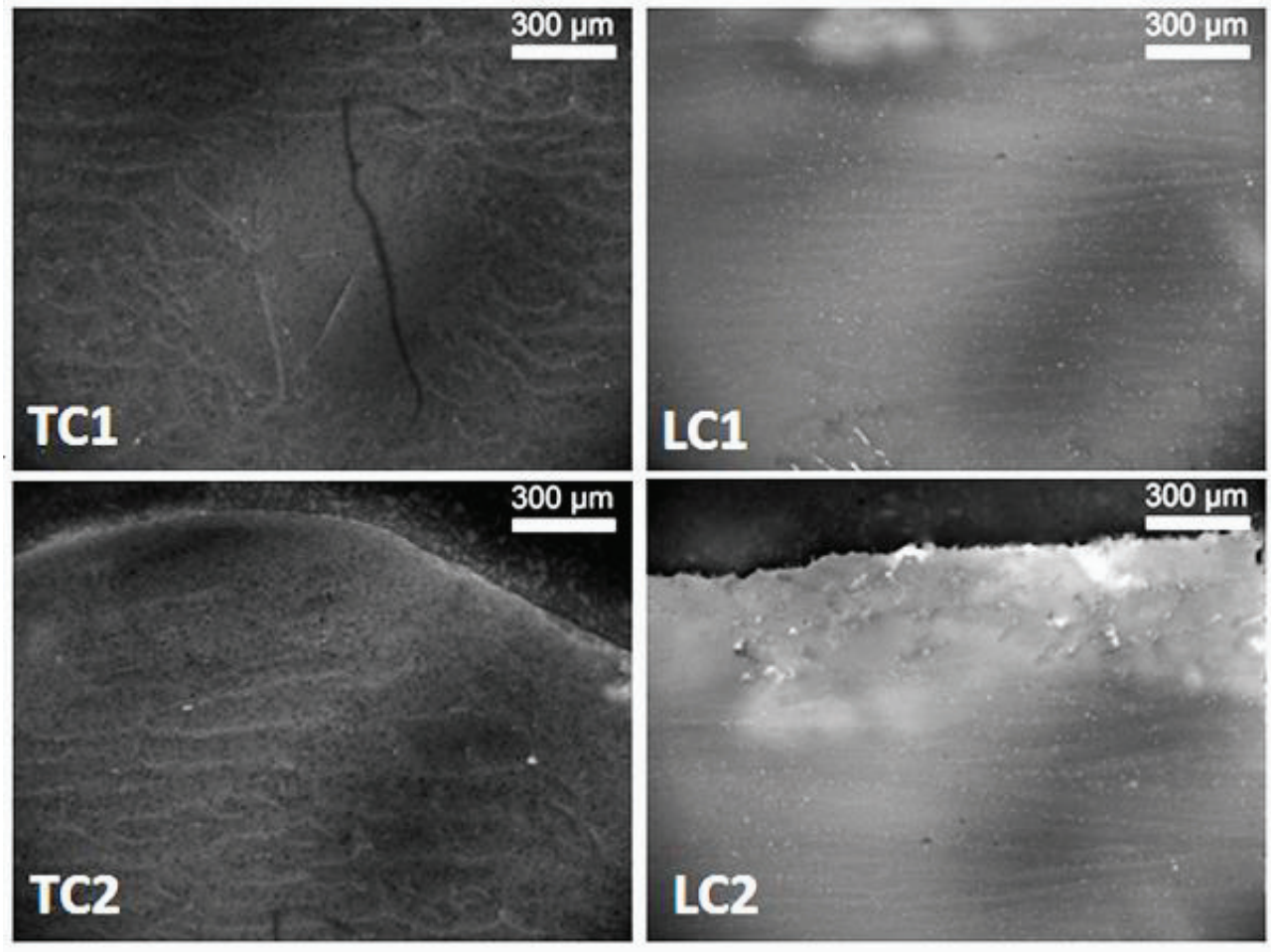

Figure III.8. Spatial distribution of PL intensity under halogen lamp excitation in the areas of samples TC and LC in locations indicated in Fig. III.7.

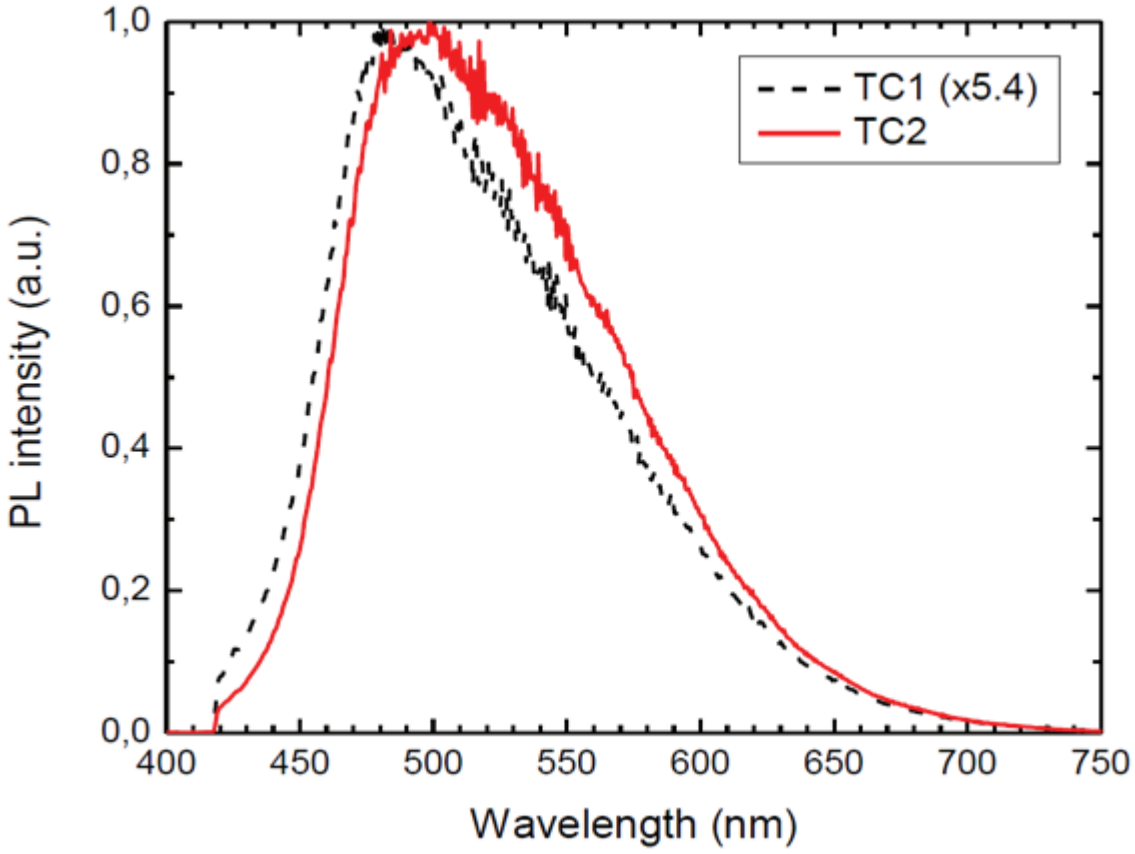

Figure III.9. Normalized spatially integrated PL spectra collected from center (TC1) and periphery (TC2) areas of 60×60 μm^2 in size. PL was excited with laser diode emitting at 405 nm.

To characterize the spatial homogeneity of PL intensity, the PL intensity variation (the standard deviation divided by the mean value) was calculated from the PL intensity mapping images (Figure III.10). The intensity variation equals 0.14 at the center of the sample and increases up to 0.27 at the periphery. High-resolution image (Figure III.10a) demonstrates that the brightest areas are concentrated along the crack that are visible as thin (~0.5 μm) stripes of lower PL intensity (marked by the arrows). The PL spectra (Figure III.10b) collected from the vicinity of the crack (area 1 in Figure III.10a) were compared with the spectra from the areas of a lower PL intensity (area 2 in Figure III.10a). The difference spectrum in Figure III.10c clearly reveals two spectral components peaked at 470 nm and 560 – 590 nm.

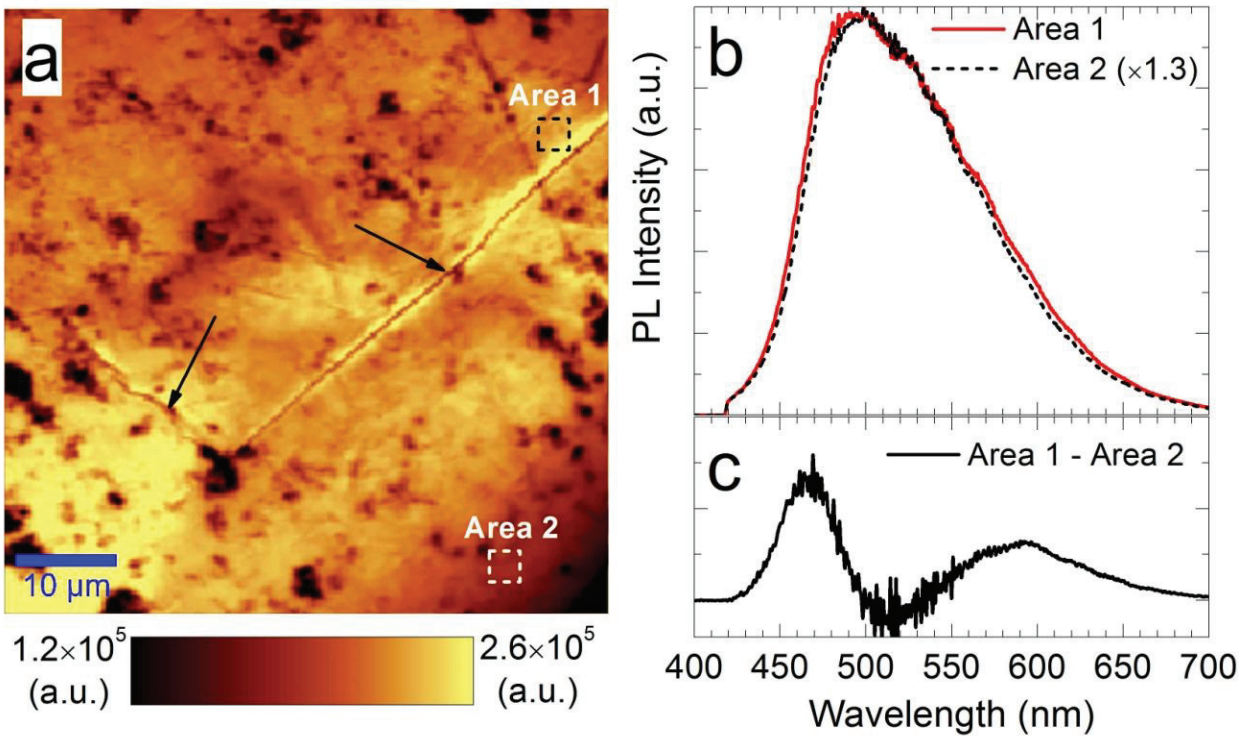

Figure III.10. Spatial distribution of PL intensity in the periphery of TC sample under 405 nm excitation (a); PL spectra from the vicinity of the crack (area 1) and from area of lower PL intensity (area 2) (b); the difference between normalized PL spectra from area 1 and area 2 (c).

The obtained results show that LGSO:Ce fibers consist of the central part of 1 mm in diameter without cracks, and the periphery with a lot of inclusions and some cracks. The diameter of the central part nearly coincides with the inner diameter of the μ-PD crucible capillary die (1 mm). There is no notable difference in the brightness between the different parts of the crystal when both Ce centers are excited (Figures III.7 and III.8). However, under selective excitation, the intensity of the CeO_6 luminescence band increases from the center to the periphery of the fiber–shaped crystal (Figure III.9). This behavior might evidence a larger Ce concentration in the periphery of the crystal or can be caused by light scattering. However, by the analogy with the Cz–

grown LGSO:Ce the presence of the characteristic "zigzag" at 420 – 500 nm and the 560 – 590 nm band at selective excitation of CeO_6 luminescence (Figure III.10c) in the inclusion area clearly indicates accumulation of both Gd and Ce in the vicinity of cracks. Therefore, the radial distribution of Gd and Ce outside the central part of the μ-PD crystal is nonuniform, with higher concentrations in the areas of cracks and inclusions. The inclusions form scattering centers and lead to a decrease in optical transparency and, as a consequence, to a decrease in the light output with increasing Ce concentration. Since the ionic radii of Ce and Gd are larger than that of Lu [57], their accumulation causes grain formation and crystal cracking. Therefore, the large difference in ionic radii of the competing Lu^{3+}, Gd^{3+}, and Ce^{3+} ions in the host impedes obtaining crack-free crystal by the μ-PD method in the specified conditions. The main impact to cracking is assumed to be due to Gd, the concentration of which is by two orders of magnitude larger than that of Ce. Cracking is expected to be minimized at lower Gd concentration. However, at the same time, it leads to the increase of melting temperature [93] up to too high values for use with iridium crucible destruction. Therefore, a reasonable balance between Gd and Ce content and technological conditions of the fiber–shaped crystal grown by μ-PD should be maintained.

Summary

LGSO:Ce fiber-shaped crystals with different Lu/Gd ratios and different Ce activator concentrations were grown for the first time by the μ-PD technique. Though all the crystals contain single monoclinic C2/c phase, only the first parts (1-4 cm in length) of them are transparent and contain no visible cracks and few inclusions.

The distribution coefficients of Gd and Ce dopant are within 0.61–0.68 and 0.35–0.41, respectively. As in the Cz-grown crystals, Gd^{3+} and Ce^{3+} tend to occupy the larger sevenfold coordinated positions in the lattice. Ce^{3+}concentration of 1 at.% in melt provides the best light yield and the lowest afterglow among the samples grown in this

study. The afterglow in LGSO:Ce crystals grown by μ-PD is 0.02 % after 5 ms, which is by a factor of 4 better than that in Cz–grown crystals with a similar Lu/Gd ratio.

The analysis of the spatial distribution of Ce^{3+} luminescence in LGSO:Ce crystals grown by μ-PD technique evidences accumulation of Gd^{3+} and Ce^{3+} in the inclusions situated in the periphery of the fiber. These inclusions form a network of distorted planes, which are mainly directed along the crystals axis (along the growth direction). Excessive accumulation of Gd^{3+} and Ce^{3+} results in crack formation.

Chapter IV: Results & Discussions: Growth and characterization of garnet fibers

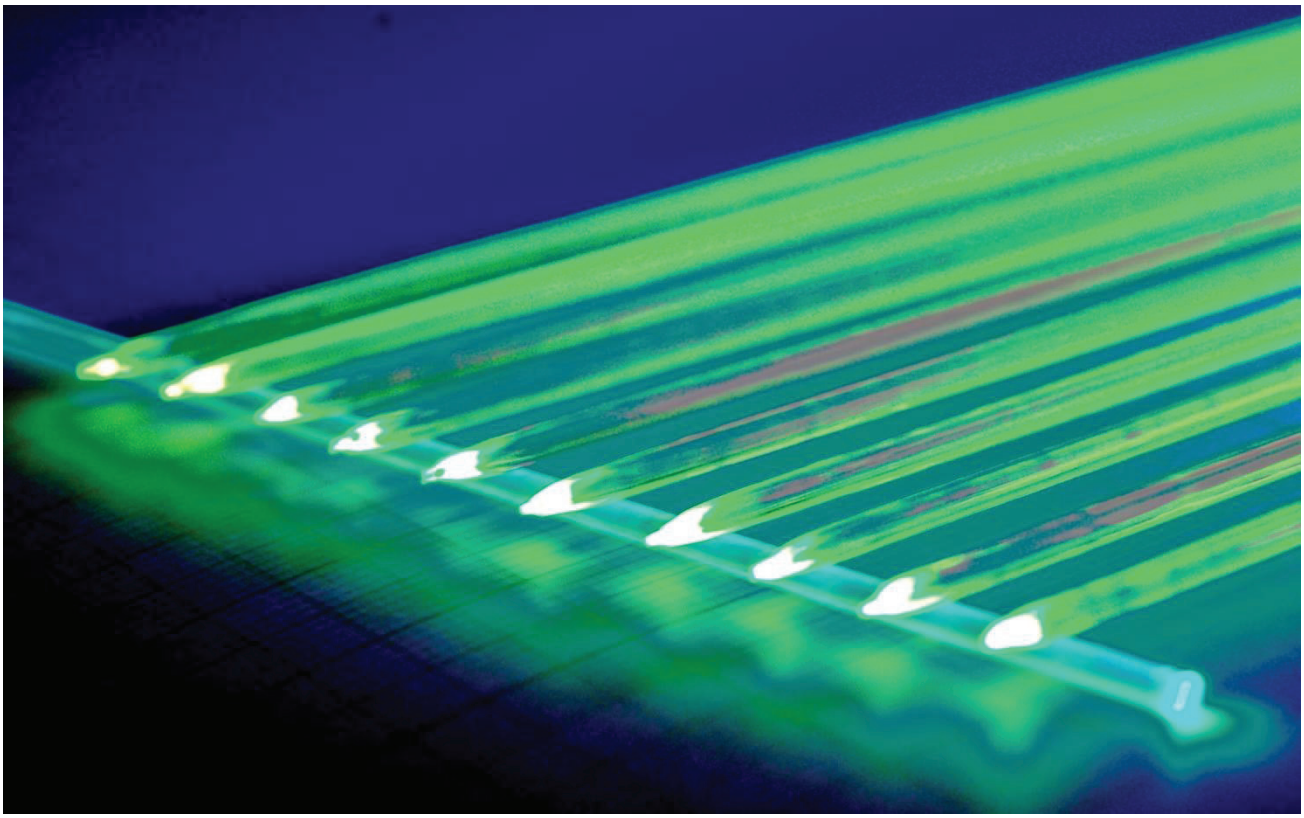

Undoped LuAG and LuYAG, Ce-doped LuAG, Pr-doped LuAG and Ce-doped YAG single crystals fibers were grown from the melt by the micro-pulling down technique under stationary stable regime. A detailed description of the different phenomenon involved in the crucible through simulation and modeling have been discussed. The grown fibers have been optically characterized through the light transmission (attenuation) and defects analysis.

4.1. Numerical study and analysis limits of the micro-pulling down technique for LuAG fiber crystal growth

Simulation is conducted to analyze the induction heated μ-PD technique for LuAG fiber crystal growth. The melt, gas flows and heat transfer around the crucible and the furnace are studied. Experimental observation are presented to verify the simulation and modeling results. A schematic diagram of the different part of the μ-PD machine which was been investigated during this study is given in figure IV.1.The modeling was carried out by the analogy to the optimization of sapphire growth process with a COMSOL Multiphysics software [131, 132, 133]. A computational domain much larger than the furnace is chosen for the accurate calculation of the electromagnetic field. However, to relieve computational load, the computational domain for fluid flow is only set to the furnace region. The thermal properties of the furnace elements are assumed constant. For calculation of the electromagnetic field, a solid copper coil is modeled, and the self -inductance of the coil is neglected. Axisymmetry of the furnace is further assumed. Our aim is to present a comprehensive analysis of the heat transfer including detailed computation of our furnace performance.

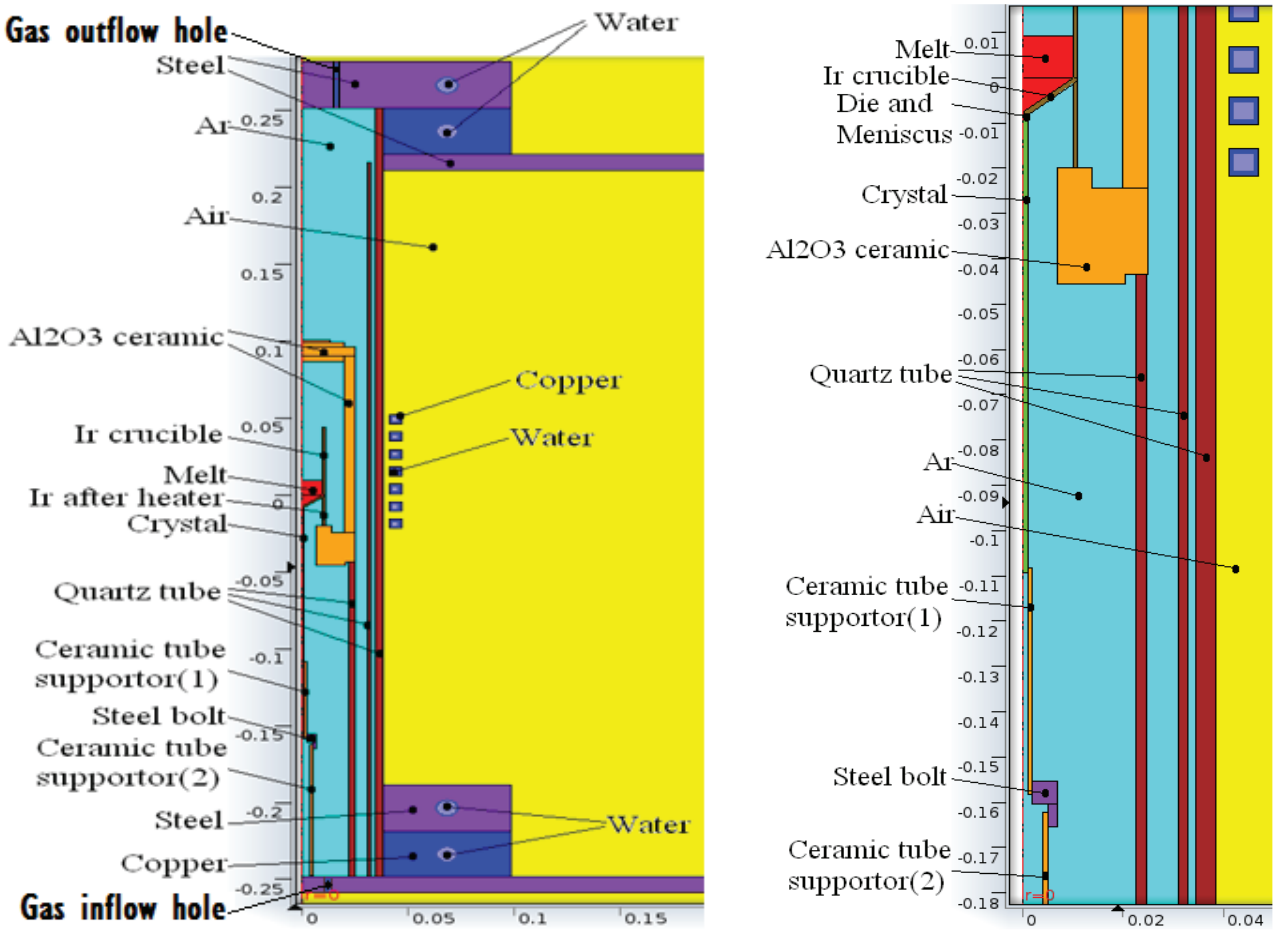

Figure IV.1. The description of the μ-PD growth setup dimensions.

Thus, with aim to concentrate on LuAG growth, the physical properties and system parameters including the used conditions are:

- Physical Model: Inductive heating , conduction, radiation, natural/forced convection
- RF heaters : Frequency=34.1 (kHz)
- Seed length/Crystal length : 0.15 (m)
- Crystal diameter : 2 (mm)
- Total charge of raw material : 12 (g)
- Pulling rate : 0.5 (mm/min)
- Meniscus height : 0.3 (mm)
- Argon inlet flow rate : 0.2 slm, Pressure : 1 bar
- Quartz tube is opaque

The grid are refined to ensure that the calculation results are not dependent on the mesh size. The simulation domain and grid system are shown in figure IV.2. The calculation mesh consisted of 59010 triangular elements, 4972 edge elements and 170 vertes elements. The recirculating flow in the melt is caused by a combination of several basic modes of convection: natural convection due to buoyancy forces, Marangoni convection due to the variation of surface tension, and forced convection due to crystal pulling and drop-down of the melt level. The effect of melt change on the molten zone is negligible during a quasi-steady simulation. Figure IV.3 shows the 2D and 3D distributions of the temperature and stream function distribution in the entire furnace. The temperature distribution in the crucible shows fluctuations in the range 2000-2380K. One can find a hot spot at the top part of the crucible where the temperature is 2380K: 147 K higher than the melting point of LuAG. It is relatively easy to melt an iridium crucible during the growth of high melting temperature materials. Localized melting cause cracking on subsequent cooling, and the failure of the crucible occurs catastrophically. So the hot spot, therefore is dangerous for the growth of LuAG. The melt in the crucible is driven from the hot to cold region, from the crucible wall to the centerline of the furnace. Two center rotating convection rolls emerge in the melt. The surface-tension related roll (Marangoni convection) is counter-clock wise and stronger than the buoyancy one that is close to the centerline of the furnace. It is important and interesting to point out that at the top of the furnace, gas convection is strong due to the large temperature difference. Weaker convection is observed for alumina thermal isolation support, where the thermal conditions, which is cold at the bottom and hot on the top, does not favor buoyancy driven flow even though there exists a large temperature difference. To surmount crucible overheating and stress in the fiber, it is very important to have more uniform temperature distribution around the crucible and less induction power applied to melt LuAG. We have also registered that the temperature distribution in the after heater is not symmetrical when only one observation window is applied. As the Solid/liquid interface located in the afterheater

affects the growth kinetics it is important to achieve more stable fiber crystal growth conditions by the control of temperature field in the molten zone.

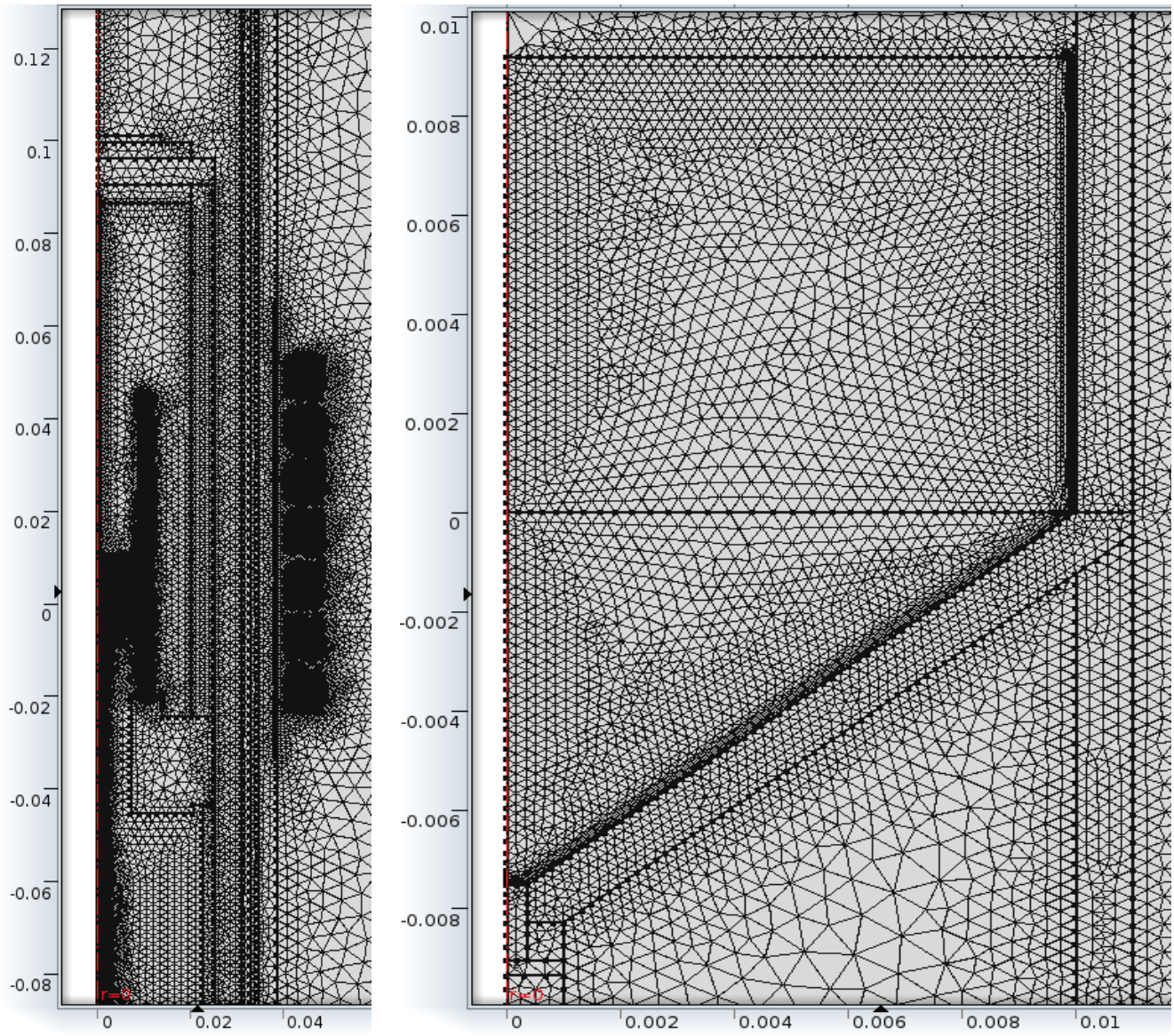

Figure IV.2. Calculation mesh for simulation of LuAG crystal growth.

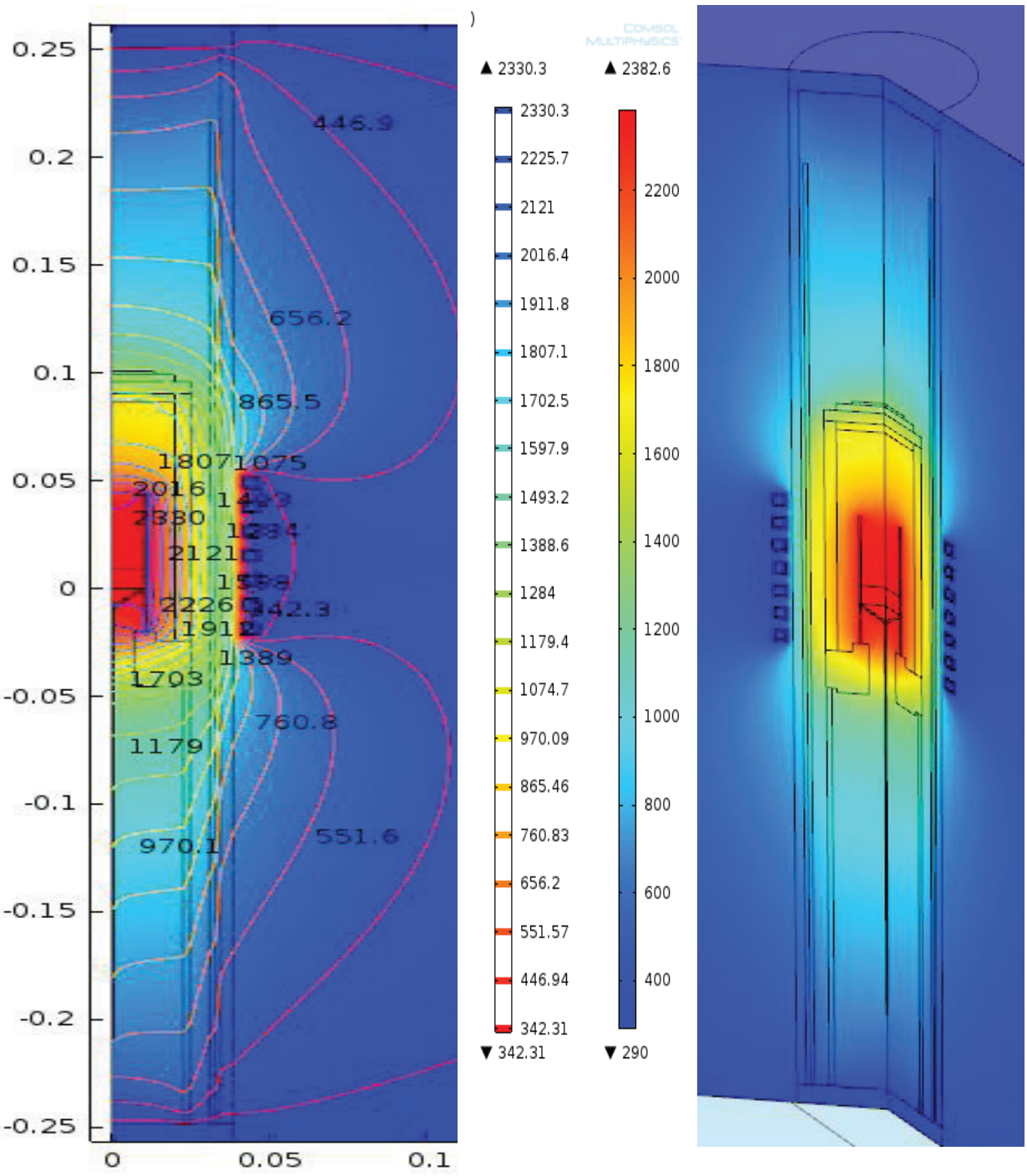

Figure IV.3. Thermal field model in 2D (left) and 3D (right) view of the μ-PD growth setup. The lines are isotherms in K.

In this research program, numerical modeling provided a set of data on temperature distribution at different elements of the crystallizer. The dependence of temperature along the fiber is of particular interest (Figure IV.4). Usually, it takes 5-7

hours (depending on the pulling rate) to grow 10 cm LuAG fiber. If the temperature of the initial part of growing fiber is high rather long time during the growth (Figure IV.4), one may suggest that initial part of the fiber will be situated longer time at the temperature range of crystal plasticity 0.7 $T_m < T < T_m$ (1500 - 2320 K for LuAG), thus, to be better annealed in the growth atmosphere (Ar) simply during the growth in comparison to the end of the fiber. After the end of growth and disconnection of the fiber from the crucible the fiber is cooled due to the heating power supply decrease to the crucible. At that moment the first part of the fiber is already 22-30 cm away from the crucible outside the hot zone. This means that different parts of the fiber are subjected to different thermal gradients during cooling down. Consequently, thermal stresses and quantity of defects may differ along the fibers due to different regimes of annealing.

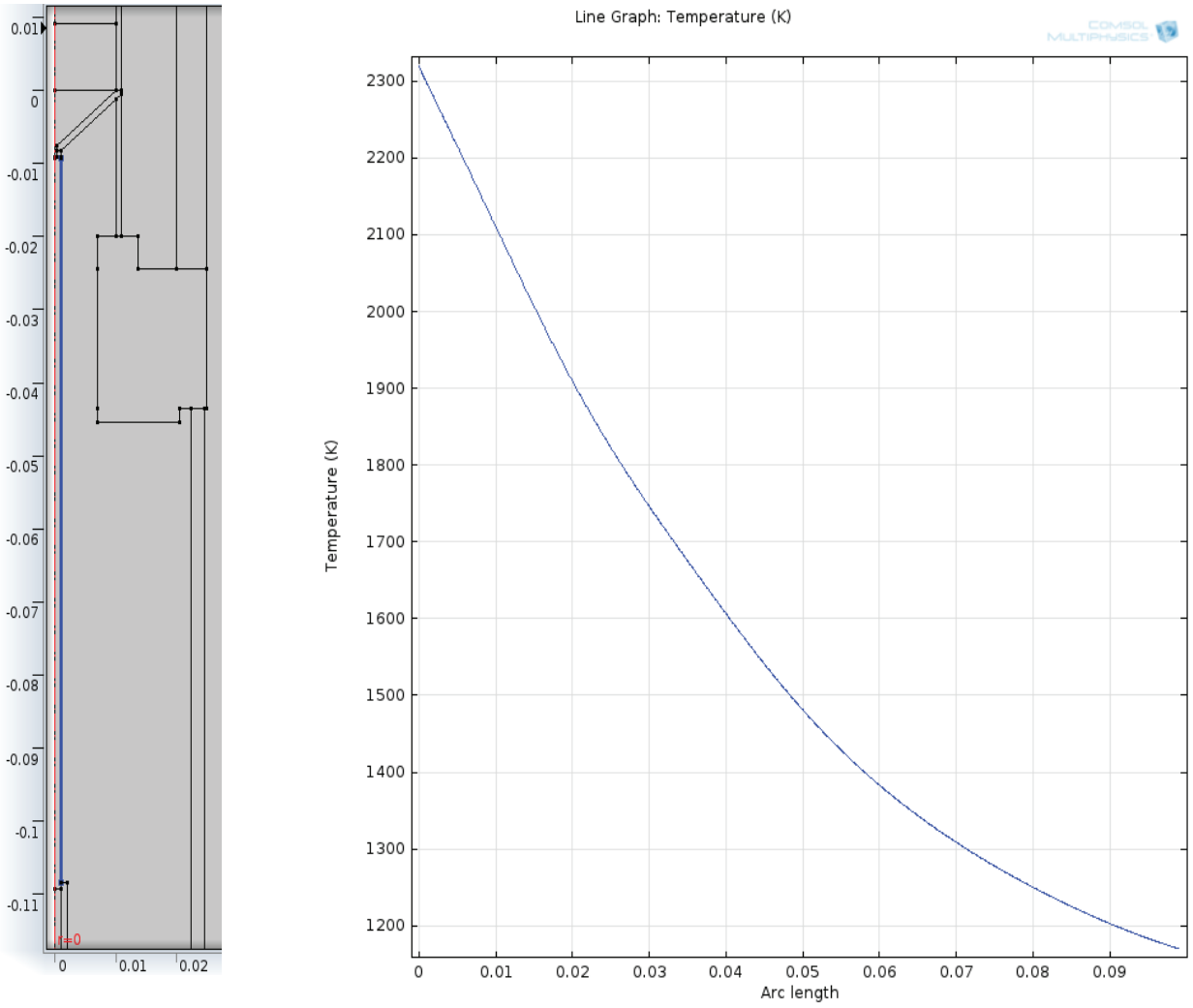

Figure IV.4. Temperature along the fiber.

Melt convention pattern in the crucible was examined (Figure IV.5). The maximal flow rate along the melt free surface was V_{max} = 0.13 mm/s and 4.37 mm/s accounting for buoyancy without and with Marangoni convection, respectively. Due to the natural convention the flow is directed upwards near the crucible walls and downwards in the crucible center, thus the system is stable.

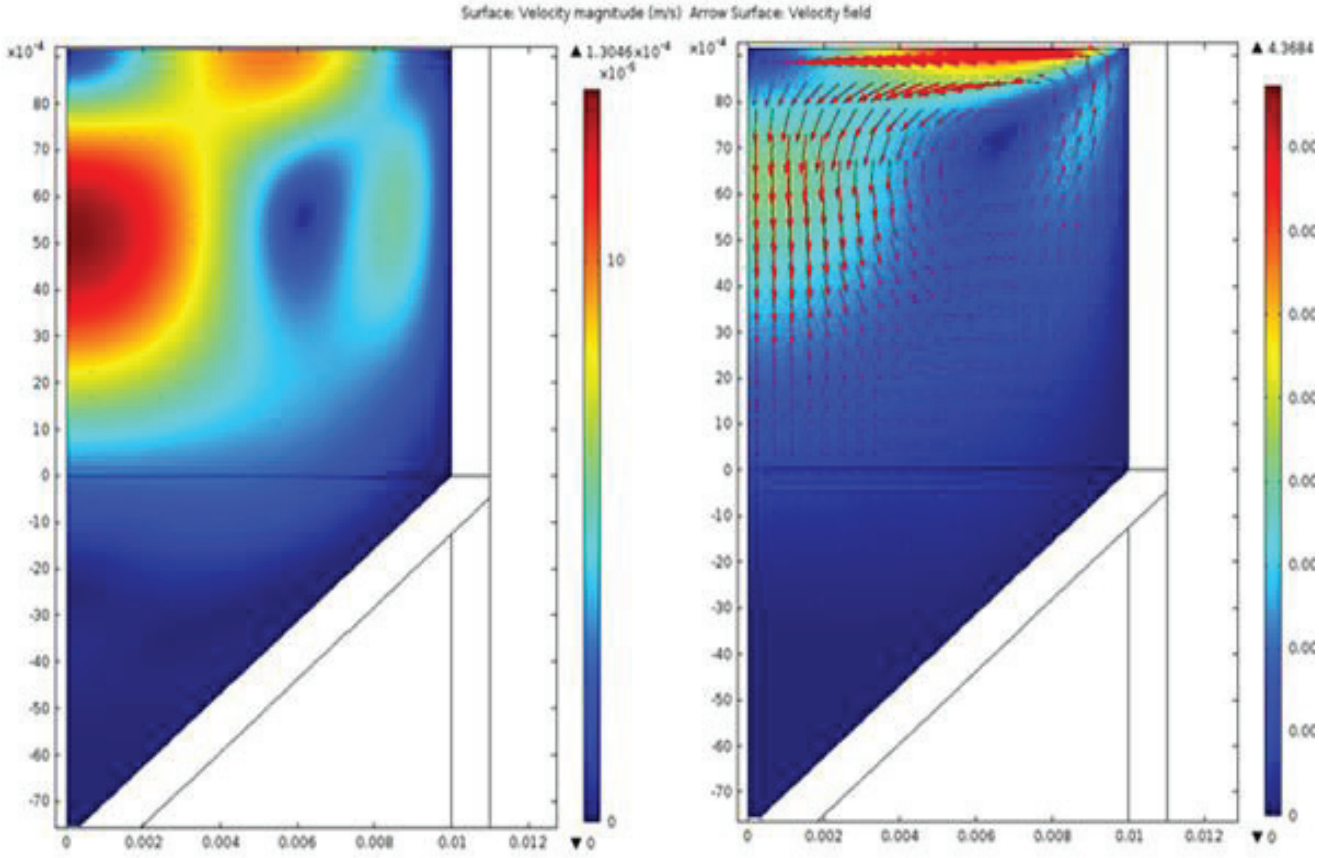

Figure IV.5. Velocity field in melt with buoyancy flow (left) and with buoyancy plus Marangoni flow (right)

Temperature along the melt free surface from the center to the periphery increases from 2356 K to 2381 K (Figure IV.6), which is the reason for the Marangoni convection. This distribution is similar to that obtained for sapphire growth process [134].

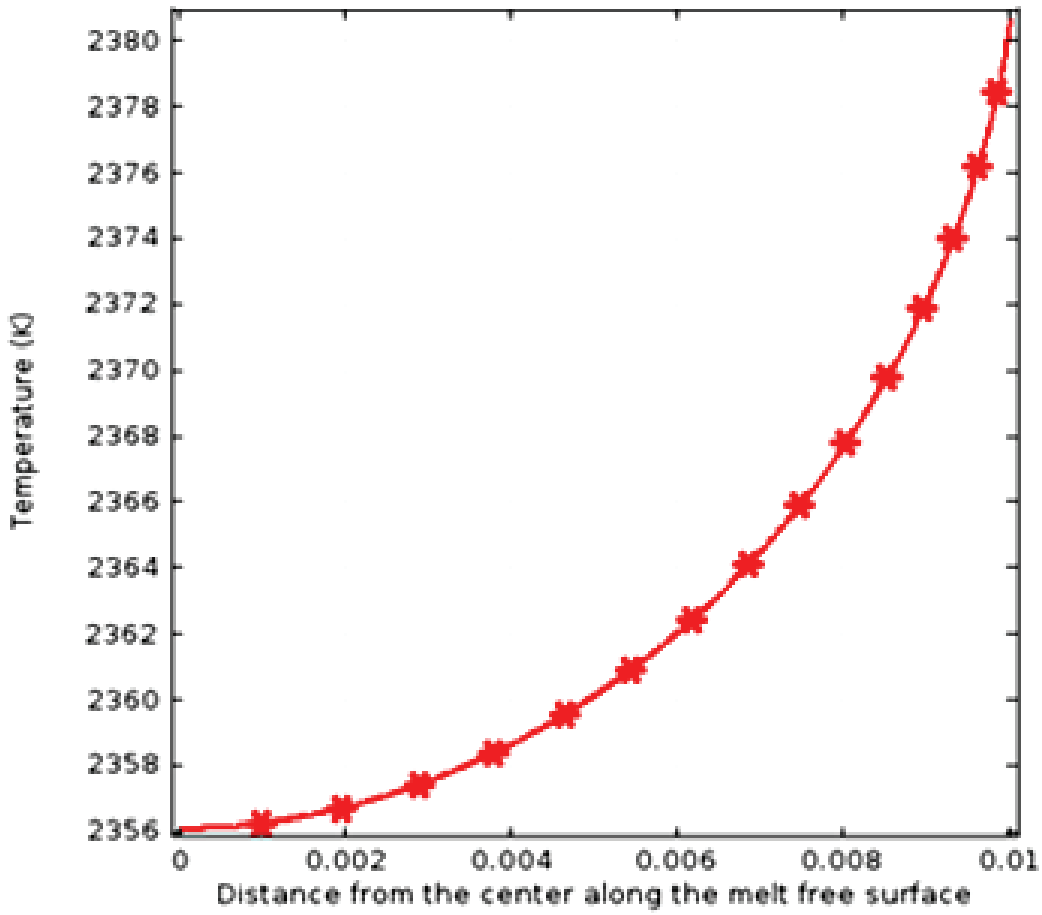

Figure IV.6. Temperature along the melt free surface inside the crucible.

Evolution of gas convention in the growth chamber at the different boundary conditions was also studied. This is an important factor, because the size of the growth chamber increases by 2-3 times during fiber growth due to elongation of the corrugated pipe mounted on the seed support. The complication is that the segments of this pipe open abruptly calling stepwise increase of the chamber volume. This, in turn, calls the drop of gas pressure and, in turn, a strengthening of the cold gas inflow into the chamber. To simulate the evolution of gas convection in the chamber after a pipe segment opening the cases with the different gas flow rates from $8.9 * 10^{-4}$ up to 1 m/s through the hole (marked in Figure IV.7) between the hot zone and the pipe were considered. The gas convection intensity strongly reinforces as the flow rate through the hole increases. In particular, maximal gas local rate increases by the 3 orders of magnitude up to 28 m/s.

The convection in the hot zone of the chamber is also affected by the chamber volume variations. This is illustrated by the 2 cases (Figure IV.8) corresponding to the most left and most right figures in Figure IV.7:

a) very weak gas inflow/outflow assumed to be in steady state conditions;
b) strong inflow/outflow assumed to correspond to the moments of opening the pipe segments.

In the second case the gas convection is much more intensive comparing to the case *a*. Such strong gas convection can cause the fiber vibration. At the same time, injection of cold gas decreases temperature in the whole growth chamber. At the end of the growth the gas convection in the chamber becomes steadier as the cold incoming gas is mixed in the chamber with bigger volume. For this reason the gas pressure in the growth setup should not exceed ~1 bar. Meanwhile, the gas pressure below the atmospheric pressure may lead to atmosphere air leakage into the chamber and oxidation of the crucible.

From the simulation and modeling results the following remarks can be addressed:

1- Changes of the temperature distribution around the crucible and the capillary die violate the steady state growth conditions and lead to the instability of liquid/solid interface.
2- The gas flow effect is significant for thermal conditions in the growth chamber. Including the crystallization zone. It may lead to the formation of inclusions in fibers and affect their optical quality
3- The axial temperature gradient along the melt free surface inside the crucible increases with the melt level drop and can strongly affect the heat transfer at the vicinity of the capillary die.
4- The dominant convection mode in the melt is the Marangoni convection, although buoyancy convection could be observed in the melt near the centerline of the furnace.

5- Since iridium crucible is heated very inuniformly, it is very important to be careful during LuAG fiber crystal growth. Otherwise the crucible will be damaged.

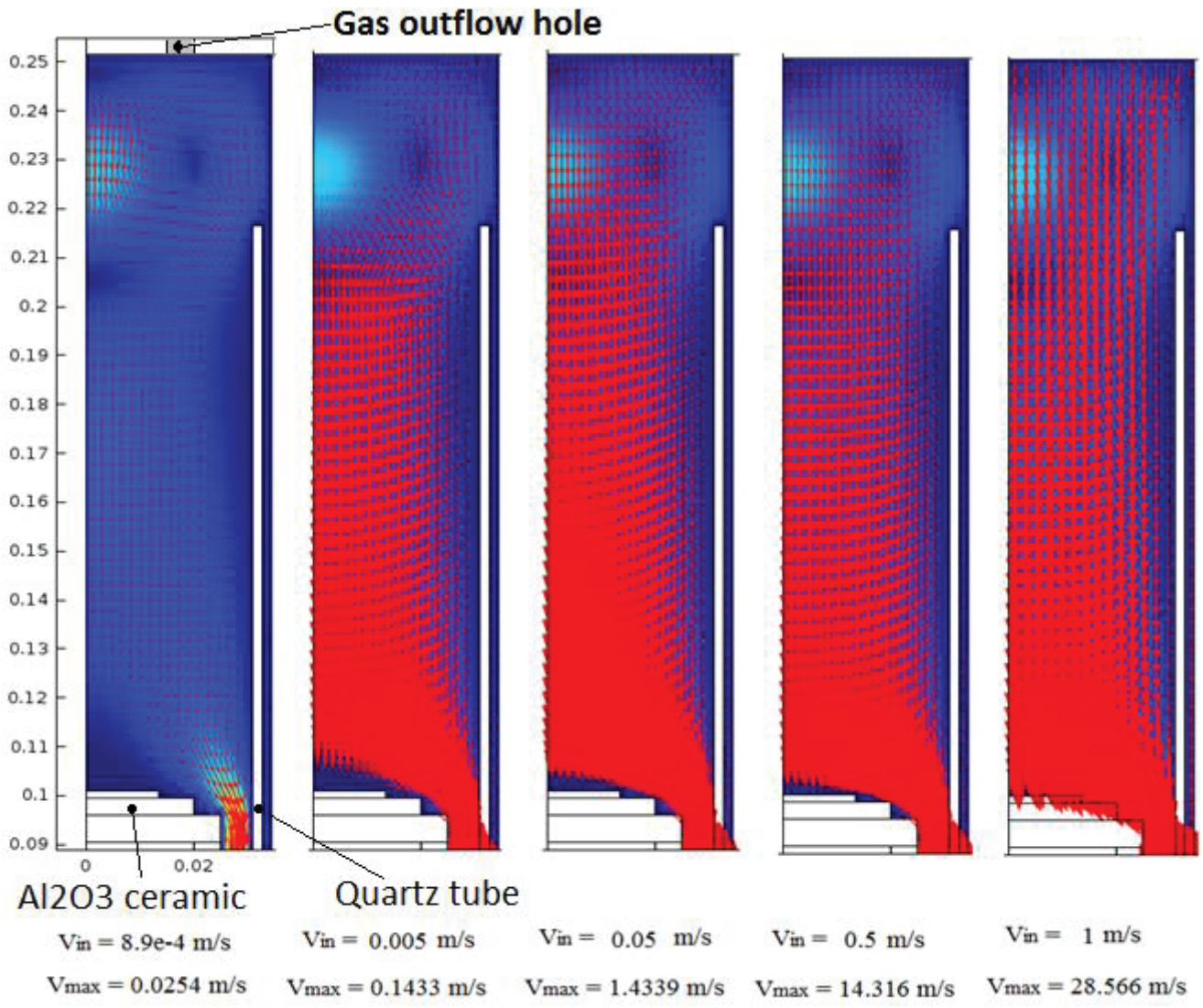

Figure IV.7. The upper part of the growth chamber. The gas convection vs. the gas flow. Red color corresponds to the gas flow direction upwards, blue – downwards. The V_{in} values represent the gas glow rate in the gas inlet hole (see Figure IV.1). The V_{max} values represent the highest flow rates obtained in this part of the chamber.

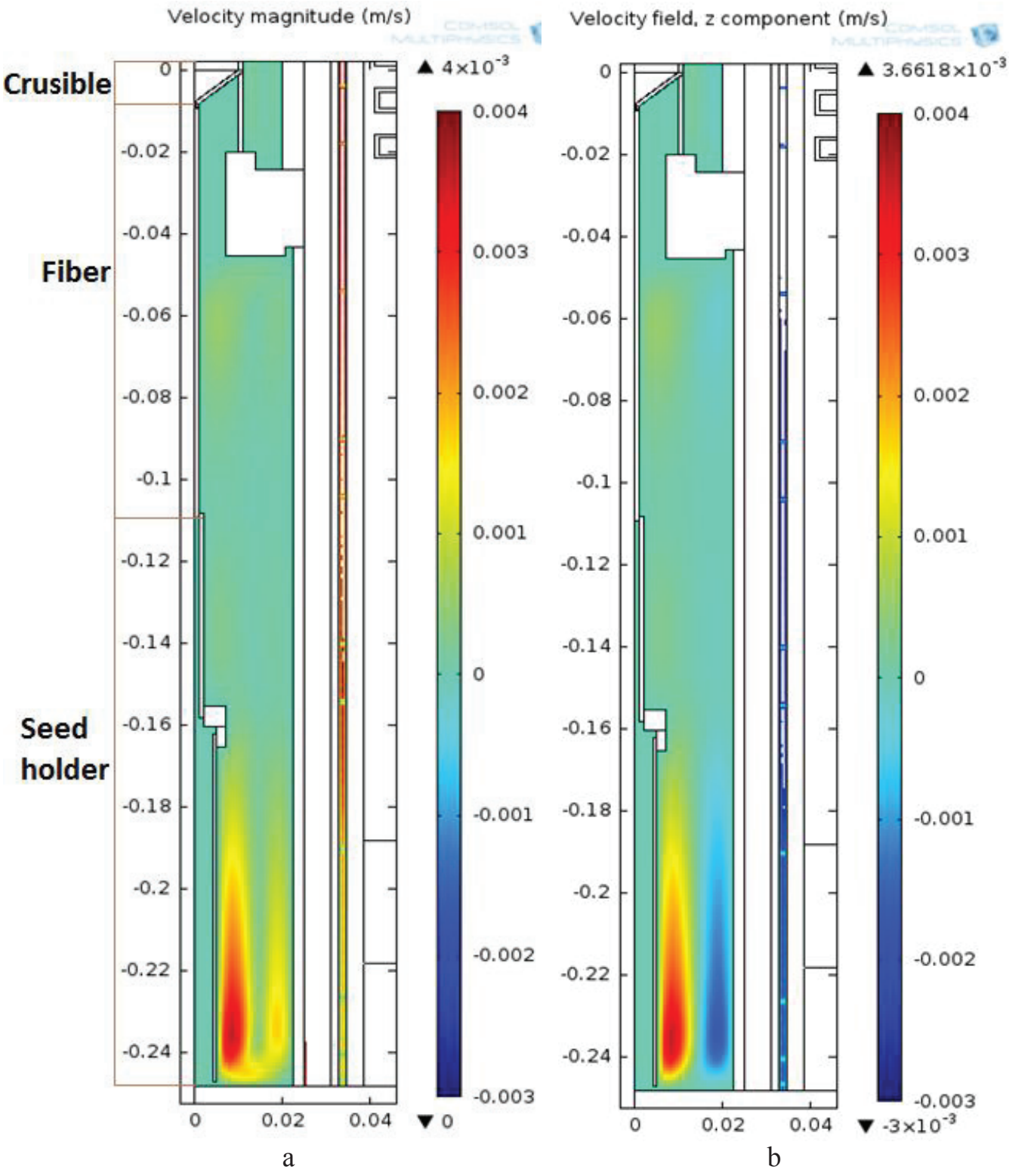

Figure IV.8. The gas convection rate in the growth chamber. Red color corresponds to the gas flow direction upwards, blue – downwards.

4.2. Growth of undoped LuAG fibers

The growth of aluminate garnets was provided in crucibles of different design. Due to the high wettability of LuAG melt the standart conical crucible not provided the constant diameter growth (Figure IV.9a). The melt wetted the outer surface of the die in the case of standard crucible design. As a consequence, regulation of the fiber diameter was impossible and caused cracking of the crystals. In contrast, stable diameter growth was possible using a modified crucible with elongated capillary die, where the melt wetted the capillary shaper perimeter (Figure IV.9b). Meniscus was formed by the contact of a LuAG <111> seed of 10 – 20 cm length with the capillary die. The height of molten zone (h) was controlled by adjusting RF heating power and fiber pulling rate (Figure IV.10). Experimentally, in the case of LuAG grown under steady-state conditions the ratio of molten zone height fiber diameter was determined to be 1: 5-10 depending on the growth parameters, capillary design (die shape) and the starting composition. Visible inclusions of iridium in the grown fibers were not observed.

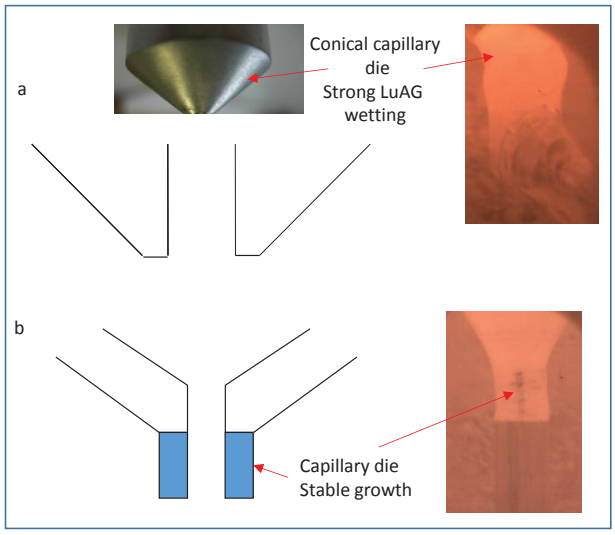

Figure IV 9. A sketch of LuAG fiber steady-state growth with different crucible designs: standart conical crucible (a) and modified crucible (b).

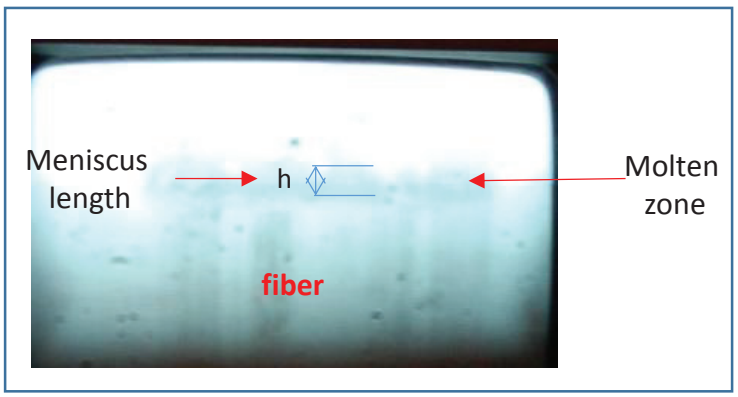

Figure IV 10. View of the meniscus via CCD camera.

In all cases and whatever the composition (undoped or Ce and Pr doped LuAG), the seeding stage at LuAG, LuAG:Ce LuYAG:Ce, LuAG:Pr growth is illustrated by the Figure IV 11. After the seed was connected to the crucible die the meniscus was formed under the capillary (Figures IV.11a, IV.11b). The melt meniscus length did not exceed 0.05 mm (Figure IV.11). The meniscus length decrease was observed with the reaching of required pulling rate and stabilization of the thermal gradients when the grown fiber achieved the 1 cm length (Figures IV.11c, IV.11d). After the growth, the first 1 cm of the fiber was cut off from the rest of the fiber as its surface was wavy due to melt fluidity at relatively long meniscus (Figure IV.11c).

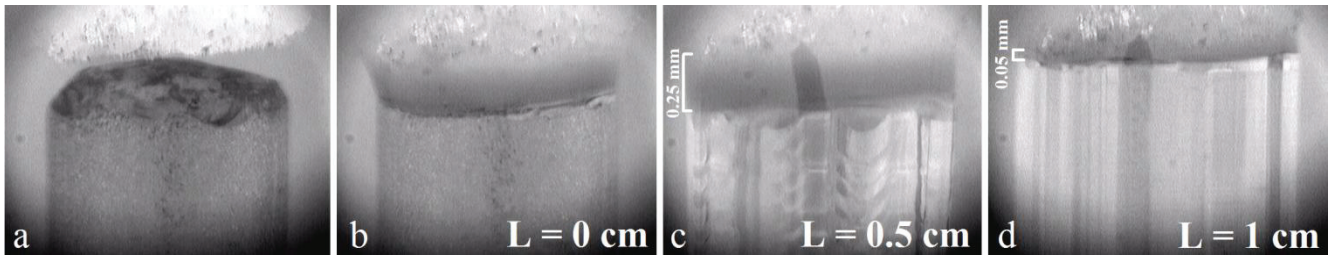

Figure IV.11. Photos of seeding stage at LuAG-based fiber growth obtained using the CCD camera: a) seed moving to the capillary, b) connected to the capillary seed caused formation of meniscus, c) growing fiber with wavy surface due to starched meniscus, d) thinning of the meniscus during the growth

21 undoped LuAG ($Lu_3Al_5O_{12}$) fibers were grown (Figure IV.12). The crystals fibers were grown at a pulling down rate belonging to the range [0.3-0.5mm/min] and were 2.2mm in diameter, close to the diameter of the crucible opening. The typical length of the molten zone corresponding to the stationary state was about 170μm and the crystallization interface was flat and stable. The length of the crystals was up to 250 mm, and 100% of the liquid was crystallized into the fibers.

All the fibers were cut after the growth to the length of 22 cm. The best results have been achieved for fibers grown with the pulling rate of 300 μm/min. It should be noticed that the power applied to the RF heater should be increased during the growth of a constant diameter fiber. Such effect is caused by the increase of heat sink from the meniscus with the elongation of the fiber.

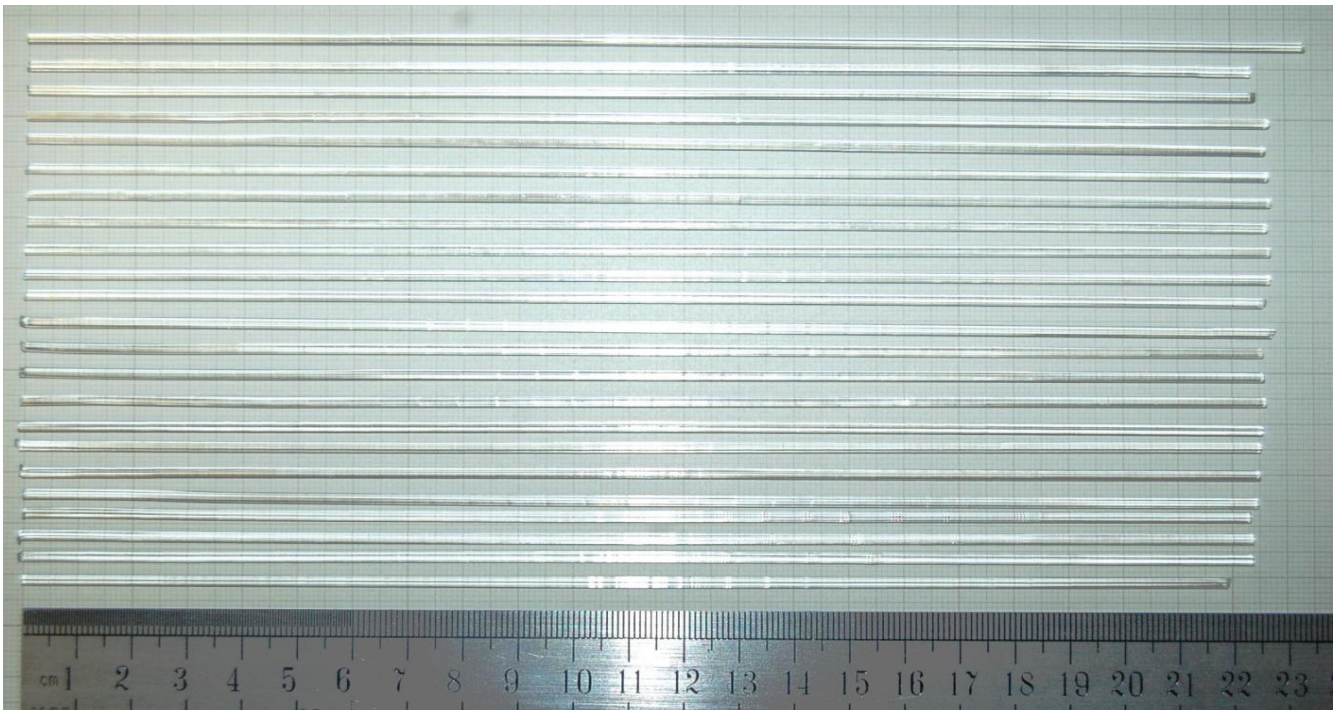

Figure IV.12. Undoped LuAG fibers with the length over 22 cm.

Often, due to the size and material the seed or seed holder have smaller heat conductivity comparing to the as-grown fiber. During the growth and elongation of the fiber the seed moves away from the crucible. Thus, the heat sink from the molten zone

increases (Figure IV.13). The delayed compensation of increased heat sink by increasing the power results in overcooling of meniscus, and appearance of fiber diameter oscillations (Figure IV.13). Temperature in the meniscus is higher closer to the edge of the capillary die (Figure IV.14). With the decrease of meniscus temperature the crystallization isotherm became convex towards the crucible and the melt inside the capillary die is partially or completely crystallized, thus, blocking the melt supply to the meniscus (Figure II.14b). As the issue, the melt does not wet the entire capillary die surface, and the diameters of the meniscus and the fiber decrease. However, quite often, the diameter restores without additional heating. With the decrease of the diameter the heat sink through the fiber reduces and the melt supply restores. With the increase of the power applied to the RF heater we avoid such complication and stabilize the diameter. Empirically we was found that, in the case of LuAG fiber, to compensate the heat sink increase, the power should be increased by ~0.12 % from the beginning (at the step of connection) till the end of the growth of 22-25 cm long fiber.

a

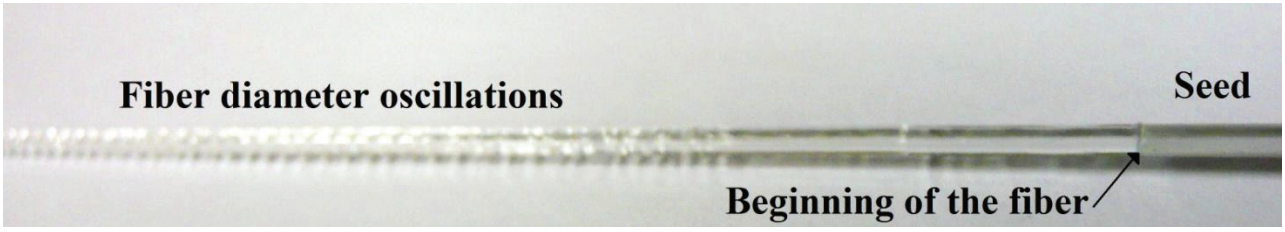

b

Fiber diameter oscillations

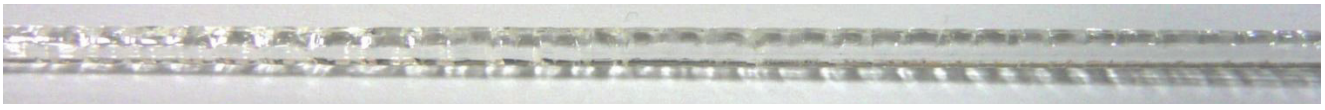

c

End of the fiber Diameter oscillations

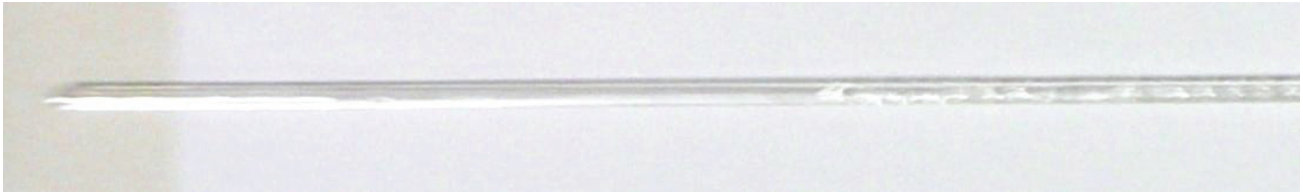

Figure IV.13. Parts of an as-grown LuAG: a) start of diameter oscillations in the beginning of growth; b) fibers with the diameter oscillations; c) end of the fiber with

the improved diameter control.

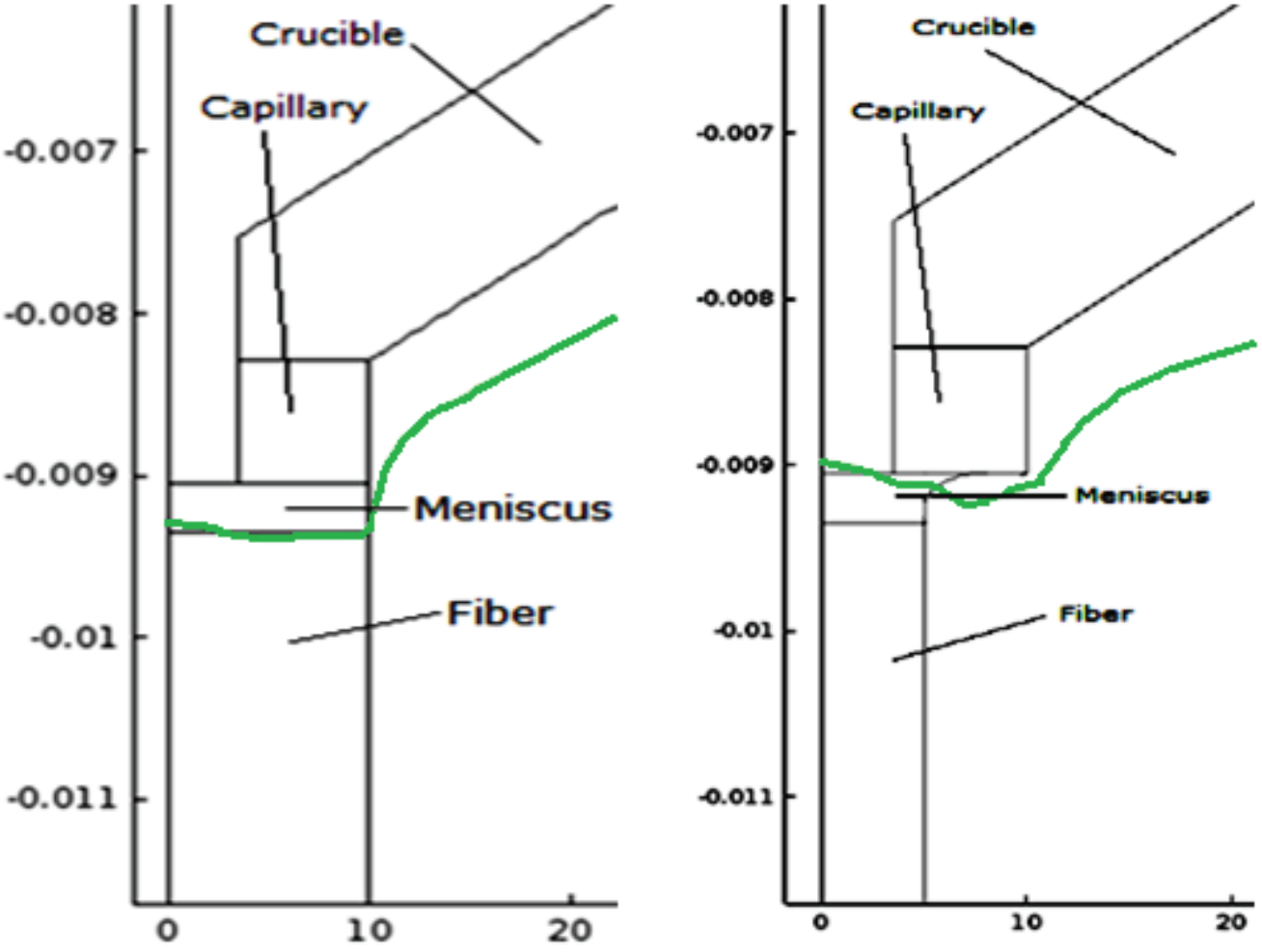

Figure IV.14. The molten zone region: a) the case of stable growth, b) the case of reduced temperature of the molten zone. The green line corresponds to the melting point isotherm.

The additional negative factor influencing the fiber shape is the abrupt change of crystallographic orientation due to decrease of meniscus temperature. Such effect was mentioned in [135] but was not explained. After a large number of growths we found that there is a recrystallization of Ir on the surface of the capillary die, thus the surface of the die is rough. As the melting point isotherm is very close to the capillary die, there

is a chance of spontaneous seeding between the surfaces of the grown crystal and the surface of the die causing nucleation with low angle shifting from the (111) growth direction. The crystallographic orientation change is manifested as the shift and miso-orientation of fiber growth direction (Fig. IV.15). More often it happens when the time-worn crucible is used.

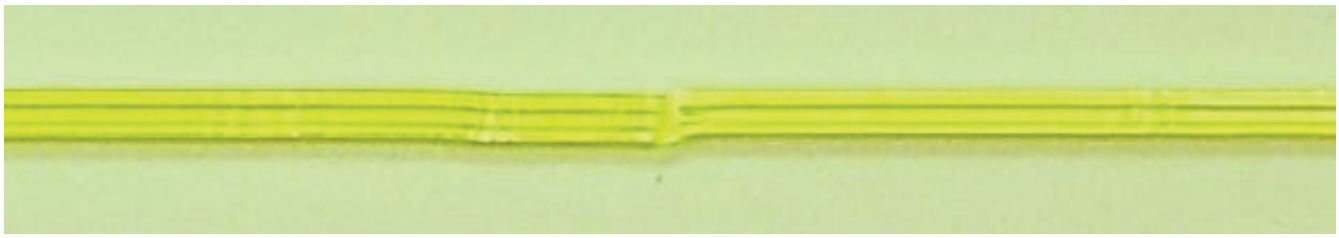

Figure IV.15 Part of an as-grown LuAG:Ce fiber with shifted direction from the initial (111) seed .

The opposite situation is also described [135]. With the increase of molten zone temperature above the acceptable range for the stationary stable regime, the diameters of the meniscus and the fiber exceed the diameter of the capillary die. In such case it is possible to obtain a drop of melt on the capillary die with higher diameter causing instability of the molten zone and uncontrolled increasing of the fiber diameter.

The grown fibers of undoped LuAG can be divided into 2 groups (Figure IV.16):

1) with the attenuation lengths <22cm
2) with the attenuation lengths >22cm.

The requirement of 22 cm length was elaborated basing on the length of current $PbWO_4$ crystals installed in the CMS experiment at CERN. The choice of 2 mm diameter fibers was a compromise between the granularity (smaller diameter means better spatial resolution) and number of fibers in the calorimeter (smaller fiber diameter

means more fibers to handle to fill the given volume and also the higher number of photodetector channels).

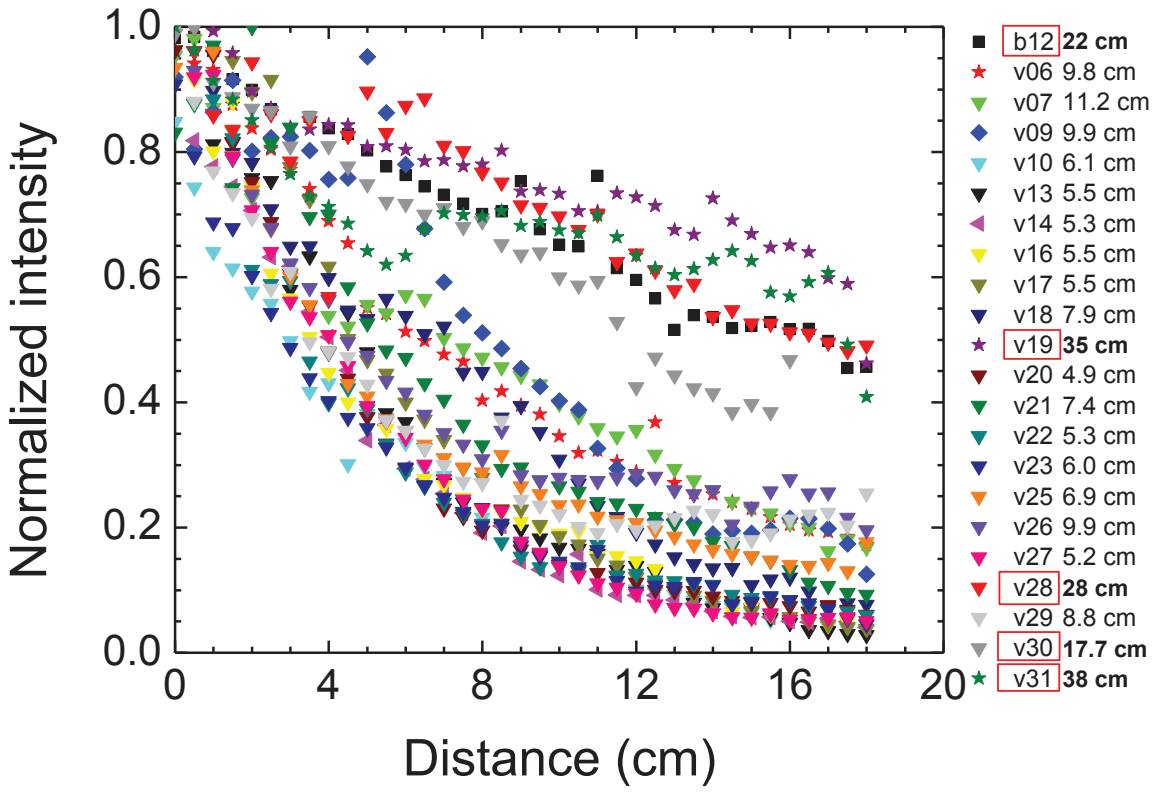

Figure IV.16. Luminescence signal intensity vs. the distance from the excited area to the photodetector in the LuAG fibers at 475 nm excitation. The attenuation lengths are quoted in the legend. Fibers grown with the following pulling rates: 350 µm/min – "quadrates", 300 µm/min – "stars", 500 µm/min – "triangles", 500 µm/min grown with [100] seed – "rhombs".

The improvement of the attenuation length at decreasing the pulling rate down to 300 µm/min can be seen on the histogram (Figure IV.17). The averaged results give the 8.7 cm attenuation length for fibers grown at 500 µm/min and 27.6 mm grown at 300 µm/min. The largest attenuation length of 38 cm was obtained with the v31 fiber grown at 300 µm/min along the [111] direction. For an unknown reason the fiber v06 didn't get to the second group though it was grown with the 300 µm/min pulling rate. Probable

reason can be that v06 was one of the first LuAG fibers grown from the beginning of experiments. The crucible was filled before with another material and contained some admixtures remained from the previous growth runs. The impurity may reduce the attenuation length of the fiber. The attenuation length of the fiber v09 with [100] orientation doesn't differ from the other fibers grown with the 500 µm/min rate.

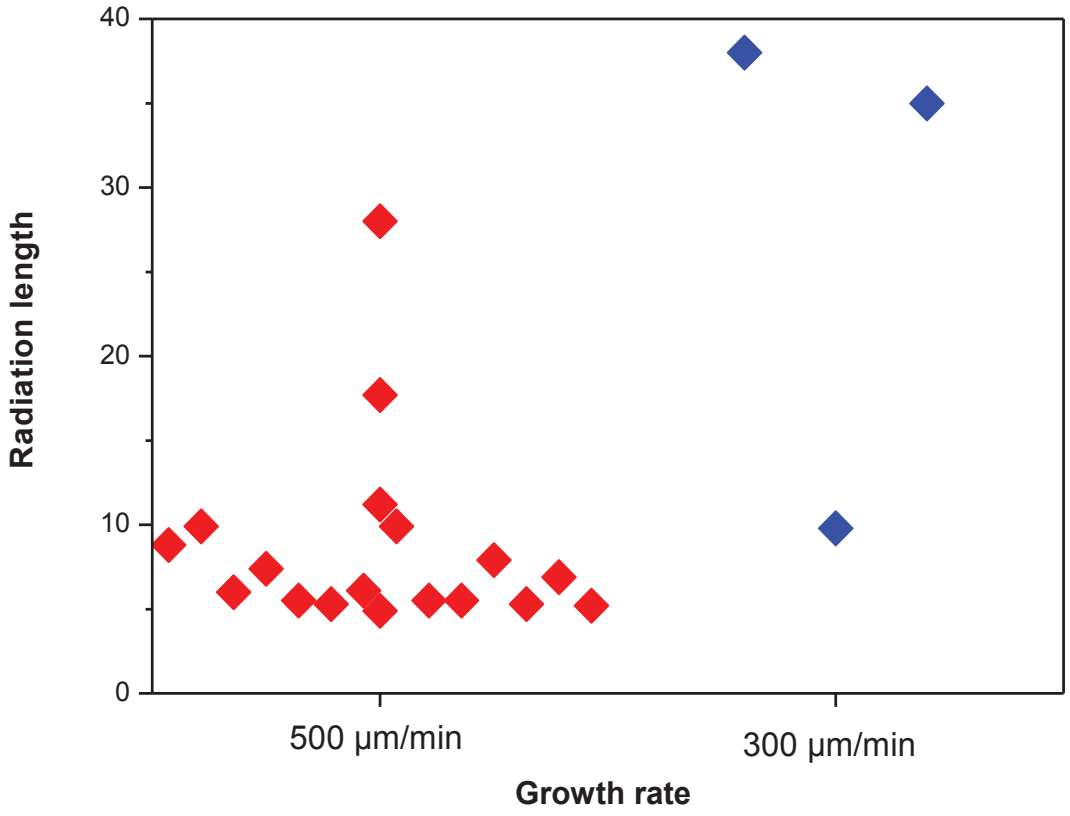

Figure IV.17. Histogram of the attenuation length of the LuAG fibers vs. growth rate.

4.3. Growth of Ce- and Pr doped LuAG fibers

In any compositions with the Ce^{3+} and Pr^{3+} doping we had not seen any composition evolution resulting in a second-phase formation. Disconnection of the fiber growing from the molten zone was never observed even in the case of changing growth parameters such as the pulling rate. High Ce concentration (Ce>0.1 at.%) cases an

increase the melt wetting, the interface becomes convex (Figure IV.18) and the diameter increases up to 2.5 mm. Figure IV.19a illustrates undoped LuAG fibers, and Figure IV.19b shows 0.06 at. % Ce-doped LuAG fibers. The transparent LuAG fibers have smooth surface (Figure IV.19a). The undoped LuAG is colorless, and Ce-activated fibers have different tints of green depending on the cerium concentration (Figure IV.19b, c, d). The coloration is caused by a broadening of Ce^{3+} absorption bands with increasing of dopant concentration. LuAG:Ce transverse slices were cut from the fibers and analyzed by optical microscopy (Figure IV.20). Strong Ce radial segregation in samples with high Ce (>0.1 at.%) concentration was observed. Difference of the Ce^{3+} (103.4 pm) atomic radii, which is larger than that of Lu^{3+} (86.1 pm) is a basic reason of activator segregation in fibers.

Figure IV.21a and IV.21b demonstrate a cross section view of LuAG:Ce with 0.12 at.% of activator concentration in raw material. The color contrast relates to the luminescence intensity difference of crystal areas. A visible concentration gradient is observed in the transversal cut of the fiber. The sample periphery had higher luminescence intensity than the middle part, which confirms higher Ce concentration in the periphery of the fiber. A constant concentration of activator along the fiber axis following the composition analysis was observed. Stable activator concentration is caused by the peculiarirties of melt convection and diffusion transport in the capillary die. At relatively high pulling rates and absence of the mixing of the melt from meniscus with the melt in the crucible the diffusion length $l=D/v$ (v-growth rate, D - diffusion speed) is smaller than the inner length of the crucible capillary (2.5 mm). Therefore, variation of Ce concentration along the grown fiber was not observed. Often we observed gas bubbles in fibers, which appear at some critical supersaturation of the melt with a gas. The tendency to increase of gas bubbles quantity with the starting Ce concentration in the melt was observed.

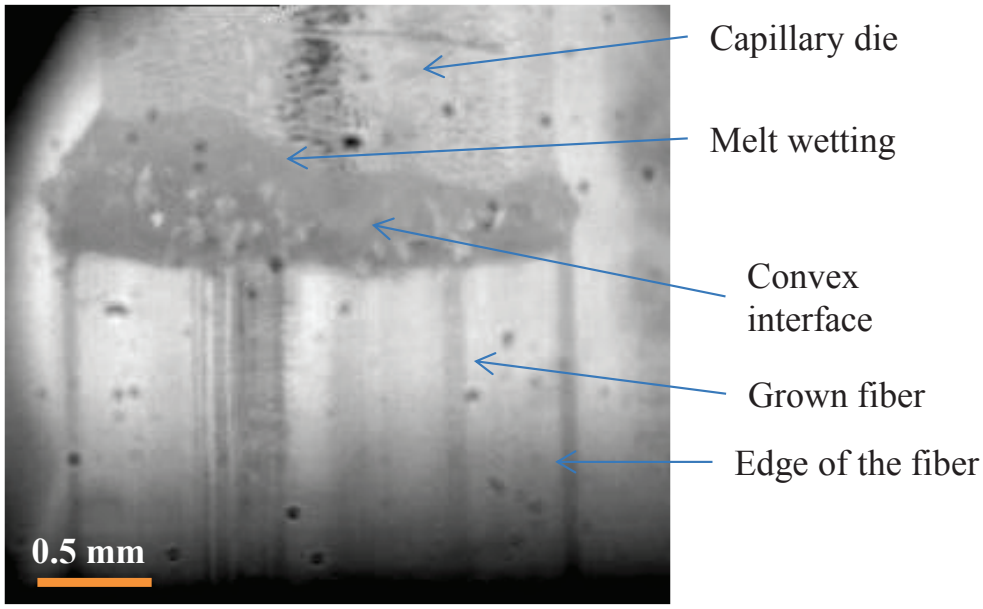

Figure IV.18. The view of LuAG:Ce (0.12 at.% of activator concnetration) growth. Convex molten zone towards the fiber and strong wetting on the periphery of the capillary die is shown.

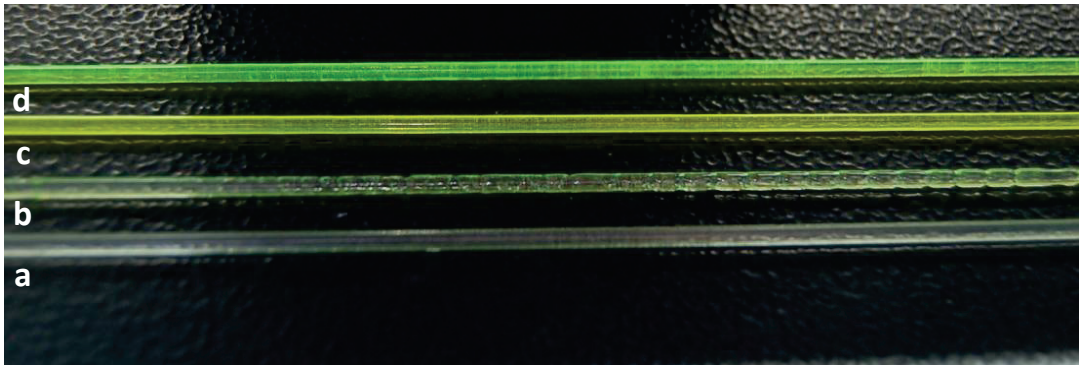

Figure IV.19. Color evolution as a function of Ce dopant concentration in undoped LuAG (a), LuAG:Ce: 0.03at.% (b) , 0.06at.% (c) , 0.12 at.%.

Figure IV.20. LuAG:Ce tranverse cut samples optically polished for microscopy analysis.

.

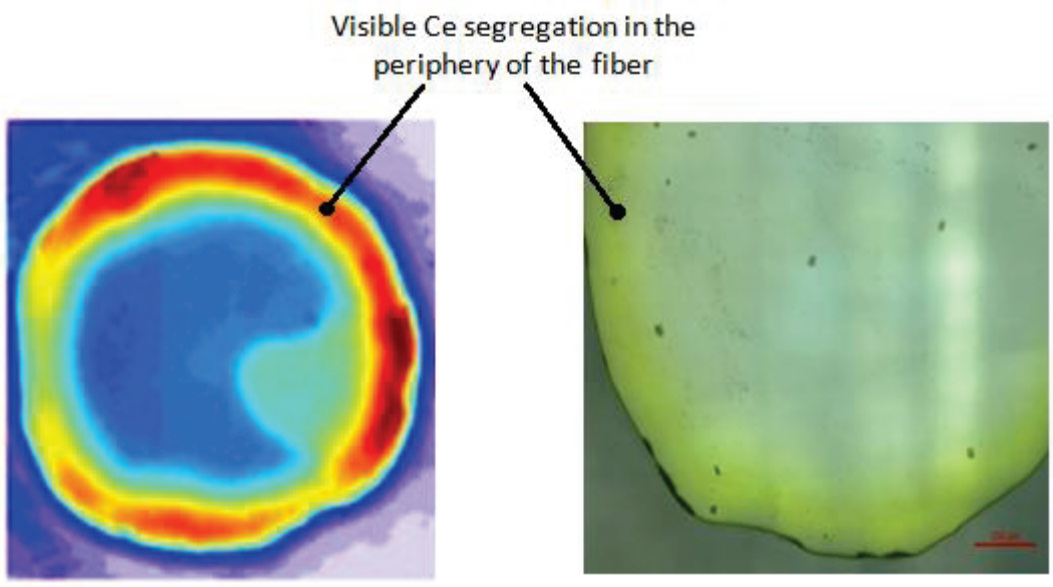

Figure IV.21. Thransverse cut of LuAG:Ce sample (0.11 at.% Ce) under x-ray excitation (a) and optical microscopy (b) illustating a conentration gradient of Ce.

The segregation of the bubbles occurs during the liquid-solid transition leading to an increase in the bubble size and their subsequent diffusion towards the top driven by the buoyancy effect. In garnet materials, the relationship between gas bubbles and dopant distribution is not clear. In undoped LuAG crystals grown with the 0.3 mm/min pulling rate no bubbles were observed (Figure IV.22a). LuAG:Ce fibers with high dopant concentration contained bubbles along the growth axis (Figure IV.22b, IV.22c).

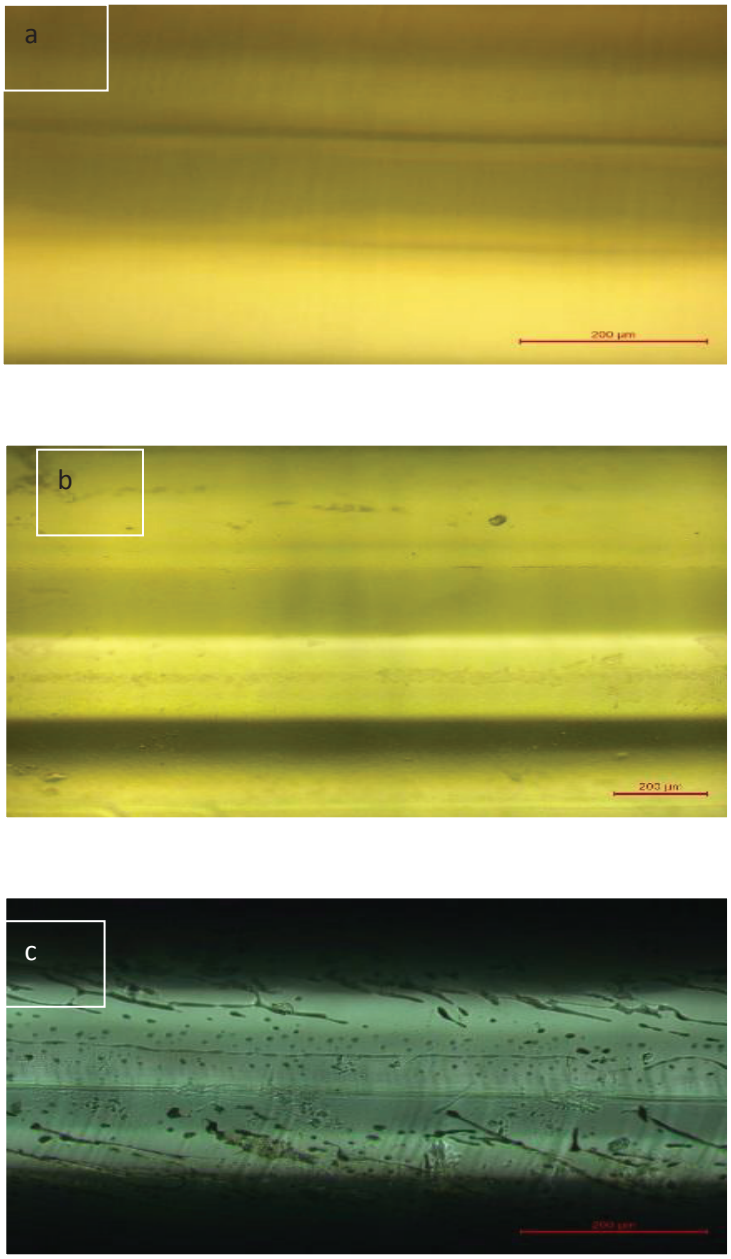

Figure IV.22. View of bubbles on the lateral periphery of undoped LuAG (a) and LuAG fibers with 0.06 at.% (b) and 0.12 at.%(c) of Ce concentration.

By analogy to [7] most bubbles had a spherical shape and some of them were elongated along the growth direction. An analogous situation has been observed in sapphire fibers at growth with similarly designed crucible [136, 137]. The bubbles were

well aligned along the fiber axis following optical microscopy pictures (Figure IV.23). At the growth with growth speed 0.3 mm/min<V<0.5 mm/min and Ce concentration in the melt <0.1 at.%, the crystallization interface is flat with only one lateral layer of bubbles. The distance from the lateral surface of the fiber to the bubble layer is ~93 μm along the whole fiber (Figure IV.24). The rest of the crystal is bubble-free. Bubbles formation is minimized in the regions with smaller component of the melt velocity above crystallization interface. In the case of faster growth, constitutional undercooling supports bubbles distribution. LuAG:Ce grown with low rate had stable diameter and smooth surface due to flat solid/liquid interface. For bubble-free growth it is significant to control the growth conditions. Following the obtained results, lowering of growth rate down to $v \leq 300$ μm/min is a way to get LuAG fiber with low bubbles concentration and reasonable quality.

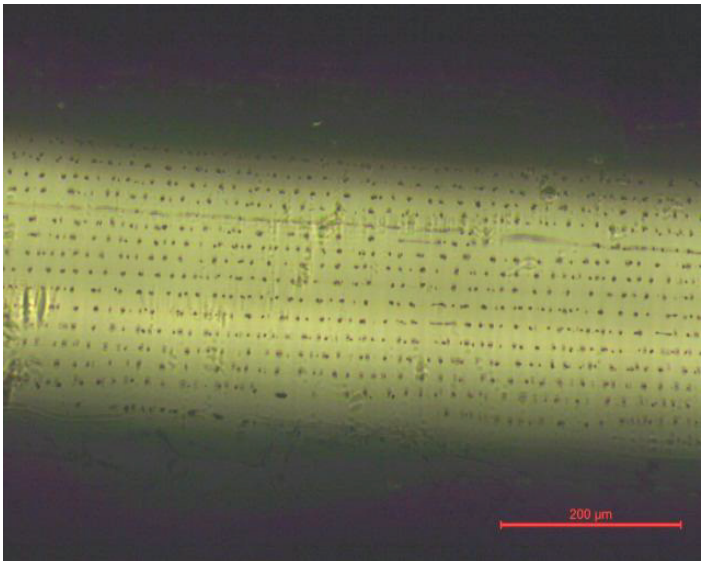

Figure IV.23. Bubbles oriented in fiber along the growth axis.

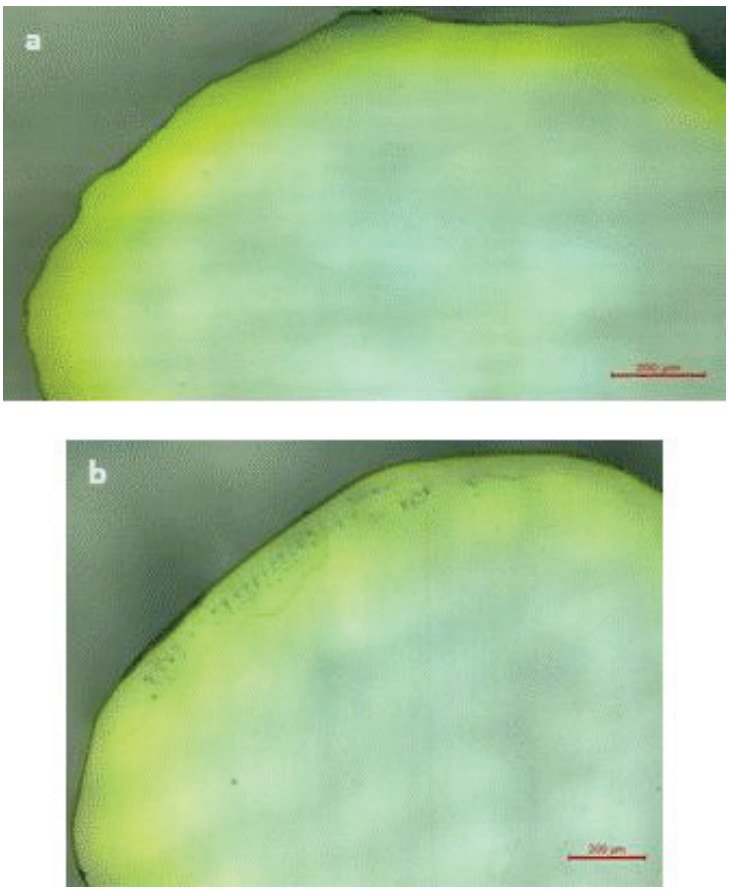

Figure IV.24. Transverse cut of Ce-doped LuAG, undoped LuAG, pulling rate = 0.3 mm/min (a), Ce = 0.06 at.%, pulling rate = 0.3 mm/min (b).

So, to continue our program, 19 LuAG:Ce and 2 LuAG:Pr fibers were grown with the pulling rate of 300 μm/min (Figure IV.25). After the growth process, all the fibers were cut to the length of 22 cm. The growth conditions for these fibers were modified compared to the undoped LuAG fibers. During the growth of doped LuAG fibers the power increase was by 3 times larger than in the case of undoped fibers growth (~0.35 % of power increase relatively to the seeding stage). Obviously, this significant difference was the issue of the larger attenuation length of Ce-doped fibers and, as the issue, stronger radiative heat sink through the fibers. The best results had been achieved for the fibers with the 0.1 at.% Ce concentration grown with the pulling rate 300 μm/min. Higher Ce segregation to the surface of fibers at higher Ce concentration could affect the transmission. Even bubbles in the volume of fibers did not influence the attenuation length so much.

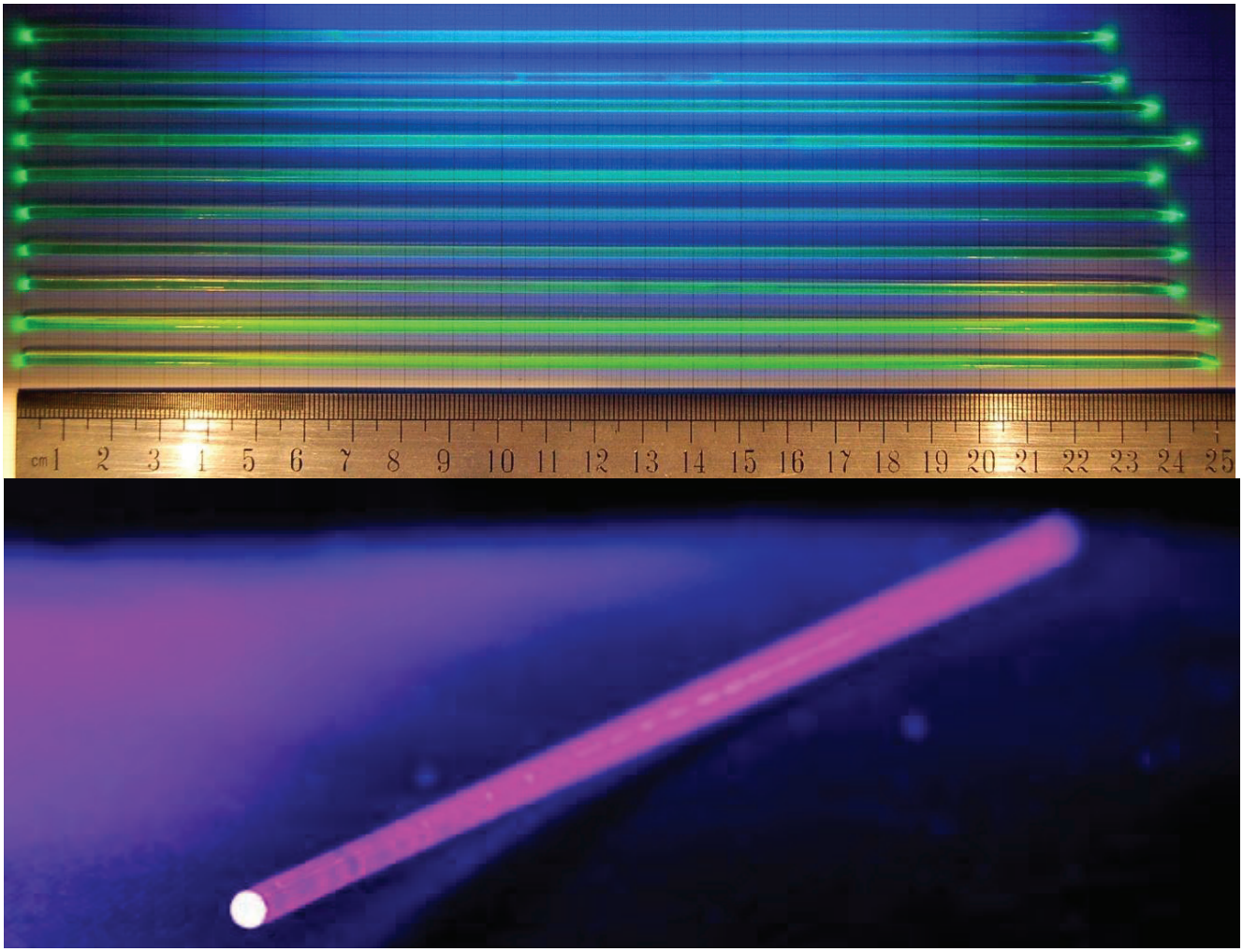

Figure IV.25. LuAG:Ce (upper)and LuAG:Pr (lower) fibers with the length over 22 cm.

With the activated fibers we faced the problem of periodical inclusions along the fibers (this was observed in some undoped fibers as well). These places could be visually observed in the transmitted light. These regions are clearly manifested on the plots of signal intensity vs. the distance between the irradiated place and photodetector (Figure IV.26). Comparing the plots of vc02 (reference) fiber with no visible inclusions, and those of vc09 and vc10 fibers containing inclusions, one can see the uniform decay of light intensity on the distance for vc02, and the splashes in the rest of plots corresponding to the places of inclusions (denoted by the arrows). We attribute these inclusions to the instability of thermal field inside the chamber calling the periodical capture of admixtures by the crystal. Meanwhile, the presence of inclusions not always

means the reduced attenuation length. For instance, vc10 fiber with strongly inhomogeneous dependence shows the higher overall intensity at the distances > 5 cm than the vc09 fiber without visible incl**u**sions.

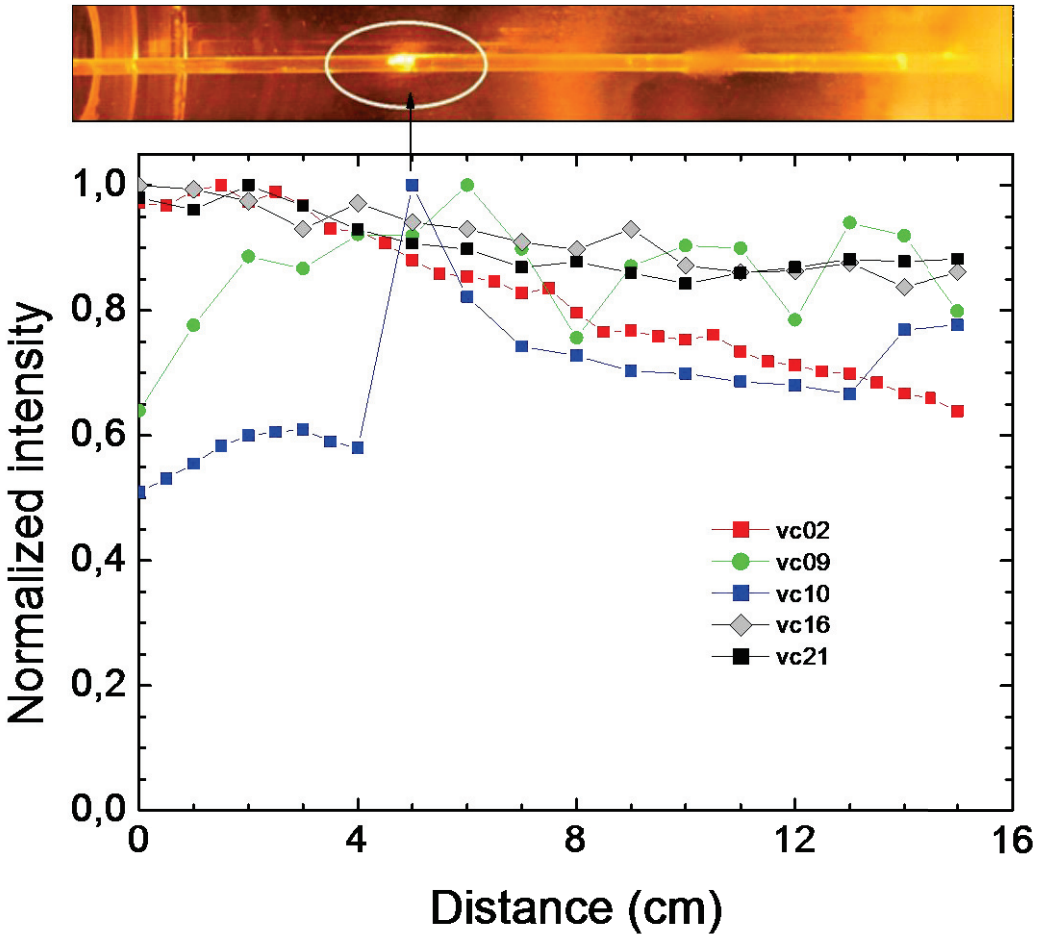

Figure IV.26. Luminescence signal intensity vs. the distance from the excited area to the photodetector in the LuAG:Ce vc02, vc09, vc010, vc16, vc21 fibers at 350 nm excitation. The intensity slope corresponds to the visible inclusion on the photo.

The fibers vc16 and vc21 grown in optimized thermal conditions have smoother attenuation curve at 350 nm excitation. Meanwhile, fiber vc10 do not have such obvious drop of intensity at 5 cm length at 475 nm excitation in contrast to a 350 nm excitation (Figure IV.26, IV.27). Fiber vc02 at the LED bench shows the moderate 16.7 cm, but

the vc09 and vc10 possess the 30.5 cm and 24.2 cm attenuation lengths. The fiber vc10 had the larger visible inclusion than those in vc09 and vc10.

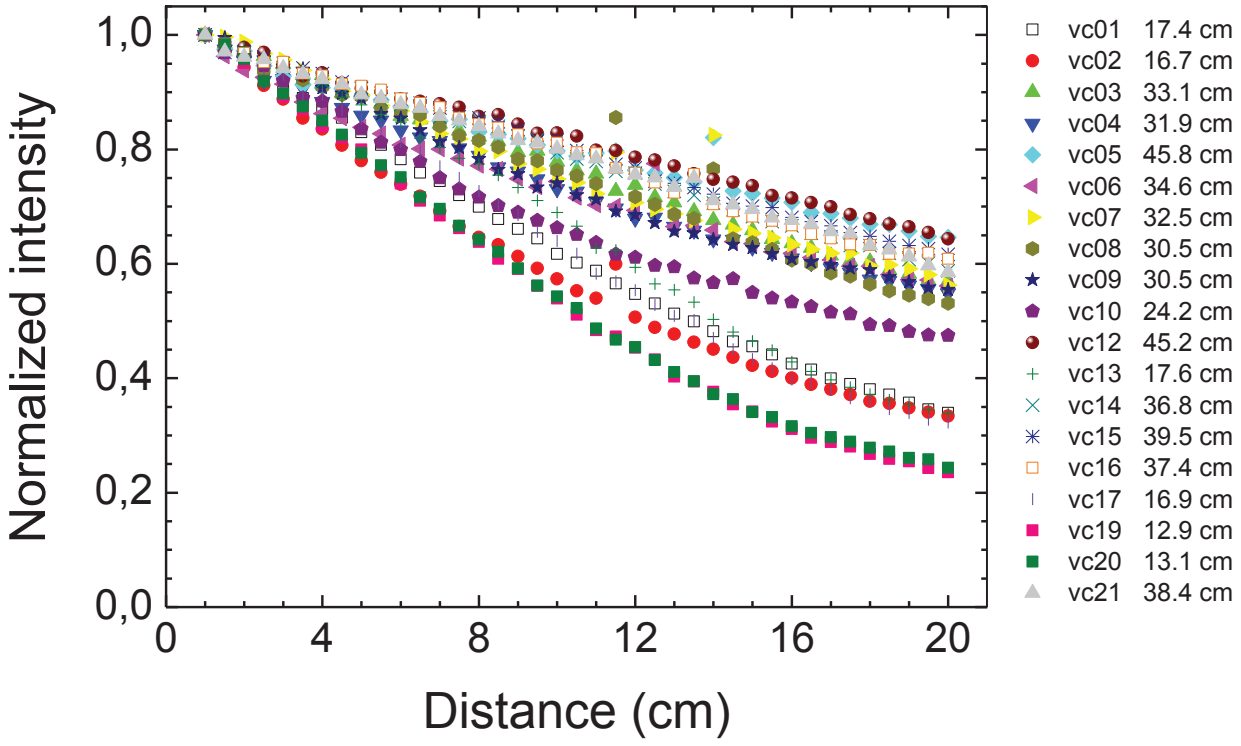

Figure IV.27. Luminescence signal intensity vs. the distance from the excited area to the photodetector in the LuAG fibers at 475 nm excitation. The attenuation lengths are quoted in the legend.

There is the tendency to improvement of the attenuation length during the course of thermal conditions optimization. The attenuation length improvement from 10 - 15 to 30 - 40 cm was achieved. As the example, Figure IV.28 represents the attenuation results for 4 typical fibers grown before (vc1, vc2) and after (vc16, vc21) optimization (the fibers are sequentially numbered starting from the beginning of the experiments). We suppose the difference is due to the better heat insulation of the crystallization zone

ensuring the improved stability of the thermal gradient in the growth chamber. To some extent this is the issue of gas convection control during the growth process. As it was shown by the modeling of the gas convection inside the chamber in the section 4.1, it may influence the growing conditions, especially in the beginning of growth. As a consequence, the fibers at the beginning of the growth contain periodical light scattering inclusions. For example, the splashes are obviously seen at 2 cm, 3 cm and 7 cm on the attenuation graph of fiber v09 (Figure IV.26). Such imperfections are absent in the vc16 and vc21 fibers grown under the optimized gas convection. Weak splashes seen at 10 cm and 12 cm in the most of fibers are experimental artifacts and not relate to fiber quality.

Pr-doped fibers attenuation lengths are significantly worse than those in LuAG:Ce (Figure IV.28). LuAG:Pr were grown under the same optimized conditions. Fibers vp01 and vp03 has [111] and [100] orientation, correspondingly.

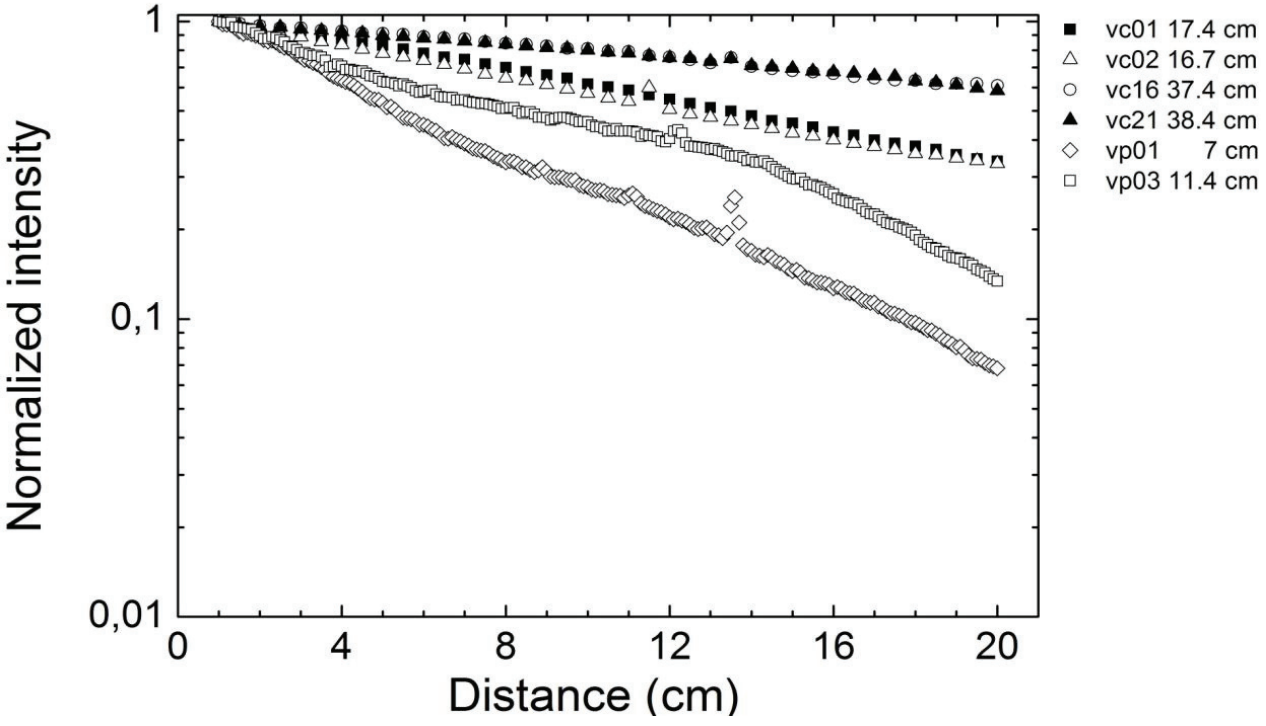

Figure IV.28. Luminescence signal intensity vs. the distance from the excited area to the photodetector in the LuAG:Ce at 475 nm excitation and LuAG:Pr fibers at 250 nm excitation.

4.4. Effect of thermal annealing on LuAG and LuAG:Ce attenuation lengths

To investigate the effect of annealing on the attenuation length, 8 fibers (4 undoped LuAG and 4 LuAG:Ce) grown with different pulling rates and crystallographic orientations were selected. All the samples were annealed during 12 hours in air atmosphere at 1200°C (Table 3). The effect of the annealing on attenuation length is the opposite in LuAG and LuAG:Ce. LuAG attenuation length not changes significantly or deteriorates. The attenuation length of LuAG:Ce is significantly improved, especially for fibers grown with the 300 μm/min rate. The biggest attenuation length of more than 1 meter is achieved in LuAG:Ce grown along [100] direction (Figure IV.29). Therefore, the annealing in air significantly improves the attenuation length of Ce-doped LuAG fibers. Meanwhile, another annealing regime should be found for undoped LuAG fibers.

Table 3. Annealing effect on the attenuation length.

Crystal		LuAG				LuAG:Ce			
Growth rate, μm/min		300		500		300		500	
Growth orientation		[100]	[111]	[100]	[111]	[100]	[111]	[100]	[111]
Attenuation length, cm	Before	15	21	9,5	29	13	17	13	18
	After	14	11	7	24	104	50	14	23

Pulling rate	300µm/min	500µm/min
Orientation	[111]	[100]
LuAG: Ce	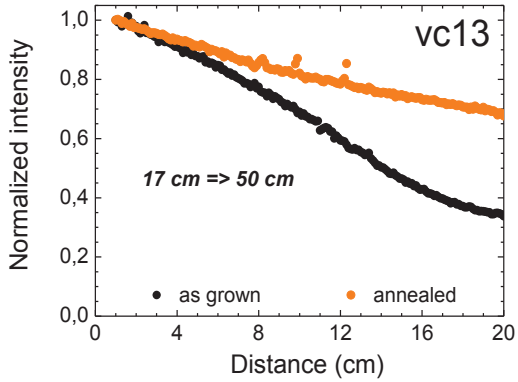	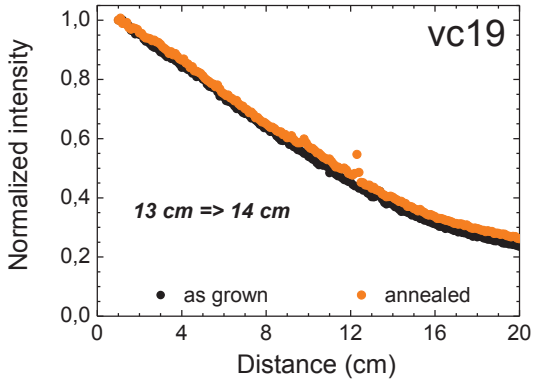
Orientation	[100]	[111]
	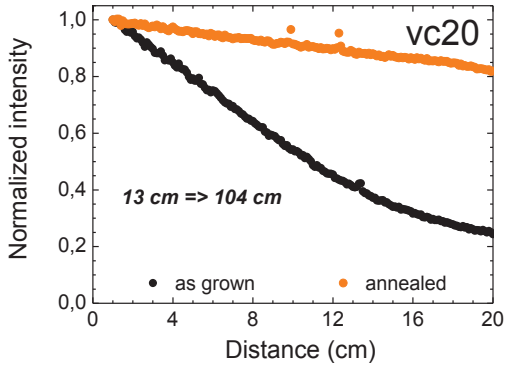	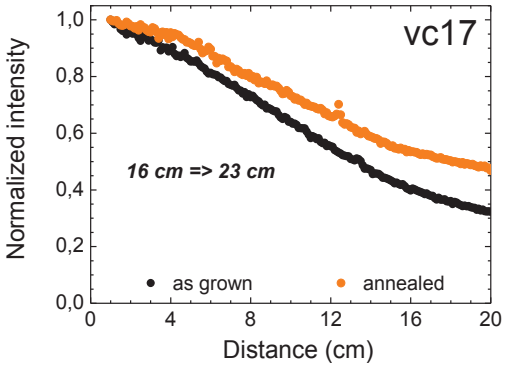
Orientation	[111]	[100]
LuAG	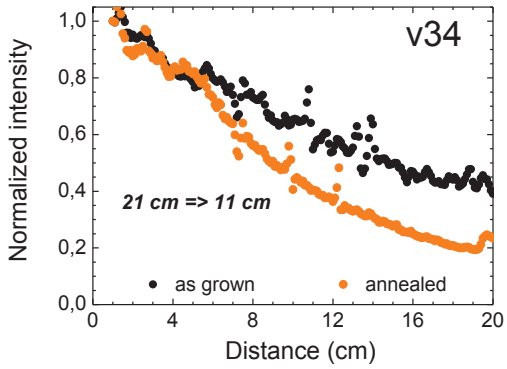	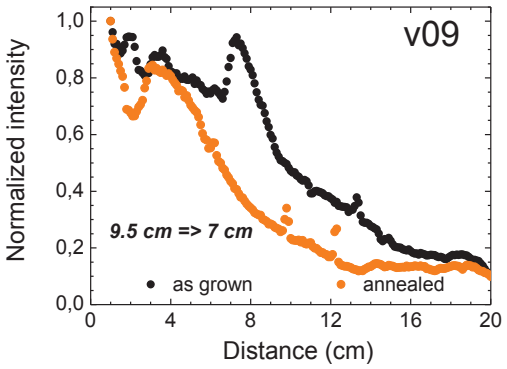

Pulling rate	300µm/min	500µm/min
Orientation	[100]	[111]
LuAG	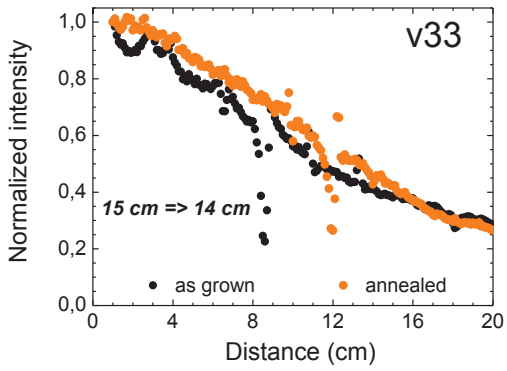	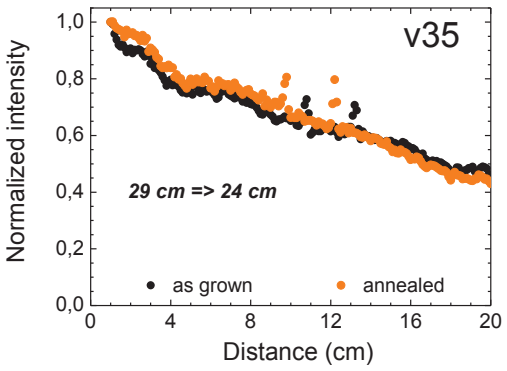

Figure IV.29. Effect of annealing on attenuation of the LuAG and LuAG:Ce fibers at 475 nm excitation. The attenuation lengths are indicated.

4.5. Growth of YAG:Ce fibers

Ce-doped YAG single crystal fibers were grown under stationary stable regime. The seeding stage was different from the case of LuAG-based fibers growth due to the smaller size of the crucible die. The melt meniscus thickness did not exceed 0.05 mm (Figure IV.30). The fibers of YAG:Ce grown with the length of 45-60 cm are presented in Figure IV.31.

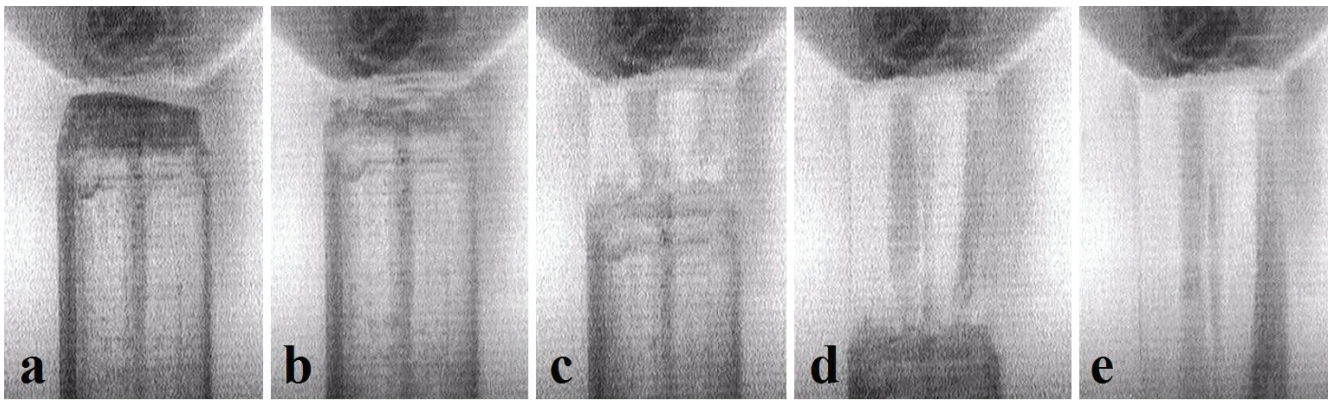

Figure IV.30. The photos of seeding stages at YAG:Ce growth obtained using the CCD camera: seed moving towards the capillary (a), connection of the seed to the capillary L = 0 cm (b); pulling of the fiber at L = 0.5 mm (c), L = 1.5 mm (d), L = 2 mm (e).

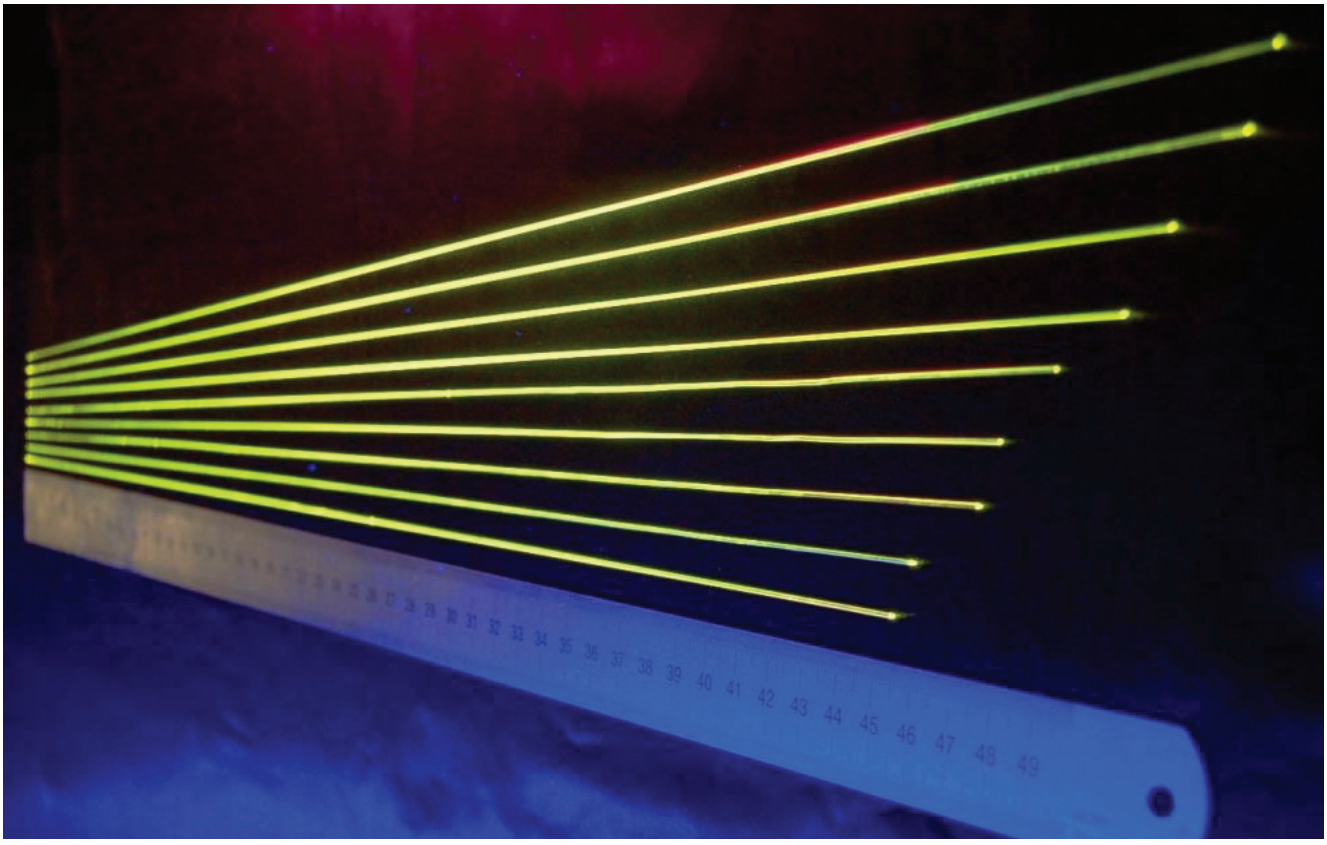

Figure IV.31. YAG:Ce fibers (45- 60 cm length).

For the attenuation measurements the fibers were cut (into 2-3 parts) to fit the LED bench dimensions. The measured attenuation lengths are accumulated in the Table 4. YAG:Ce fibers showed smaller attenuation lengths compared to LuAG:Ce fibers, however, the results are acceptable taking into account the smaller diameter of 1 mm of YAG:Ce fibers (Figure IV.32). Note the good reproducibility of the results from fiber to fiber.

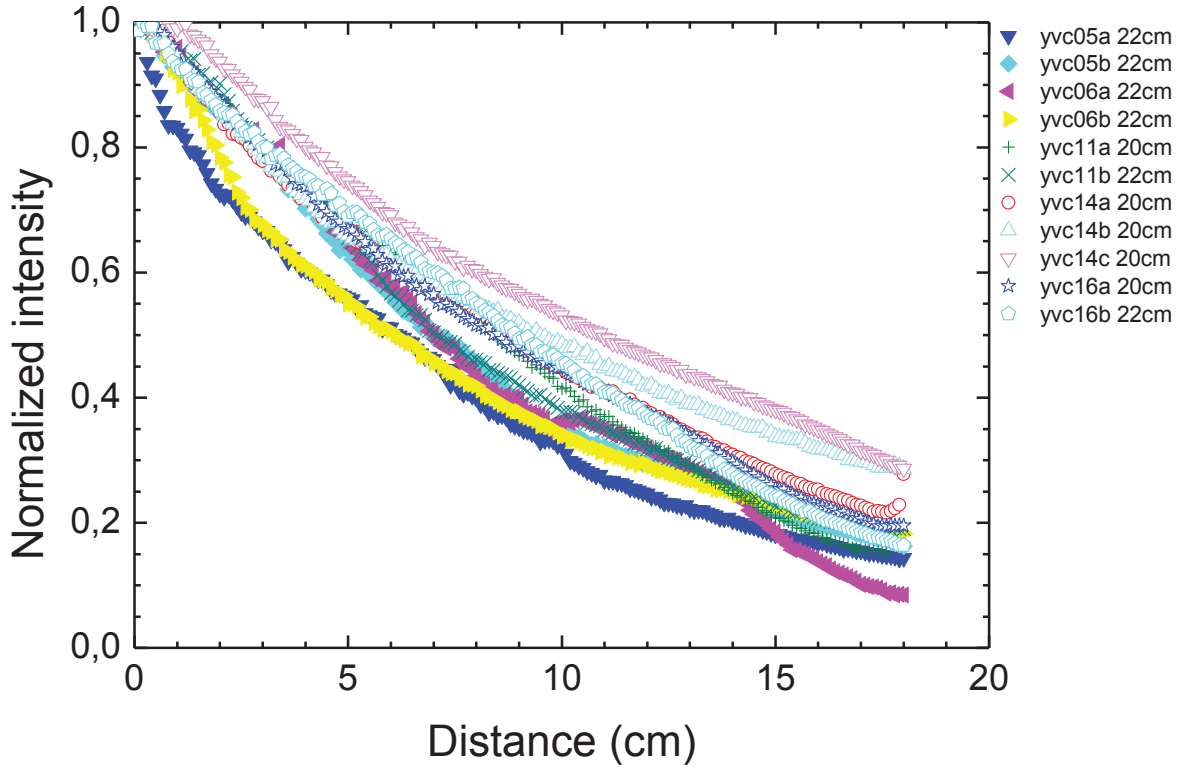

Figure IV.32. Luminescence signal intensity vs. the distance from the excited area to the photodetector in the YAG:Ce fibers at 475 nm excitation. The physical length of the fibers is quoted in the legend.

Table 4. Attenuation lengths of YAG:Ce fibers at 475 nm excitation.

yvc	Part of the fiber	Length of the sample, cm	Attenuation length, cm
5	A beggining	22	9.2
5	B end	22	9.6
6	A beginning	22	9.1
6	B end	22	9.7
11	A beginning	22	9.9
11	B end	20	10.3
14	A beginning	20	11.8
14	B middle	20	13.9
14	C end	20	14.5
16	A beginning	22	11.3
16	B end	20	11.3

4.6. Homogeneity plots

Homogeneity plots were obtained with the LED setup. These curves are taken from the two bottoms of the fiber by two oppositely settled PMT at the same time and averaged by analogy to [6]. Thus, it is possible to evaluate the intensity of luminescence along the fiber.

From the homogeneity plots of undoped LuAG we can see the fibers with better attenuation lengths (b12, v19, v28, v30, v31) demonstrate more flat dependences due to the good transmittance of the fiber, while the fibers with bad transparency the signal from the middle of the fiber is 3-5 times weaker than the signal registered from the fiber ends (Figure IV.33). In the case of LuAG:Ce the luminescence intensity plot is more smooth than that in undoped LuAG, which coincides with the better transparency of the Ce-doped fibers (Figure IV.34.). The reason of the low intensity of some points at the distance 10-15 cm is measurement artifacts not related to the fiber quality.

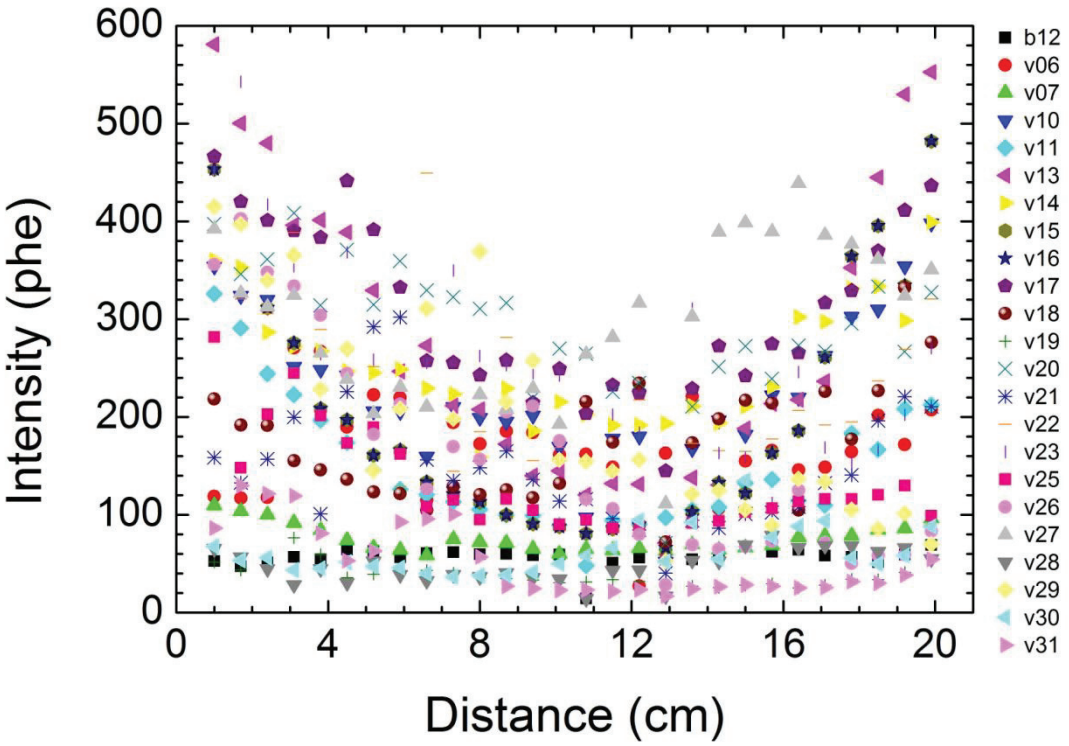

Figure IV.33. The homogeneity plot for LuAG fibers at 475 nm excitation.

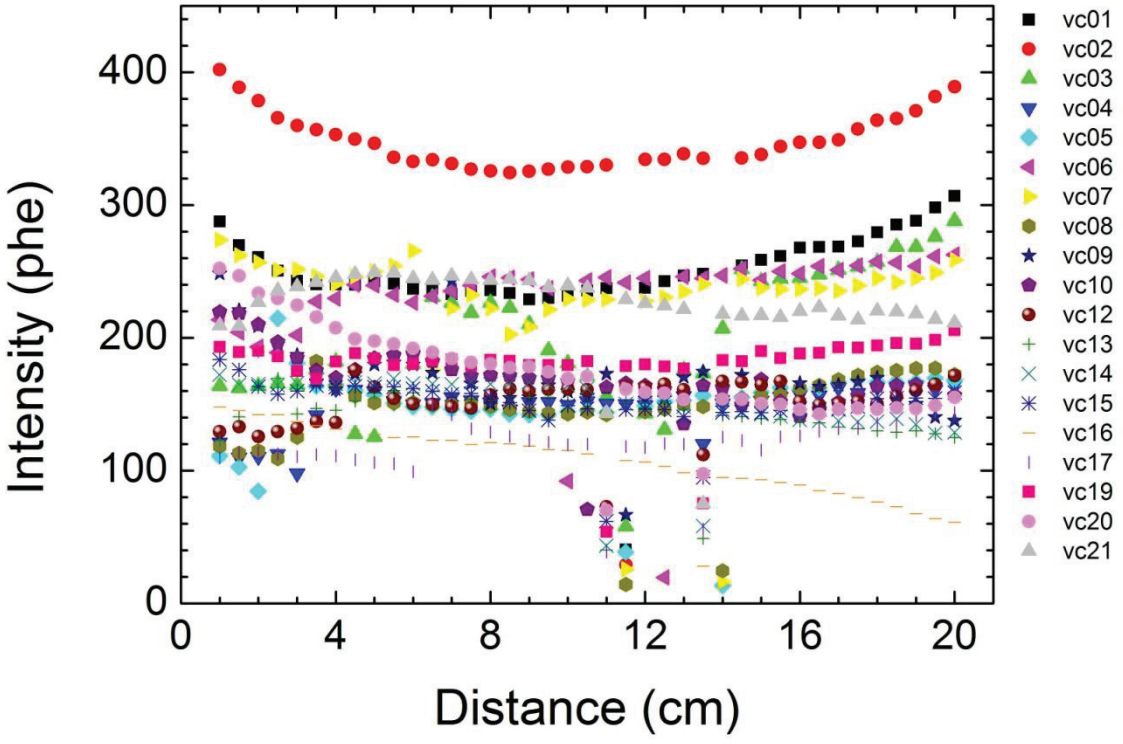

Figure IV.34. The homogeneity plot for LuAG:Ce fibers at 475 nm excitation.

In the case of LuAG:Pr the situation is similar to the undoped LuAG, the transmission of the signal from the middle part of the fiber to its ends is shown in Figure IV.35. The vp01 attenuation length was 22 cm and the one for fiber vp03 was 25 cm (the latter fiber was not cut to 22 cm). The non-symmetrical shape of the attenuation curves reflects the inhomogeneity distribution of Pr^{3+} dopant along the fibers. In other words, the registered luminescence intensity is higher in the ends of the fiber with higher Pr^{3+} concentration.

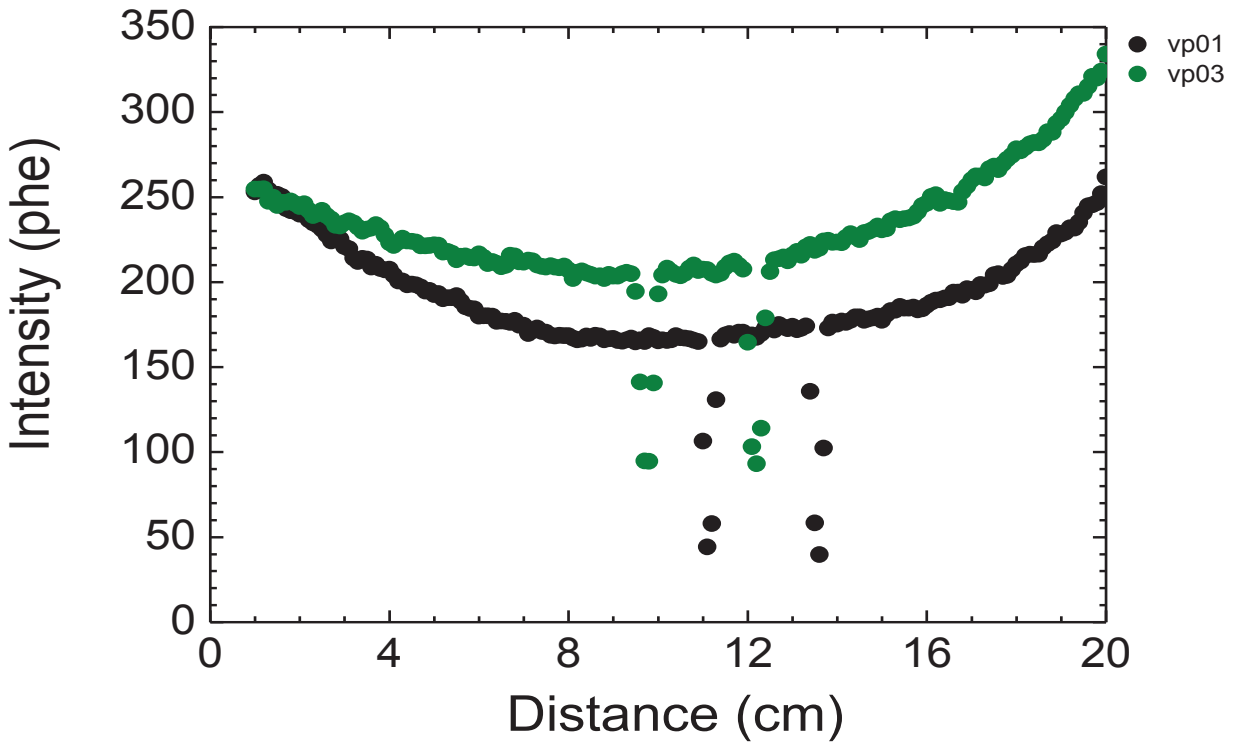

Figure IV.35. The homogeneity plot for LuAG:Pr fibers at 250 nm excitation

In the YAG:Ce the homogeneity differs from sample to sample (Figure IV.36), but the shapes of attenuation curves are more similar, if to compare them with the spread of the curves for the LuAG:Ce fibers (Figure IV.34). This can be an issue of higher activator distribution coefficient in YAG:Ce. It can be also related to using the standard conical crucible, where the diameter of fibers could be changed with lowering of melt level in crucible during the growth. While the melt column height drops the wetting of the meniscus decreases as well. As a consequence, the molten zone height changes. However, the attenuation length results taken from one side of the fiber demonstrated not significant difference between the samples as it was shown above.

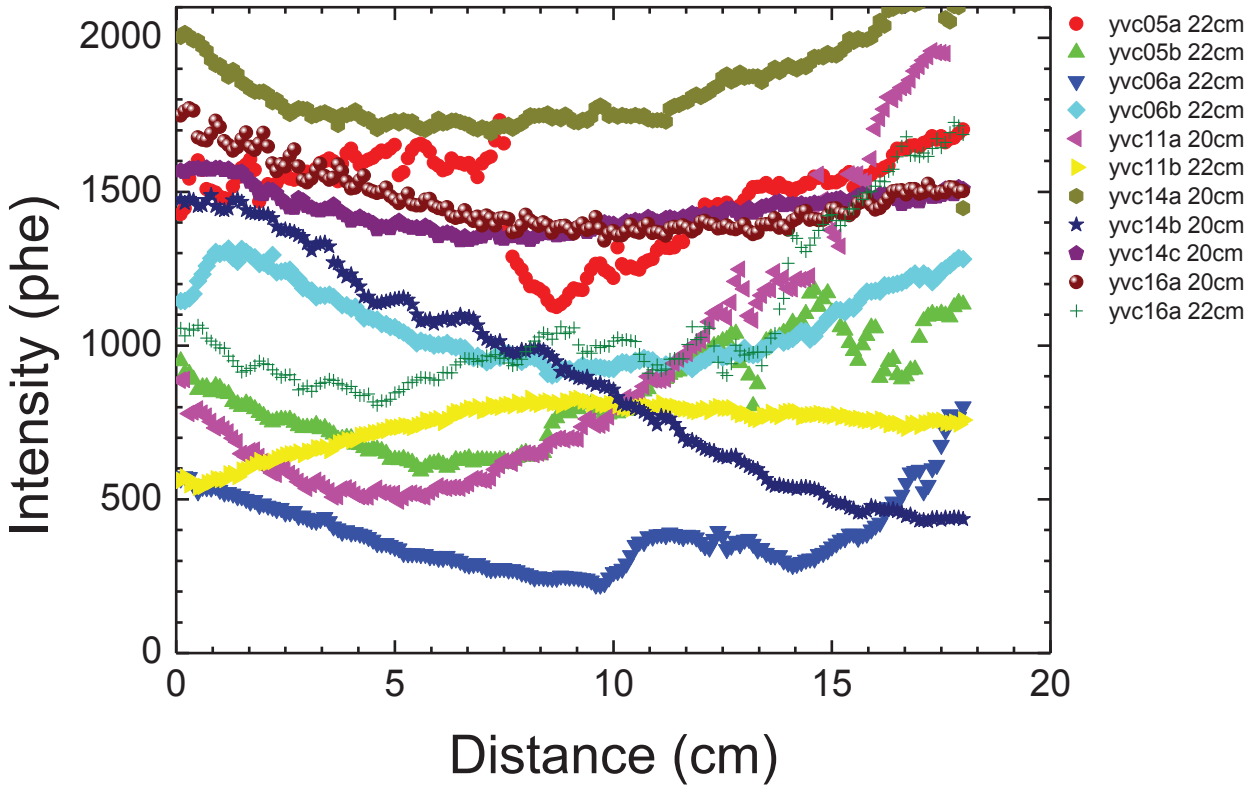

Figure IV.36. The homogeneity plot for YAG:Ce fibers at 475 nm excitation.

4.7. Activator distribution in the LuAG:Ce and LuYAG:Ce fibers.

Low Ce^{3+} distribution coefficient in crystals is a serious negative factor for LuAG and other rare earth garnet hosts. Meanwhile, in the micro-PD method, a substantial gradient of the Ce concentration might appear also in the radial direction [68] and have a negative impact on the scintillation characteristics. Cathodoluminescence microscopic imaging of the fiber cross section is the easiest method to evaluate the activator distribution in the fibers (if to presume the proportionality between the activator concentration and the emission intensity).

For the cathode luminescence experiments we used samples from LuAG:Ce fibers grown at the different rates. For reference we used $Lu_{3-x}Y_xAl_5O_{12}$:Ce (LuYAG:Ce) sample with the Y content 85 at.% and Ce concentration 0,15 at % grown under the same conditions. All the regions, from which the samples were cut, are ~1 cm distant from the beginning of the fibers. Regarding the brightness distribution at the shots the most of activator is concentrated at the fiber periphery (Table 5.).

Meanwhile, the periphery-to-center difference in the cathodoluminescence intensity is ~ 3 times independently on the growth rate. As one would expect, quite another picture is observed with the LuYAG:Ce grown with 300 μm/min growth rate. The intensity variation along the radii does not exceed 2 times just like in the LuAG:Ce fiber grown with 500 μm/min,. Accounting that in LuAG:Ce grown with lower pulling rates luminescence attenuation length is larger, the smoother distribution of activator across the diameter of the fiber is reguired. With decrease of pulling rate below 350 μm/min at growth of mixed LuYAG:Ce one may achieve more smooth Ce radial distribution.. Therefore, transfer to mixed crystals, such as LuYAG:Ce, is a relevant way to improve the scintillation parameters of μ-PD grown fibers by controlling Ce segregation behavior and can be a good way as future work.

Table 5. Photos and radial distributions of cathodoluminescence intensity in some fibers.

LuAG:Ce C35 350 µm/min	LuAG:Ce C19 500 µm/min	LuYAG:Ce C6 350 µm/min
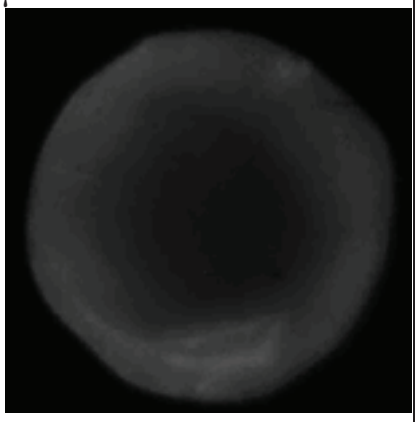	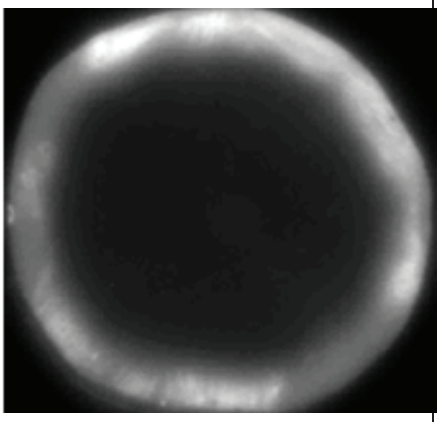	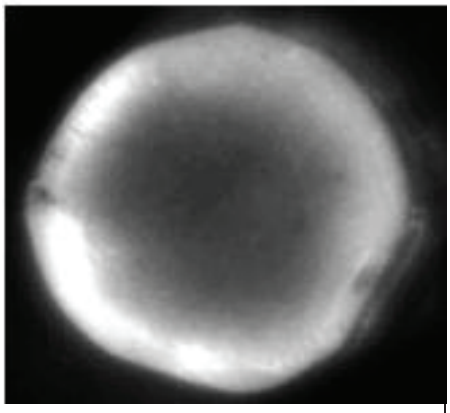
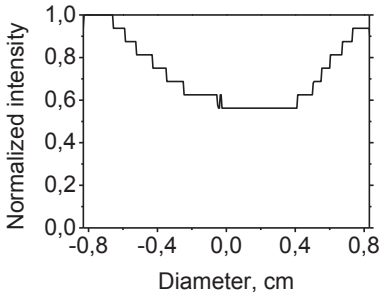	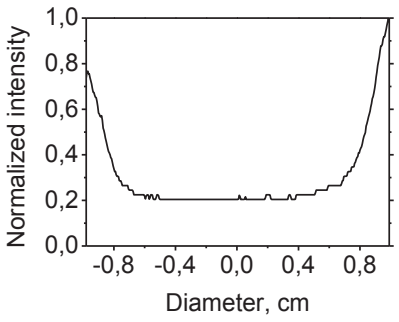	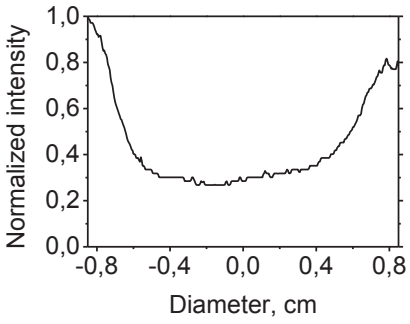

4.8. Results of LuAG and LuAG:Ce fibers testing for calorimetry applications.

4.8.1. Construction of the test beam setup

In order to test the grown undoped and Ce-doped LuAG fibers, 64 samples of 22 cm length and 2 mm diameter were embedded into a brass absorber (25 x 17 x 7 cm^3) [4]. Eight undoped LuAG fibers and part of the 56 LuAG:Ce fibers tested were taken from the fibers pulled from the melt in the frame of this Phd thesis work (Figure IV.37) and the rest of Ce-doped fibers were grown by Fibercryst. One end of fibers was optically coupled to a Ketek SiPM using standard optical grease whereas a LED-based light injection system was used to flash a reference signal into the opposite end of each

fiber, providing a system to monitor the channel response. The signals from the 8 x 8 array of SiPMs were readout with two PADE boards of 32 channels, allowing for an on-line data monitoring using a standard PC. An additional module made of a 3 x 3 matrix of BaF_2 crystals was positioned on the back of the fiber module to provide information on shower leakage. The whole module was installed in the T-1041 beam line at the Fermilab Test Beam Facility in Chicago (USA) and the performance of the module has been tested using electrons and pions in the 2-32 GeV energy range.

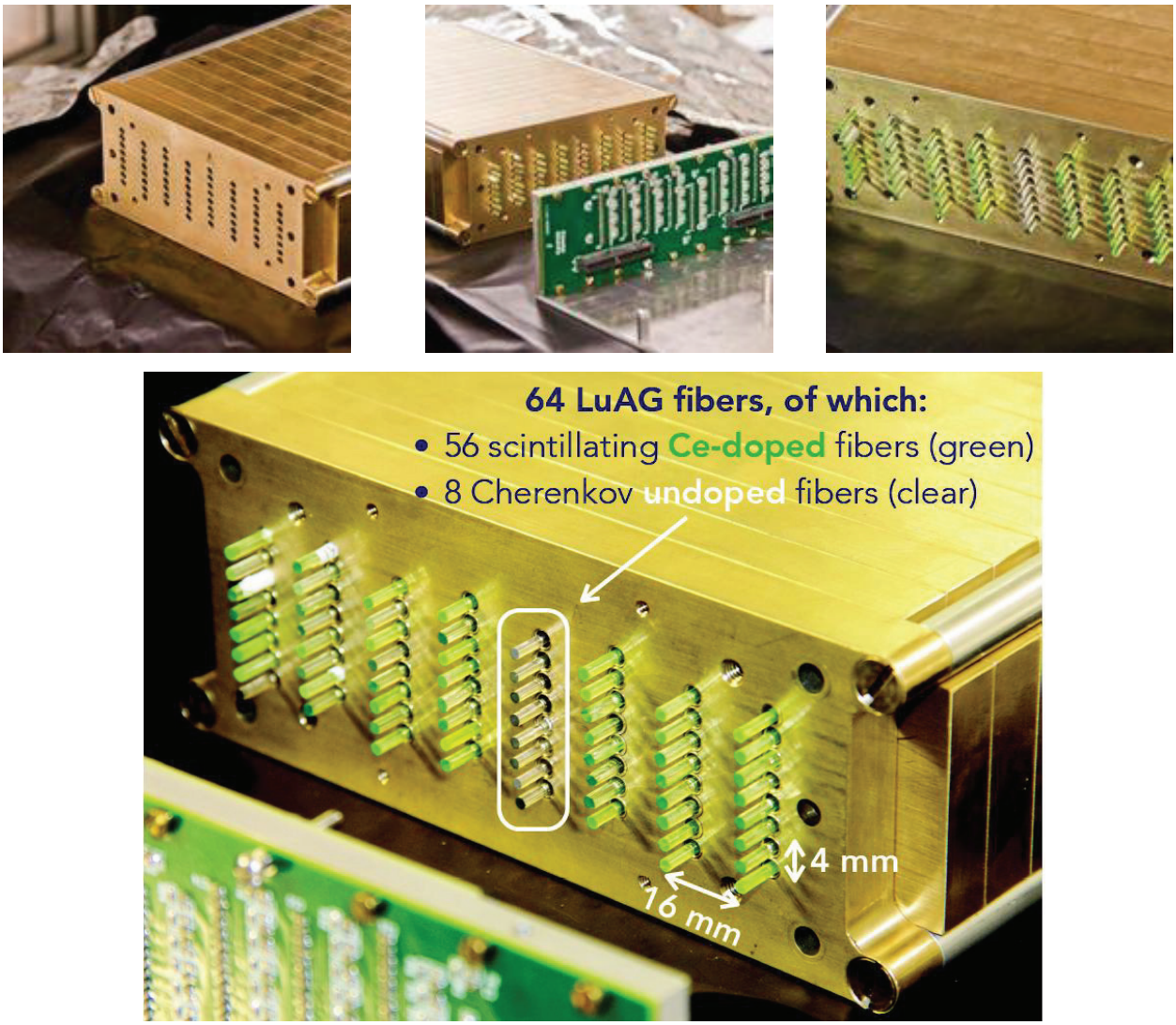

Figure IV.37. Picture of the calorimetric module, the fourth layer from the right contains the undoped LuAG fibers.

4.8.2. Cherenkov and scintillating fiber response.

The pulses obtained from all the channels were averaged and compared. The undoped fibers registering the Cherenkov signal had shown faster and narrower pulse shape comparing to the Ce-doped fibers registering the scintillation signal (Figure IV.38).

The response of the fibers on electrons and pions of energy between 2 – 32 GeV was linear in the range 2 – 8 GeV. At the higher energy range there was no significant deviation due to increasing of shower leakage (Figure IV.39).

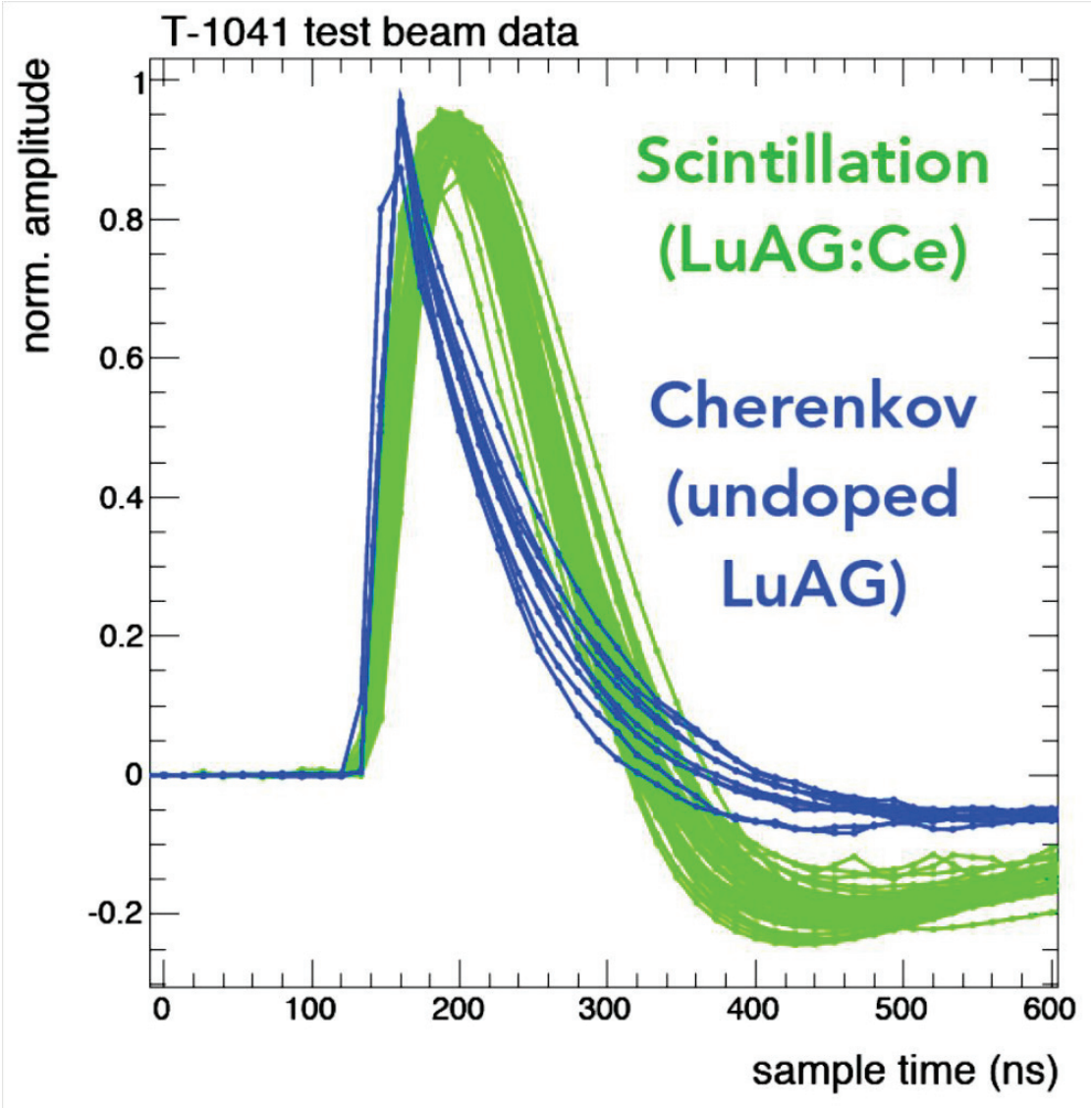

Figure IV.38 Average normalized pulse shapes of undoped LuAG (blue) and Cedoped LuAG (green) fibers.

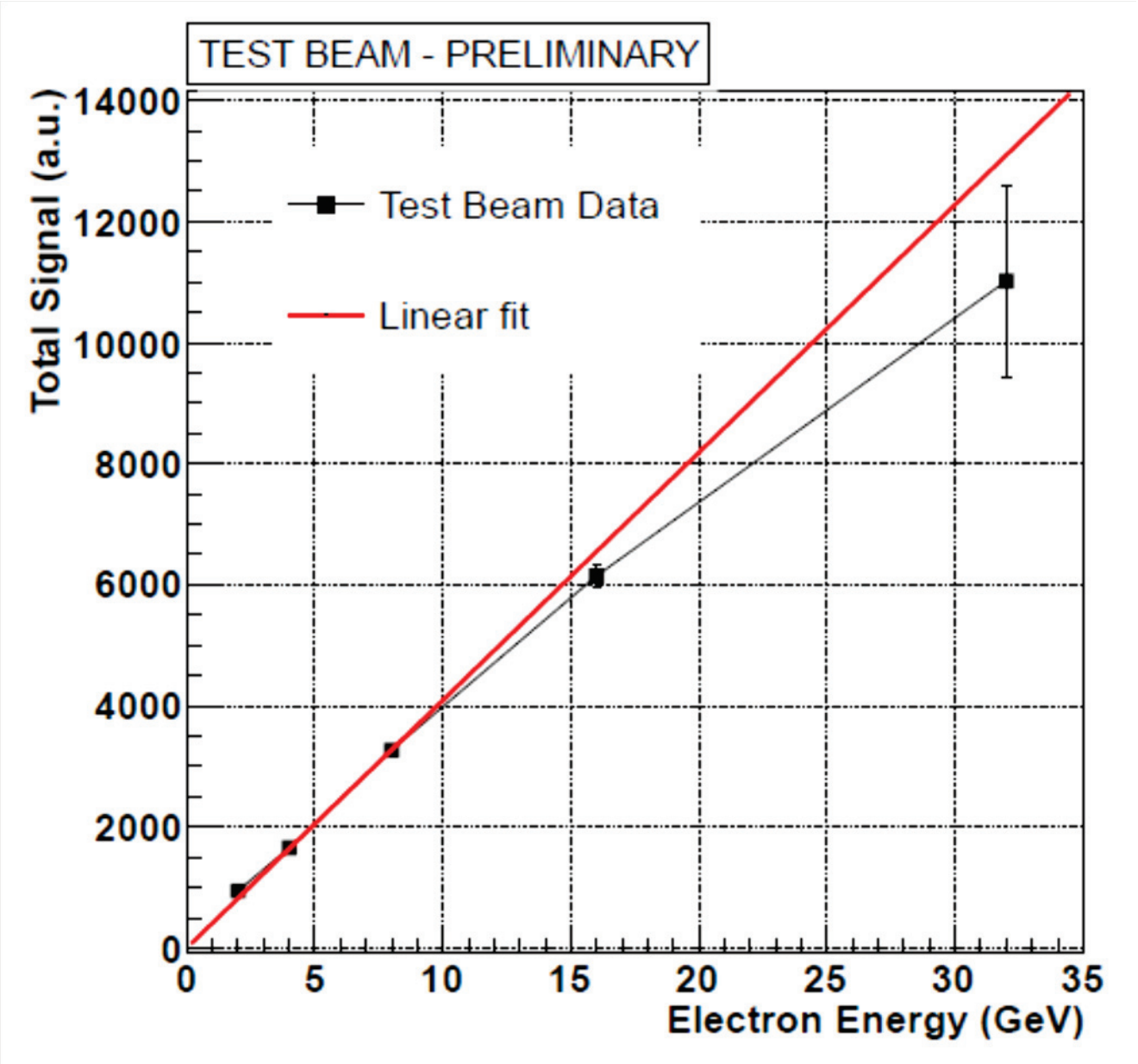

Figure IV.39. Position of electron peak reconstructed by summing up the signal of all the fibers as a function of beam energy. Deviation from linearity at high energies is due to the higher longitudinal shower leakage.

Summary

We have demonstrated that by the optimization of the pulling rate and Ce concentration of the LuAG single crystal fiber grown by μ-PD, significant improvement of the optical quality of the fibers can be achieved. Low Ce concentration (≤0.1at%) and low pulling rate (≤0.32mm/min) were identified as a good compromise to get a good surface quality and light propagation. Moreover high pulling rate (>0.3 mm/min) and high Ce concentration (>0.1at%) strongly affect the surface quality and increase the attenuation through the fiber. We have also grown Pr-doped LuAG and Ce-doped LuAG, Ce-doped YAG and mixed Ce-doped LuYAG fibers single crystal. The grown fibers are transparent without visible macroscopic defects such cracks. The optical attenuation of the scintillation light within the fiber is a critical parameter, since the scintillating signal has to propagate along all the fiber. The optical attenuation is connected to the crystal quality and surface roughness. The defects also strongly affect the fiber quality.

Chapter V: Results & Discussion:
Growth and characterization of $Y_3Al_{5-x}Ga_xO_{12}$:Ce mixed scintillation crystals.

The promising results regarding the improvement of activator distribution in fibers were shown in the previous section. $Y_3(Al_{1-x}Ga_x)_5O_{12}$:Ce crystals are the another example of mixed crystal formed by isovalent cation substitution. A series of crystals were grown in the whole Al/Ga substitution range. Some of crystals contain significant number of cracks, as one can see in Figure V.1. All the crystals were exposed to post growth annealing in O_2-containing atmosphere at 1500 ºC. Coloration weakened after this procedure, certifying, probably, the compensation of oxygen vacancies which was formed at crystal growth in inert atmosphere.

5.1. Structure and composition of $Y_3Al_{5-x}Ga_xO_{12}$:Ce solid solutions

$Y_3(Al_{1-x}Ga_x)_5O_{12}$:Ce system demonstrates a continuous series of solid solutions (Figure V.2). The lattice parameter smoothly increases with Ga content (Figure V.3). No visible deviation from Vegard's law was observed for YAG and YAGG, contrary to the results in [138]. Accordingly to XRD data, Ga fraction in crystals is 15.4, 36.6, and 66.2% at growth from melt with the Ga fractions 20, 40, 60%, correspondingly. Therefore, Al and Ga distribution coefficients are around 1. Besides this, Y^{3+} or trivalent lanthanide cation may occupy Al^{3+} or Ga^{3+} sites in garnet lattice (''antisite defects'') [122,139].

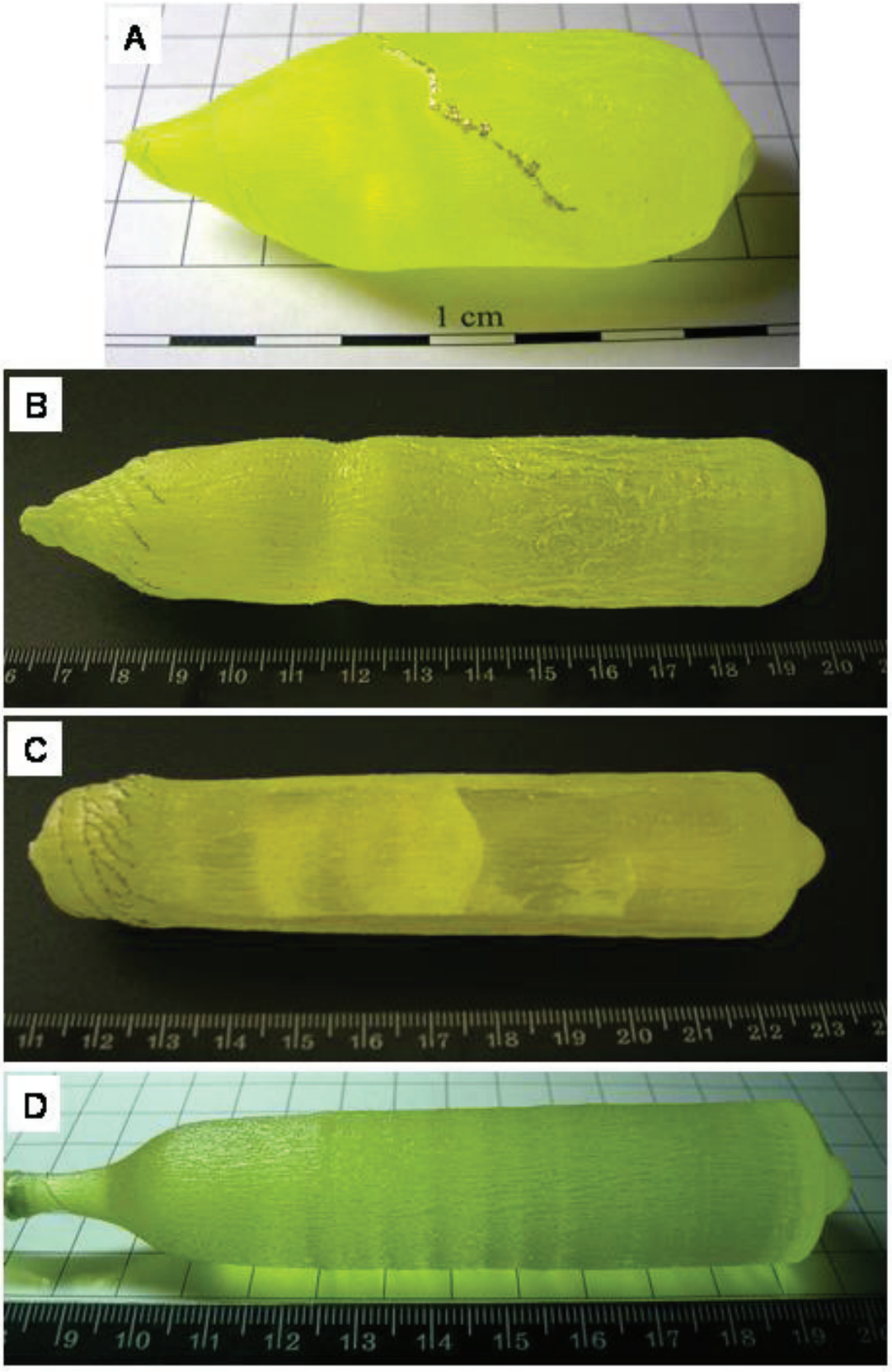

Figure V.1. As-grown YAG:Ce (A), YAGG:Ce (B,C), YGG:Ce (D) crystals.

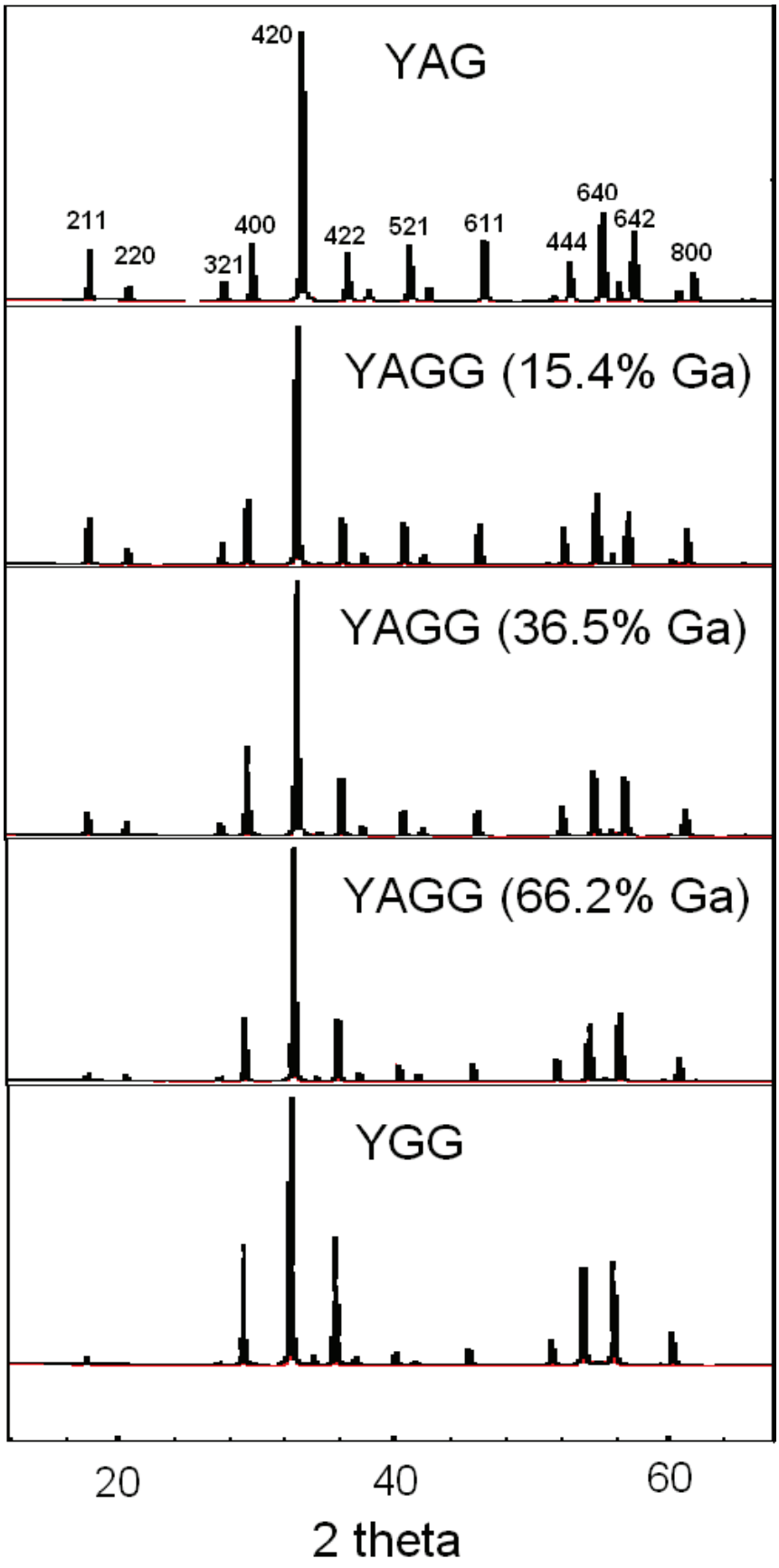

Figure V.2. XRD patterns of the crystals.

Basically, formation of antisite defects in rare-earth garnets is considered as a negative factor leading to deterioration of light yield and increase of slow component contribution in scintillation decay [140, 116]. Probability of this substitution increases at reduction of the difference between ionic radii of Al^{3+} (Ga^{3+}) on the one hand, and Y^{3+} or lanthanide on the other hand. It was shown [122] that in YGG, Y excess in crystal is formed due to Ga^{3+} substitution with Y^{3+} in octahedral positions. That is, real composition of crystal should be determined by the formulae $Y_3(Y_xGa_{2-x})Ga_3O_{12}$ [122,139].

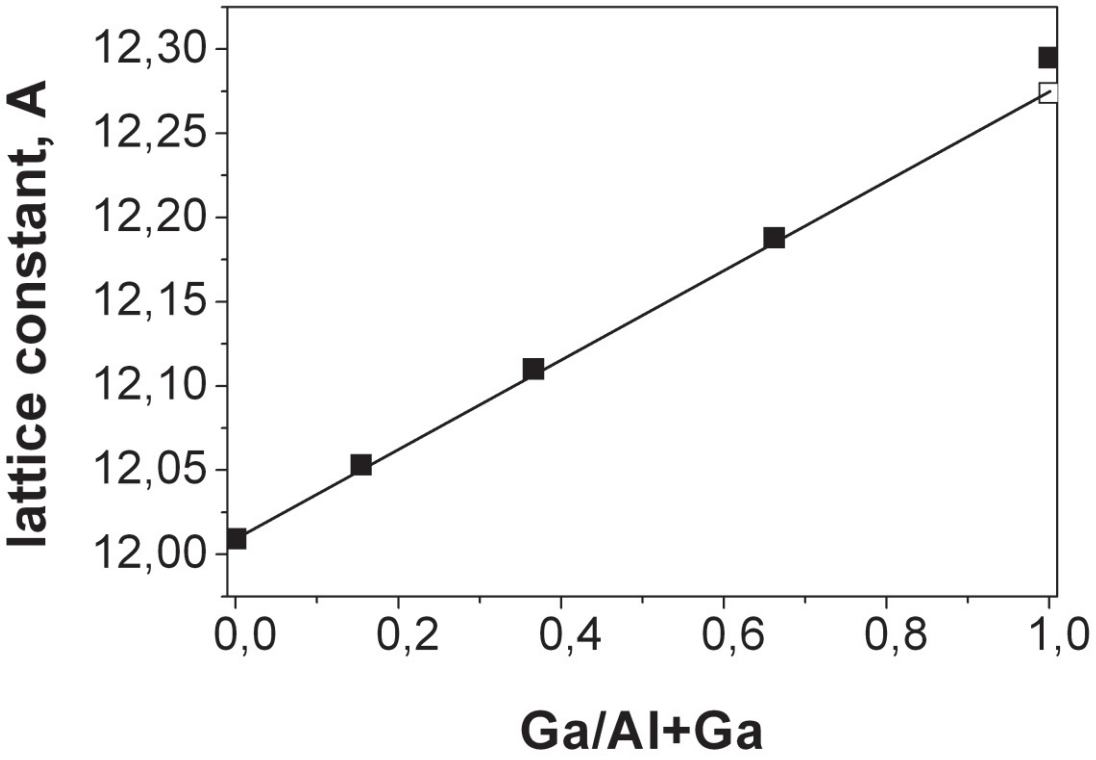

Figure V.3. Dependence of lattice constant vs. Ga fraction in $Y_3(Al_{1-x}Ga_x)_5O_{12}$:Ce crystals. Filled symbols correspond to experimental values, hollow symbol corresponds to the data taken from [122].

Lattice constant of stoichiometric YGG is 12.274 A˚, and it increases with x in case of $Y_3(Y_xGa_{2-x})Ga_3O_{12}$ substitution [122]. In accordance with these data, the 12.295

A˚ lattice constant value in the YGG crystal grown in the present work corresponds to x around 0.1, that is, 5% of Ga^{3+} in octahedral sites is substituted with Y^{3+}. However, this is a rough estimation, because the data in [122] were obtained on powders or crystals grown from solution. Additionally, in our case, crystals also contain large Ce^{3+} cations, which may increase the lattice constant. As a sequence, one can see the deviation of the experimental point for YGG from the Vegard's law in Figure V.2. Since no such deviation is observed in mixed crystals, it is reasonable to conclude that there is no noticeable quantity of antisite defects in YAG and YAGG.

ICP-AES data give the detailed picture of cation distribution in solid solutions. The ICP-AES and XRD data on Ga/Al + Ga ratio coincide within ~1% (see the Ga/Al + Ga columns in Table 6). Some increase in Y/(Al + Ga) ratio is observed with Ga content (Table 6). The Y/Y + Al + Ga ratio clearly increases from YAG to YGG confirming the increase of antisite defect quantity. However, only ~1% Y excess above the theoretical value (3/8 = 0.375) is obtained by ICP-AES in YGG.

Measurements of Al and Ga concentrations in different parts of crystals show fairly small deviations of Al/Ga ratio along the crystals indicating good homogeneity of the grown crystals. Ce segregation coefficient increases with Ga addition into the host. The obtained values indicate non-monotonous dependence of k_{eff} (Ce) vs. Ga content, however, much more experimental points is needed to make an unambiguous conclusion.

Table 6.Fractions of the host atoms in the YAGG:Ce crystals.

Melt composition	Measured concentrations (at.%)			Ga/(Al + Ga)		Y/(Y + Al + Ga)	k_{eff} (Ce)
	Y	Al	Ga	ICP-AES	XRD		
$Y_3Al_5O_{12}$:Ce							
Top	13.11	22.59	–	0	0	0.367	0.075
Bottom	13.52	23.47				0.365	
$Y_3(Al_{0.8}Ga_{0.2})_5O_{12}$:Ce							
Top	13.13	18.73	4.03	0.1771	0.154	0.366	0.074
Bottom	13.37	19.25	4.06	0.1742		0.364	
$Y_3(Al_{0.6}Ga_{0.4})_5O_{12}$:Ce							
Top	13.40	14.96	8.24	0.3550	0.366	0.368	0.095
Bottom	13.58	15.23	8.37	0.3546		0.367	
$Y_3(Al_{0.4}Ga_{0.6})_5O_{12}$:Ce							
Top	13.92	8.24	15.43	0.6519	0.662	0.370	0.133
Bottom	14.05	8.27	15.48	0.6518		0.372	
$Y_3Ga_5O_{12}$:Ce							
Top	14.74	–	23.48	1	1	0.386	0.166
Middle	14.82		23.79			0.384	
Bottom	14.87		23.74			0.385	

5.2. Scintillation and luminescence properties

Light yield of mixed crystals reaches 130% of the YAG:Ce value (Figure V.4) contrary to [122] where decrease of light output efficiency with Ga addition was observed. No yield is registered in YGG:Ce, the same result was reported for Ce-doped lutetium– and gadolinium–gallium garnets [18]. In addition, the trend of light yield vs. Ga fraction fairly coincides with the results on $Lu_3(Al_{1-x}Ga_x)_5O_{12}$:Ce presented in the

same publication – in both cases the maximal values are observed at x = 0.4. Increase of light yield magnitude in mixed crystals is an important practical result opening a room for further improvement of scintillation characteristics by optimization of host composition, activator concentration, and choice of other activators (e.g., Pr^{3+}) (Figure V.5).

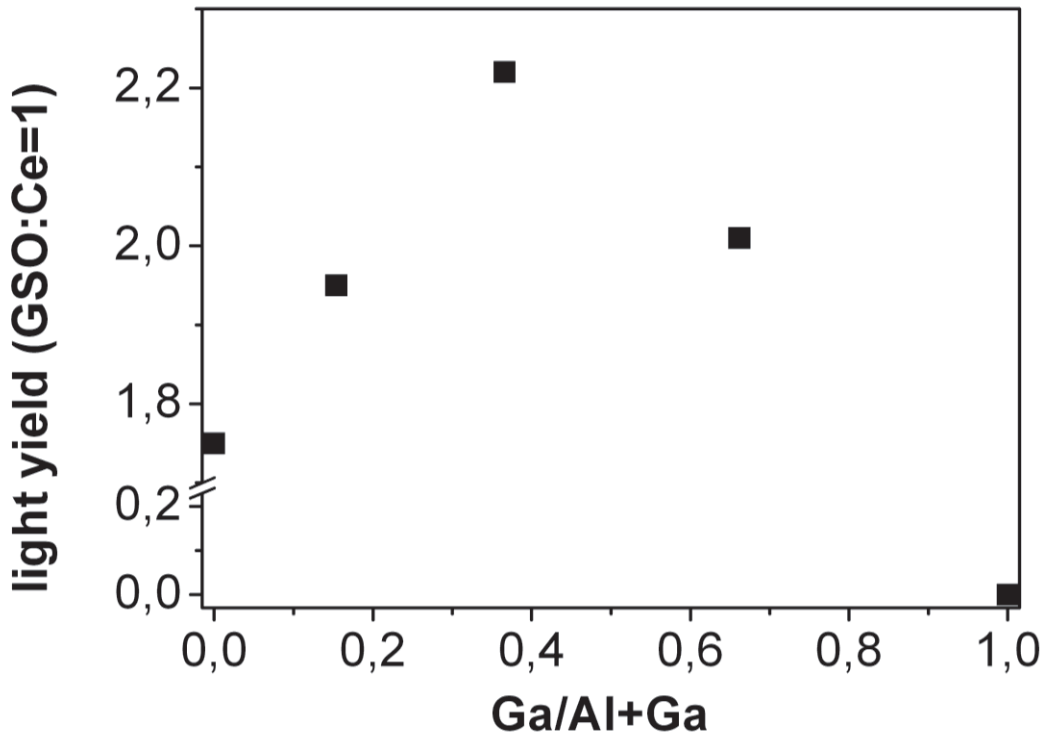

Figure V.4. Light yield in $Y_3(Al_{1-x}Ga_x)_5O_{12}$:Ce vs. Ga fraction

Mechanisms of the observed light yield improvement are evidently similar to those proposed for Al–Ga mixed Lu garnet crystals [141]. It was claimed there that light yield may increase with Ga^{3+} fraction due to the bandgap change (‘‘bandgap engineering’’), such that energy levels of shallow defects is no longer in the forbidden gap where electrons can be trapped. The principles of ‘‘bandgap engineering’’ may be valid for yttrium garnets with similar electronic structure. By the analogy, further Ga^{3+} addition leads to the situation when Ce^{3+} 5d levels are buried inside the conductance band that results in absence of Ce^{3+} luminescence in both $Lu_3Ga_5O_{12}$:Ce and

$Y_3Ga_5O_{12}$:Ce. Considering the behavior of light yield in solid solutions, it's worth to note also the work [142] where the increase in light yield in LuYAP crystals at Y/Y + Lu = 0.3–0.7 was attributed to creation of atomic clusters enriched by one of the components of mixed crystal. As a sequence, modulation of crystal potential by the boundaries of such clusters may decrease the diffusion length of secondary electrons and holes and promote the energy transfer efficiency from the crystal lattice to activator ions. Deeper study of short-range ordering in crystals and luminescence mechanisms in them should check the eligibility of the latter mechanism in Al/Ga substituted garnets and other mixed scintillators.

X-ray luminescence spectra of some crystals are presented in Figure V.5. The curves are obtained in the same conditions, and one may compare relative intensities of the peaks. Luminescence band shifts by ~50 nm at addition of 66% of Ga into YAG:Ce is in agreement with [74, 120]. At the same time, only host weak luminescence is observed in YGG:Ce.

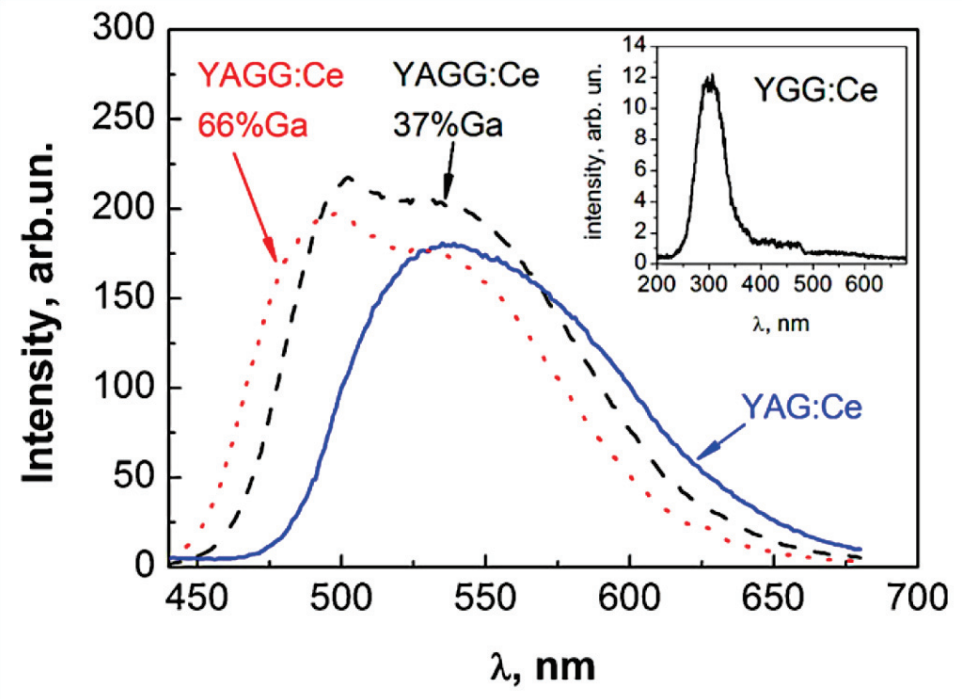

Figure V.5. X-ray excited luminescence spectra of Ce-doped YAG, YGG, and YAGG crystals.

Summary

A continuous series of solid solutions is formed in $Y_3(Al_{1-x}Ga_x)O_{12}$ system. Lattice constant monotonously increases with Ga fraction in crystals. Deviation of lattice constant value from Vegard's' law, and increase of the measured Y/Y + Al + Ga ratio evidences existence of ~1% of antisite defects in YGG formed by substitution of Ga^{3+} by Y^{3+} in octahedral positions. At the same time, for the rest of crystals this ratio does not exceed the theoretical value of 3/8 = 0.375. Light output of mixed crystals reaches 130% of the YAG:Ce value at x = 0.4. Ce^{3+} luminescence band is blue-shifted by ~50 mm at introduction of 66% of Ga^{3+} into YAG:Ce, and only host weak luminescence is observed in YGG:Ce.

Conclusion and future works

In this PhD thesis manuscript, the background, motivation, theory, methodology, and results of this research have been presented and discussed. There is no end in pursuing high quality performed scintillating materials and the development of new detection application based on material design. Up to now, four directions can be forward:

Elaboration (invention) of new host materials, including new chemical composition

1) Improvement of the quality and the performance of the existent materials especially the oxides family
2) Development of the growth process allowing the obtainment of high quality single crystals
3) Development of the numerical simulation of the relevant phenomena, not currently available in any industrial software. In our case, this concerns the participating (semi-transparency) of garnet scintillating crystals, dopant and impurity chemical segregation (leading to bubbles and interface instability). A special research effort will be on the simulation of dopant segregation (here Ce), which is a completely new field in crystal growth numerical modelling.

In the frame of this thesis, we have grown scintillators crystals under steady state conditions and Ce^{3+} dopant was used as activator element. In addition, micro-pulling down technique (μ-PD) was used to grow undoped and Ce and Pr doped scintillator crystal fibers to develop new dual-readout calorimeter design based on fiber-shaped detectors.

By micro-pulling down technique we have successfully grown LGSO mixed crystal for the first time. My studies were the first to systematically show the effect of Ce concentration and the Lu/Gd ratio on the structure stability and scintillating performance on LGSO shaped mixed crystal grown by μ-PD technique. A choice of

host composition and activator concentration in LGSO:Ce crystals has to be aimed at minimization of Ce^{3+} content in CeO_6 polyhedra and energy transfer between Ce_1 and Ce_2 luminescent centers. The Gd atoms preferably occupy sevenfold site in LGSO with C2/c symmetry. In spite of the low melting temperature, in comparison to YAG and LuAG fibers, it was quite difficult to stabilize the growth and obtain long LGSO:Ce (length =40 cm) long fibers. Though all the crystals contain single monoclinic C2/c phase, only the first parts (1-4 cm in length) of them are transparent and contain no visible cracks and few inclusions. The difficulties related to the control of the growth process can be related to the non congruent melt behavior of the LGSO solid solution, possible melt decomposition because of SiO_2 volatility and also to the strong segregation of Ce^{3+} dopant. So it compromises the chance to develop calorimeter based on LGSO single crystal fibers design. But the scintillation performance (light yield) and the afterglow in LGSO:Ce shaped crystals grown in the frame of thesis are better than the bulk crystal grown by Czochralski technique which is encouraging for future work.

We have demonstrated that by the optimization of the pulling rate and Ce concentration of the LuAG single crystal fiber grown by μ-PD, significant improvement of the optical quality of the fibers can be achieved. Low Ce concentration (≤0.1 at.%) and low pulling rate (≤0.3mm/min) were identified as a good compromise to get a good surface quality and light propagation. Moreover high pulling rate (>03mm/min) and high Ce concentration (>0.1 at.%) strongly affect the surface quality and increase the attenuation through the fiber. Photoluminescence and scintillation experiments showed effective attenuation lengths in different LuAG fibers. Surface diffusion and bubbles are favoring the light escape through lateral faces. So, growing Ce-doped LuAG fibers with low pulling rate is essential to pull good optical quality fibers and good light propagation. The results concerning Pr-LuAG are unsatisfactory. Even the Pr-grown fibers present a good qualitative visible quality, but the attenuation results are not good compared to the Ce-doped LuAG. YAG:Ce is mechanically very stable, inexpensive, and easy to grow, we succeeded to pull transparent single crystal fibers to look for the best composition to develop the concept of an inorganic scintillating fiber and SiPM

based particle tracking calorimeter. The obtained attenuation results are encouraging and it can be also a good way to use Ce-doped YAG fiber for calorimeter. The research is still under progress and more complementary experimental data are needed. The test beam results obtained on a sampling calorimetric module made of brass filled with undoped and Ce-doped LuAG crystal fibers has been done in the frame of collaboration with CERN and Fermi lab in USA. We have shown the first proof of fiber concept for the implementation of this technology in real calorimeters and address the different challenges related to high energy physics.We did a great effort to improve the light propagation in undoped and Ce-doped LuAG fiber, the next step will be the study of the radiation hardness of garnet crystal fibers such the degradation of their optical properties which is limited to about 10% after an integrated exposure of 1 MGy.

This work was also focused at two Ce-doped mixed systems with the garnet structure – $(Lu_{1-x}Y_x)_3Al_5O_{12}$ and $Y_3(Al_{1-x}Ga_x)O_{12}$. Following the cathodoluminescence data achieved in $(Lu_{1-x}Y_x)_3Al_5O_{12}$ fibers samples this compound should be grownwith lower then 350 μm/min pulling rate to obtain smoother Ce radial distribution. The study of $Y_3(Al_{1-x}Ga_x)O_{12}$ system as a function of aluminum substitution by gallium confirms the existence of continuous solid solution range between YAG and YGG. The set of crystals were grown from the melt by Czochralski technique, and their qualities depend on the starting Ga concentration in the melt (initial charge). Light output of mixed crystal reaches 130% of the YAG:Ce value at x=0.4. The obtained results increase the attraction of mixed garnets for scintillator applications and promote deeper study of scintillating crystals based on solid solutions.

References

[1] CERN/LHCC 97-33, CMS TDR 4/15 December 1997
Internet source: https://cds.cern.ch/record/349375/files/ECAL_TDR.pdf

[2] Erni W. et al. Technical Design Report for PANDA Electromagnetic Calorimeter (EMC) //arXiv preprint arXiv:0810.1216. – 2008.

[3] Chatrchyan S. et al. Observation on a new boson at a mass of 125 GeV with the CMS experiment at the LHC //Physics Letters B. – 2012. – I. 716. – № 1. P. 30-61.

[4] Lucchini M. et al. Test beam results with LuAG fibers for next-generation calorimeters //Journal of Instrumentation. – 2013. – I. 8. – №. 10. – P. P10017.

[5] Behnke T. et al. The International Linear Collider Technical Design Report-Volume 4: Detectors //arXiv preprint arXiv:1306.6329. – 2013.

[6] Pauwels K. et al. Single crystalline LuAG fibers for homogeneous dual-readout calorimeters //Journal of Instrumentation. – 2013. – I. 8. – №. 09. – P. P09019.

[7] Xu X. et al. Ce-doped LuAG single-crystal fibers grown from the melt for high-energy physics //Acta Materialia. – 2014. – I. 67. – P. 232-238.

[8] Claudia Kuntner DISSERTATION Evaluation of New Inorganic Scintillators for Application in a Prototype Small Animal PET Scanner May 2003

[9] Moszyński M. et al. Energy resolution and non-proportionality of scintillation detectors–new observations //Radiation Measurements. – 2010. – I. 45. – №. 3. – P. 372-376.

[10] Van Eijk C. W. E. Inorganic scintillators in medical imaging// Physics in Medicine and Biology. – 2002. – V. 47. – P. 85-106

[11] Hitomi K. et al. Evaluation of LGSO scintillators with Si PIN photodiodes //Nuclear Science Symposium Conference Record, 2007. NSS'07. IEEE. – IEEE, 2007. – I. 3. – P. 2033-2035.

[12] Shimizu S. et al. Characteristics of LuGdSiO:Ce (LGSO) for APD-based PET detector //Nuclear Science, IEEE Transactions on. – 2010. – I. 57. – №. 1. – P. 55-62.

[13] Tonami H. et al. Sophisticated 32× 32× 4-layer DOI detector for high resolution PEM scanner //Nuclear Science Symposium Conference Record, 2007. NSS'07. IEEE. – IEEE, 2007. – I. 5. – P. 3803-3807.

[14] Pepin C. M. et al. Physical characterization of the LabPET™ LGSO and LYSO scintillators //Nuclear Science Symposium Conference Record, 2007. NSS'07. IEEE. – IEEE, 2007. – I. 3. – P. 2292-2295.

[15] Chen J. et al. Large size LYSO crystals for future high energy physics experiments //Nuclear Science Symposium Conference Record, 2004 IEEE. – IEEE, 2004. – I. 1. – P. 117-125.

[16] Petrosyan A.G et al. Growth and light yield performance of dense Ce^{3+}-doped $(Lu,Y)AlO_3$ solid solution crystals// J. Cryst. Growth. – 2000. – I. 211. – P. 252–256

[17] Totsuka D. et al. Crystal growth and characterization of Tm doped mixed rare-earth aluminum perovskite //Materials Research Bulletin. – 2012. – I. 47. – №. 4. – P. 993-997.

[18] Kamada K. et al. Composition engineering in cerium-doped $(Lu,Gd)_3(Ga,Al)_5O_{12}$ single-crystal scintillators //Crystal Growth & Design. – 2011. – I. 11. – №. 10. – P. 4484-4490.

[19] Sidletskiy O. et al. Impact of Lu/Gd ratio and activator concentration on structure andscintillation properties of LGSO:Ce crystals// Journal of Crystal Growth. – 2010. - V. 312, № 4. – P.601-606.

[20] Kamada K. et al. Basic experiments on radiation imaging by using $Pr:Lu_3Al_5O_{12}$ (LuAG) small crystalline pixels with various reflector //2007 IEEE Nuclear Science Symposium Conference Record. – 2007. – T. 2. – P. 1417-1420.

[21] Braem A. et al. Novel design of a parallax free Compton enhanced PET scanner //Nuclear Instruments and Methods in Physics Research Section A: Accelerators, Spectrometers, Detectors and Associated Equipment. – 2004. – I. 525. – №. 1. – P. 268-274.

[22] Lecoq P. et al .New crystal technologies for novel calorimeter concepts //Journal of Physics: Conference Series. – IOP Publishing, 2009. – I. 160. – №. 1. – P. 012016.

[23] Mavromanolakis G. et al. Studies on sampling and homogeneous dual readout calorimetry with meta-crystals //Journal of Instrumentation. – 2011. – I. 6. – №. 10. – P. P10012.

[24] Verneuil A. Production artificielle du rubis par fusion //Comptes Rendus. – 1902. – V. 135. – P. 791-794.

[25] Chudoba K. Dichte und Struktur des Zirkons II //Zeitschrift für Kristallographie-Crystalline Materials. – 1937. – I. 97. – №. 1. – P. 252-262.

[26] Keck P. H. et al. Crystallization of silicon from a floating liquid zone// Physical. Review. – 1953. – V. 89. – P. 1297-1297

[27] Czochralski J. Ein neues verfahren zur messung der kristallisationsgeschwindigkeit der metalle // Z. Physik.Chem. - 1918. – V. 92. - P. 219-221.

[28] Kyropoulos S. A method of producing large crystals //Zeitschrift fuer anorganische und allgemeine chemie. - 1926. – V. 308. - P. 154

[29] Petrosyan A. G. et al. Crystal growth of laser oxides in the vertical Bridgman configuration //Journal of crystal growth. – 1994. – I. 139. – №. 3. – P. 372-392.

[30] Petrosyan A. G. et al. The Lu_2O_3–Al_2O_3 system: Relationships for equilibrium-phase and supercooled states //Journal of crystal growth. – 2006. – I. 293. – №. 1. – P. 74-77.

[31] Bridgman P.W. Certain physical properties of single crystals of tungsten, antimony, bismuth, tellurium, cadmium, zinc and tin // Proceedings of the American Academy of Arts and Sciences. – 1925. – V. 60, № 6. - P. 305-383.

[32] Pastor R.C. et al. Crystal growth above 2200°C by Verneuil method // Material Research Bulletin. – 1966. – V. 1, № 4. – P. 275-282

[33] Chase J. D. et al. Plasma-growth rutile single crystals and their distinctive properties // Journal of Crystal Growth. – 1969. – V. 5, № 4. – P. 294-298.

[34] Falckenberg R. Growth of stoichiometric Mg-Al spinel single crystals by a modified Verneuil technique // Journal of Crystal Growth. – 1972. – V. 13-14. – P. 723-725.

[35] Demianets L. N. et al. Verneuil technique for crystal growth of high temperature superconducting Bi-Sr-Ca-Cu-oxides // Solid State Ionics. – 1990. – V. 40-41, № 2. – P. 836-839.

[36] Ueltzen M. et al. Crystal growth of barium cuprate by Verneuil's Technique // Crystal Research Technology. – 1993. - V. 28, № 7. – P. 69-72.

[37] Takaki S. et al. A new induction heating floating-zone refining furnace for ultrapurification of iron-chromium alloys //Journal de Physique IV France. – 1995. – V. 5, № 7. – P. 159-164.

[38] Souptel D. et al. Vertical optical floating zone furnace: Principles of irradiation profile formation // Journal of Crystal Growth. – 2007. – V. 300, № 2. – P. 538-550.

[39] Takekawa S. et al. Single crystal growth of the superconductor $Bi_2(Bi_{0.2}Sr_{1.8}Ca)Cu_2O_8$ // Journal of Crystal Growth. – 1988. – V. 92. – P. 687-690.

[40] Kamada K. et al. 2inch diameter single crystal growth and scintillation properties of Ce: Gd_3Al_2 Ga_3O_{12} //Journal of Crystal Growth. – 2012. – I. 352. – №. 1. – P. 88-90.

[41] Sugiyama M. et al. Crystal growth and luminescence properties of Pr-doped $LuLiF_4$ single crystal //Radiation Measurements. – 2013. – I. 55. – P. 112-115.

[42] Kuwano Y. et al. Crystal growth and properties of $(Lu, Y)_3Al_5O_{12}$ //Journal of crystal growth. – 2004. – I. 260. – №. 1. – P. 159-165.

[43] Sidletskiy O. et al. Structure–Property Correlations in a Ce-Doped $(Lu,Gd)_2SiO_5$:Ce Scintillator //Crystal Growth & Design. – 2012. – I. 12. – №. 9. – P. 4411-4416.

[44] Simura R., Yoshikawa A., Uda S. The radial distribution of dopant (Cr, Nd, Yb, or Ce) in yttrium aluminum garnet ($Y_3Al_5O_{12}$) single crystals grown by the micro-pulling-down method //Journal of Crystal Growth. – 2009. – I. 311. – №. 23. – P. 4763-4769.

[45] Sugiyama M. et al. Crystal growth and scintillation properties of Nd-doped $Lu_3Al_5O_{12}$ single crystals with different Nd concentrations //Optical Materials. – 2011. – I. 33. – №. 6. – P. 905-908.

[46] Yoshikawa A. et al. Challenge and study for developing of novel single crystalline optical materials using micro-pulling-down method //Optical Materials. – 2007. – I. 30. – №. 1. – P. 6-10

[47] Fukuda T. et al. Shaped crystals: growth by micro-pulling-down technique. – Springer, 2007. – I. 8.

[48] Rudolph P. et al. Fiber crystal growth from the melt //Crystal Research and Technology. – 1999. – I. 34. – №. 1. – P. 3-40.

[49] Sangla D. et al. Yb-doped $Lu_3Al_5O_{12}$ fibers single crystals grown under stationary stable state for laser application //Journal of Crystal Growth. – 2009. – I. 312. – №. 1. – P. 125-130.

[50] Batarin V. A. et al. Comparison of radiation damage in lead tungstate crystals under pion and gamma irradiation //Nuclear Instruments and Methods in Physics Research Section A: Accelerators, Spectrometers, Detectors and Associated Equipment. – 2004. – I. 530. – №. 3. – P. 286-292.

[51] Lecoq P. New crystal technologies for novel calorimeter concepts //Journal of Physics: Conference Series. – IOP Publishing, 2009. – I. 160. – №. 1. – P. 012016.

[52] Hautefeuille B. et al. Shaped crystal growth of Ce^{3+}-doped $Lu_{2(1-x)}Y_{2x}SiO_5$ oxyorthosilicate for scintillator applications by pulling-down technique //Journal of crystal growth. – 2006. – I. 289. – №. 1. – P. 172-177.

[53] Fukuda T. et al. Fiber crystal growth from the melt. – Springer, 2004. – I. 6.

[54] Maier D. et al. Dopant segregations in oxide single-crystal fibers grown by the micro-pulling-down method //Optical Materials. – 2007. – I. 30. – №. 1. – P. 11-14.

[55] Chani V. et al. Evaporation induced diameter control in fiber crystal growth by micro-pulling-down technique: $Bi_4Ge_3O_{12}$ //Crystal Research and Technology. – 2006. – I. 41. – №. 10. – P. 972-978.

[56] Koroleva T. S. et al. Ce-doped $Li_6Ln(BO_3)_3$(Ln= Y,Gd) Single crystals fibers grown by micro-pulling down method and luminescence properties //Optical Materials. – 2013. – I. 35. – №. 5. – P. 868-874.

[57] Shannon R. D. Revised effective ionic radii and systematic studies of interatomic distances in halides and chalcogenides //Acta Crystallographica Section A: Crystal Physics, Diffraction, Theoretical and General Crystallography. – 1976. – I. 32. – №. 5. – P. 751-767.

[58] Melcher C. L. et al. A promising new scintillator: cerium-doped lutetium oxyorthosilicate // Nuclear Instruments and Methods in Physics Research Section A. – 1992. – V. 314. – P. 212-214.

[59] Melcher C. L. et al. Crystal growth and scintillation properties of the rare earth oxyorthosilicates // International Conference on Inorganic Scintillators and Their Applications (SCINT 95). –Delft, The Netherlands, August 28 - September 1, 1995: book of abstracts. –P. 309.

[60] Takagi K. et al. Cerium-activated Gd_2SiO_5 single crystal scintillator // Applied Physics Letters. – 1983. – V. 42. – P. 43-45.

[61] Balcerzyk M. et al. YSO, LSO, GSO and LGSO. A study of energy resolution and nonproportionality //Nuclear Science, IEEE Transactions on. – 2000. – V. 47. – №. 4. – P. 1319-1323.

[62] Moszynski M. et al. Large size LSO:Ce and YSO:Ce scintillators for 50 MeV range γ-ray detector //Nuclear Science, IEEE Transactions on. – 2000. – V. 47. – №. 4. – P. 1324-1328.

[63] Felsche J. Rare earth silicates with the apatite structure // Journalof Solid State Chemistry. – 1972. – V. 5, № 2. – P. 266-275.

[64] Felsche J. The crystal chemistry of rare-earth silicates // Structure and Bonding. – 1973. - V. 13. – P. 99-197.

[65] Felsche J. et al. The polymorphs of the rare-earth pyrosilicates $RE_2Si_2O_7$ [RE: La, Ce, Pr, Nd, Sm] // Journal of the Less CommonMetals. – 1970. – V. 18. – P. 131-137

[66] Cooke D. W. et al. Crystal growth and optical characterization of cerium-doped $Lu_{1.8}Y_{0.2}SiO_5$ // Journal of Applied Physics. – 2000. – V. 88. – P. 7360-7362.

[67] Pat. 6921901 B1 USA, G01T 1/202, C09K 11/08. Lutetium yttrium orthosilicate single crystal scintillator detector / B. H. T. Chai, Y. Ji. – Appl. № 10/623226; filed 18.07.2003; date of patent 26.07.2005.

[68] Bondar V. et al. Optico-luminescent properties and mechanical strength of G(Y)SO:Ce crystals //International Conference on Inorganic Scintillators and Their Applications (SCINT 2005). – Alushta, Ukraine, September 19-23, 2005: book of abstracts. – P. 98-100.

[69] Jie M. et al. Crystal growth and optical properties of $Gd_{1.99-x}Y_xCe_{0.01}SiO_5$ single crystals // Journal of Crystal Growth. – 2005. – V. 277. – P. 175-180

[70] Pat. 5264154 USA, C09K 11/79. Single crystal scintillator / S. Akiyama, H. Ishibashi, T. Utsu, C. L. Melcher, J. S. Schweitzer. – Appl. № 31051; filed11.03.1993; date of patent 23.11.1993.

[71] Loutts G. B. et al. Czochralski growth and characterization of $(Lu_{1-x}Gd_x)_2SiO_5$ single crystals for scintillators // Journal of Crystal Growth. – 1997. – V. 174. – P. 331-336.

[72] Yoshikawa A. et al. Czochralski Growth and Properties of Scintillating Crystals //Acta Physica Polonica, A. – 2013. – V. 124. – №. 2.

[73] Patent US 7,132,060 /Zagumennyi A. I. et al. //PST Filed: Mar. – 2004. – V. 12.

[74] Kobayashi M. et al. Radiation hardness of cerium-doped gadolinium silicate Gd_2SiO_5:Ce against high energy protons, fast and thermal neutrons //Nuclear Instruments and Methods in Physics Research Section A: Accelerators, Spectrometers, Detectors and Associated Equipment. – 1993. – I. 330. – №. 1. – P. 115-120.

[75] Kobayashi M. et al. Excellent radiation-resistivity of cerium-doped gadolinium silicate scintillators //Nuclear Instruments and Methods in Physics Research Section B: Beam Interactions with Materials and Atoms. – 1991. – I. 61. – №. 4. – P. 491-496.

[76] Lee W. G. et al. Growth and Characteristics of Gd_2SiO_5 Crystal Doped Ce^{3+} //JOURNAL OF NUCLEAR SCIENCE AND TECHNOLOGY. – 2008. – P. 572-574.

[77] Meijerink A. et al. Photostimulated luminescence and thermally stimulated luminescence of Y_2SiO_5-Ce, Sm //Journal of Physics D: Applied Physics. – 1991. – Т. 24. – №. 6. – P. 997.

[78] Sidletskiy O. et al. Gadolinium pyrosilicate single crystals for gamma ray and thermal neutron monitoring //Radiation Measurements. – 2010. – I. 45. – №. 3. – P. 365-368.

[79] Melcher C. L. et al. Advances in the scintillation performance of LSO:Ce single crystals //Nuclear Science, IEEE Transactions on. – 2003. – I. 50. – №. 4. – P. 762-766.

[80] Melcher C. L. Scintillation crystals for PET //Journal of nuclear medicine: official publication, Society of Nuclear Medicine. – 2000. – I. 41. – №. 6. – P. 1051-1055.

[81] Blahuta S. et al. Evidence and Consequences of Ce in LYSO: Ce, Ca and LYSO: Ce, Mg Single Crystals for Medical Imaging Applications. – 2013. - VOL. 60. - P.3134-3141

[82] Spurrier M. A. et al. The effect of co-doping on the growth stability and scintillation properties of lutetium oxyorthosilicate //Journal of Crystal Growth. – 2008. – I. 310. – №. 7. – P. 2110-2114.

[83] Melcher C. L. et al. Cerium-doped lutetium oxyorthosilicate: a fast, efficient new scintillator //Nuclear Science, IEEE Transactions on. – 1992. – I. 39. – №. 4. – P. 502-505.

[84] Dorenbos P. et al. Afterglow and thermoluminescence properties of Lu_2SiO_5:Ce scintillation crystals //Journal of Physics: Condensed Matter. – 1994. – I. 6. – №. 22. – P. 4167.

[85] Moszynski M. et al. Energy resolution of LGSO scintillators //Nuclear Science Symposium Conference Record, 2006. IEEE. – IEEE, 2006. – I. 3. – P. 1493-1499.

[86] Patent US 7297954 / K. Kurashige, H. Ishibashi, T. Usui, S. Shimizu, N. Shimura //PST Filed: May. – 2006

[87] Patent US 7618491 /Y. Kurata, N. Shimura, T. Usui, K. Kurashige // PST Filed: Jun. – 2005

[88] Patent 5,264,154 /S. Akiyama, H.Ishibashi, T.Utsu, and C.L.Melcher, U.S. //PST Filed: – 1999

[89] Toropov N. A. Diagrams of silicate systems : A Handbook. - Science , Leningrad fin -tion , 1969 - Volume 1

[90] Melcher C. L. et al Proceedings of the International Conference on Inorganic Scintillators and Their Applications (SCINT_95), Delft University of Technology, The Netherlands, August 28–September 1, 1995, P. 309

[91] Sidletskiy O. T. et al. Growth of LGSO:Ce crystals by the Czochralski method //Crystallography Reports. – 2009. – I. 54. – №. 7. – P. 1256-1260.

[92] Kuwano Y. et al. Crystal growth and properties of $(Lu,Y)_3Al_5O_{12}$ //Journal of crystal growth. – 2004. – I. 260. – №. 1. – P. 159-165.

[93] Glowacki M. et al. Growth conditions, structure, Raman characterization and optical properties of Sm-doped $(Lu_xGd_{1-x})_2SiO_5$ single crystals grown by the Czochralski method //Journal of solid state chemistry. – 2012. – I. 186. – P. 268-277.

[94] Patent US 6,278,832 / A.I. Zagumennyi, Yu. D. Zavartsev, P.A. Studenikin,// PST Filed: – 2001.

[95] Yu. D. Zavartsev et al. In: Proceedings of the fourth International Workshop on Crystal Growth Technology, Beatenderg, Switzerland: - 2008. - P. 85

[96] O. Sidletskiy, Scintillation crystals based on solid solutions of orthosilicates// Functional materials. – 2010. - I.17. - No.4. – P. 414

[97] Yang, K et. Al// IEEE Trans. Nucl. Sci. – 2011. - I.58. - №3. - P.1394−1399

[98] Papagelis K. et al. High Pressure Raman Study of $Lu_3Al_5O_{12}$ //Physica status solidi (b). – 1999. – I. 211. – №. 1. – P. 301-307.

[99] Yamaguchi O. et al. Formation of alkoxy-derived yttrium aluminium oxides //Journal of materials science. – 1992. – I. 27. – №. 5. – P. 1261-1264.

[100] Wu P. et al. Coupled thermodynamic-phase diagram assessment of the rare earth oxide-aluminium oxide binary systems //Journal of alloys and compounds. – 1992. – I. 179. – №. 1. – P. 259-287.

[101] Roth R. S. Phase Equilibria Diagrams: Phase Diagrams for Ceramics, //The American Ceramic Society, Westville, OH. – 1995. - V.11 - P. 107

[102] Alshourbagy M. et al. Optical and scintillation properties of Ce^{3+} doped $YAlO_3$ crystal fibers grown by μ-pulling down technique //Journal of crystal growth. – 2007. – I. 303. – №. 2. – P. 500-505.

[103] Derdzyan M. V. et al. Radiation hardness of LuAG:Ce and LuAG:Pr scintillator crystals //Journal of Crystal Growth. – 2012. – I. 361. – P. 212-216.

[104] Dujardin C. et al. LuAG:Ce fibers for high energy calorimetry //Journal of Applied Physics. – 2010. – I. 108. – №. 1. – P. 013510.

[105] Petrosyan A. G. et al. Bridgman growth and site occupation in LuAG:Ce scintillator crystals //Journal of Crystal Growth. – 2010. – I. 312. – №. 21. – P. 3136-3142.

[106] Nikl M. et al. Development of novel scintillator crystals //Journal of crystal growth. – 2006. – I. 292. – №. 2. – P. 416-421.

[107] Di J. et al. Crystal growth and optical properties of LuYAG:Ce single crystal //Journal of Crystal Growth. – 2012. – I. 351. – №. 1. – P. 165-168.

[108] Babin V. et al. Luminescence and ESR Study of Irregular Ce Ions in LuAG:Ce Single Crystals //Nuclear Science, IEEE Transactions on. – 2008. – I. 55. – №. 3. – P. 1156-1159.

[109] Nikl M. et al. Energy transfer and storage processes in scintillators: The role and nature of defects //Radiation measurements. – 2007. – I. 42. – №. 4. – P. 509-514.

[110] Pedrini C. Scintillation mechanisms and limiting factors on each step of relaxation of electronic excitations //Physics of the Solid State. – 2005. – I. 47. – №. 8. – P. 1406-1411.

[111] Moszyński M. et al. Properties of the YAG:Ce scintillator //Nuclear Instruments and Methods in Physics Research Section A: Accelerators,

Spectrometers, Detectors and Associated Equipment. – 1994. – I. 345. – №. 3. – P. 461-467.

[112] Mares J. A. et al. Scintillation response of Ce-doped or intrinsic scintillating crystals in the range up to 1MeV //Radiation Measurements. – 2004. – I. 38. – №. 4. – P. 353-357.

[113] Dong Y. et al. Color centers and charge state change in Ce: YAG crystals grown by temperature gradient techniques //Journal of crystal growth. – 2006. – I. 286. – №. 2. – P. 476-480.

[114] Moszynski M. et al. Absolute light output of scintillators //Nuclear Science, IEEE Transactions on. – 1997. – I. 44. – №. 3. – P. 1052-1061.

[115] Zorenko Y. et al. Single-crystalline films of Ce-doped YAG and LuAG phosphors: advantages over bulk crystals analogues //Journal of luminescence. – 2005. – I. 114. – №. 2. – P. 85-94.

[116] Nikl M. et al. The antisite LuAl defect-related trap in $Lu_3Al_5O_{12}$:Ce single crystal //physica status solidi (b). – 2005. – I. 242. – №. 14. – P. R119-R121.

[117] Ogino H. et al. Scintillation characteristics of Pr-doped $Lu_3Al_5O_{12}$ single crystals //Journal of crystal growth. – 2006. – I. 292. – №. 2. – P. 239-242.

[118] Mares J. A. et al. Scintillation properties of Ce^{3+}-and Pr^{3+}-doped LuAG, YAG and mixed $Lu_xY_{1-x}AG$ Garnet Crystals. Nuclear Science //IEEE Transactions on. – 2012.

[119] Drozdowski W. et al. 33000 photons per MeV from mixed $(Lu_{0.75}Y_{0.25})_3Al_5O_{12}$:Pr scintillator crystals //Optical Materials Express. – 2014. – I. 4. – №. 6. – P. 1207-1212.

[120] Robertson J. M. et al. Cathodoluminescent garnet layers //Thin Solid Films. – 1984. – I. 114. – №. 1. – P. 221-240.

[121] Galindo R. et al. Synthesis and characterisation of chromium lutetium gallium garnet solid solution //Materials research bulletin. – 2007. – I. 42. – №. 3. – P. 437-445.

[122] Geller S. Crystal chemistry of the garnets //Zeitschrift für Kristallographie-Crystalline Materials. – 1967. – I. 125. – №. 1-6. – P. 1-47.

[123] Liu B. et al. Luminescence and energy transfer processes in $Lu_2SiO_5:Ce^{3+}$ scintillator //Journal of luminescence. – 2006. – I. 117. – №. 2. – P. 129-134.

[124] Ricci P. C. et al. Ce^{3+}-doped lutetium yttrium orthosilicate crystals: Structural characterization //Materials Science and Engineering: B. – 2008. – I. 146. – №. 1. – P. 2-6.

[125] Pidol L. et al. EPR study of Ce^{3+} ions in lutetium silicate scintillators $Lu_2Si_2O_7$ and Lu_2SiO_5 //Journal of Physics and Chemistry of Solids. – 2006. – I. 67. – №. 4. – P. 643-650.

[126] Melcher C. L. Manufacturing a cerium-doped lutetium oxyorthosilicate boule // patent WO. – 2002. – I. 2002068733.

[127] Bondar V. et al. Optico-luminescent properties and mechanical strength of G(Y)SO:Ce crystals //Proceedings of SCINT. – 2005. – P. 251–253.

[128] Voloshina O. V. et al. Growth and scintillation properties of gadolinium and yttrium orthovanadate crystals //Nuclear Instruments and Methods in Physics Research Section A: Accelerators, Spectrometers, Detectors and Associated Equipment. – 2012. – I. 664. – №. 1. – P. 299-303.

[129] Brandle C. D. et al. Czochralski growth of rare-earth orthosilicates (Ln_2SiO_5) //Journal of Crystal Growth. – 1986. – I. 79. – №. 1. – P. 308-315.

[130] Usui T. et al. 60 mm Diameter $Lu_{0.4}Gd_{1.6}SiO_5$:Ce (LGSO) Single Crystals and Their Improved Scintillation Properties //Nuclear Science, IEEE Transactions on. – 2007. – I. 54. – №. 1. – P. 19-22.

[131] Samanta G. et al. Analysis of limits for sapphire growth in a micro-pulling-down system //Journal of Crystal Growth. – 2011. – I. 335. – №. 1. – P. 148-159.

[132] Samanta G. et al. Parametric sensitivity and temporal dynamics of sapphire crystal growth via the micro-pulling-down method //Journal of Crystal Growth. – 2012. – I. 359. – P. 99-106.

[133] Fang H. et al. Study of melt convection and interface shape during sapphire crystal growth by Czochralski method //International Journal of Heat and Mass Transfer. – 2012. – I. 55. – №. 25. – P. 8003-8009.

[134] Fang H. S. et al. Numerical Study of the Micro-Pulling-Down Process for Sapphire Fiber Crystal Growth //Crystal Growth & Design. – 2010. – I. 11. – №. 1. – P. 121-129.

[135] Wildermuth S. et al. Crystalline $Bi_4Ge_3O_{12}$ fibers fabricated by micro-pulling down technique for optical high voltage sensing //Procedia Engineering. – 2011. – I. 25. – P. 507-510.

[136] Ghezal E. A. et al. Effect of Pulling Rate on Bubbles Distribution in Sapphire Crystals Grown by the Micropulling Down (μ-PD) Technique //Crystal Growth & Design. – 2012. – I. 12. – №. 8. – P. 4098-4103.

[137] Ghezal E. A. et al. Observation of Gas Bubble Incorporation during Micropulling-Down Growth of Sapphire //Crystal Growth & Design. – 2012. – I. 12. – №. 11. – P. 5715-5719.

[138] Nakatsuka A. et al. Cation distribution and crystal chemistry of $Y_3Al_{5-x}Ga_xO_{12}$ (0 x 5) garnet solid solutions //Acta Crystallographica Section B: Structural Science. – 1999. – I. 55. – №. 3. – P. 266-272.

[139] Ashurov M. K. et al. Spectroscopic study of stoichiometry deviation in crystals with garnet structure //physica status solidi (a). – 1977. – I. 42. – №. 1. – P. 101-110.

[140] Stanek C. R. et al. The effect of intrinsic defects on RE3Al5O12 garnet scintillator performance //Nuclear Instruments and Methods in Physics Research Section A: Accelerators, Spectrometers, Detectors and Associated Equipment. – 2007. – I. 579. – №. 1. – P. 27-30.

[141] Nikl M. et al. Shallow traps and radiative recombination processes in $Lu_3Al_5O_{12}$: Ce single crystal scintillator //Physical Review B. – 2007. – I. 76. – №. 19. – P. 195-121.

[142] Belsky A. N. et al. Progress in the development of $LuAlO_3$-based scintillators //Nuclear Science, IEEE Transactions on. – 2001. – I. 48. – №. 4. – P. 1095-1100.